Modeling and characterization of the time-dependent behavior of the fractured zone around underground storage structures in Callovo-Oxfordian claystone

Sophie Jung

Thèse

soumise pour l'obtention du grade de
Docteur de l'Université Gustave Eiffel
Ecole Doctorale Sciences, Ingénierie et Environnement (SIE)

par

Sophie JUNG

Modeling and characterization of the time-dependent behavior of the fractured zone around underground storage structures in Callovo-Oxfordian claystone

---

Spécialité : *Géotechnique*

To be defended on 22 September 2022 before the jury:

Chloé	Arson	Georgia Institute of Technology	Reviewer
Philippe	Causenza	Université de Poitiers	Reviewer
Mountaka	Souley	Ineris	Examinator
Jian-Fu	Shao	Université de Lille	Examinator
Amade	Pouya	Université Gustave Eiffel	Supervisor
Michel	Bornert	Ecole des Ponts ParisTech	Co-Supervisor
Siavash	Ghabezloo	Ecole des Ponts ParisTech	Co-Supervisor
Minh Ngoc	Vu	ANDRA	Co-Supervisor
Jean	Sulem	Ecole des Ponts ParisTech	Invited

Abstract

The French national agency for radioactive waste management (ANDRA) is studying the feasibility of a radioactive waste burial project in the Callovo-Oxfordian clay formation (COx). To carry out its studies, ANDRA has supervised the construction of an underground laboratory (URL) at Bure (Meuse/ Haute Marne, France). In the framework of the study presented here, we are particularly interested in the convergence measurements of these galleries, and in the effect of the fracturing zone, induced by the excavation of the tunnels. The instrumentation of the URL tunnels revealed two types of drifts in terms of fractured zones and convergences depending on whether the tunnels are excavated in the direction of the major principal horizontal stress or the minor principal horizontal stress. In the first case, the state of stress in a section is almost isotropic and the horizontal convergence is greater than the vertical convergence, while in the other type of gallery, where the horizontal stress is greater than the vertical stress, the vertical convergence is greater than the horizontal convergence. In the scientific literature, there is a lot of work on modeling these two types of galleries. Many approaches have been considered to try to model the anisotropy of both the convergence and the convergence rate measured in these two types of galleries. In the work presented here we have assumed that the long-term behavior is governed by viscous slip on shear fractures present in the fractured zones around the drifts. In a first approach we model the environment in which the galleries are excavated by a continuous homogeneous transverse isotropic material. The model used is already available in the FEM code Disroc under the name ANELVIP [35]. The anisotropy (elastic-plastic and viscous) represents the fracture behavior, and the direction of the isotropy plane corresponds, in a simplified way, to the direction of the main shear fractures present in the fractured zone. The different anisotropy parameters are numerically calibrated on the convergence measurements of the URL galleries. The convergence and convergence rates of the two types of galleries are thus modeled, keeping the same parameters of the elasto-visco plastic laws, simply by changing the orientation of the isotropy plane between the two models and the anisotropy parameters. However, the link between the anisotropy parameters and the behavior that a fracture would exhibit is not clear and the physical understanding of the anisotropy parameters is the subject of the second part of this numerical modeling work. We set up an experimental device to study the creep of a fracture. The purpose of this study is to measure experimentally the physical parameters describing the creep along the fracture and then to introduce the fracture behavior in numerical models. This experimental protocol allows a detailed understanding of fracture behavior thanks to Digital Image Correlation.

We have linked, by homogenization techniques, the anisotropy parameters of the ANELVIP model to physical parameters of the fractures. A coring campaign around the ANDRA galleries provided us with the statistical data necessary to propose a description of the fractured zone around the two types of URL galleries, in terms of fracture density and orientation. All this allowed us to make new simulations with a medium divided into several zones, first the healthy rock supposed to be isotropic, then the anisotropic fractured zone, itself subdivided into 3 zones of different orientation and fracture density.

Abstract (different language)

L'agence nationale pour la gestion des déchets radioactifs (ANDRA) étudie la faisabilité d'un projet d'enfouissement de déchets radioactifs dans la formation argileuse de Callovo-Oxfordien (COx). Pour mener à bien ses études, l'ANDRA a supervisé la construction d'un laboratoire souterrain (URL) à Bure (Meuse/ Haute Marne). Les galeries constituant le laboratoire font l'objet de nombreuses expérimentations. Dans le cadre des travaux présentés ici, nous nous sommes plus particulièrement intéressés aux mesures de convergences sur ces galeries, ainsi que l'effet de la zone de fracturation, induite par l'excavation des tunnels sur la convergence de ces galeries. L'instrumentation des galeries de l'URL a mis en évidence deux types de galerie en terme de zone fracturée et de convergences selon si les galeries sont excavées dans la direction de la contrainte principale majeure ou de la contrainte principale mineure. Dans le premier cas, l'état de contrainte dans une section est quasiment isotrope et la convergence horizontale est plus grande que la convergence verticale, alors que dans l'autre type de galerie, où la contrainte horizontale est supérieure à la contrainte verticale, c'est la convergence verticale qui est supérieure à la convergence horizontale. On trouve dans la littérature scientifique beaucoup de travaux de modélisation de ces deux types de galerie. En effet, beaucoup d'approches ont été envisagés pour essayer de modéliser l'anisotropie à la fois du taux de convergence et de convergence mesurées dans ces deux types de galeries. Dans les travaux présentés ici nous choisissons une approche un peu différente, en supposant que le comportement à long terme est régi par le glissement visqueux sur les fractures en cisaillement présent dans les zones fracturées autour des galeries. Dans une première approche nous modélisons le milieu dans lequel les galeries sont excavées par un matériau continu homogène transverse isotrope. Le modèle utilisé est présent dans le code Disroc sous le nom d'ANELVIP [35]. L'idée étant que l'anisotropie (élastique-plastique et visqueuse) représente le comportement des fractures, faisant ainsi correspondre, de façon simplifié, la direction du plan d'anisotropie, à celles des frprincipales fractures en cisaillement présentes dans la zone fracturée. Les différents paramètres d'anisotropie sont calibrés numériquement

sur les mesures de convergence des galeries de l'URL. On parvient ainsi à reproduire les convergence et taux de convergence des deux types de galeries, en modifiant l'orientation du plan d'isotropie entre les deux modèles et les paramètres d'anisotropie, tout en conservant les mêmes paramètres des lois élasto-visco plastique. Toutefois, le lien entre les paramètres d'anisotropie et le comportement qu'aurait une fracture n'est pas clair et la compréhension physique des paramètres d'anisotropie fait l'objet de la deuxième partie de ce travail de modélisation numérique. En effet, dans la mesure où l'hypothèse de ce travail est que le comportement dominant les déformations à long terme autour des galeries excavées dans le COx est le glissement visqueux des fractures, nous avons mis en place un dispositif expérimental pour étudier précisément le fluage d'une fracture dans le COx. L'objet de cette étude est de mesurer les paramètres physiques décrivant le glissement élasto-visco plastique le long de la fracture pour pouvoir ensuite introduire le comportement des fractures dans les modèles macroscopiques de convergences des galeries. Cette campagne expérimentale s'appuie sur la Corrélation Numérique d'Image pour obtenir une vue détaillée de ce qui se passe le long de la fracture. Enfin, nous avons lié les paramètres d'anisotropie du modèle ANELVIP à des paramètres physique des fractures par techniques d'homogénéisation. Une campagne de carottage autour des galeries de l'ANDRA nous a fourni les données statistiques nécessaires pour proposer une description de la zone fracturée autour des deux types de galeries de l'URL, en terme de densité et d'orientation des fractures. Tout cela nous a permis de faire de nouvelles simulations avec un milieu découpé en plusieurs zones: d'une part la roche saine supposé isotrope, puis la zone fracturée anisotrope, elle-même subdivisée en 3 zones d'orientation et de densité de fractures différentes.

Acknowledgement

This thesis work carried out in the Navier laboratory was an unexpected opportunity for me to discover the world of research in the best possible conditions. Over the past four years, I have been able to benefit from the knowledge and support of many people without whom this work would not have been possible, and whom I would like to thank.

I would like to thank Chloé Arson, Philippe Cosenza, Minh Ngoc Vu, Jian Fu Shao, Mountaka Souley for agreeing to form my thesis jury and for the review and enriching comments made on this thesis.

Je continue ensuite en français. Je tiens tout d'abord à remercier Amade Pouya mon directeur de thèse qui m'a donné l'opportunité de préparer ma thèse au laboratoire Navier avec lui. Je tiens à le remercier pour la liberté de travail dont j'ai pu bénéficier et pour sa patience, car je sais que je ne suis pas toujours la personne la plus organisée dans ma réflexion et mes présentations. Ensuite j'aimerais remercier Siavash Ghabezloo, Michel Bornert et Jean Sulem qui ont également participé à l'encadrement de ma thèse. J'ai eu la chance de travailler avec vous, et j'ai particulièrement apprécié le fait qui avez su vous rendre très disponible pour discuter avec moi. Mes nombreux échanges avec vous m'ont tant appris, merci !

Je tiens également à remercier l'équipe technique, à savoir Emmanuel, Marine, Baptiste, Loïc et Xavier pour leur aide lors des différents tests effectués au laboratoire. Avec une mention spéciale à Marine, Baptiste et Loïc que j'ai tant sollicité et qui ont toujours répondus présent et avec bonne humeur.

Aussi un grand merci à Julien et Mathias sans lesquels ma manip et mes essais n'auraient jamais vu le jour. Merci d'avoir passé tant de temps à travailler avec moi et d'avoir la plupart du temps fait preuve de beaucoup plus de patience que moi. Si nos discussions m'ont permis d'éclaircir beaucoup de bizarreries expérimentales, j'ai aussi beaucoup rigolé et vous avez rendu mon travail, même dans les moments les moins agréable, plaisant.

J'aimerai ensuite remercier tous les gens du cermes ; Sabrina Chartier, l'équipe technique, les différents chercheurs et évidement tous les autres doctorants. Venir travailler pendant 4 années avec vous a été un vrai bonheur et j'espère continuer de prêt ou de loin à travailler avec vous. J'ai eu le plaisir de discuter avec vous de mes travaux mais aussi de pleins

d'autres choses. Une mention spéciale aux footeux du mercredi midi, et aux copains du café Phil, Axelle et Baptiste.

J'aimerais également remercier tous ceux qui pendant 4 ans, voir même beaucoup plus longtemps, ont passé du temps avec moi quand je n'étais pas au laboratoire. Merci aux ami.e.s du KD qui ont su manifester leur soutien bien au-delà de nos rdv hebdomadaire du mardi soir. Merci à tous les copains de défoulage, Arthur et Charles pour l'escalade, Axelle pour les "petits" run à champs, Yann, Marine et Julien les meilleurs compagnons de trail. Mais aussi merci Antonin, Hanna, Amandine, Céline, Eliot, Philippe, Manon, Sophie, Hélène, Céline, Léa, Mélanie, Anaïs, Thomas, YaYa, Lucie, Inès, Oriane, Anaïs, Anne, Charlotte et Antonin ! Comme promis merci Kuz. Merci à ma famille de m'avoir soutenu toutes ces années, Théa, Denis, Anna, Lucie, Thomas et Lily. Et merci d'être venu fêter avec moi cette thèse. Bravo Lily d'avoir patiemment assisté à ma soutenance, promis je serais au moins toute aussi sage pour la tienne. Merci aussi à vous Hubert, Cathy, Anne et Antoine d'avoir fait le voyage jusqu'à Champs-sur-Marne pour assister à ma soutenance. J'ai aussi une pensée toute particulière pour Bom et Jo qui n'ont pas être là. Merci à Judith et Vincent pour votre amitié sans faille et pour tout le soutient que vous m'avez apporté pendant la rédaction de mon manuscrit. Marine et Julien également: A vous tous, le simple mot merci n'est pas à la hauteur de ce que je pense, mais il résume néanmoins synthétiquement la situation, alors pour finir merci à toi aussi Mathieu.

Contents

1 Introduction

Background

In France, nuclear power is the leading source of electricity production, representing 70% of the energy mix. It comes from 56 reactors of different power plants spread throughout the country. At a time when European countries have decided to achieve carbon neutrality by 2050, when reliance on Russian gas is a concern, and when energy prices are skyrocketing, nuclear energy represents a crucial asset. Moreover, in the current context of global warming, nuclear energy is positioned as an interesting option as it is a low carbon energy, which is why the European Commission has decided to consider nuclear energy as a transitional energy. Furthermore, regardless of the politicians' position on nuclear energy, a solution must be found for the already existing nuclear waste. The waste produced by the nuclear industry is not recyclable and in France the decision has been taken to store the waste. This is already the case for 90% of the waste, which is qualified as Low- and Intermediate-Level, Short-Lived wastes, and Very Low-Level wastes which are stored in sub-surficial locations. Nevertheless, the 10% of waste qualified as High-Level and Intermediate-Level, Long-Lived wastes, which represents more than 90% of the total radionuclide emissions, is the main problem [84]. France, as some other countries, is considering using deep disposal facilities for radioactive waste. The deep geological repository is based on the identification of favorable geologic formations characterized by structural, hydromechanical, and geochemical properties able to efficiently isolate radionuclide dispersal and ensure the construction and operation of storage facilities. These types of formations are identified as host rocks because of their geologic characteristics (e.g., salt, clays and shales). In France, it the responsibility of the French national radioactive waste management agency, ANDRA (Agence Nationale pour la gestion de déchets radioactifs) to identify a host rock and supervise the feasibility studies for a deep geological repository. Because of characteristics such as very low permeability and reduced molecular diffusion, Callovo-Oxfordian (COx) claystone is currently being studied as a potential candidate host rock [5, 28]. The mission of ANDRA is to design a geological repository and to ensure its safety for millions of years after its closure. Moreover a medium-term reversibility for about 100 years is also required. To carry out its mission, ANDRA has designed the Cigéo project (Centre Industriel de Stockage Géologique, which stands for Industrial center for geological disposal). The main level of the disposal will be divided into two main zones depending on the type of

waste (Intermediate level long lived waste or high level waste) and the type of excavation method.

Objectives of the work

Clay formations seem to present, in their natural undisturbed state, a very favorable environment for nuclear waste disposal due to their confinement properties: low permeability, low diffusion coefficients and good retention capacity for radionuclides. Nevertheless, the excavation of the galleries induces a stress redistribution which generally leads to the creation of a damaged zone. This damaged zone has different mechanical and hydraulic properties compared to the undisturbed rock and its effects on the global behavior of the rock formation around the drifts needs to be taken into account.

The fracturing pattern that is induced by the excavation of drifts in clay rock formation is a complex problem to study by itself. Theoretically it is expected that in any bedded rock exhibiting an anisotropic (transversely isotropic) behavior, a circular hole is deformed into an overall oval shaped hole, with its principal axes parallel and orthogonal to the bedding planes, even if the far field stress would be isotropic [47]. The difficulty is that when observations are made in two different bedded rocks (Opalinus Clay and Boom Clay), for the same mechanical conditions, the damaged zone is developing in reverse direction. This observation seems to indicate two different modes of failure in these two clays. Shear failure along conjugated planes seems, in the plastic Boom Clay, to result in a damaged zone extending in the horizontal direction, while bedding plane splitting and buckling occur in the indurated Opalinus Clay resulting in a damaged zone extending in the vertical direction [47]. Moreover, when it comes to the COx claystone, which is the rock investigated in this work, even though it is a hard and indurated rock more like Opalinus Clay, a fracture pattern similar to that observed in Boom Clay is observed for drifts and micro-tunnels parallel to the major horizontal stress (e.g. GCS drift) [4]. This shows the complexity of the mechanisms leading to the fracture pattern in the excavation damaged zone.

In-situ observations at the Meuse/Haute-Marne Underground Research Laboratory (MHM URL) provide valuable data regarding the impact of excavation rate, excavation techniques and support types on the convergence of the drifts. They show that the mechanical response of the COx claystone to the excavation of the drifts depends on different features such as the in-situ stress state, the orientation of the drift with respect to the principal horizontal stresses, the excavation method, and the intrinsic anisotropy of the rock. Continuous monitoring of the drifts' convergences and the excavation zones has shown a progressive anisotropic convergence and the development of an asymmetrical fractured zone around the drifts, with extensional and shear fractures [4]. It seems that the convergence anisotropy can

be explained by the geometry of the fractured zone. The directions of the convergence anisotropy and the geometry of the fractured zone depend on the direction of the drift with respect to the principal horizontal stresses, as will be explained in more details in the first chapter.

The aim of this work is to model the mechanical behavior of the rock formation containing the fractured zone around different drifts in the MHM URL, and mainly its viscous behavior observed during the convergence monitoring of the drifts post-excavation. The modeling of the viscous behavior of the rock mass around the drifts is important to ensure the long-term integrity and performances of the linings. The development of the fractured zone around the drifts during the excavation process is beyond the scope of this work and we will focus on providing a time-dependent model reproducing the displacement measured at the wall of the two types of tunnels of the URL. This will provide an efficient tool to design the supports, which takes into account the long term rock/lining interaction. As a matter of fact, the convergences of the drifts have to be well reproduced and extrapolated to long time periods in order to estimate the pressures applied by the drift convergence on the lining. The objective is to propose an effective model and sufficiently simple model which can be used for design of the drifts linings, as well as for the reliability analysis [30]. The mechanisms of fracturing are not explicitly modeled, but their effects are taken into account. We focus on reproducing the long term anisotropic convergences resulting from the anisotropic viscous behavior of the fractured zone with its specific directions. It should be noted that the undisturbed COx claystone has also its proper anisotropy due to its bedded microstructure. The directions of this anisotropy are the same for all the galleries, whereas the direction of the induced anisotropy is different in drifts excavated in different directions. In all along the work the focus is on the viscous behavior of the fractures in the fractured zone. In addition, the sole anisotropy under consideration is the one related to the effect of the fractures. In other words, the intrisic anisotropy of the bedded rock is assumed to be negligible with respect to the anisotropy induced by the fractures.

Structure of the manuscript

The present manuscript is organized in five chapters, separated in numerical and experimental parts, and preceded by an introduction and completed by a conclusion. Eventually, two chapters are dedicated to numerical simulations at the scale of the drifts, followed by two other chapters dedicated to the setting up of an original experimental device to study the creeping behavior of a fracture in COx claystone.

After the introduction, chapter two is a general presentation of the context of this research. The Underground Research Laboratory is first presented along with the main features of the

COx claystone. A brief section is devoted to rock discontinuities. Finally, some mechanical features helpful to the full understanding of the work are recalled.

Chapter three presents a first approach to numerical simulations of the long term convergences of drifts of the URL. Continuous transverse isotropic models are used to reproduce the convergences of the two types of drifts excavated in the URL. The approach chosen in this work is focused on the viscous anisotropy of the COx claystone induced by the fractures. The models presented in this chapter are the most simplified way to take this anisotropy into account.

Chapter four presents another approach to numerical simulations. In a way, the models presented in this chapter are a deepening of the models presented in the previous chapter. But above all, it consists of numerical models that make the bridge between the numerical part and the experimental part of this thesis. Therefore, an explicit link between the anisotropy parameters and the behavior of the fractures is established in this chapter.

Chapter five is dedicated to the presentation of the experimental set up design to study the viscous slip of a fracture in COx claystone. First, the device is described, its objectives are presented and the experimental protocol is given. The second part of the chapter is dedicated to the presentation of Digital Image Correlation used to track the displacement along the interfaces.

Chapter six presents the experimental results. First, numerical simulations of the experience are conducted to provide a key to reading the experiments. The rest of the chapter mostly focuses on two tests. First one in which several increasing shear stresses are applied (referred to as the multilevel test) and another one with only one, larger, loading level (so-called single level test). The chapter ends by proposing an improved experimental protocol to fully succeed in characterizing the viscous slip of a fracture.

Chapter seven is a synthesis of the different conclusions drawn from the different chapters as well as the perspectives opened by the work presented in the manuscript.

Preliminary considerations

2

In this first chapter, the background of this thesis work is given. The objective is to model the long-term behavior of the URL tunnels, which are excavated in the COx claystone. Since the excavation of these tunnels causes the creation of a fractured zone and that the measured convergences seem to be correlated to it, it was assumed that the viscous behavior of the fractured rock is the key element controlling the long-term behavior of the tunnels. Thus, the work presented in this manuscript is articulated at two scales: at the structural scale, we are interested in the time-dependent behavior of the drifts. And, at the fracture scale, we are interested in the viscous slip along a discontinuity in the COx claystone. The idea is to eventually combine these two studies by proposing a tunnel convergence model in which the fracture behavior would be introduced.

The numerical simulations in the next two chapters are performed at the tunnel scale (a few meters), while all the work related to the characterization of the fracture behavior was carried out at the laboratory sample scale (a few centimeters). With respect to the work at the tunnel scale, a description of the underground research laboratory is presented. Particular attention is given to two galleries, as most of the *in situ* observations and measurements mentioned throughout the manuscript relate to them. A general description of the COx claystone is provided since all the work presented in the manuscript is related to this specific material. The first half of the manuscript being devoted to the time-dependent modeling of drift, the relevant theoretical framework is recalled. The second part of the manuscript is placed at the scale of a fracture. Thus, the classical approach to study and describe the behavior of a fracture is presented.

2.1 The Underground Research Laboratory

2.1.1 Drifts network

The feasibility phase of the Cigeo project is supported by the Underground Research Laboratory (URL), found between 420 and 550m below the ground level, which has started to be constructed in 2000 in Meuse/Haute-Marne. It consists of a network of main drifts, service galleries, micro-tunnels and two access shafts to enable the access from the surface

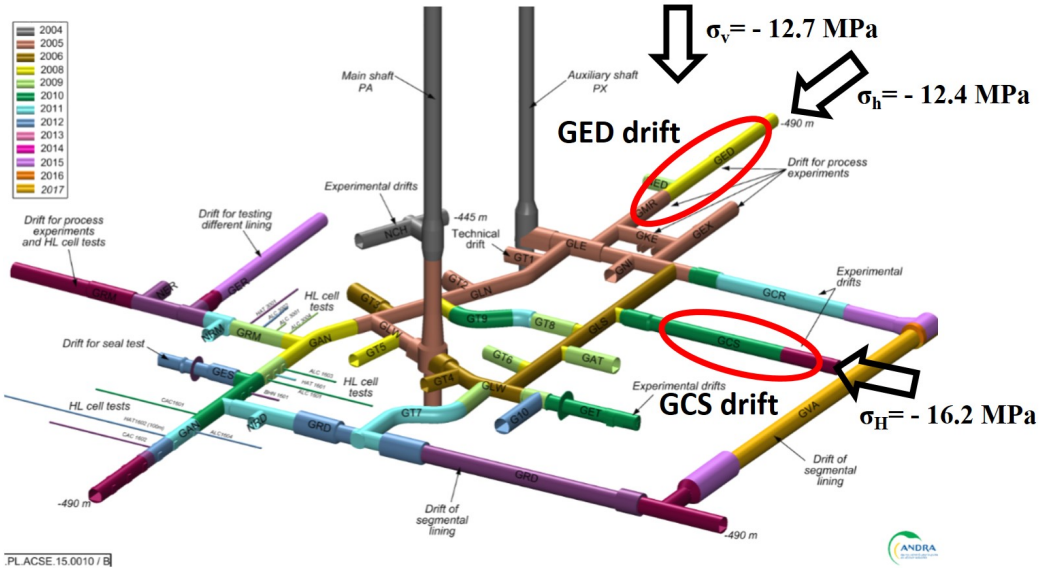

Fig. 2.1.: Map of the drifts at the Meuse/Haute-Marne Underground Research Laboratory

facilities. The different drifts have different diameter extensions, from 1 meter for the micro-tunnels, to 4 to 9 meters for the other drifts. The laboratory, represented in Figure 2.1, has been built to test and demonstrate the feasibility of the geological repository. The laboratory is designed as a real-scale experiment to characterize the response of the rock. The monitoring of the drifts of the URL provides valuable data regarding the impact of excavation rate, excavation techniques and support types on the convergence of the drifts. They show that the mechanical response of the COx claystone to the excavation of the drifts depends on different features such as the *in situ* stress state, the orientation of the drift with respect to the principal horizontal stresses, the excavation method, and the intrinsic anisotropy of the rock.

The *in situ* stress state in MHM URL is anisotropic with $\sigma_v \approx -12.7$ MPa, $\sigma_h \approx -12.4$ MPa and $\sigma_H \approx -16$ MPa [91]. Consequently, depending on its orientation, a drift may be subjected to an isotropic or anisotropic stress state in its cross sections. Drifts of the URL have been horizontally excavated, and they follow, in most cases, the direction of the two principal horizontal stress components σ_h and σ_H [5, 4, 28]. **Throughout the work presented here, we will only consider these two types of drifts and most of the time we will use the data related to the GCS drift to account for the behavior of drifts excavated in the direction of the major principal horizontal stress σ_H, and the data related to the GED drift to account for the behavior of drifts excavated in the direction of the minor principal horizontal stress σ_h.** The two drifts are circled in red in Figure 2.1. The GCS

drift is subjected to a rather isotropic stress state (σ_h , σ_v) in its cross section, while the GED drift is subjected to an anisotropic stress state (σ_H, σ_v). The excavation of the drifts in the COx claystone have shown to create a *fractured zone* in the vicinity of the tunnels wall. Since fractured rock can affect the overall behavior of drifts, extensive surveys have been conducted to investigate the fractured zone. 3D map of the excavation induced fractured zone, in the front and sides of the drifts, was obtained by a scan procedure. The analysis of

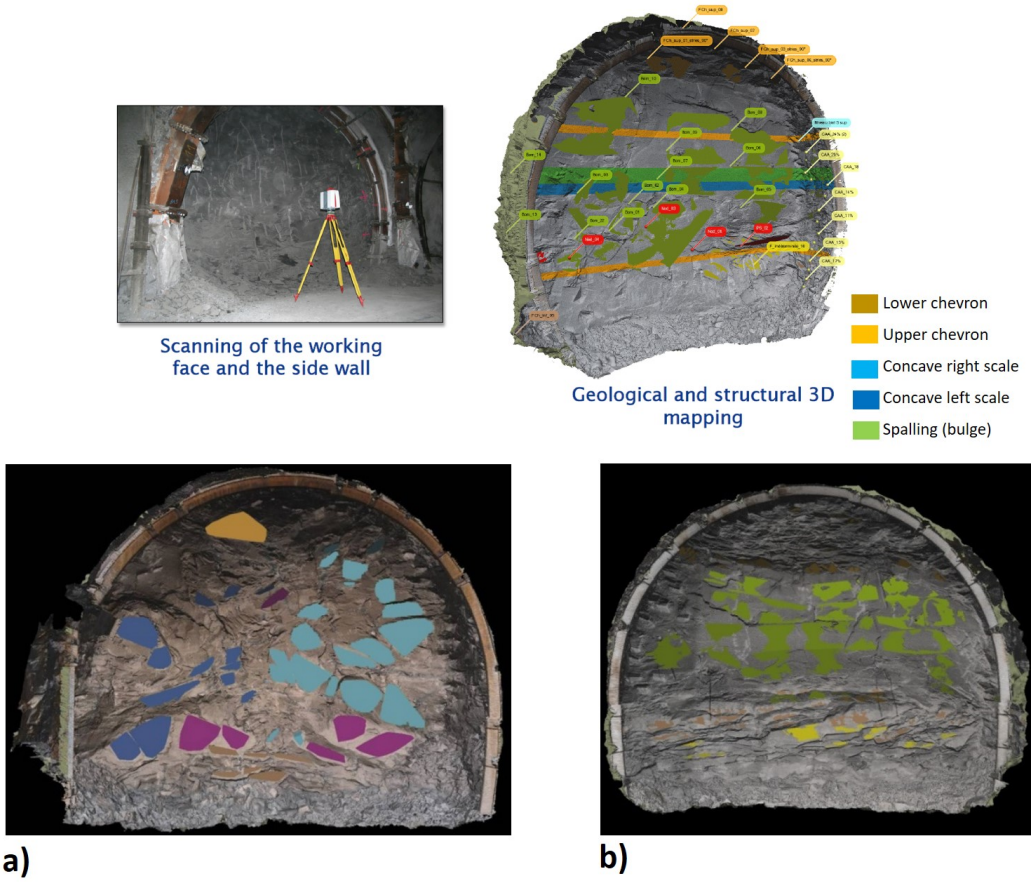

Fig. 2.2.: 3D scan analysis around the inside of the drifts [4] a) interpretation of the scan for the GED drift, b) interpretation of the scan for the GCS drift.

the scans is presented in Figure 2.2. Besides, resin-injections tests have been carried out before core were drilled around the drifts as presented in Figure 2.3. This procedure consists in injecting resin into a small diameter borehole and then come over-core around this first borehole to visualize the network of fractures that has been impregnated. Further discussion on the description of fractured zones will be conducted in section 4.2 of Chapter 3.

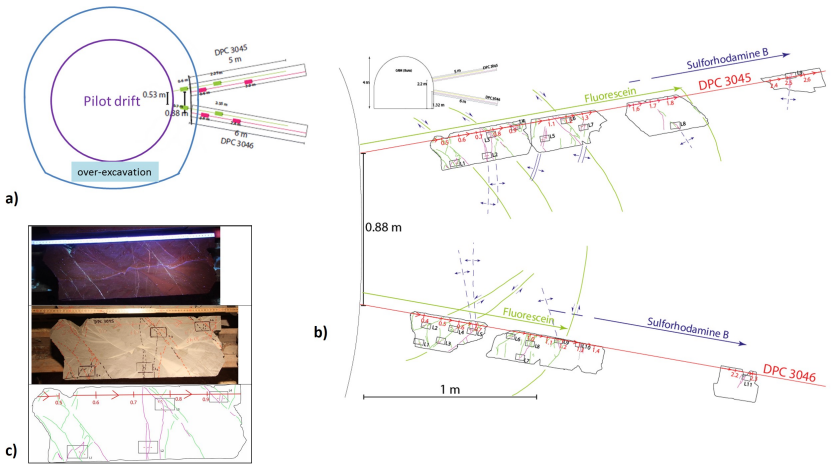

Fig. 2.3.: a) and b) Procedure of resin injection before operating an over-excavation, c) analysis of the core with UV light to reveal the fractures.

GED drift

The GED drift was excavated in 2008 along the minor principal horizontal stress at -490 m, which corresponds to the main level of the laboratory. The state of stress in its cross section is anisotropic, with the horizontal stress being about 30% larger than the vertical one. The drift has a horse shoe section with a radius of approximately 2.3m. Convergence has been measured in six sections and two sections of extensometers have been emplaced [5]. A great number of boreholes have been drilled and cored to analyze the excavation induced fractured zone. It expands mainly in the vertical direction by 0.6 to 0.8 times the diameter of the excavation (Figure 2.4) [4]. Its extension is more limited in the horizontal direction and reaches only about 0.1 diameter. Inside the fractured zone, there is the connected fractured zone where both extensional and shear fractures coexist. The extent of this zone is about 0.3 to 0.4 diameter from the drift wall in the vertical direction. Beyond the connected fractured zone, there are only shear fractures.

Figure 2.4 presents the convergence measurements at six instrumented sections. The observations show a clear anisotropic time-dependent behavior both in terms of magnitude and rate. The ratio between vertical and horizontal convergences is about 4 after the first three months. The horizontal convergence seems to stabilize after six months while the vertical convergence increases with a strain rate of about $10^{-12}s^{-1}$ one year after the excavation.

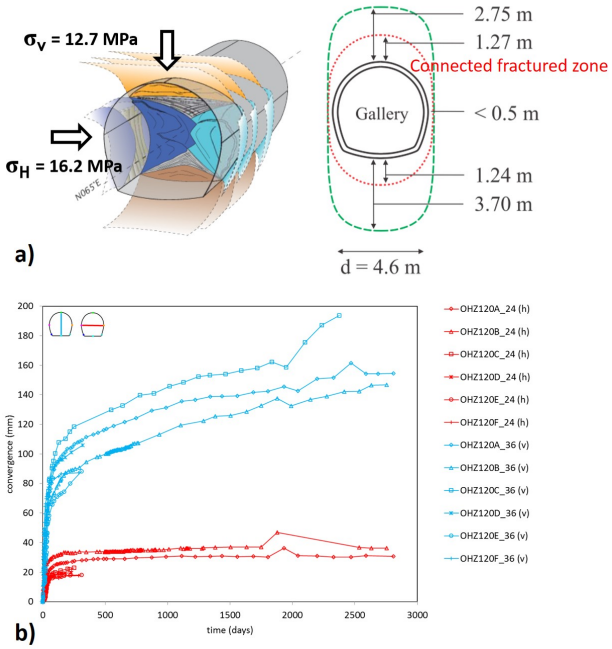

Fig. 2.4.: Conceptual model of GED: Figure taken from [4]. a) Schematic representation of the extension of the fractured zone, b) vertical and horizontal convergences measured on different cross-sections of the GED drift.

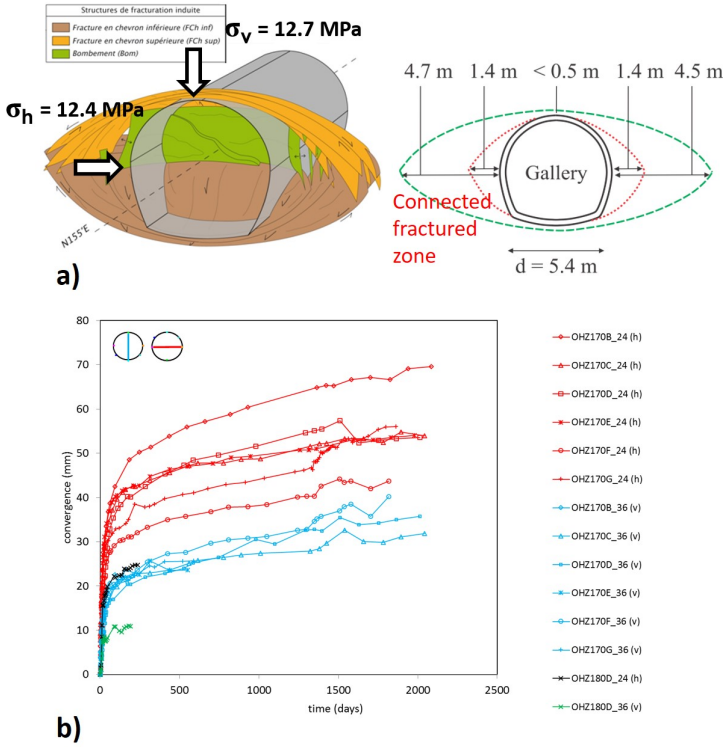

Fig. 2.5.: Conceptual model of GCS: Figure taken from [4]. a) Schematic representation of the extension of the fractured zone, b) horizontal and vertical convergences measured on different cross-sections of the GCS drift.

GCS drift

The GCS drift was excavated along the major principal horizontal stress at the main level of the MHM URL. The state of stress in its cross section is rather isotropic with $\sigma_v = -12.7$ MPa and $\sigma_h = -12.4$ MPa. The drift was excavated with a road header, and its sections are circular with a 2.6 meters radius. The fractured zone expands mainly in the horizontal direction by 0.9 times the diameter of the excavation (Figure 2.5) [4]. Its extension is more limited in the vertical direction, and reaches less than 0.1 diameter. Similarly to the fractured zone around the GED drift, inside it, there is a connected fractured zone where both extensional and shear fractures coexist. The extent of this zone is about 0.3 diameter from the drift wall in the horizontal direction. Beyond the connected fracture zone, there are only shear fractures. Figure 2.5 presents the convergence measurements at six instrumented sections, showing a bigger horizontal convergence than the vertical one.

For more than 10 years, modeling the hydro-mechanical responses to the excavation of both above described drifts of the MHM URL (GED and GCS drifts) has been the center of interest of several numerical research teams. A benchmark exercise supervised by ANDRA

provides an overall view of the modeling results aiming at reproducing the field observations [75]. Many different approaches have been proposed to try to reproduce the extension of the fractured zone: Modeling based on discrete elements as shown in Figure 2.6 [95], as

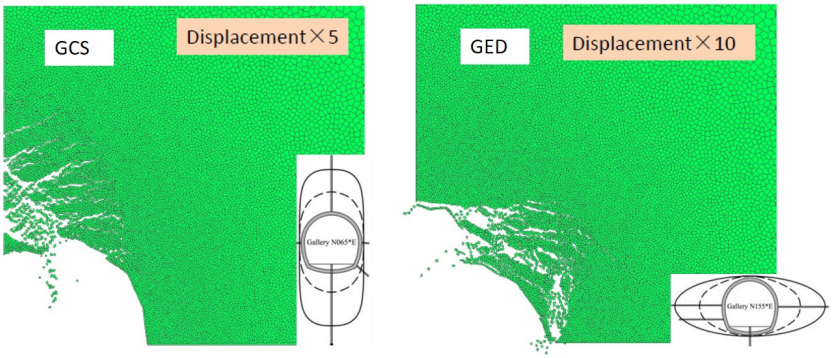

Fig. 2.6.: Simulations of the extension of the fractured zones in both types of drifts using a rigid body spring model with hydromechanical couplings and with anisotropy in the strength resistance [95].

well as continuum mechanics approaches have been considered [55, 62, 61, 78, 83]. In Figure 2.7, simulations of the extension of the fractured zone have been reproduced with softening damage. Isotropic elasto-visco-plastic models have been adapted to reproduce

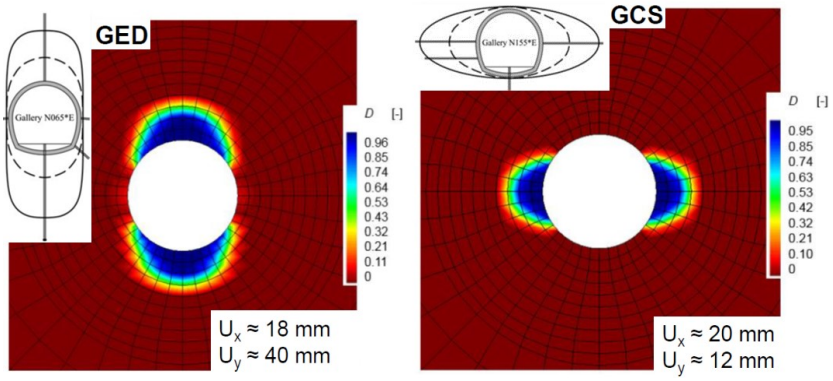

Fig. 2.7.: Simulations of the extension of the fractured zones in both types of drifts using a softening damage model [83].

satisfactorily the observations around the GED drift but failed in the case of the GCS drift [78, 26]. Inherent anisotropy in plasticity or the introduction of weakness planes were often required to model the anisotropic responses both in the excavation damage zone, and in the convergence [55, 62, 61, 79, 80]. Moreover, in order to succeed in modeling the *in situ* observed convergences and damaged zones, the hydro-mechanical coupling and advanced numerical models had to be introduced, such as non-local constitutive models shown in Figure 2.8 [58, 56, 57], second gradient regularization [61], or phase-field type models for

fractures [96, 97], allowing to improve the results. However, some *in situ* observations

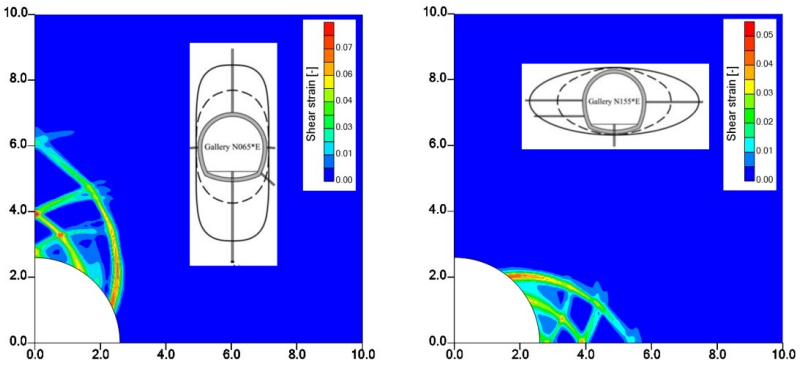

Parallel to the minor horizontal stress Parallel to the major horizontal stress

Fig. 2.8.: Simulations of the extension of the fractured zones in both types of drifts introducing non-local plasticity modeling of strain localization [58].

seem to be out of reach for such approaches, among which one can particularly mention the anisotropic time-dependent convergences of the GED drift in terms of its vertical/horizontal convergence ratio and rate. As mentioned earlier, while this drift is under an anisotropic stress state in its cross section, with the horizontal stress bigger than the vertical one, the vertical convergence is four times bigger than the horizontal one. While elasto-plastic models are rather easily able to predict a bigger vertical convergence than the horizontal one, they generally fail to reproduce the magnitude of the vertical/horizontal convergence rate ratio. However, looking at the convergence curves of the GED drift (see Figure 2.4), one can notice that the vertical convergence is evolving with a higher rate than the horizontal one for more than four years after the excavation. In other words, the *in situ* measurements in the GED drift show a progressive increase of the vertical/horizontal convergence ratio with time. This observation, which is also highlighted by [42], clearly shows the need for an anisotropic time-dependent model to reproduce the measured convergence in the GED drift. Moreover, the GCS drift also presents an anisotropic convergence, despite its quasi isotropic stress state in its cross section. However, the anisotropy in viscosity has not been taken into account in the above mentioned constitutive models.

2.1.2 The Callovo-Oxfordian claystone

Argillaceous rocks have been extensively studied for more than 20 years. The Callovo-Oxfordian claystone is one of the well-known soft rock/hard soil formations, such as Boom Clay in Belgium and Opalinus Clay in Switzerland, which are widely studied for European nuclear waste disposal projects [11, 47]. The mineralogical composition of the COx includes

mainly illite and smectite clay minerals, quartz and carbonate [70]. Microstructural analysis reveals a mean pore diameter of about 20 nm [73], which leads to very low permeability values. The average claystone porosity is equal to 18±1% and natural water contents of core samples is between 5 and 8% [40]. Callovo-Oxfordian clay is a sedimentary rock, and because of its layered structure, it exhibits anisotropic behavior. In fact, it has a double anisotropy, both in the hydromechanical properties and in the *in situ* stress state [91]. Different Young's moduli are measured when the direction of the uniaxial loading changes from parallel to perpendicular to the horizontal bedding planes [19, 98]. Compressive strength of the material also depends on the loading orientation regarding to the bedding planes as presented in Figure 2.9. The minimum peak deviatoric stress is reached at about 45°. Figure 2.11 provides a summary of the basic properties of the COx claystone according

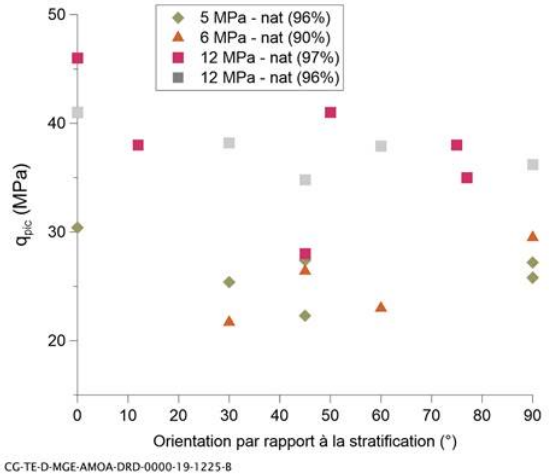

Fig. 2.9.: Peak deviatoric stress as a function of loading orientation with respect to the bedding planes during triaxial tests at different confinements [3].

to some databases in the literature. The stress-strain relation and failure of the COx-

Elastic		Plastic		Hydraulic		Microstructure	
Young's modulus (MPa)	3500-8000	Friction angle (°)	24	Biot's coeffcient	0.6	Mean pore diameter (nm)	20
Poisson's ratio	0.2-0.35	Cohesion (MPa)	3-7	Water content	0.05-0.08	Void ratio	0.22
		Uniaxial compressive strength (MPa)	17-25	Permeability (m^2)	5.10^{-20}-5.10^{-21}	Density (kg/m^3)	2300-2400
		Uniaxial tensile strength (MPa)	1.5				

Fig. 2.10.: Summary of the average properties of the COx claystone from[5, 19, 24, 37, 73, 74, 84, 90]

claystone, including its coupled thermal and hydraulic phenomena, have been extensively studied at the material point scale as well as at the drift's scale (e.g. [19, 10, 5]). Based on

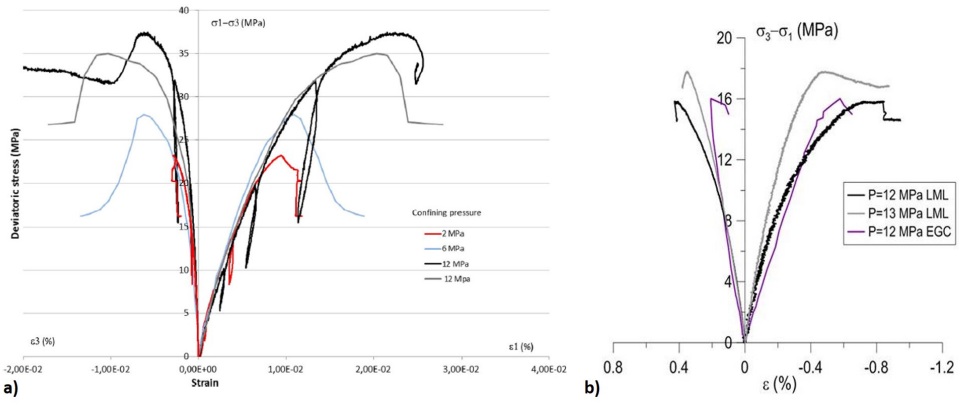

Fig. 2.11.: Triaxial tests under different confining stress a) in compression, b) in extension [6].

the laboratory studies' one can describe the COx behavior by: (a) a non-linear stress-strain behavior with a yield limit at about 50% of the maximum deviatoric stress (preceded by a short linear elastic phase under low deviatoric stresses), (b) a change in failure type upon increase in confining stress, going from brittle towards ductile, with a softening post-peak behavior [6].

Time-dependent behavior of the COx claystone

Many experimental campaigns have been dedicated to the investigation of the time-dependent behavior of the COx claystone, starting in 1996 with multi-stage creep and relaxation tests in undrained conditions under 10 MPa confinement by Ghoreychi [38]. Already in 2011, Yang et al. were interested in the time-dependent behavior of the Cox claystone [94]. They used DIC to observe the shrinkage, swelling and creep of a sample under uniaxial compression. They were particularly interested in the effect of hydration and dehydration on the response of the sample. They showed that the strain rate increases when the moisture increased: it is one order of magnitude larger at a relative humidity of 75% than at a dry state (relative humidity =25%). A few years later, the experimental campaigns have been further pursued and Liu et al. [52] have been interested in the influence of deviatoric stress and anisotropy on the creep of the COx claystone under compressive stress. They have shown that creep strains are bigger when the load is applied perpendicular to the bedding plane than when it is applied parallel to the bedding planes. Increasing strain rates are observed for higher deviatoric stresses as shown in Figure 2.12. Zhang et al., have more particularly focused on investigating the anisotropy of the mechanical properties of the COx claystone [98]. While they have observed significant time effects on the deformation and strength of the rock, they concluded that no significant anisotropic effect on creep is observed. They proposed two

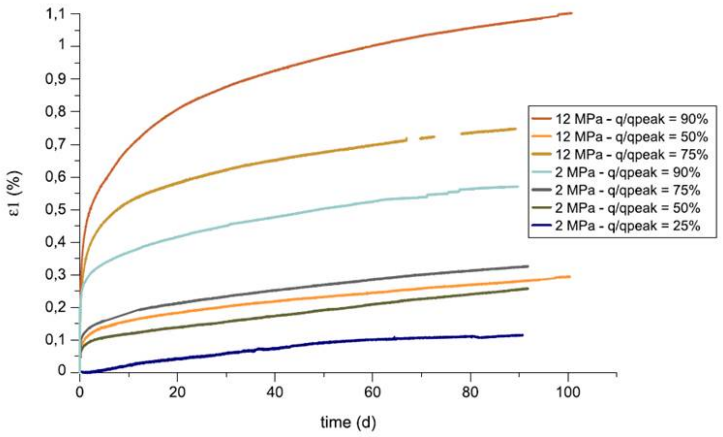

Fig. 2.12.: Triaxial creep tests under different confining stress [6].

different creep mechanisms depending on whether the rock is subjected to low or high stress. More recently, Shi et al., have analyzed the local creep strain field and cracking process in the COx claystone with micro-tomography [77]. They performed uniaxial compression tests, and they noticed a very heterogeneous strain field correlated to material heterogeneity. Due to the difference in elastic properties between a soft clay matrix and stiff inclusions, a strong stress concentration occurs at the inclusion-matrix interfaces under the applied axial stress, leading to important strain concentration in those zones. The creep deformation in the clay matrix tends to progressively relax the stress concentration and eventually the whole strain field becomes more uniform. In this experimental campaign the intrinsic anisotropy of the rock has not been further investigated.

2.1.3 Some theoretical framework

Time-dependent behavior of geomaterials

When a solid is subjected to a certain stress, an instantaneous deformation first occurs, which can be followed by a delayed response. In particular, when the applied load is kept constant, this delayed response measures the creep properties of the material. The total measured strain is usually separated into the *time-independent* and *time-dependent* strain and whether it is *stress dependent* or not. Another categorization is related to whether the strain is irreversible or not. Irreversible strain remains even when the material is unloaded. Time-independent reversible strain is referred to as *elastic* strain, while time-independent irreversible strain is referred to as *plastic* strain, and time-dependent strain is called *viscous* strain. The manifestation of delayed strain depends not only on the material itself but also on

the conditions in which the stress is applied. For instance, the time-dependent mechanical response of rocks depends on both the rock itself (mineralogy, porosity, water content) and the test conditions (applied stress, strain rate, temperature, relative humidity). The mechanical response of geomaterials in time is often studied in the framework of creep tests (under uniaxial or triaxial conditions). The principle is to apply a constant, usually deviatoric stress on a sample which is also in a controlled environment in terms of temperature and relative humidity. The viscous strain is determined by subtracting the elastic strain to the measured total strain. Note that the separation of the time-independent response from the time-dependent might not be straightforward and is particularly debatable when the loading time is not negligible compared to the total duration of the experience. During a creep test, three phases may be observed, as shown in Figure 2.13. At the beginning of the experiment,

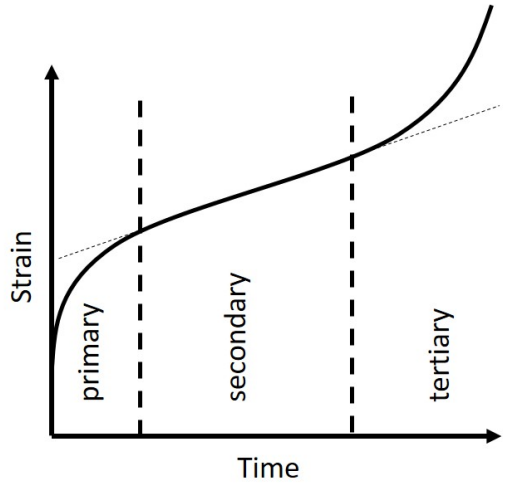

Fig. 2.13.: Three creep phases possibly observed in a sample submitted to constant stress.

primary creep phase, also called *transient creep* phase, corresponds to a decrease in creep rate. It is followed by *secondary phase* during which the creep rate remains constant. Finally, *tertiary creep* phase, characterized by an increase in the strain rate due to the appearance of progressive damage, ultimately leading to failure.

A law describing the time-dependent behavior of a material is an equation that relates at every instant t the stress tensor to the strain tensor. When formulating such a law, three general principles need to be verified [23]:

– Principle of *determinism*. It states that the stress state of a body is determined by its motion history.

– Principle of *objectivity*. This principle imposes that a physical quantity is independent of the chosen coordinate system. This principle is commonly respected as only the stress and strain tensors and their invariants are involved.

– Principle of *local action*. It means that the stress tensor at some point in a continuum medium only depends on the history of the local strain at this same point.

Different kinds of models have been developed and studied to describe the time-dependent behavior of rock. The most widely used models for geomaterials can be divided into two categories: the analogical approaches and the models based on general overstress theory.

Rheological models are often used to describe the unidimensional time-dependent behavior of materials by assembling analogical elements in parallel, in series, or by mixing them. Elements in parallel have the same deformation and elements in series have the same stress. Two simple rheological models, the Kelvin model and the Maxwell model, are commonly

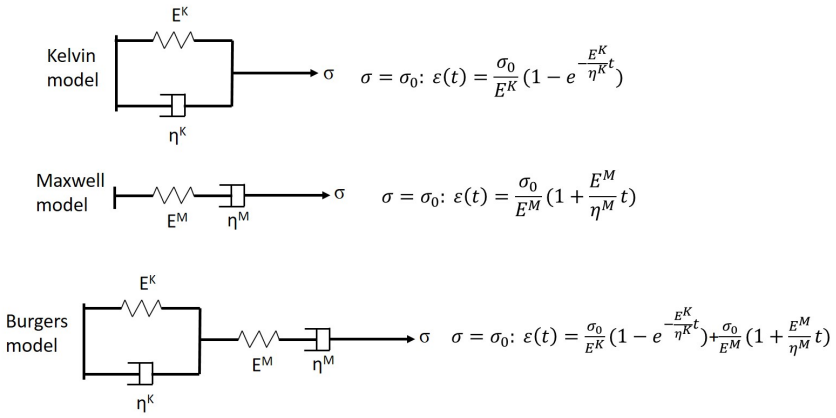

Fig. 2.14.: Analogical representation of the three visco-elastic rheological models.

used to describe the visco-elastic behavior. They are created by coupling an elastic spring with a dashpot, in parallel in the case of Kelvin model and in series in the case of Maxwell model. The Kelvin model allows to model the primary stage of creep with decreasing strain rate with time, and Maxwell model allows to model the secondary stage of creep with linear strain-time behavior. More complicated visco-elastic models, which have a better performance in modeling the various behaviors of rocks, can eventually be constructed with the aforementioned models. The Burgers model, by combining the Maxwell model in series with the Kelvin model allows to capture both the primary creep (short-term) and the secondary creep (long-term). The analogical representation of the different models is presented in Figure 2.14. Plasticity can be introduced by another analogical element: the slider. The Bingham model, composed of a slider in parallel with a damper, helps to describe the tertiary creep stage of a rock. By adding the Bingham model to other elements,

visco-plastic models can be produced to model different rock behaviors. For instance, the model proposed by Lombardi using two Bingham elements and a linear elastic spring in series, allowed the authors to reproduce the convergence data of the Saint Gothard tunnel [53]. Finally, the passage from these 1D rheological models to tensor relations is often done using stress invariants (assuming isotropic behavior).

The overstress theory sometimes referred to as the Perzyna theory [65] is a viscoplasic theory first developed for metals but which was later adopted to model the viscoplastic behaviors of geomaterials. The overstress theory is based on a static yield surface in the stress domain assuming that the current stress state can cross the yield surface during loading. Contrary to the classical elasto-plastic constitutive relations, here the yield function f can assume positive or negative values, and the consistency conditions of the classical theory of elasto-plasticity are not satisfied. In the space of principal stresses, a point representing the stress state, belongs in a yield surface which is a function of the norm of the strain rate $||\dot{\varepsilon^{vp}}||$. The yield function splits the stress space into two different areas.

– An elastic domain inside the yield surface ($f < 0$, $||\dot{\varepsilon^{vp}}|| = 0$), where deformation increments are elastic and can be determined using Hooke's law.

– An elasto-visco-plastic one beyond the yield surface ($f > 0$, $||\dot{\varepsilon^{vp}}|| > 0$), where the deformation increment, given in equation 2.1 is elasto-visco-plastic and the strain rate can be divided into an elastic component and a visco-plastic component.

Thus Perzyna proposed a model based on the strain rate as principal parameter. The total strain rate is the sum of the elastic and the viscoplastic strain rates:

$$\dot{\varepsilon}_{ij} = \dot{\varepsilon}^{e}_{ij} + \dot{\varepsilon}^{vp}_{ij} \tag{2.1}$$

Assuming that $F = 0$ defines a reference loading surface, with no viscosity in the elastic domain: Thus the following definition of the loading surface is given by Perzyna:

$$F(\sigma, \varepsilon) = \frac{f(\sigma)}{\kappa(\varepsilon_{vp})} - 1 \tag{2.2}$$

With f the yield function depending on the stress state and κ a hardening function. Assuming that the loading surface $F = 0$ is continuous and convex, the visco-plastic component proposed by Perzyna $\dot{\varepsilon}^{vp}_{ij}$ can be evaluated by the following flow rule:

$$\dot{\varepsilon}^{vp}_{ij} = \gamma \langle \Phi(F) \rangle \frac{\partial F}{\partial \sigma_{ij}} \tag{2.3}$$

With γ a fluidity parameter, $\Phi(F)$ the viscous nucleus, F the loading function, and σ_{ij} the considered state of stress.

$$\langle \Phi(F) \rangle = \begin{cases} 0 & \text{if } F \leq 0 \\ \Phi(F) & \text{if } F > 0 \end{cases} \tag{2.4}$$

Different variants of Perzyna's theory have appeared over the years to model the behavior of geomaterials. They are based on the behavior of soils and rocks, and in particular they often use non-associated laws in order to better take into account the dilatant character of geomaterials. The main variants of the viscoplastic laws with potential are based on the adaptation of the flow law $\Phi(F)$, which directly conditions the long-term behavior. Thus Lemaitre (1996) [50] proposed a viscous law with strain hardening. He considered a power-type $\Phi(F)$ flow law:

$$\Phi(F) = (\frac{F}{F_0})^n \tag{2.5}$$

Where n is a constant value greater than 1 and $F_0 = 1$ MPa corresponds to the reference unit. He assumed that creep depends on the deviatoric stress state of the material and not on the overstress defined by Perzyna. The loading function F is of the following form:

$$F(\sigma_{ij}, \varepsilon_{kl}^{vp}) = \frac{f(\sigma_{ij})}{\kappa(\varepsilon_{kl}^{vp})} \tag{2.6}$$

where f is a function only depending on the stress state. Lemaitre has chosen in particular f according to Von Mises type, in other words $f = q$, with q the second stress invariant. This means that only the deviatoric part of the stress tensor will be responsible for the creep. Note that a stress threshold σ_s may be introduced in the f function. κ is a function of hardening, it has the form of a power law:

$$\kappa(\varepsilon_{vp}) = \varepsilon_{vp}^{-\frac{m}{n}} \tag{2.7}$$

Where m is a constant value verifying $1 - n < m < 0$, and ε_{vp} is the second strain invariant. The rheological model representing the viscoplastic law of Lemaitre can be represented as in Figure 2.15. The conical damper reflects the non-linearity of the viscosity γ in parallel

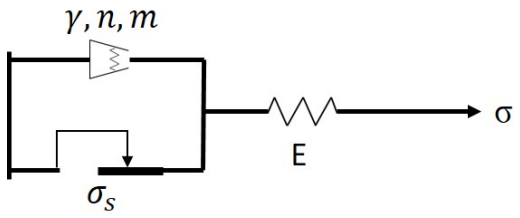

Fig. 2.15.: Rheological model representing the viscoplastic law of Lemaitre [14].

with a stress threshold σ_s. The flow law for positive isotropic hardening simplifies into:

$$\dot{\varepsilon_{ij}^{vp}} = \frac{3}{2}\frac{\dot{\varepsilon^{vp}}}{q}s_{ij} \tag{2.8}$$

with $\dot{\varepsilon^{vp}} = \gamma(\frac{q-\sigma_s}{\varepsilon_{vp}^{\frac{m}{n}}})^n = \gamma(q-\sigma_s)^n\varepsilon_{vp}^m$. With $\dot{\varepsilon^{vp}}$ the equivalent viscoplastic deformation rate.

A further description of Lemaitre's creep, as used in our numerical simulations, is provided in section 3.2.4. Finally, a brief reminder of the mechanical behavior of rocks and stress fields around a 2D excavation is given. The stress solution around the drift is useful to know in order to determine a first order of magnitude of normal and shear stresses involved in our problem. In appendix A.1 we present simple models of theses stresses for the cases of elastic and elastoplastic behavior.

2.2 Fractures

Interfaces can be either naturally present or result from the contact between the structure and the hosting rock or soil. Some of the most destructive natural disasters of recent history are correlated with geological hazard such as landslides and seisms. Considering that the behavior of fractured rock mass, seismology, slopes stability, and soil structure interaction clearly comes down to studying the behavior of interfaces, more and more research teams are nowadays studying the behavior of rock discontinuities. Insofar as fractures in the rock mass are very difficult to access, or even totally inaccessible, the understanding of their behavior requires laboratory experimental campaign. The first experiments investigating the behavior of a rock joint date back to the 1960's, and were conducted under direct shear test, and aimed at establishing a relationship between the shear strength and the normal stress, [63, 48]. Barton [9] was the first to establish a criteria linking the shear stress and the normal stress through the introduction of a new coefficient, taking the morphology of the rock surfaces into account, the JRC (Joint Roughness Coefficient). The time-dependent behavior of the fracture was beyond the scope of the experiments conducted on rock joints. Today, one can find more and more experimental setups in the literature designed to study rock joints under constant shear stress, mostly in the context of studying earthquakes, for example, one can name the pioneer work of Dieterich [29]. More recently, in the context of the project of nuclear waste storage [81], Stavropoulou has investigated the long-term behavior of the Callovo-Oxfordian claystone-concrete interface.

2.2.1 Description of an interface

In rock mechanics, a discontinuity, which is nothing but a physical interruption of the rock matrix, can be referred to as a fault, a crack, a joint or a fracture. The choice of one term over another is often related to the scope of the problem being studied. In all cases, the presence of discontinuities in a rock mass often greatly influences the overall behavior of the rock, because if they are generally of small thickness (and thus contribute little to the overall volume of the rock) they are characterized by a great deformability. The description of a discontinuity involves the description of its morphology, which can be broken down into several parameters as shown in Figure 2.16. In a rock mass an interface is subject to a

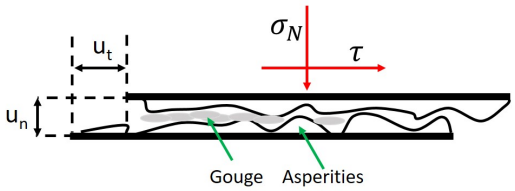

Fig. 2.16.: Schematic representation of an interface in contact and in relative movement under the effect of applied stresses.

certain state of stress characterized by a stress normal to the faces σ_N, and a shear stress τ. In Figure 2.16, u_N measures the interlocking of the two sides of the interface and u_t the relative slip between the two sides of the interface. The description of the surfaces in contact gives the roughness of the discontinuity. Often part of the roughness has been broken by the loading history experienced by the interface which creates a filler material present in the fracture called gouge.

Four principal factors influencing the mechanical behavior of an interface are identified and presented bellow:

– *Fracture roughness*. Experimental campaigns show the importance of the roughness on the response of the joint. However, the precise characterization of the roughness remains a great challenge. Moreover, the roughness is strongly correlated to other aspects of the interface behavior such as scale effects, anisotropy, stress dependency, which make it even more important to represent quantitatively the joint roughness.

– *Scale effect*. The scale effect observed in joint behavior is most likely a manifestation of the scale dependency of the roughness. In fact, the larger the size of the discontinuity, the smoother it appears. It is therefore the ratio of the average size of the roughness to the length of the tested joint that is important. Bandis et al., [7] have shown that as the sample size increases, the shear strength decreases.

– *Gouge materials*.The joint behavior is affected by the production of gouge material during the tests. This is due to damage to the asperities, and it is very difficult to know the amount of gouge produced and its distribution along the joint. In general, the gouge tends to decrease the shear strength of the joint.

– *3-D effects*. *In situ* rock joint description is three-dimensional. Indeed, the orientation of the joint surface in space, its roughness and dimension, as well as its state of stress are simplified when moving to the shear tests which are two dimensional.

Mechanical quantities on a discontinuity

We consider a continuous body Ω, representing the rock matrix, and a discontinuity surface Γ as represented in Figure 2.17. We are interested in the deformations and stresses in the vicinity of the discontinuity. We represent our discontinuity, made of two surfaces in contact, by a mathematical surface of zero thickness. The material is thus discontinuous because the two parts of the body in contact on Γ can separate. We will note $\underline{u}^+$ and $\underline{u}^-$ the displacements on both sides of the discontinuity, which is oriented by the vector $\underline{n}$. The

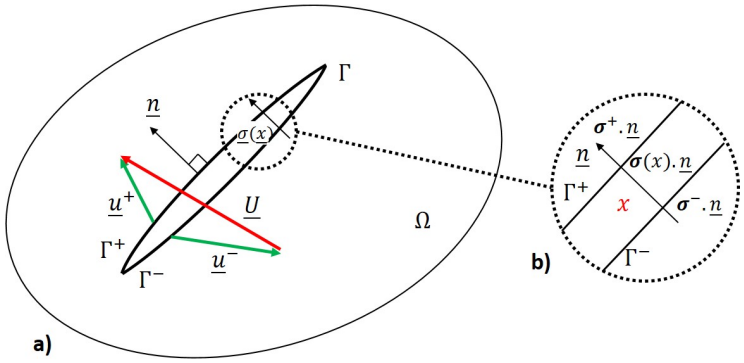

Fig. 2.17.: a) Model of a discontinuity Γ in a rock mass Ω, b) zoom on the stress state in x in the discontinuity.

relative displacement vector is define by:

$$\underline{U} = \underline{u}^+ - \underline{u}^- \tag{2.9}$$

The displacement $\underline{U}$ can be decomposed into a normal displacement: $u_n = \underline{U}.\underline{n}$, and a tangential displacement: $\underline{u_t} = \underline{U} - U_n.\underline{n}$.

Concerning the stress field in the vicinity of the Γ discontinuity, two cases can be distinguished. First, if the discontinuity is assumed to be empty, either the two surfaces are in contact in which case the vector $\sigma(x).\underline{n}$ is continuous at the passage of Γ, or the two surfaces

are not in contact, and so this vector is zero on the two sides Γ^+ and Γ^-, and of course also in the void separating the two sides of the interface (which also comes to be continuous). Else, the discontinuity is assumed to be filled with a thin layer of materials as represented in Figure 2.17b). For every point x in the discontinuity:

– the vector $\sigma.\underline{n}$ is continuous going from the rock matrix to the material inside the discontinuity through Γ^-.

– the variation of $\sigma.\underline{n}$ remains negligible because the discontinuity is assumed to be of low thickness and low stiffness.

– the vector $\sigma.\underline{n}$ is continuous going from the material inside the discontinuity to the rock matrix through Γ^+.

So if we make the thickness of the layer tend towards zero, in other word by confusing Γ^- and Γ^+ in Γ, then at any point x of Γ we will have a unique stress vector $\sigma(x).\underline{n}$ which will represent the stress at the passage of the two sides of the discontinuity as well as the projection according to $\underline{n}$ of the stress in the filling material. This unique value of $\sigma(x).\underline{n}$ is the stress vector $\underline{\sigma}$.

$$\sigma(\underline{x}) = \sigma^-(\underline{x}).\underline{n}(\underline{x}) = \sigma^+(\underline{x}).\underline{n}(\underline{x}) = \sigma(\underline{x}).\underline{n}(\underline{x}) \tag{2.10}$$

This vector can be decomposed into a normal stress: σ_N and a tangential stress (also called shear stress): $\underline{\tau}$.

$$\sigma_N = \underline{\sigma}.\underline{n} \tag{2.11}$$

$$\underline{\tau} = \sigma_N.\underline{n} + \underline{\tau} \tag{2.12}$$

The normal stress given in equation 2.11 and the shear stress given in equation 2.12 are represented in red in Figure 2.16. The behavior of a fracture is thus described by a relation between the stress vector $\underline{\sigma}$ and the displacement vector $\underline{U}$. The modeling of the behavior of the discontinuity requires the expression of a law f which relates the stress vector and the displacement vector: $\underline{\sigma} = f(\underline{U})$ In the case of an elastic behavior, a normal stiffness K_n and a tangential stiffness K_t will be defined to link the stress to the displacement.

Note that the displacement $\underline{U}$ of the discontinuity can have a plastic and viscous part. In the context of small deformations, we decompose the displacement into an elastic part and a plastic part and a viscous part.

$$\underline{U} = \underline{U}^e + \underline{U}^p + \underline{U}^v \tag{2.13}$$

The elastic displacement is related to the stress by the stiffness tensor $\mathbf{R}$ (defined by the quantities K_t and K_n).

$$\underline{U^e} = \mathbf{R}^{-1}\underline{\sigma} \tag{2.14}$$

The plastic displacement is given by the flow rule defined from a yield criterion f and a plastic potential g. The yield function depends on the stress tensor and it defines the range of stress states for which the displacement is elastic $f(\underline{\sigma}) \leq 0$. The flow rules give the expression of the plastic displacement increment by means of a function of the stress state called plastic potential. In the following, an associated flow rule is considered thus $g = g$. The flow rules are the following:

$$\underline{\dot{U}^p} = \lambda \frac{\partial f}{\partial \underline{\sigma}} \tag{2.15}$$

$$\begin{array}{ll} \lambda = 0 & \text{if } f(\underline{\sigma}) < 0 \text{ or if } f = 0 \text{ and } \frac{\partial f}{\partial \underline{\sigma}}.\underline{\dot{\sigma}} < 0 \\ \lambda \geq 0 & \text{otherwise} \end{array} \tag{2.16}$$

With λ the plastic multiplier. The definition of $\frac{\partial f}{\partial \underline{\sigma}}$ assumes that f is differentiable. The derivative with respect to time $\underline{\dot{\sigma}}$ refers to a fictitious time (not physical time) which indicates the direction of evolution of the physical process. In perfect plasticity, the condition $f \leq 0$ remains always true, thus we must have $\dot{f} \leq 0$ when $f = 0$.

More complicated behavior can be thought, including non linearity, viscosity. Therefore, in order to choose a model adapted to the real behavior of the interfaces, and prior to the determination of the relationship $\underline{\sigma} = f(\underline{U})$, experimental campaigns, as described in the next subsection, enable to study the behavior of the interfaces.

2.2.2 Short-term behavior

Compression test

In a compression test, a normal stress is applied on the joint interface and the resulting normal displacement is measured. The assumption that the shear stress and the shear displacement are null during a compression test is generally reasonable. However, if the joint is not smooth, dilatation or contracting phenomena can occur due to the asperities. The simple compression behavior of a joint is shown in Figure 2.18. The initial phase, which can be described as *clamping*, corresponds to the positioning of the two faces of the interface. This phase is characterized by an increase in the normal stiffness K_n with the increasing applied load. The stiffness increases up to that of the sound rock. The first few cycles of unloading depend on the material under study. The hysteresis that occurs during the cycles can be more or less important depending on the tested joint, in

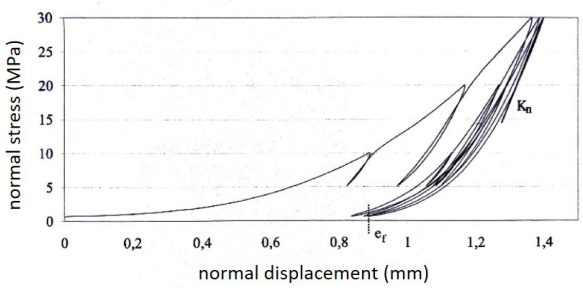

Fig. 2.18.: Simple compression test on a natural gneiss discontinuity. Test carried out at the LRPC of Toulouse[49].

particular its initial opening, its interlocking and its possible filling. It should be noted that improper placement of the faces of the interface will result in bigger deformability of the joint. After unloading, a normal permanent closure will remain, it is noted e_f in the Figure 2.18. Also, the measurement of the normal displacement must be done as close as possible to the interface, otherwise one should keep in mind that the measurement also contains the deformation of the rock matrix under the applied normal stress. The increase of the normal stress increases the contact area, with possible development of plastic strain in some areas. The normal stiffness depends on the size of the interface [7]: initial normal stiffness decreases with the increase in the contact surface.

Shear test

A shear test consists in shearing at constant speed an interface which can in addition be subjected to a normal stress or not. Usually, the normal stress σ_N is applied (for example with weight) and the test is conducted by applying a tangential relative displacement u_t or a velocity $\dot{u}_t$., while measuring the shear stress τ and the normal displacement u_n. The response of the joint is highly dependent on its roughness. The response of an ideal smooth joint would be relatively simple, with two distinct phases: first an increase in tangential stress as a function of tangential displacement, then, when the limit value of friction is reached, a relative displacement starts between the two faces of the interface, and the shear stress remains constant, as shown in Figure 2.19 a). The Mohr-Coulomb criterion, which is very commonly used as a first approximation, essentially reproduces the behavior of smooth joints. Indeed, the main disadvantage of this criterion is that it does not explicitly describe the dilatation of the joint and thus its roughness. It also tends to overestimate the shear strength of the failure for low normal stresses. Between the smooth joint and the complex natural discontinuity, the study of a regularly indented discontinuity provides a better understanding of the effect of roughness on the joint response [63]. Compared to

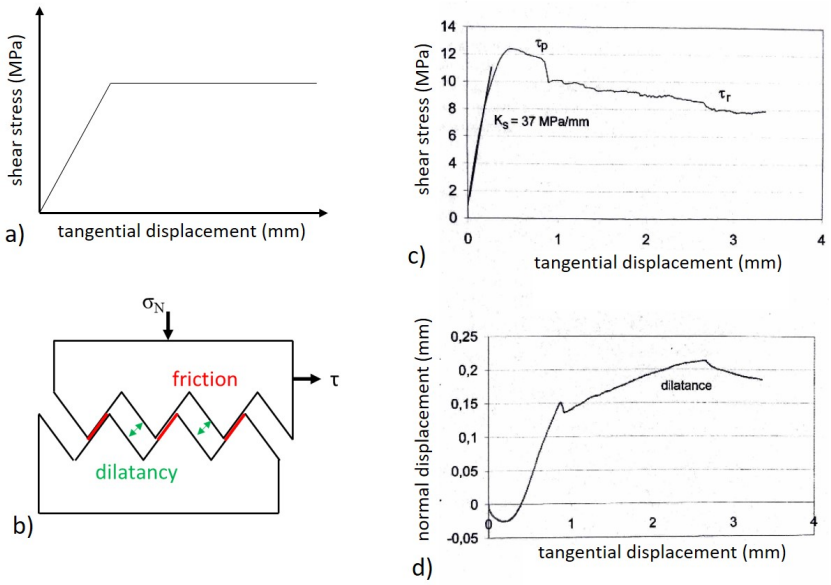

Fig. 2.19.: Different response of a joint to a shear test. a) response of a smooth joint: Evolution of the shear stress as a function of the tangential displacement, b) simplified view of the roughness: shearing of a discontinuity with regular indentation. Response of a natural gneiss joint. Test carried out at the LRPC of Toulouse under 10 MPa normal stress and on a sheared surface of 5500 mm^2, c) evolution of the shear stress as a function of the tangential displacement, d) dilatancy curve [49].

a smooth joint, the friction surface is considerably reduced because contact is only made on part of the facets, which guides the displacement and induces separation at the other asperities. This reduction of the contact surface induces stress concentrations that can cause local damage on certain asperities. In general, the fact that some areas may be locally out of contact during the test raises the question of the value of the average stress to be used, because if the applied force is well known, the contact area varies.

The behavior of a natural discontinuity shown in Figure 2.19 c) and d) shows an example of more complex response [49]. During this test, the shear stress increases progressively with the tangential displacement until it reaches the peak strength τ_p then decreases progressively to reach a plateau characterizing the residual strength τ_r. The values of the maximum and residual strengths as well as the tangential stiffness depend on the applied normal stress and the roughness of the joint. The non-linear part of the curve, before the peak, corresponds to the damage of the asperities. Once the peak is passed, the degradation of the friction surfaces can be observed. The curve representing the normal displacement as a function of the tangential displacement, also called the dilatancy curve, allows to characterize the opening of the joint (on the curve presented in Figure 2.19 d), a positive displacement jump corresponds to an opening of the joint). This curve is characterized by a phase of contraction

for small tangential displacements, followed by dilatancy. The dilatancy angle is defined by the slope $\arctan(\frac{\Delta u_n}{\Delta u_t})$ and is generally maximal for a tangential displacement close to the peak of shear stress. The greater the normal stress applied to the joint, the more damage to the asperities will result from tangential displacement. It is recalled that the response of the joint depends on the factors mentioned at the beginning of this section.

The direct shear test (constant normal stress test) is the most commonly used test. However in the literature other loading paths have been proposed as this test essentially represents the sliding of a block under its own weight along a failure surface [49]. We mention the test at controlled volume and the test at constant normal stiffness. In the first type of test, the normal displacement is kept constant by varying the normal stress: it is increased in case of dilatation and decreased in case of contraction. In the second type of test, the stiffness is kept constant by an adequate control of the device. This ratio allows to represent the normal stiffness of the mass surrounding the fracture which should not be confused with the normal stiffness characteristic of the joint. The normal stress varies proportionally to the normal displacement of the joint.

Finally we can also mention the existence of shear tests carried out *in situ* on natural joints. Note that such tests are very rare because they are very expensive and if the conditions represent perfectly the reality, the analysis is very complicated because the parameters and conditions of the test are even less well mastered than in a simplified test carried out in laboratory. Nevertheless, we can mention the test carried out during the construction of the Varouglans dam [32]. In an existing gallery, an excavation was made around a pillar of 2×3 m, and the head of the pillar was suppressed in order to enclose the block to be sheared in a reinforced concrete shell. The normal force was applied via two flat cylinders in series and the shear force via four flat cylinders also in series. The tested joint area was 4.4 m^2.

2.2.3 Long-term shear behavior

In this work, the time-dependent behavior of an interface is understood as the displacement $\underline{U}$ defined in equation 2.9 that occurs when the interface is subjected to an average constant normal and shear stress $\underline{\sigma}$ along its length. The time-dependent behavior of an interface, is still a fairly new topic, the approaches are diverse between different studies. Some investigations are conducted through numerical simulations [92, 88]others conduct experimental campaign [89, 87]. All of them investigate to some extend the influence of joint roughness in the time-dependent behavior of joints. In [89] the roughnesses are according to Barton's JRC classification, and in [87] the authors investigate shear and tensile fractures that were induced in intact rock samples respectively in a modified shear device and Brazilian split test. They have identified different type of viscous slip mechanisms between those two

types of fractures. They have stated mostly, shear cutting of microasperities is the main mechanisms in tensile fractured rock, while frictional shear of macroasperities is a main mechanism in shear fractured rock. However, they also notice that the mechanisms tend to differ in function of the different loading stage of the shear creep process. In all the experimental campaigns mentioned herein, the viscous slip of the fracture is measured at the scale of the sample with Linear Variable Displacement Transducers. Wang et al., [87] does, however, have a local sense of what is going on, at least in terms of asperities degradation, as they scan and analyze the surfaces being tested. Another work worth mentioning on the long-term behavior of interfaces is the study done by Stavropoulou [81] on the COx claystone /concrete interfaces in the context of nuclear waste storage. In her tests, she showed that the long-term behavior of the interface is largely influenced by the exchange of water between the COx claystone fresh concrete. In fact, the wetting of the COx claystone results in the appearance of cracks at the interface. Tests conducted with dry concrete showed that in that case there was no damage. An initial variability in the different test results is also attributed to this damage as the interfacial zone is probably subjected to closure of voids and/or breakage of asperities. The study also shows an evolution of the interface with creep and a more complementary geometry, meaning a better interlocking of the interfaces after creep. This study shows with creep tests conducted under the same normal stress, that higher time-dependent shear strain and strain rate are measured for higher applied shear stress. Lemaitre's creep law, among other, was used to model the experimental results.

2.3 Discussion

In the work presented in this manuscript, we are interested in the effect of fracture behavior on the overall response of a tunnel over time. In particular, we focus on tunnels excavated in the COx claystone and thus on the behavior of fractures in this same rock. The approach, which consists of modeling the long-term behavior of URL drifts by focusing on the effect of shear fractures, is quite different from the approaches proposed so far in the scientific community. This approach is based on two separate studies, on the one hand the modeling of the time-dependent behavior of URL tunnels, which is based on a macroscopic description of the structures. On the other hand, the study of chevron fractures is based on a laboratory scale description of the interfaces in the COx claystone.

The approach presented in this work is motivated by the idea of simplifying the problem as much as possible, in order to retain only what seems to us to be the main cause of the observations made in the underground laboratory: fractures. Indeed, all this work is based on the hypothesis that it is the viscous slip on the chevron fractures that causes the

anisotropic convergences of the structures. Part of the work presented therefore consists of modeling the time-dependent behavior of the two tunnels presented in this chapter: the GED and the GCS drifts belonging to the URL network of drifts. Indeed, these two tunnels are considered here as models of behavior of drifts excavated respectively in the direction of the principal minor and major horizontal stress.

The other important part of this work is based on the description of the long-term behavior of a fracture in the COx claystone. A mechanical description of an interfaces is provided in this chapter. We explicitly modeled fractures principally twice, once to establish expressions for equivalent continuum models in Chapter 4, and another time, in Chapter 6, fractures are explicitly introduced in a simulation of the experimental setup. Fracture modeling is based on an experimental campaign designed to characterize viscous slip along an interface in the COx claystone. The observation of viscous slip along fractures in this rock has never been done before thus this study required the design of a new experimental setup. The absence of any previous studies on the time-dependent response of COx/COx interfaces, resulted to a literature research on the time-dependent behavior of the COx claystone, and of the time-dependent behavior of interfaces in other geomaterials. Thus, the study of the viscous slip of fractures could however be based on existing works describing the behavior of fractures and works describing the time-dependent behavior of the COx claystone.

The numerical and experimental work carried out during this thesis in order to provide an easy to handle but reliable model of the time-dependent behavior of the URL drifts are presented in the following chapters. Indeed, the Cigéo project is an industrial project and the engineering offices will have to dimension the structures that constitute it. It is therefore important for ANDRA to have a functional model that faithfully reproduces the displacements at the tunnel walls and thus allows an optimized design and the safety of the structures.

3 Numerical simulation of the drifts convergence: Continuous transverse isotropic model

> *All models are wrong, but some are useful*
>
> **— George Box**
> Mathematician

In this chapter a presentation of the Finite Element code, Disroc [68] used for the numerical simulations is provided. The three-fold anisotropic model ANEVLIP, already present in Disroc, is presented for its general framework. A special attention is paid to the parameters of anisotropy and their deviation from the isotropic behavior. The framework of the 2D plane strain simulations of the drifts is presented as for their geometry, the mesh and boundary conditions but also the detailed description of the excavation procedure and the underlying assumptions. The attention, in this thesis, is focused on the viscous, or long-term, behavior of fractures in order to provide a trustworthy simulation of the long-term anisotropic convergences of the drifts of the URL. Nevertheless, the fracturing process and its modeling represents a research topic in itself, which was actually addressed, among other, by Trivellato et al., and Pardoen et al., [85, 61]. In this thesis, the assumption is made that fracture deformation governs the long-term deformation of URL structures, specifically viscous fracture slip. Furthermore, the distribution of fractures in fractured zones induces anisotropy in the behavior of the excavated rock. Therefore, we work with a triply anisotropic model, which means that the three constitutive laws: elastic, plastic and viscous, are anisotropic with independent anisotropy parameters. While most of the work consists in determining these anisotropy parameters, they always, in every different approach presented in the manuscript, account for fracture behavior. It is true that the bedded Callovo-Oxfordian claystone is inherently transverse isotropic, but its intrinsic anisotropy is assumed to be negligible compared to the anisotropy induced by the fractures. In this chapter the anisotropy parameters are numerically calibrated on *in situ* observations and measurements operated on the drifts of the URL. For a better understanding of the ANELVIP model, the choice has been made to present its theoretical framework here in

the scope of its application to the first simulations. However, the ANELVIP model is also used in the following chapter with a slightly different approach to the numerical simulations of the drifts. Here, the values of the parameters of the model are determined to describe, in a continuous equivalent way, the whole rock medium (the combination of intact rock and fractured rock) with direction of anisotropy chosen following the direction of the main fractures observed at the vicinity of GED or GCS drifts. The results of the simulations are presented and discussed.

3.1 Description of the numerical tool

The numerical simulations presented throughout the manuscript were performed with the 2D Finite Element code (FEM) Disroc developed by the software company Fracsima [68]. Disroc is conceived to model coupled Thermo-Hydro-Mechanical (THM) and chemical phenomena in fractured media. The software is designed for research studies with numerous nonlinear constitutive laws already available. Moreover, subroutines can be implemented in Fortran90 in order to bring changes to the code that are specific to the studied problem. For instance, in this work, the time increment is automatically adapted to prevent convergence problems due to the viscous part of the constitutive law. Another useful modification in the user module allows to trace a specific contour plot for one or more state variables for the GiD post-processing phase.

In this work, Disroc is employed as a processor to solve the FEM problem according to the characteristics defined in the pre-processing phase. For every numerical simulation the pre -processing phase, constituted by the definition of the materials, boundary conditions, initial conditions and spatial 2D discretization (mesh), and the post-processing phase are operated with the software GiD (https://www.gidhome.com/). One specificity of Disroc is the possibility to introduce discontinuities in the FEM model (e.g. rock interfaces, fractures, bolts) with hydro-mechanical couplings between the aforementioned discontinuities and the matrix (continuous material). Thus Disroc is able to process a FEM mesh containing pre-orientated or random discontinuities with joint elements. The discontinuities can either be directly inserted in the geometry by tracing them as any line in the model, then after having meshed the surfaces and the lines of the geometry, the mesh of the discontinuities are splitted and transformed into joint element. It is also possible to transform the sides of whatever number of surface elements into a network of discontinuities. For every nonlinear behavior and dissipation (yielding) law f, and for each calculation increment, Disroc performs a local check (with one Newton-Raphson iteration) in each Gauss point of each element (surface or joint elements) of the mesh. This verification allows to check if the displacements convergence and the failure criterion tolerance (according to the consistency law $f = \dot{f} = 0$)

are respected. If the check is validated the calculus goes forward to the next calculation step, otherwise the code has to locally execute a new Newton-Raphson iteration.

3.2 ANELVIP model

The equations defining the constitutive ANELVIP model, as presented in Disroc Catalog of Materials [35], are described here for their general framework and in the following sections, for their elastic, plastic and viscous deformation components. A sub-section is devoted to the construction of the plastic and viscous anisotropies and their parameters. As it is customary in infinitesimal strain constitutive models, the total strain rate is decomposed in three, elastic, plastic and viscous components as follows:

$$\dot{\varepsilon} = \dot{\varepsilon^{\mathbf{e}}} + \dot{\varepsilon^{\mathbf{v}}} + \dot{\varepsilon^{\mathbf{p}}} \tag{3.1}$$

The mathematical expressions for the elastic, plastic and creep strains are given below:

$$\dot{\varepsilon}^{e} = \mathbb{C}^{-1} : \dot{\sigma} \tag{3.2}$$

$$F(\sigma) \leq 0; \quad \dot{\varepsilon}^{\mathbf{p}} = \dot{\lambda} \frac{\partial G}{\partial \sigma} \tag{3.3}$$

$$\dot{\varepsilon}^{\mathbf{v}} = \psi(\sigma, \xi) \tag{3.4}$$

where $\mathbb{C}$ is the elastic tensor with transverse isotropy. F is the Mohr-Coulomb yield surface (assumed to be perfectly plastic), G is the plastic potential which is chosen equal to F assuming an associated flow rule and $\dot{\lambda}$ is the plastic multiplier with the standard plastic flow rule conditions: $\dot{\lambda} \geq 0$ and $\dot{\lambda} = 0$ if $F(\sigma) < 0$ or if $F(\sigma) = 0$ and $\frac{\partial F}{\partial \sigma}\dot{\sigma} < 0$. The choice of an associated flow rule and its implication in our modeling of the drifts convergence is further discussed in section 3.2.3. The function ψ corresponds to an anisotropic Lemaitre creep law with ξ the strain hardening parameter. The creep law is explained in details in section 3.2.4.

3.2.1 Transverse isotropic elasticity

The general form of the elastic anisotropy is described by a constitutive law with 21 independent parameters. However, this number of parameters can be reduced by the presence of planes of symmetry in the described material. We use here the transverse isotropy, which describes the behavior of a material for which the properties are invariant

by change of direction obtained by rotation around a privileged axis. In this case, any plane passing through the privileged axis is plane of symmetry. This is for example the case of stratified rocks. As a result, only 5 parameters are needed to describe the transverse isotropic behavior: two Young's moduli, two Poisson's ratio and one shear modulus. In the case of transverse isotropy around the y-axis, perpendicular to the plane of isotropy, we denote $E_y = E_v$ (perpendicular to the plane of isotropy) and the two Young's moduli parallel to the plane of isotropy become equal $E_x = E_z = E_h$.

$$\begin{pmatrix} \varepsilon_{xx} \\ \varepsilon_{yy} \\ \varepsilon_{zz} \\ \gamma_{yz} \\ \gamma_{xz} \\ \gamma_{xy} \end{pmatrix} = \begin{pmatrix} \frac{1}{E_h} & -\frac{\nu_{hv}}{E_v} & -\frac{\nu_h}{E_h} & 0 & 0 & 0 \\ -\frac{\nu_{hv}}{E_h} & \frac{1}{E_v} & -\frac{\nu_{hv}}{E_h} & 0 & 0 & 0 \\ -\frac{\nu_h}{E_h} & -\frac{\nu_{hv}}{E_v} & \frac{1}{E_h} & 0 & 0 & 0 \\ 0 & 0 & 0 & \frac{1}{G_{hv}} & 0 & 0 \\ 0 & 0 & 0 & 0 & \frac{1}{G_h} & 0 \\ 0 & 0 & 0 & 0 & 0 & \frac{1}{G_{hv}} \end{pmatrix} \begin{pmatrix} \sigma_{xx} \\ \sigma_{yy} \\ \sigma_{zz} \\ \tau_{yz} \\ \tau_{xz} \\ \tau_{xy} \end{pmatrix} \tag{3.5}$$

3.2.2 Plastic and viscous anisotropies

The viscoplastic anisotropy in ANELVIP is built by replacing the stress tensor σ by a modified tensor $\tilde{\sigma}$ obtained by a linear transformation of σ. This is a classical method of defining anisotropic nonlinear materials used in plasticity first by [45] and more recently, only for plasticity, by [8] and by [55]. This linear transformation is defined, in a specific coordinates system, by the following relation:

$$\tilde{\sigma} = \begin{pmatrix} \sigma_{xx} & f_T \sigma_{xy} & 0 \\ f_T \sigma_{xy} & f_N \sigma_{yy} & 0 \\ 0 & 0 & \sigma_{zz} \end{pmatrix} \tag{3.6}$$

This makes the constitutive model anisotropic and the coefficients f_N and f_T are determined in a way to obtain the desired anisotropy ratios. This relation is defined in a coordinate system (X,Y) making an angle ω with the reference system of coordinates allowing to specify the principal directions of anisotropy. The anisotropy ratio is then expressed preferentially by two parameters a_N and b_T related to the coefficients f_N and f_T by:

$$f_N = 1 + a_N \tag{3.7}$$

$$f_T = \sqrt{f_N + b_T} \tag{3.8}$$

The parameters a_N and b_T express the deviation from the isotropy; $a_N = 0$ and $b_T = 0$ corresponding to the isotropic material. We define two pairs of parameters (a_N^p, b_T^p) and

$(a_N^v,\ b_T^v)$ respectively for the anisotropy of the plastic and viscous behavior. Using this method, we can transform an isotropic Mohr-Coulomb strength criterion to an anisotropic one by replacing the stress σ by the transformed stress $\tilde{\sigma}$. In this anisotropic model, one can define the anisotropy function β^p, for uniaxial loading, as the ratio of the UCS (Uniaxial Compressive Strength) in any direction with respect to a reference direction, as can be seen in equation 3.9. This function depends on the parameters a_N^p and b_T^p with the expressions given by equation 3.11. Taking into account the symmetries of the material, this function can be defined only for $\overline{\theta}$ between 0° and 90°.

$$\beta^p(\overline{\theta}) = \frac{\mathrm{UCS}(0^\circ)}{\mathrm{UCS}(\overline{\theta})} \tag{3.9}$$

$$\overline{\theta} = \theta - \omega \tag{3.10}$$

$$\beta^p(\overline{\theta}) = \begin{cases} \dfrac{\sqrt{(1+a_N^p \sin^2\overline{\theta})^2 + 4b_T^p \sin^2\overline{\theta}\cos^2\overline{\theta}} - (1+a_N^p \sin^2\overline{\theta})\sin\phi}{1-\sin\phi} & \text{if } b_T > 0 \\ \frac{1}{2}(1+a_N^p \sin^2\overline{\theta} + \sqrt{(1+a_N^p \sin^2\overline{\theta})^2 + 4b_T^p \sin^2\overline{\theta}\cos^2\overline{\theta}}) & \text{if } b_T < 0 \end{cases} \tag{3.11}$$

In the same way, one can transform a creep law for an isotropic material to an anisotropic one by replacing the stress tensor σ by the transformed stress tensor $\tilde{\sigma}$. Considering that the creep law is based on the Von Mises equivalent stress, one can define a function β^v (equation 3.12) as the ratio of the transformed Von Mises equivalent stress to the non-transformed one for uniaxial stress in different directions. Note that $\sigma_e = \sqrt{\frac{3}{2} S_{ij} S_{ij}}$ with $S_{ij} = \sigma_{ij} - \frac{1}{3}\sigma_{kk}\delta_{ij}$. The expression of the function β^v depends on the parameters $(a_N^v,\ b_T^v)$ and is given by equation 3.12.

$$\beta^v(\overline{\theta}) = \frac{\tilde{\sigma}_e}{\sigma_e} \quad \text{(in the case of uniaxial stress)} \tag{3.12}$$

$$\beta^v(\overline{\theta}) = \sqrt{(1+a_N^v \sin^2\overline{\theta})^2 + 3b_T^v \sin^2\overline{\theta}\cos^2\overline{\theta}} \tag{3.13}$$

Some examples of the anisotropy functions β^p and β^v are given in Figure 3.1 for different value of a_N and b_T to demonstrate how different situations of anisotropy can be reproduced by varying the values of these parameters. The functions β^p and β^v are always equal to 1 for the reference direction $\overline{\theta} = 0$. In order to determine the two parameters of anisotropy, a_N and b_T, only to particular values in two different direction (other than the reference direction) are needed. Their values for $\overline{\theta} = 90^\circ$ allow determining the parameters a_N^p and a_N^v easily from $\beta(90^\circ) = 1 + a_N$. If both parameters a_N and b_T are set equal to zero, the isotropic behavior is retrieved and the functions β describe a circle. A value of $a_N > 0$ (respectively $a_N < 0$) results in a value of β at $\overline{\theta} = 90^\circ$ greater (respectively smaller) than

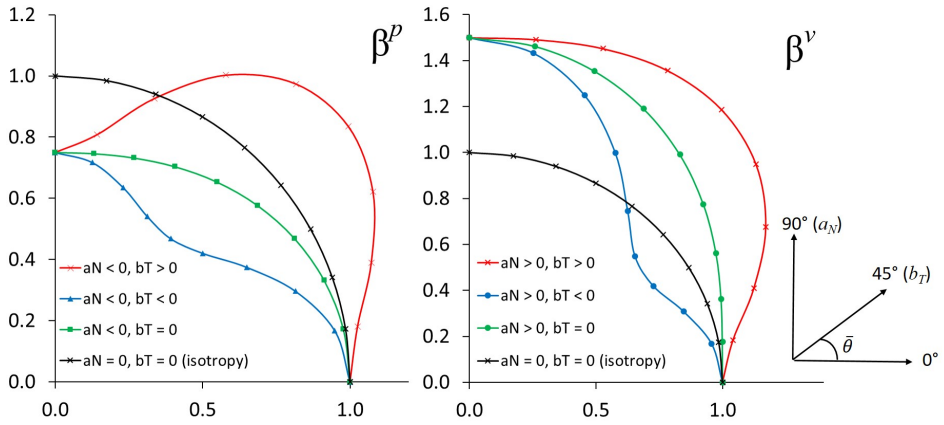

Fig. 3.1.: Examples of anisotropy functions β^p and β^v in the polar coordinate system for different values of a_N^p, b_T^p, a_N^v and b_T^v. The Figure illustrates the theoretical behavior of isotropic transverse rock. Function β^p is directly linked to the UCS, with UCS_0 the uniaxial compressive strength in the reference direction. Function β^v is multiplied to parameter a in the viscous strain law, hence it influences directly the viscous strain rate.

1. For the case of plasticity, a value of $b_T^p > 0$ (respectively $b_T^p < 0$) results in a maximum (respectively minimum) value of the function β^p at $\overline{\theta} = 45°$.

3.2.3 Anisotropic Mohr-Coulomb Plasticity

Experimental investigations have shown that the yield criteria of material can also be anisotropic. Thus the anisotropy in the elasto-plastic behavior can be modeled in different ways [33]. It can either be managed by working on the strength parameters, fourth order projection tensor or second order micro-structure tensor resulting in continuous approaches [45, 76]. Or it can be introduced in the model by adding a plane of weakness [46] or patches of weakness [34] which comes to adopt a discontinuous criterion.

In ANELVIP, an anisotropic Mohr-Coulomb perfectly plastic yield function is implemented.

$$F(\tilde{\sigma}) = \frac{\tilde{\sigma_3} - \tilde{\sigma_1}}{2} + \frac{\tilde{\sigma_3} + \tilde{\sigma_1}}{2} \sin\phi - C\cos\phi \leq 0 \tag{3.14}$$

Where C and ϕ are the cohesion and friction angle respectively. $\tilde{\sigma_1}$ and $\tilde{\sigma_3}$ are the major and minor principal stresses calculated from the transformed stress $\tilde{\sigma}$, which is further described in section 3.2.2.

3.2.4 Anisotropic Lemaitre's creep law

The expression of Lemaitre creep law [51] called also the strain hardening law for an isotropic material under uniaxial stress is the following:

$$\varepsilon(t) = a\,\langle \sigma - \sigma_c \rangle^n t^\alpha \tag{3.15}$$

The constitutive law depends on four parameters: a, n, σ_c and α. The parameter a is related to the magnitude of viscous strain, n is making the viscous strain nonlinear as a function of the stress, σ_c is the stress threshold for time-dependent deformations. To determine σ_c by laboratory tests, small stresses must be applied to the sample to see below which limit there is no more creep. Another way to assess this threshold is to consider that the *in situ* stresses existing in the geological layers provide a lower bound of this threshold because it can be assumed that these layers have remained in the same creep free state for millions of years. By this reasoning, we get σ_c equal to the Mises equivalent stress for the *in situ* stresses which is about 3.6 MPa at the MHM URL location. The parameter α indicates the strain hardening in the creep law, with $0 \leq \alpha \leq 1$, as it can be seen in the equation 3.16, the smaller it is, the smaller the viscous strain rate is going to be. For $\alpha = 1$, the Norton-Hoff model, the model without strain hardening is retrieved.

In the ANELVIP model, the general form of the viscous deformation rate is expressed by:

$$\dot{\varepsilon}^v = \frac{3}{2}\alpha \xi^{\alpha-1} \dot{\xi} \frac{\tilde{\mathbf{S}}^v}{\tilde{\sigma}_e^v} \tag{3.16}$$

$$\dot{\xi} = \left[a\beta^v \left\langle \tilde{\sigma}_e^p - \sigma_c \right\rangle^n \right]^{1/\alpha} \tag{3.17}$$

The tilde is referring to the transformation operated on the stress tensor making the model anisotropic, as explained in equation 3.6. We note $\tilde{\sigma}_e^v = \beta^v \sigma_e$ and $\tilde{\sigma}_e^p = \beta^p \sigma_e$. The function $\langle x \rangle$ is defined as:

$$\langle x \rangle = \begin{cases} 0 & \text{if } x < 0 \\ x & \text{if } x \geq 0 \end{cases} \tag{3.18}$$

Besides, to avoid numerical problems near $\xi = 0$, this law is completed by: $\dot{\varepsilon}^v = \frac{3}{2}\alpha \varepsilon_0^{\alpha-1} \dot{\xi} \frac{\tilde{\mathbf{S}}}{\tilde{\sigma}_e}$ if $\xi^\alpha \leq \varepsilon_0$ where ε_0 is a small valued parameter introduced to avoid errors related to the division by zero. The transformed stresses in equation 3.16, $\tilde{\sigma}_e$, $\tilde{S}^v$ and $\tilde{\sigma}_e^v$ are defined by a transformation with parameters (a_N^v, b_T^v) as explained in a previous section. Two different β functions are related to the anisotropy of viscous strain: the anisotropy of

viscous strains rate and the anisotropy of stress threshold, namely β^v and β^p respectively. The equation 3.19 can thus be written, function of the non-transformed stress as:

$$\dot{\xi} = \left[a\beta^v(\overline{\theta}) \left\langle \beta^p(\overline{\theta})\sigma_e - \sigma_c \right\rangle^n \right]^{1/\alpha} \tag{3.19}$$

Going back to the viscous law considered in ANELVIP, if the uniaxial stress $\sigma_{\overline{\theta}}$ is applied in a direction making an angle $\overline{\theta}$ with respect to x_1 (parallel to the fracture planes) then the axial creep strain measured in this direction is given by:

$$\varepsilon_{\overline{\theta}}(t) = a\beta^v(\overline{\theta}) \left\langle \beta^p(\overline{\theta})\sigma_{\overline{\theta}} - \sigma_c \right\rangle^n t^\alpha \tag{3.20}$$

3.3 Application to modeling the drifts of the URL

3.3.1 Continuous modeling of the drifts

As already stated, the idea in this work was to attribute the anisotropy of the behavior of the rock mass to the fractures around the tunnels. The fractures are assumed to influence the long-term convergences because they would be subjected to viscous slip, which is precisely the object of the experimental campaign described in Chapter 5 and Chapter 6. This viscous slip oriented along the fractures induces the anisotropic convergences and convergence rates of the drifts of the URL. As consequence, it was thought that it is possible to model this effect of fractures with an anisotropic viscous model. Thus in a first approach, the simplest way to model the response of the drift and test this hypothesis is by modeling the excavation of the drifts in a transverse isotropic medium. Also, the main difficulty in modeling URL drifts is to propose a model capable of reproducing the behavior of both types of galleries. The idea is, in order to account for the different orientations of the fractures in the two fractured zones, to rotate the isotropy plane by 90 degrees between the two types of galleries as shown by Figure 3.2. By proceeding as follows, the orientation of the isotropy plane matches the dominant orientation of the chevron fractures in the modeled drift. However, because the two fractured zones do not exhibit 90-degree rotational symmetry (in particular the extension of the fractured zone is different), it is expected that the anisotropy parameters will need to be slightly adjusted when switching from one gallery model to the other.

The viscous and plastic anisotropies in this work are related to the fracture anisotropy. In other words, the direction of anisotropy (or plane of isotropy) is given by the main direction of the fractures as shown in Figure 3.2, and therefor is not related to the intrinsic sedimentary bedding structure of the COx claystone.

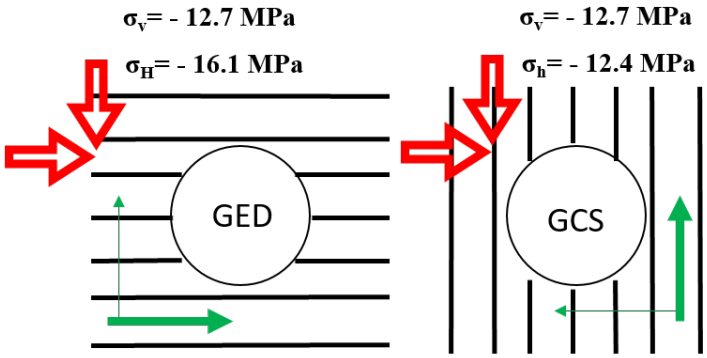

Fig. 3.2.: In the simulations the viscoplastic model is related to the fracture anisotropy and the whole medium is transverse isotropic with the plane of isotropy orientated in the direction of the fractures.

Based on observations of the *in situ* fractured zones in GED and GCS drifts, we have considered that the shear fractures are mainly horizontal in the case of GED drift, while they are mainly vertical in the case of GCS drift. This is schematically presented in Figure 3.3. Of course, in reality the shear fractures are not plane, but in a first approximation, we consider that their global effect can be represented by a fractured material with some dominant direction of plane fractures. This assumption allows us to take into account the effects of the fractures forming the damaged zone on the drifts convergence, only by using a transverse isotropic model. In other words, the drifts are modeled in a medium crossed by parallel horizontal or vertical fractures as schematized in Figure 3.3. The advantage of this approach is its simplicity, permitting to reproduce the convergence of both drifts, GED and GCS, only by changing the orientation of anisotropy: $\omega = 0°$ for the mostly horizontal fractures around GED drift, and $\omega = 90°$ for the mostly vertical fractures around GCS drift. The parameters of anisotropy are not the same for the two drifts since the density and the extent of the fractured zones are not the same. We calibrate the four parameters a_N^p, b_T^p, a_N^v and b_T^v on the convergence measurements of GCS and GED drifts. Knowing that the COx claystone is a bedded rock, its intrinsic anisotropy resembles the anisotropy induced by planes of parallel fractures. Experimental data obtained on sound rock samples were used to get a first estimation of the anisotropy parameters, before the numerical calibration.

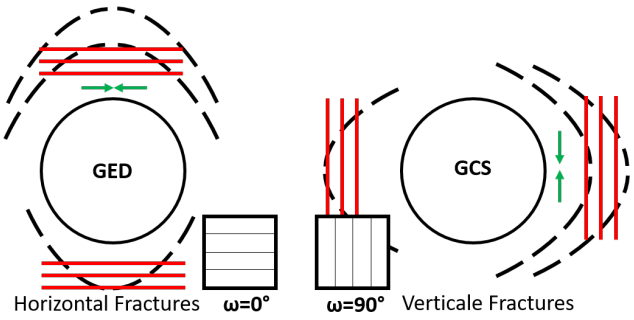

Fig. 3.3.: Schematic representation of the direction of the fractures (black) and of the dominant direction of fractures anisotropy (red) for GED and GCS drifts. The green arrows represent the hoop stress at the vicinity of the drifts applied in the direction of reference.

3.3.2 ANELVIP model parameters for URL gallery modeling

Elastic parameters

The numerical values of the parameters have been evaluated from available experimental results. As a matter of fact, [19] and [98] have shown that the anisotropy ratio between vertical and horizontal Young's moduli is between 1.6 and 1.8. The following numerical values are considered: $E_{\parallel} = E_x = 5000$ MPa, $E_{\perp} = E_y = 3000$ MPa, $\nu_{yx} = 0.3$, $\nu_{xz} = 0.2$ and $G = 1700$ MPa. The shear modulus and the Poisson's ratios have been taken from [41]. Actually, in the numerical simulations presented in this chapter, the anisotropy of the elastic part does not account for the fracture behavior but the elastic parameters are those measured in the laboratory experiments on COx claystone. As a consequence, the anisotropy of the elastic part in this chapter stands for the effects of the bedding planes. In the next chapter the coefficients of anisotropy are calculated to account for the fractures. Indeed, the elastic anisotropy does not explain the anisotropy of convergence of the drifts. According to an elastic simulation, GED drift tends to have a bigger horizontal convergence than vertical convergence, because the horizontal stress in a cross section is bigger than the vertical stress (16MPa vs. 12.7 MPa). It is the result of the development of irreversible plastic deformation at the roof and bottom of the tunnel section that the vertical convergence is bigger than the horizontal convergence. At the very beginning of the excavation, when the fractured zone does not yet exist, the anisotropy of rock elasticity prevails, whereas at the end of the excavation and after, the anisotropy of rock due to fractures is decisive for plasticity and then visco-plasticity.

Plastic parameters

More sophisticated plastic criteria than Mohr-Coulomb have been considered in other works, but as the main objective of this work is to analyze the anisotropic time-dependent effects, a simple plastic model was on purpose considered. However, the plastic behavior of the material determines the state of stress immediately after excavation and in this way influences the development of the viscous strain field. The UCS (given by equation 3.9) depends on the direction in which the load is applied with respect to the fractures. Positive values of parameter b_T^p allow to take into account the fact that the UCS is minimum when the load is applied at 45° to the fractures (the minimum is reached at 45° when $a_N = 0$). The lower material strength at 45°is qualitatively similar to the measurements done on sound sample of COx, thus a first order of magnitude of the parameter b_T^p is calculated with the experimental data from research campaign supervised by ANDRA. The strength parameters, cohesion and friction angle, have been taken according to the values stipulated in ANDRA's documents, with $C = 5$ MPa and $\phi = 24°$.

The dilatancy angle is unknown, and there are no experimental data available to our knowledge to determine it. Dilatancy may be described as the change in volume that is associated with shear distortion of an element in the material. A suitable parameter for characterizing a dilatant material is the dilatancy angle ψ. This angle represents the ratio of plastic volume change over plastic shear strain. As the theory of plasticity established for metals began to be applied to materials like soils, rocks or concrete, some research teams have started to work on the meaning and manipulation of this parameter to describe geomaterials [1, 60]. Associated flow are clearly useful since the number of functions needed to model the plastic response will be reduced by one (as it comes to assume that the failure criterion and plastic potential forms are the same). However, some authors disregard associated flow rules since, theoretically, these involve plastic deformation without energy dissipation, which is inconceivable. Nevertheless, without experimental data, two simple hypothesis are possible: the dilatancy can be considered equal to the friction angle or it can be set to zero. Assuming that the dilatancy angle is equal to the friction angle comes to an overestimation of the plastic volumetric strains. However, the angle of dilatancy cannot reasonably be set to zero as the plastic behavior is identified during the excavation phase during which irreversible volumetric strains develops for sure, at least due to the creation and opening of fractures related to the deconfinement of the drift wall. Thus an associated flow rule is used in our simulations. The plastic strain field is controlled by checking the short-term convergences. As a matter of fact, Guayacan-Carrillo et al., [41] succeeded in separating the instantaneous response to the excavation process from the time-dependent one, making it possible to calibrate the elasto-plastic parameters of the constitutive law on the short-term response of the claystone. They suppose that all displacement occurring during the front advancement

time corresponds to the instantaneous behavior of the rock while the displacements which occurred between the excavation steps (time to install the support system and the measurements) corresponds to the time-dependent rock behavior. The front advancement does not provoke any additional instantaneous displacement when the drift's front is sufficiently far (at about two diameters distance) from each section.

Viscous parameters

The six parameters governing the viscous behavior of the material, a, n, α, a_N^v, b_T^v and σ_c are first fitted on experimental data on the intact rock. The three parameters a, n, α of Lemaitre's creep law are fitted on a triaxial creep test provided by ANDRA. These parameters are fitted supposing an isotropic viscous behavior of the rock. As a matter of fact, the anisotropy in viscosity is carried by the functions β^p and β^v and not by the parameters a, n, α, and σ_c. The tests are conducted under a confining pressure of 12 MPa, while applying 50%, 75% and 90% of the peak stress, resulting in three curves giving axial strain evolution with time. The calibration is done by performing a linear regression with multiple parameters after linearizing Lemaitre creep law (equation 3.21), allowing to determine the time dependency parameter α.

$$\ln(\varepsilon) = \ln(a) + n\ln(\sigma - \sigma_c) + \alpha\ln(t) \tag{3.21}$$

Indeed, the first linear regression gives $\ln(a) + n\ln(\sigma - \sigma_c)$ and α for the three different loading. The parameter α is taken as an average value supposing that it does not depends on the stress. As we know the numerical value of $\ln(a) + n\ln(\sigma - \sigma_c)$ and $\ln(\sigma - \sigma_c)$, performing another linear regression on loading's to 50%, 75% and 90% of the peak stress, allows to determine the two other parameters of the law, a and n. The theoretical curves corresponding to the model with the parameters resulting from these linear regressions are given in Figure 3.4. The parameters found are $a = 1.5\ 10^{-4}$ MPa^{-1}day$^{-\alpha}$, $\alpha = 0.215$ and $n = 1$.

3.4 Excavation modeling procedure

Modeling tunnel excavation is essentially a four dimensional problem, as it not only concerns with the three spatial dimensions but also with a temporal dimension, which corresponds to the advancing process of the tunnel face. Numerous works have been conducted to analyze the stresses and displacements induced by the excavation (e.g. [13, 20, 54, 39]). In this work, we did not focus on modeling the fracturing of the rock around the structures due to excavation. Nevertheless, the elasto-plastic response following excavation of the model has consequences on the stress and strain state of the tunnel and thus has some influence

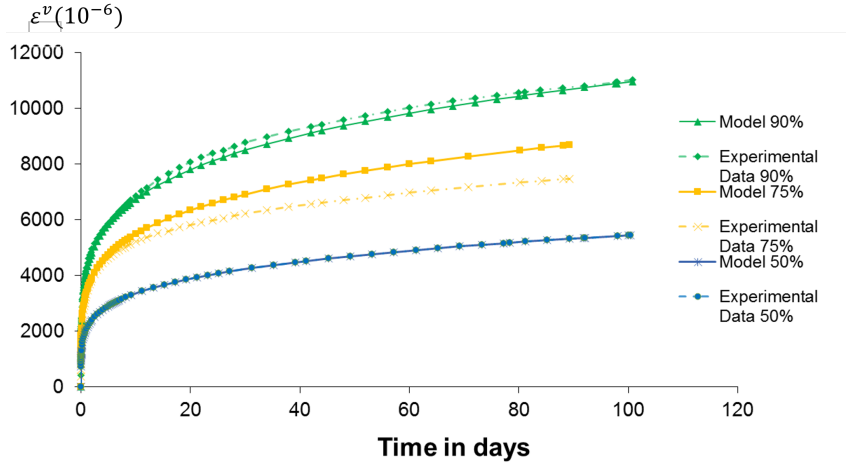

Fig. 3.4.: Axial viscoplastic strain for creep tests performed at 50, 75 and 90% of the peak strength. Experimental and numerical results.

on the long-term convergences of the drifts. Moreover, as our objective is to compare the results of numerical simulations with *in situ* measurements (e.g. with measurement strings), the excavation has to be simulated such as the numerical convergences and are actually comparable *in situ* measurement. This implies that the numerical simulations need to represent, at least to some extent, the specific work schedule of the excavation of GED and GCS drifts. This ensures that the numerical estimations of convergence actually correspond to the way the convergences were measured *in situ*. First simulations have been performed with the excavation option in Disroc which enable to calculate, the unloading of a 2D cavity. Considering a long tunnel without deviations, the assumption of plane strains is commonly used. This approach is then used in all drift simulations, both in this chapter and in the following chapter. While it is well known that plane strain models are not able to completely account for the actual stress history and tend to underestimate the deformations, Cantieni et al., [21] have shown that for support completion close to the face and for flexible linings (which is the case for GED and GCS drifts), the error in the results is not significant.

Disroc allows to easily model the excavation phase, as represented in Figure 3.5. Indeed, by removing the mesh inside the tunnel, after the application of the geostatic state, it creates a file containing the forces which balance the stresses in the rock mass. The geostatic stress state σ can be anisotropic. Then we make these forces tend towards zero to model the excavation. In order to take into account the viscous deformations that develop during the excavation of the tunnel, the discharge of the forces on the drift wall is separated into two parts, a time-independent part and a time-dependent part during which viscous deformations develop. In fact, it would be possible to do the whole unloading as a function of time, but this would considerably lengthen the calculation time. Moreover, the objective of our numerical simulations being to reproduce the convergences of the instrumented tunnels at

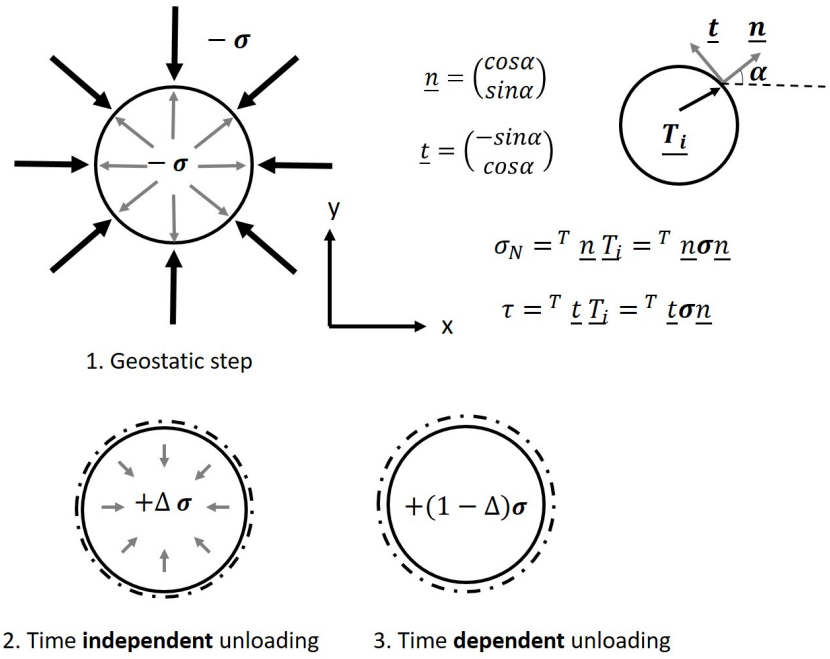

Fig. 3.5.: 1) Geostatic state, 2) time-independent unloading, 3) time-dependent unloading.

the URL, it is necessary to simulate only the phases actually measured, and a first phase of the excavation is not measured (before the advancing front reaches the section) because it is only once the advancing front has reached the section that the measuring instruments are put in place.

In order to perform a time-based unloading is to set the unloading time corresponding to the desired unloading rate. For example, a time of 1 corresponds to an unloading of 100%, so to perform 50% of the unloading, we set the end time of the calculation to 0.5. Then, to take into account the fact that this unloading of x% is done in t days, the parameter a of the viscosity law, given in equation 3.16 of the model written a^{COx} is modified into a^e, so that the viscous deformation occurring after x days simulated, corresponds to the viscous deformation after t days.

$$a^e = \frac{a^{\mathrm{COx}} t^\alpha}{x^\alpha} = \frac{1.95 \times 10^{-4} \times 28^{0.215}}{0.7^{0.215}} \tag{3.22}$$

Equation 3.22 is the calculation of modification of parameter a assuming that we want to simulate 70% excavation in 28 days. Knowing that the calibration of the viscosity law on the creep tests on COx claystone gives that $a^{\mathrm{COx}} = 1.95\ 10^{-4}$ and $\alpha = 0.215$.

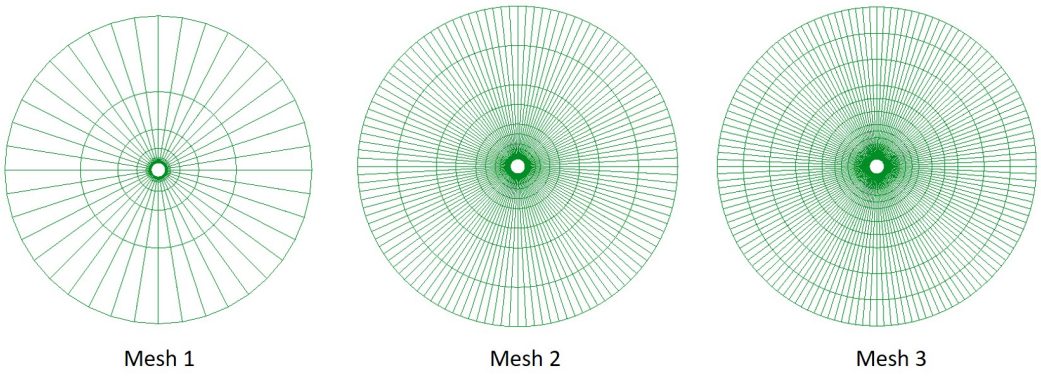

Fig. 3.6.: The geometry is meshed by quadrilateral elements with three different refinements.

3.4.1 Sensitivity analysis of the mesh

The sensitivity analysis of the mesh, that is used for the numerical simulations presented in the following sections, has been made on the excavation procedure. Three different mesh presented in Figure 3.6 have been compared for plastic isotropic excavations, as analytic solutions allow to assess the numerical error. The mesh is constructed by subdividing concentric circles around the tunnel into a number of divisions (depending on the refinement required). The mesh is refined near the tunnel walls but has larger elements further away in order to reduce the computation time [59]. The mesh which is actually used in the numerical simulations is *Mesh 2* in Figure 3.6. It has been validated by comparison with one more refined (*Mesh 3*) and one mesh less refined (*Mesh 1*). The plastic radius that develops around a tunnel is given by equation 3.23 and thus it enables to evaluate the quality of our mesh by comparing the result obtained numerically with that expected theoretically.

$$R_p = R[\frac{2}{K_p+1}\frac{(K_p-1)\sigma_0+\sigma_c}{(1-\lambda)(K_p-1)\sigma_0+\sigma_c}]^{\frac{1}{K_p-1}} \tag{3.23}$$

With $K_p = \frac{1+sin\phi}{1-sin\phi}$, $\sigma_0 = 12.4$ MPa, the strength under compressive stress $\sigma_c = \frac{2Ccos\phi}{1-sin\phi}$. The strength parameters of the COx claystone are used: $C = 5$ MPa and $\phi = 24°$. It is found that theoretically $R_p = 3.03$ m, and the relative error is estimated as:

$$\frac{|r_p(mesh) - r_p(theoretical)|}{r_p(theoretical)}\% \tag{3.24}$$

The analysis presented in Figure 3.7, shows that the less refined mesh would not be a reliable option. The adopted mesh (referred to as *Mesh 2*) constitutes an acceptable numerical choice since the extension of the plastic radius and values are almost the same as for the refined mesh. Another sensitivity analysis was conducted by taking the viscous effect into consideration presented in Appendix A.3.

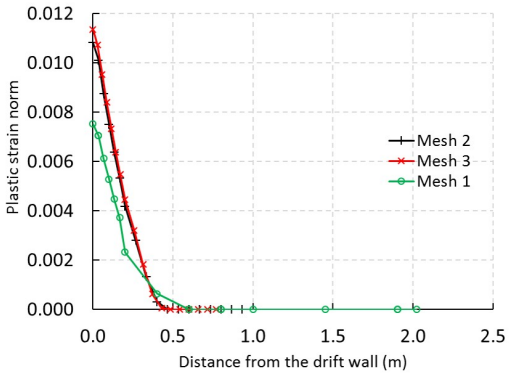

	Mesh 1	Mesh 2	Mesh 3
Error (%)	5.6	0.33	0

Fig. 3.7.: Evaluation of the error due to the finite elements approximation. a) Plot of the plastic strain norm in function of the distance from the wall of the drift. b) Evaluation of the difference between the plastic radius determined by the finite element method and the theoretical value.

Tab. 3.1.: Excavation Data for section C of GCS drift and section A of GED drift.

Drift / Section	Step 1	Step 2	Step 3
GCS / C	14 days: $\lambda = 30\%$	0 day: $\lambda = 0\%$	28 days $\lambda = 69\%$
GED / A	14 days: $\lambda = 30\%$	1 day: $\lambda = 18\%$	35 days $\lambda = 51\%$

3.4.2 Modeling of the excavation of GED and GCS drifts

The correspondence between the actual excavation procedure of the drifts and the procedure used in the numerical modeling of the excavation is presented in Figure 3.8. Note that the time needed to complete the excavation of one section in a given drift is different between the sections, which is why two specific sections have been considered (one for each drift: section C for GCS drift and section A for GED drift). Thus the work schedule of those two sections provided by [42] and [5] has been analyzed more precisely, and they are the basis for the proposed tunnel excavation modeling. Those sections were chosen because they correspond to the sections for which the data were the most trustworthy according to ANDRA. The sections of interest of each drifts are treated in the same way only with different values reported in Table 3.1. The excavation procedure in Figure 3.8 is explained for the section A of GED drift.

As can be seen in Figure 3.8, at the initial equilibrium state, the section of interest in each drift is submitted to the natural state of stress. Then as the drift front reaches the section of interest, 30% of the initial stress has been removed. This first step is performed by a time independent calculus in our model, as we are not able to assess the time-dependent displacements that could have occurred in the section before the front drift reaches the section. Then, based on ANDRA's data, the measurements were installed in 1 day, which

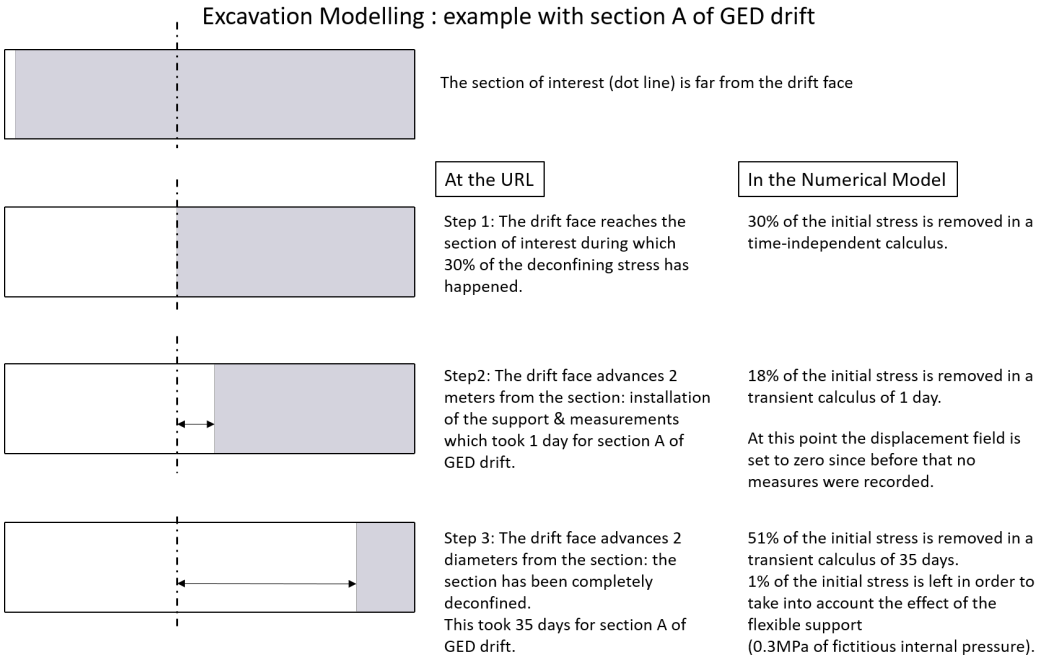

Fig. 3.8.: Description of the excavation modeling of section A of GED drift.

corresponds to 18% additional deconfinement according to the deconfinement rate curve given by ANDRA [75]. This step is modeled by a transient simulation. At this point in the model, by keeping the resulted stress field, the displacement field is set to zero since the displacements correspond to the lost convergence. Finally, it has been considered that the drift face has no more influences on the section deconfinement when it is 2 diameters away from the section. Hence, the last 51% of the initial stress is deconfined in a transient simulation. As a matter of fact, we leave 1% of the initial stress in order to take into account the effect of the flexible support. The comparison between the displacements measured *in situ* during the excavation and the predictions of the numerical models was plotted in Figure 3.9. It is assumed that the short-term convergences are sufficiently well reproduced to constitute the initial state to simulate the long-term convergence of the drifts.

3.5 Numerical model of the convergence

Studies conducted on URL tunnels have shown that the behavior tunnel convergences cannot be represented without taking into account the fractures around the structures. In this work, the approach considered to build the numerical models is based on the assumption that the long-term behavior of the tunnels of the URL, i.e., after the fractured zone has been created by excavation, can be represented by an anisotropic viscous model that accounts for

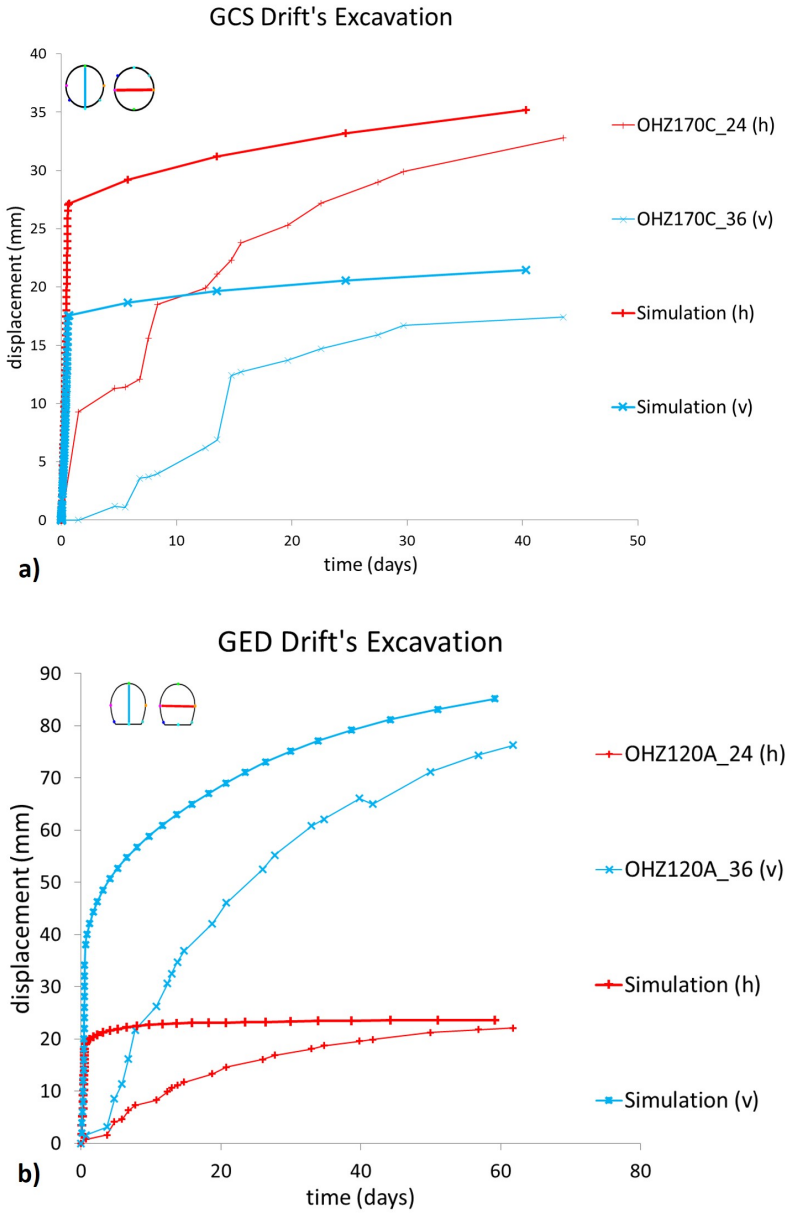

Fig. 3.9.: Comparison between excavation displacements measured *in situ* and numerical model predictions for a) GCS drift b) GED drift.

viscous slip on the chevron fractures, anisotropy that is due to the non-isotropic distribution of the fractures around the tunnels. In addition, one difficulty is to model the two types of galleries, excavated according to the major or minor principal horizontal stress, with the same constitutive model. Indeed, in both cases, the fractured zone develops in opposite directions (in horizontal direction for one gallery and vertical for the other), which makes modeling both types of galleries, although they are effectively excavated in the same material, with a single model far from obvious. In this chapter we assume that the mechanical model of the rock, in which GCS and GED drifts are excavated, can be represented by that of a medium containing a family of parallel fractures. The continuous equivalent mechanical behavior, understood as the macroscopic behavior of the rock and the fractures induced by the excavation, of this fractured medium can then be reasonably represented by a transverse isotropic behavior. The orientation of the fractures corresponds to the dominant orientation in the fractured zone (Figure 3.3) which develops during the excavation of the drifts. Three different anisotropies, elastic, plastic and viscous, are taken into account based on the *in situ* convergence measurements and the available knowledge on the rock's behavior. Two different models were used for GCS drift and for GED drift. Figure 3.10 shows the

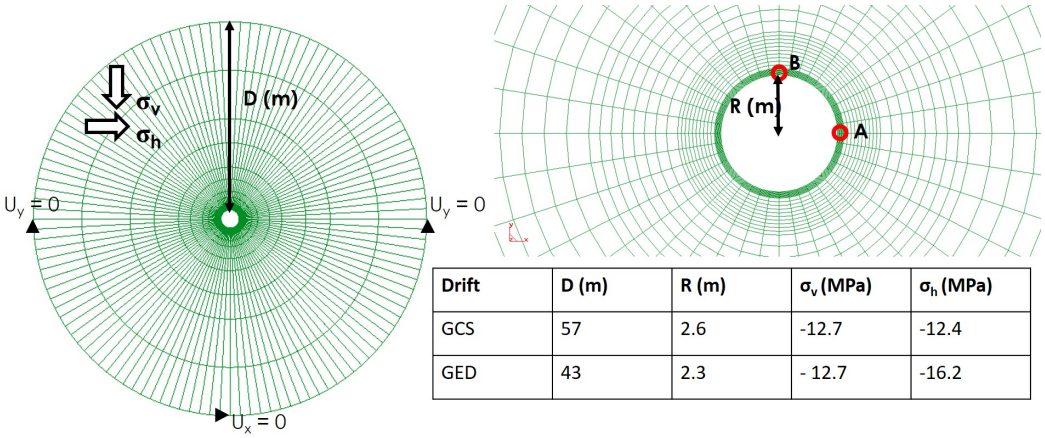

Drift	D (m)	R (m)	σ_v (MPa)	σ_h (MPa)
GCS	57	2.6	-12.7	-12.4
GED	43	2.3	- 12.7	-16.2

Fig. 3.10.: Geometry and mesh support to the numerical simulations. Both vertical and horizontal convergence are respectively measured in points A and B.

mesh used for the simulation of GED and GCS drift. The only difference in the boundary conditions of the two models is the horizontal stress, which is $\sigma_h = -12.4$ MPa for GCS drift and $\sigma_H = -16.2$ MPa for GED drift.

3.5.1 Identification of anisotropy parameters

The isotropic model parameters for the elastic, plastic and viscous parts have been evaluated based on the available experimental results on intact rocks and presented in sections 3.2.1 3.2.3 and 3.2.4 respectively.

It is assumed that the anisotropy is induced mostly by the fractures, and the effect of the intrinsic anisotropy of COx claystone (related to the bedding planes) is negligible in comparison to the effect of the fractured zone. The anisotropy parameters related to the plastic and the viscous deformations, a_N^v, b_T^v, a_N^p and b_T^p, are obtained by numerical calibration through a simulation of the drift's convergence and comparison with *in situ* measurements. In this way, the effect of the fractured zone around each drift will be indirectly taken into account in the calibrated values of the parameters. The calibrated model can then be used to extrapolate the drift's convergence to longer time periods.

Before the numerical calibration of the parameters of anisotropy, first guesses are estimated based on the available experimental results on intact rock samples. Even though, the effect of the fractured zone on the anisotropy was assumed to be much more important than the intrinsic anisotropy of the rock, however, the estimations based on experimental results can be considered as starting points, probably lower bonds, of the calibration procedure, especially in the case of the GED drift where the fractures and the bedding planes are in the same direction (horizontal planes). Four anisotropic parameters need to be determined: (a_N^p, b_T^p) regarding the plastic behavior and (a_N^v, b_T^v) regarding the viscous behavior. Among them, two parameters can easily be pre-determined with laboratory experiments on sound rock. As a matter of fact, experimental campaign investigating the compressive strength of COx claystone (triaxial tests) show that minimum strength is found for stress applied at 45° with respect to the bedding plane. These experimental results give a first order of magnitude of parameter b_T^p because it expresses the slip on the planes of weakness formed by the bedding, eventually our objective is to account for a similar slip on the planes of weakness formed this time by the fractures. Also, uniaxial creep tests performed under stress applied parallel and perpendicular to the bedding planes give a first order of magnitude of parameter a_N^v. The evaluation of parameters b_T^p and a_N^v is described in appendix A.2, and gives that $b_T^p = 0.8$ and $a_N^v = 0.43$.

The numerical simulations are compared with field measurements with a configuration schematically represented in Figure 3.11. The green line and dot line represent the two convergence measurement strings that were installed during the drift excavation: (OHZ170_24, OHZ170_36) in GCS drift and (OHZ120_24, OHZ120_36) in GED drift. Moreover, for GCS drift, an extensometer has been emplaced from an adjacent drift (GAT) (see Figure 2.1) in order to measure the rock displacement not only at the drift wall, but also in the rock at 0.78, 1.82, 3.38, 4.68, and 5.72 meters away from the drift wall, which are represented by green crosses in Figure 3.11. The set of model parameters are presented in table 3.2 for GCS drift and in table 3.3 for GED drift.

In the case of GCS drift, the identified anisotropy parameters for plasticity are $a_N^p = -0.25$ and $b_T^p = 2.75$. The negative value of a_N^p ensures that for the fractured rock the value of UCS

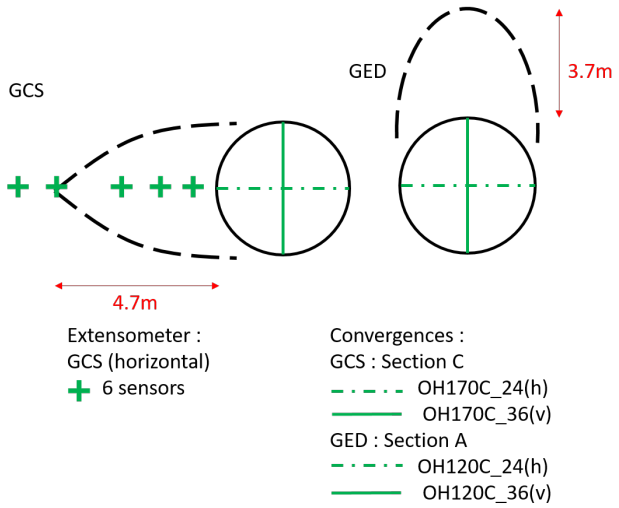

Fig. 3.11.: Schematic representation of the *in situ* measurements configuration in GCS and GED drifts.

Tab. 3.2.: Numerical values of the parameters used for the simulation of GCS drift.

Elasticity	Plasticity	Viscosity	Anisotropy
$E_{\parallel} = 5000$ MPa	$C = 5$ MPa	$a = 1.95 \times 10^{-4}$ MPa^{-1}day$^{-0.2}$	$\omega = 90°$
$E_{\perp} = 3000$ MPa	$\phi = 24°$	$n = 1$	$a_N^p = -0.25$
$\nu_{xy} = 0.3$	$\psi = 24°$	$\alpha = 0.215$	$b_T^p = 2.75$
$\nu_{xz} = 0.2$		$\sigma_c = 3.6$ MPa	$a_N^v = 0.43$
G= 1700 MPa			$b_T^v = -0.3$

Tab. 3.3.: Numerical values of the parameters used for the simulation of GED drift.

Elasticity	Plasticity	Viscosity	Anisotropy
$E_{\parallel} = 5000$ MPa	$C = 5$ MPa	$a = 1.95 \times 10^{-4}$ MPa^{-1}day$^{-0.2}$	$\omega = 0°$
$E_{\perp} = 3000$ MPa	$\phi = 24°$	$n = 1$	$a_N^p = -0.3$
$\nu_{xy} = 0.3$	$\psi = 24°$	$\alpha = 0.215$	$b_T^p = 1.3$
$\nu_{xz} = 0.2$		$\sigma_c = 3.6$ MPa	$a_N^v = 1$
G= 1700 MPa			$b_T^v = 0.9$

in direction perpendicular to the fractures is greater than its value in direction parallel to the fractures, which is qualitatively consistent with the effect of bedding planes. Moreover, as presented in section 3.2.4, the parameter a_N^p also controls the viscous stress threshold. For the anisotropy in viscous stress threshold, $a_N^p < 0$ means that the viscous strains start to develop for a smaller stress in the fractured rock than in the sound rock. With $b_T^p > a_N^p$, the UCS of the fractured rock is minimum when the load is applied at about 45°of the fracture plan. The calibrated functions β^p for GCS and GED drift's with their corresponding UCS are presented in Figure 3.12.

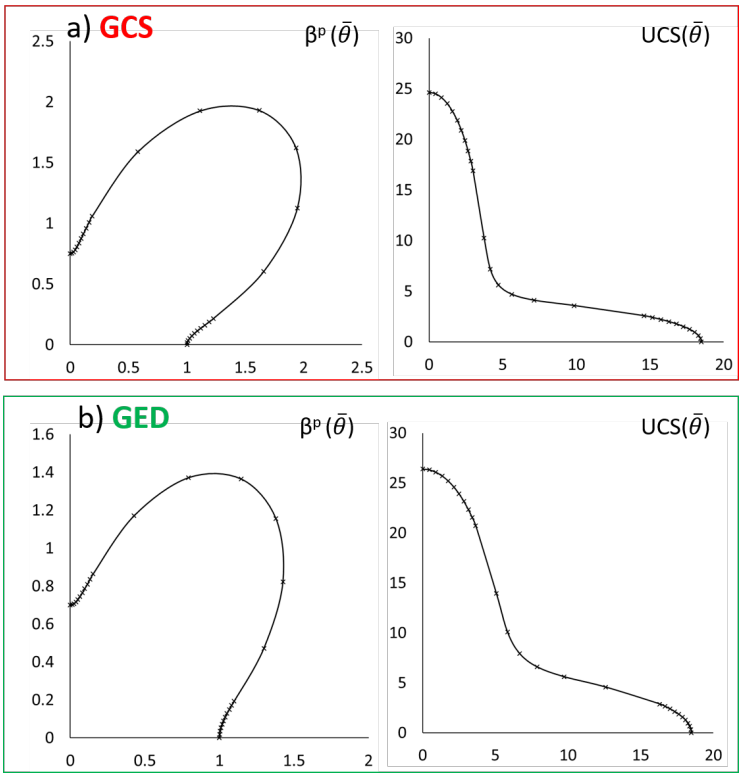

Fig. 3.12.: Polar representations of the functions β^p and UCS (the horizontal axis corresponds to the bedding plane) for a) GCS drift with a_N^p = -0.25 and b_T^p= 2.75, b) GED drift with a_N^p = -0.3 and b_T^p= 1.3

The calibrated functions β^v for GCS and GED drifts are presented in Figure 3.13. The numerical simulation results are presented in the next section and permit to verify the model ability to reproduce the observed drift's convergence and its anisotropy.

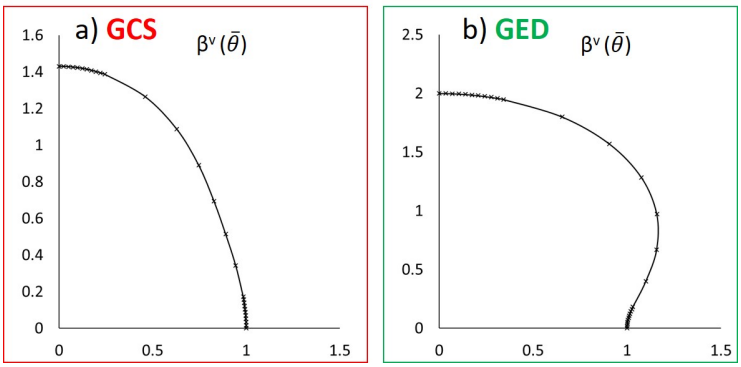

Fig. 3.13.: Polar representation of the function β^v for a) GCS drift with a_N^v = 0.43 and b_T^v= -0.3, b) GED drift with a_N^v = 1 and b_T^v= 1.1

3.5.2 Results and discussion

After the application of the far field stress and modeling the drift's excavation, according to the procedure explained in section 3.4.2, the drifts viscous convergences are calculated under constant applied loads for over 2500 days, which allows to compare the numerical results with the field observations. Every simulation lasts at least a couple of hours (about 3 days for the simulations of GED and GCS drifts), with the duration of the simulation increasing with the viscosity. As a matter of fact, the time increment must be small enough to avoid numerical instabilities but not too small to limit the computation time. One can find in the literature critical time increments for Lemaitre creep law [25, 14]. Indeed, a critical time increment can be established knowing that the mechanical system has to always remain in mechanical equilibrium, which means that the time-dependent stress increment cannot become too big compared to the strain dependent stress increment. We have implemented an automatically changing time increment which starts at $\mathrm{d}t = 10^{-19}$ day to reach at the end of the simulation a total time = 2500 days with $\mathrm{d}t = 1$ day. The time step $\mathrm{d}t$ is expressed as a function of the current time given by equation 3.25.

$$\mathrm{d}t = \frac{A \times t^n}{1 + t^n} + C \tag{3.25}$$

Its expression is such that for the beginning of the calculation ($t << 1$), the time step varies slowly, then when the time becomes large enough, which corresponds to smaller variation of the viscous deformations, the time step is increased in order to decrease the total calculation time. In equation 3.25, when $t \to \infty$: $\mathrm{d}t = A$ and when $t \to 0$: $\mathrm{d}t = C$. In our simulations $A = 1$, $n = 1.43$ and $C = 10^{-19}$. When increasing viscosity it may be necessary to increase parameter n and decrease parameter C.

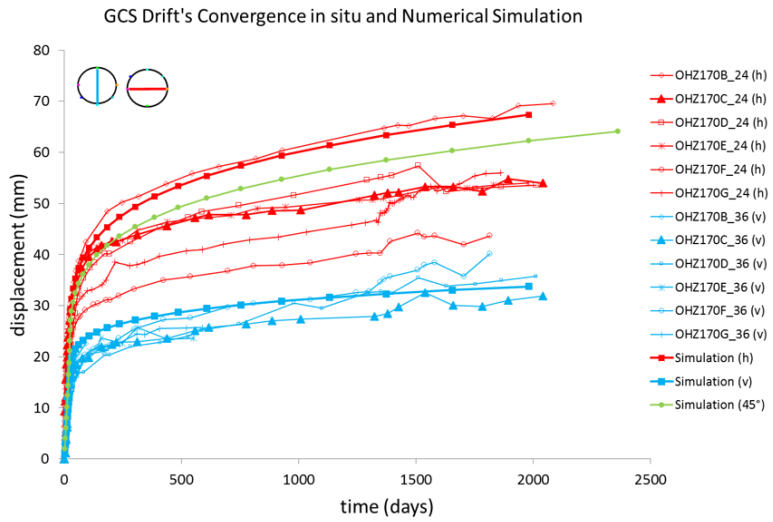

Fig. 3.14.: Convergences of GCS drift, comparison between field measurements and numerical model.

GCS drift

First the simulated convergence for GCS drift are presented in Figure 3.14 using the calibrated parameters as given in Table 3.2. The convergences obtained by numerical simulation are plotted in bold: in red the horizontal convergence, in blue the vertical convergence and in green the convergence at 45°. The other curves correspond to the horizontal and vertical convergences measured in different cross sections of the GCS gallery. Because the numerical excavation was defined based on the excavation data for section C, measurements related to this specific section are highlighted by solid triangle marks in the graph. One can see that the drift's convergence and its anisotropy show a quite good compatibility with *in situ* measurements.

It is precisely because of the anisotropy of both plasticity and viscosity that the convergences and convergence rates measured *in situ* can be reproduced. Indeed, Figure 3.15 shows a) the convergence models if an isotropic viscoplastic law is considered. In that case the material is isotropic and only the slight anisotropy in the state of stress is taken into account. With no surprise, the results are not in agreement with the *in situ* measurements. In another simulation, the results are a little bite improved by making the plasticity anisotropic as shown in Figure 3.15 b). The results are already quite good just with plastic anisotropy because, in the case of the GCS gallery, the convergence rates are not very anisotropic. In fact, the average horizontal convergence rate between 500 and 2000 days is 0.0062 mm/day and 0.0079 mm/day in the vertical direction. Eventually it is by taking into account the viscoplastic anisotropy that we better fit the *in situ* convergences. Figure 3.16 presents

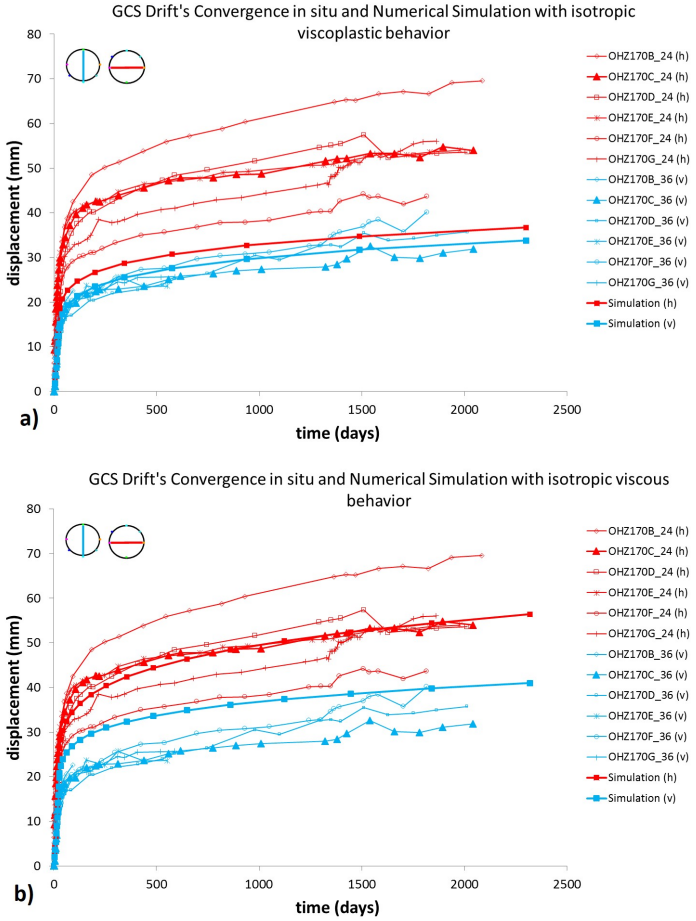

Fig. 3.15.: Comparison between field measurements and numerical model of a) Convergences of GCS drift with viscoplastic isotropic behavior, b) with plastic anisotropy and viscous isotropy.

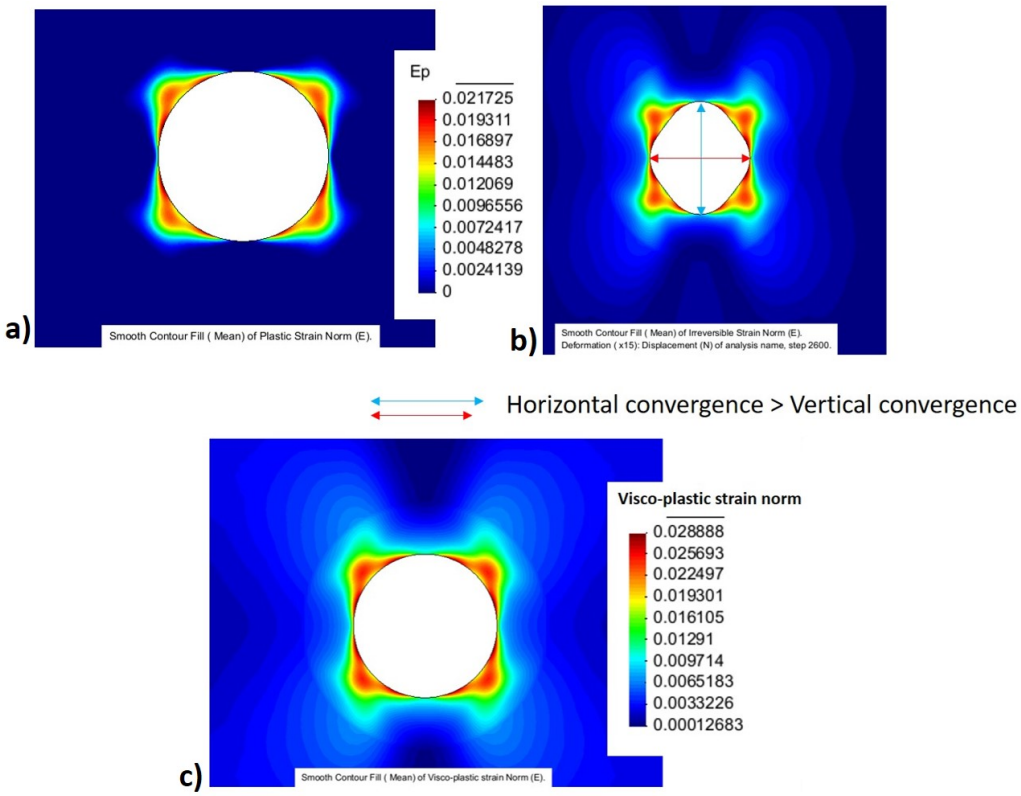

Fig. 3.16.: a) Plastic strain norm after 2800 days around GCS drift with the optimum anisotropy parameters (Table 3.2) b) As a) plastic strain norm but with the deformation magnified $\times 15$ to stress the fact that horizontal convergence are bigger than vertical convergence. c) Visco-plastic strain norm after 2800 days around GCS drift with the optimum anisotropy parameters (Table 3.2).

the simulated plastic strain norm and visco-plastic strain norm which develops around the drift. The deformed shape of the mesh, magnified fifteen times, shows a bigger convergence in the horizontal direction than in the vertical direction. The objective of the model is to reproduce the measured convergences of the tunnel, however we do not pretend to reproduce the fractured zone with the deformation field.

Figure 3.17 shows a comparison between the displacement measured in the rock at 0.78, 1.82, 3.38, 4.68, and 5.72 meters away from the drift wall with an extensometer. Up to 3.6 m from the tunnel walls, the numerical model predicts the displacements in the rock quite well. However, when leaving the fractured zone, as shown in the green curve, our model overestimates the displacements. This is not surprising since in our model, the whole rock mass is "fractured". This is not critical as only the displacements at the drift wall are necessary to estimate the stresses in the linings. Our objective was not to model what happens far from the tunnel wall, but to reproduce as simply as possible the convergences measured at the wall.

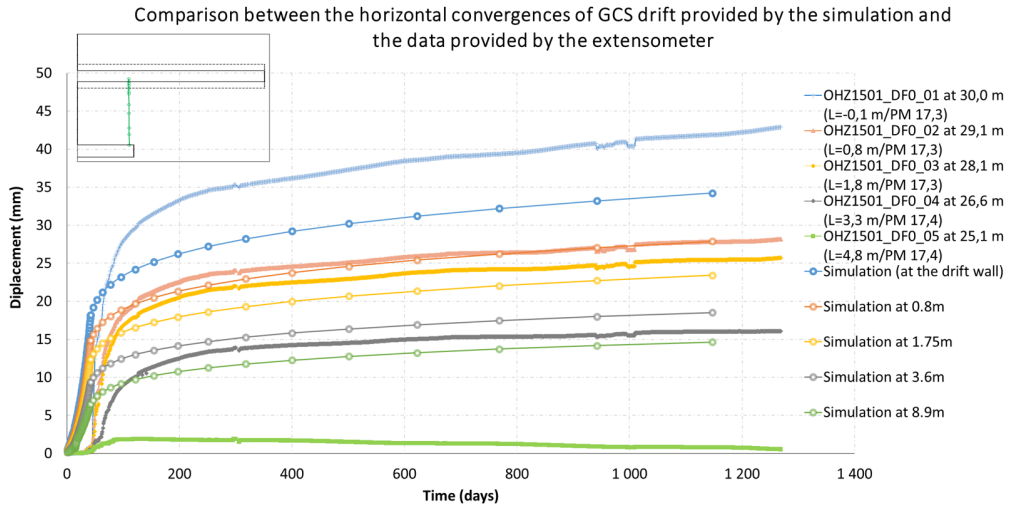

Fig. 3.17.: Horizontal displacement in the rock mass nearby GCS drift (at 0.78, 1.82, 3.38, 4.68, and 5.72 meters away from the drift wall), comparison between field measurements and numerical model.

GED drift

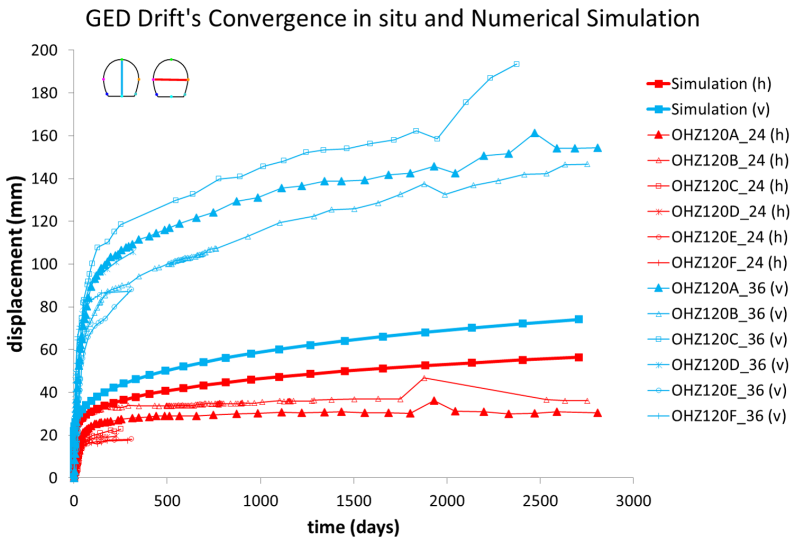

Fig. 3.18.: Convergences of GED drift, comparison between field measurements and numerical model, with the parameters of anisotropy of GCS drift with just a 90° rotation of the isotropy plane.

Before presenting similar results of parameters calibration for GED drift, it is interesting to see if its convergence can be simulated only by a 90° rotation of the anisotropy direction in the calibrated GCS model and of course by applying the far stress boundary conditions of GED drift. Note that $\omega = 90°$ for GCS drift and $\omega = 0°$ for GED drift. The results, in Figure

3.18, show that only by changing the orientation of the plane of anisotropy (corresponding to the fracture planes), the GCS model can predict qualitatively the convergence anisotropy in GED drift with vertical convergence bigger than the horizontal one. Nevertheless, the vertical convergence is highly underestimated which is mainly due to the fact that the fractured zone in GCS and GED drifts are not equivalent. Indeed, applying the anisotropy parameters of the GCS gallery to the GED gallery simply by rotating the isotropy plane by 90 degrees is equivalent to assuming that the two fractured zones are symmetric by a 90 degree rotation. The study of the fractured zones, detailed in the following chapter, shows that they do not have the same extension and that the density and orientation of the fractures are not the same around the two types of drifts. The irreversible strain field, corresponding

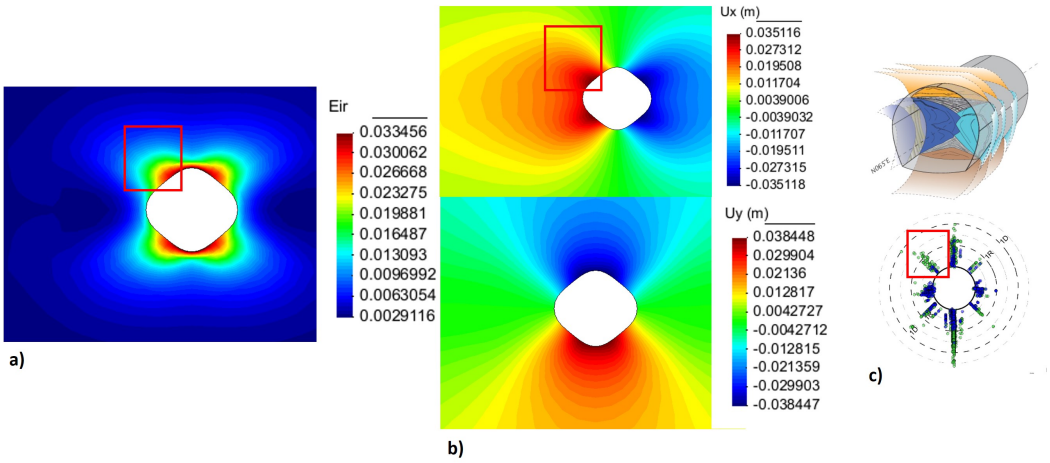

Fig. 3.19.: a) Irreversible strain norm (with deformation $\times 17$) that has developed after 2800 days around GED drift with the parameters of anisotropy calibrated for GCS drift but with $\omega = 0°$. b) Vertical U_y and horizontal U_x displacements in meters (with deformation $\times 17$). c) Representation of the fracture zone around GED drift.

to the visco-plastic deformation, is presented in Figure 3.19, alongside with the vertical and horizontal displacement. In this figure, we have represented alongside the results of the numerical simulation a representation of the fractures around GED drift. The graph represents a survey of the fractures counted around the galleries excavated in the same direction as the GED gallery. We can relate the fractures that develop mainly in the vertical direction but also the 45 degree behavior boxed in red in Figure 3.19 with the results of the numerical simulations.

Though, the parameters of anisotropy need to be readjusted in order to obtain a better compatibility between the simulation and measured drift convergence. The simulation results with the calibrated parameters given in table 3.3 are presented in Figure 3.20 and show a good compatibility between the measured and simulated convergence. The same remarks, as for GCS drift, regarding the importance of the anisotropy in both viscosity and plasticity, can be formulated for GED drift. Figure 3.21 shows that the results for

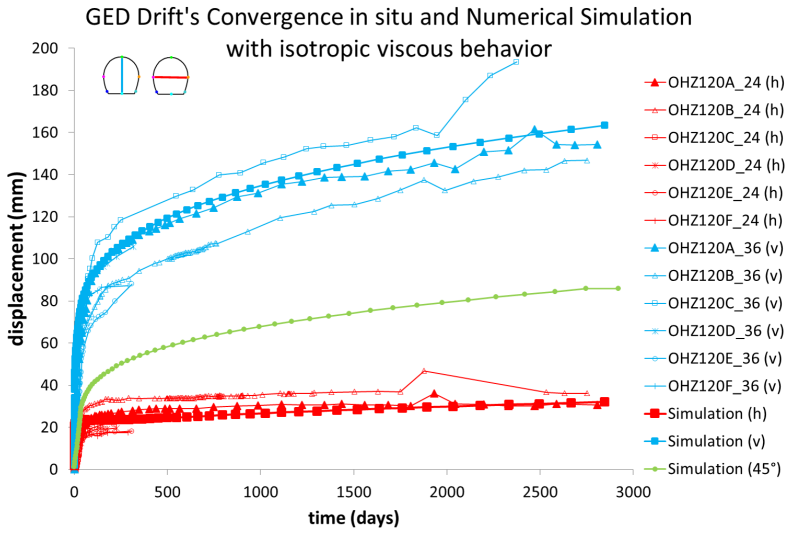

Fig. 3.20.: Convergences of GED drift, comparison between field measurements and numerical model with the anisotropy parameters presented in Table 3.3.

viscoplastic isotropy don't even reproduce the fact that the vertical convergence are greater than the horizontal convergence. Only, considering an anisotropic plastic behavior do not really improve the results, nevertheless by adding the anisotropy in viscosity, a good reproduction of the *in situ* measurements is achieved. The simulated irreversible strain field, corresponding to the visco-plastic deformation, is presented in Figure 3.22, with the deformed shape magnified fifteen times. A bigger convergence in the vertical direction than in the horizontal direction is clearly shown by the deformed mesh.

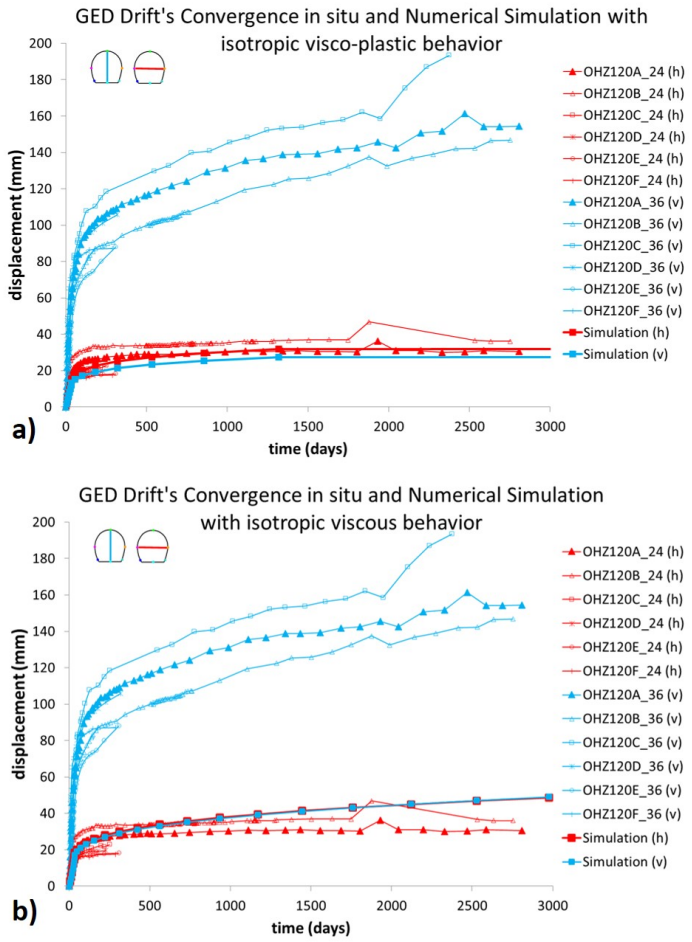

Fig. 3.21.: Comparison between field measurements and numerical model of a) Convergences of GED drift with viscoplastic isotropic behavior, b) with plastic anisotropy but viscous isotropic behavior.

3.6 Conclusion

As a reminder, the objective of the work presented in this chapter was to propose the simplest possible model capable of reproducing the convergences of the two types of drifts excavated at the URL. By the simplest, we mean the most easily applicable by the design offices that are going to be in charge of the design of the drifts' supports. Working with a continuous model helps reducing the computation time compared to models in which the discontinuities (fractures) are explicitly represented. Also the constitutive models used, Mohr-Coulomb criterion and Lemaitre creep law are well known models in the community of rock mechanics and well known by the engineers working in this field.

Numerical simulations have been used to reproduce the convergence of the drifts (GCS and GED) of the MHM URL with a continuous and homogeneous but anisotropic model. The

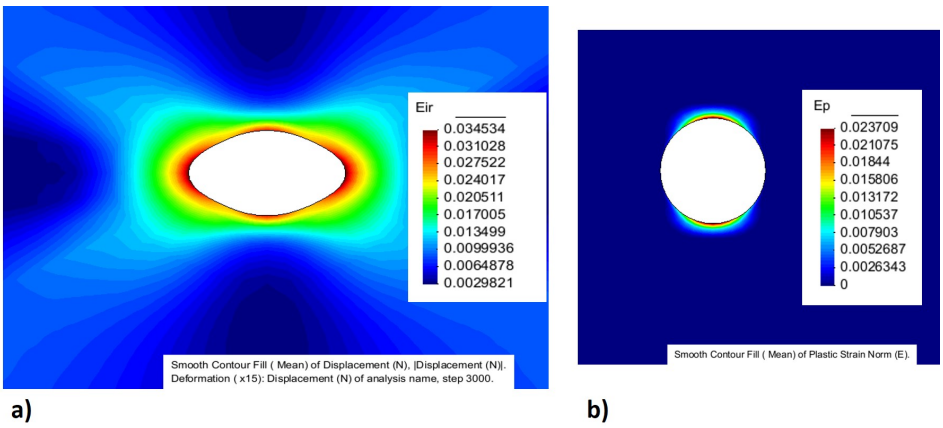

Fig. 3.22.: a) Irreversible (visco-plastic) strain field developed after 2800 days around GED drift with the optimum anisotropic parameters (Table 3.3) (with deformation $\times 15$). b) Representation of the plastic strain norm.

effects of the fractured zone on the convergence are taken into account with a threefold, elasto-visco-plastic, anisotropy. The anisotropy thus represents the global behavior of the rock mass around the drifts, which is made of both sound rock and fractured rock. The modeling approach presented allows the fractured zone to be considered in a fairly simple manner. In particular, the construction of these models does not require precise knowledge of the density or orientations of fractures in the fractured zones around the drifts to calibrate the parameters. We simply considered vertical fractures in the case of the GCS drift and horizontal fractures in the case of the GED drift. Finally, the models proposed as design tool are two continuous, transverse isotropic models. The elasto-viscoplastic parameters (Young's moduli, Poisson's ratios, cohesion, friction angle etc.) are characteristic values of the Callovo-Oxfordian claystone provided by ANDRA plus four anisotropy parameters for each gallery. Despite the overall simplicity of the model, it is thanks to the introduction of both viscous strain rate and viscous stress threshold anisotropy in the creep law, which allow us to get a more accurate response of the rock to the stress field for its viscous deformation.

While the simplicity of the model does not permit to explain the initiation of the fractured zone around the drifts itself, it enables a trustworthy reproduction of the vertical and horizontal convergences and convergence rates, at the drifts wall, after the excavation. With relevant reproduction of the convergences, we aim to provide a reliable tool for the design of the linings. In fact, the model presented here will enable us to do a first approximation of the long-term stresses in the support system. Moreover, as our viscous model takes into account a stress threshold, the stresses in the linings predicted by our model should be more realistic than the models considering the rock as a viscous fluid (without stress threshold).

Nevertheless the main deficiency of these models is the understanding of the anisotropy parameters. Indeed, the link between the anisotropy parameters and the fracture behavior is not explicit and thus the calibration of the parameters is not obvious. One must be aware of the complexity that is absorbed by these anisotropy parameters. As a matter of fact, when we say that we neglect the intrinsic anisotropy of COx claystone and consider only the anisotropy induced by the chevron fractures, this is true in our logic but in reality, when we calibrate the anisotropy parameters on the *in situ* measurement data, our anisotropy parameters intrinsically contain the effects of the chevron fractures but also those of the tensile fractures, the effects of the bedding planes and even the effects of the hydro mechanical couplings. Eventually, the anisotropy parameters are a black box containing the complexity of the fractured rock behavior. As a matter of fact, the presented models are applicable only to model GED and GCS drift. In order to model other drifts the process of calibration of the anisotropy parameters has to be done once again, which is quite time consuming. Therefore, while keeping the general philosophy of the model, i.e. to represent the effect of fractures in shear thanks to the viscoplastic anisotropy, we try in the following models to establish a clear link between the behavior of the fractures and the anisotropy parameters. The idea is also to launch an experimental campaign to study the viscous slip of an interface in the COx claystone.

4 Continuous equivalent model of fractured rock

> *La théorie, c'est quand on sait tout et que rien ne fonctionne. La pratique, c'est quand tout fonctionne et que personne ne sait pourquoi. Ici, nous avons réuni théorie et pratique : Rien ne fonctionne... et personne ne sait pourquoi !*
>
> **— Albert Einstein**

This chapter is still devoted to the finite element modeling of the URL tunnels. As we had noted in the previous chapter, the link between the parameters of anisotropy and the behavior of the fractures was not clear, to fill this gap, in this chapter we have been working on linking the anisotropy parameters of the ANELVIP model to the parameters describing the behavior of a fracture. Moreover, with this new modeling approach, one can feed the numerical models from the experimental results. Even though the convergences were very well reproduced by the first models, a more straightforward approach to determine the parameters of anisotropy is presented in this chapter. The idea is to divide the fractured zone into different zones, where in each zone a given orientation and density of fractures is assumed. A transverse isotropic material modeled by the ANELVIP model (which was presented in Chapter 3) is then affected to each zone. The parameters of anisotropy are expressed as a function of the fracture geometry and constitutive parameters. The first part is devoted to the calculation of the elastic, plastic and viscous macroscopic strain of a representative elementary volume of a rock sample crossed by a fracture plane family, in order to express the parameters of anisotropy in terms of the fracture deformation. Then we present a suggested division of the fractured zone, based on core data provided by ANDRA. One model for the drifts excavated along the major principal horizontal stress, and another for those excavated along the minor principal horizontal stress are presented, and their results are discussed.

4.1 Continuous Equivalent Model

The ANELVIP model, already available in the code Disroc [68], is used as a continuous equivalent model of the fractured COx claystone considered as a rock medium crossed by a family of plane and infinite parallel fractures of spacing D. It is reminded that in the model the anisotropy accounts for the behavior of the fractures. The ANELVIP model was presented in the section 3.2 for its elastic, plastic and viscous constitutive laws.

Upscaling is a common method used to describe the mechanical behavior of a locally heterogeneous material at a macroscopic level. The macroscopic behavior is deduced from relationships between equivalent macroscopic strains and stresses defined in a Representative Elementary Volume (REV), as represented in Figure 4.1. As a matter of fact, in continuum micro-mechanics a material is understood as a macro-homogeneous but micro-heterogeneous body. A REV is defined to represent the material. A hypothesis of separation of scales is formulated on the REV. Indeed, the heterogeneity have to be very small in front of the REV dimension, which himself has to be sufficiently small compared to the structures built up by the material, which comes to: $d << l$ and $l << L$. With l the characteristic length of the REV, d the characteristic length of the heterogeneity and L the characteristic length of the geometry. The relation between homogeneous deformations acting on the boundary of the REV and resulting stresses can be estimated from the mechanical behavior of the aforementioned heterogeneity, their density in the REV, their geometry and their interactions. Ultimately, the continuous equivalent mechanical behavior of the overall material is deduced from the mechanical behavior of the REV. However, when it comes to modeling the rock medium surrounding the drifts of the URL, which means defining a REV containing a representative amount of the fractures of the fractured zone, the separation of scale is not verified. In the approach presented in this chapter, we simply compare the mechanical behavior of a REV described in Figure 4.1 to our equivalent continuous model. We will verify that each of the individual responses, elastic, plastic, and viscous, of the continuous model best reproduces the response of the fractured rock domain for the applied load. Many assumptions have been made to simplify the models as much as possible, the application to the modeling of the GED and GCS galleries will tell us the relevance of this approach. In this chapter the parameters of anisotropy (a_N^p and b_T^p, for its plastic part and a_N^v and b_T^v, for its viscous part) are expressed as to take the behavior of the fractures into account, in the plastic and viscous macroscopic deformations, alongside with their geometry (fracture density and orientation).

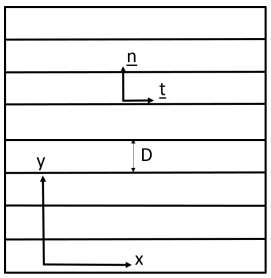

Fig. 4.1.: Representation of the considered REV

4.1.1 Elastic equivalent model

We assume that the geometry is constituted of parallel infinite plane fractures regularly spaced, as presented in Figure 4.1. The continuous equivalent elastic behavior of the fractured zone presents a transverse isotropy around the axis $\underline{n}$ and depends on five independent parameters. According to Pouya et al., [67], by taking into account the fracture planes the five parameters become:

$$\frac{1}{E_{\perp}} = \frac{1}{E^0} + \frac{1}{K_n D} \tag{4.1}$$

$$\frac{1}{E_{\parallel}} = \frac{1}{E^0} \tag{4.2}$$

$$\frac{1}{G} = \frac{1}{G^0} + \frac{1}{K_t D} \tag{4.3}$$

With K_n and K_t the normal and tangent elastic stiffness of the fractures and D the fractures spacing. E^0 and G^0 are respectively the Young modulus and the shear modulus of the sound rock. The Poisson's ratio remains the same as for the sound rock.

4.1.2 Plastic continuous equivalent model

The parameters of plastic anisotropy, which have been presented in the section 3.2.2, are calibrated in order to approximate the Uniaxial Compressive Strength (UCS) of a rock sample crossed by a fracture plane family inclined by an angle θ as represented in Figure 4.2. Assuming that a Mohr-Coulomb perfectly plastic yield function can be used to model the yield function of the rock matrix and the fracture with respectively C the cohesion and φ the friction angle for the rock matrix and C^f and φ^f the same parameters of the fracture.

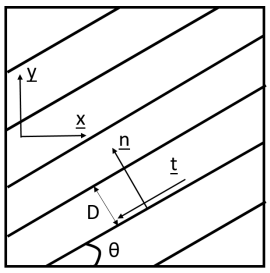

Fig. 4.2.: Representation of a REV containing parallel fractures with inclination θ.

The fractures are orientated by vectors $\underline{n}$ (normal to the fracture plane) and $\underline{t}$ (tangential to the fracture plane), given by equations 4.4 and 4.5.

$$\underline{n} = \begin{pmatrix} -\sin\theta \\ \cos\theta \end{pmatrix} \tag{4.4}$$

$$\underline{t} = \begin{pmatrix} -\cos\theta \\ -\sin\theta \end{pmatrix} \tag{4.5}$$

The normal and shear stress in the fracture, for a constant stress σ applied in the direction $\underline{y}$, is given by equation 4.6 and equation 4.7.

$$\tau = \sigma \sin\theta \cos\theta \tag{4.6}$$

$$\sigma_n = \sigma \cos^2\theta \tag{4.7}$$

The uniaxial compressive stress for which the yield function is reached in the fracture is given by equation 4.8, and the UCS of the sound rock is given by equation 4.9.

$$\text{For} \quad \theta > \varphi^f \text{ and } \quad \theta \neq 0 : \sigma_f = \frac{C^f \cos\varphi^f}{\cos\theta \sin(\theta - \varphi^f)} \tag{4.8}$$

$$R_c(0) = \frac{2C\cos\varphi}{1-\sin\varphi} \tag{4.9}$$

The UCS of the fractured rock represented in Figure 4.2, named UCS_{REV}, is thus the minimum between the UCS of the intact rock matrix and the critical stress for which the yield limit is reached in the fractures given by equation 4.10.

$$UCS_{\mathrm{REV}}(\theta) = Min[\frac{2C\cos\varphi}{1-\sin\varphi}; \frac{C^f \cos\varphi^f}{\cos(\theta)\sin(\theta-\varphi^f)}] \tag{4.10}$$

The minimum of σ_f in equation 4.8 is reached for an angle $\theta = \frac{\pi}{4} + \frac{\varphi^f}{2}$. The idea is to calibrate the plastic anisotropy of the ANELVIP model, which is carried by the parameter b_T^p, such that the UCS of the continuous anisotropic model is as close as possible to the UCS of the fractured rock. In ANELVIP model, the UCS for an uniaxial compressive stress applied in a direction θ is given by equation 4.11 [35].

$$UCS_{\text{ANELVIP}}(\theta) = \frac{2C\cos\varphi}{\sqrt{1+4b_T\sin\theta^2\cos\theta^2}-\sin\varphi} \tag{4.11}$$

With C the cohesion and φ the friction angle of the rock and b_T is the parameter of plastic anisotropy.

$$b_T = \frac{1}{4\sin\theta^2\cos\theta^2}\left[\left(\frac{2C\cos\varphi}{UCS_{\text{ANELVIP}(\theta)}}+\sin\varphi\right)^2-1\right] \tag{4.12}$$

Considering that the minimum of the function UCS_{ANELVIP} is reached for $\theta = \frac{\pi}{4}$ while the minimum of the function UCS_{REV} is reached for $\theta = \frac{\pi}{4} + \frac{\varphi^f}{2}$, one can make different hypothesis in order to determine the value of the parameter b_T. Three different hypothesis are presented in table 4.1. One can assume that the minimums of the two functions reached for different angle must be equal, or it can be assumed that two functions should have the same value at the angle $\theta = \frac{\pi}{4}$ (corresponding to the value of θ for which the minimum of the function UCS_{ANELVIP} is reached) or at the angle $\theta = \frac{\pi}{4} + \frac{\varphi^f}{2}$ (corresponding to the value of θ for which the minimum of the function UCS_{REV} is reached). These three assumptions lead to three different values for the parameter b_T. The three hypothesis are plotted in polar

Tab. 4.1.: Three different possible ANELVIP model

Hypothesis	UCS ANELVIP	UCS fractured rock
1	$UCS_{\text{ANELVIP}}(\frac{\pi}{4})$	$= UCS_{\text{REV}}(\frac{\pi}{4}+\frac{\varphi^f}{2})$
2	$UCS_{\text{ANELVIP}}(\frac{\pi}{4})$	$= UCS_{\text{REV}}(\frac{\pi}{4})$
3	$UCS_{\text{ANELVIP}}(\frac{\pi}{4}+\frac{\varphi^f}{2})$	$= UCS_{\text{REV}}(\frac{\pi}{4}+\frac{\varphi^f}{2})$

graph in Figure 4.3 alongside with the UCS of the fractured rock in blue. All the hypothesis made for the ANELVIP model, tend to slightly overestimate the UCS for $\theta > 45°$. But the ANELVIP model tend to underestimate the UCS for $\theta < 45°$, which is not such a conservative hypothesis considering that in reality the fractured planes are not all perfectly parallel, and the fracture planes might be crossed by few secondary fractures. Thus, the parameter of plastic anisotropy depends only on the strength parameters C^f and ϕ^f of the fracture, and does not depend on the fracture density considered. This means that the plastic anisotropy parameter will be the same for the entire fractured zone. The numerical values $C^f = 0.5$ MPa and $\phi^f = 27°$ were used to estimate parameter b_T^p.

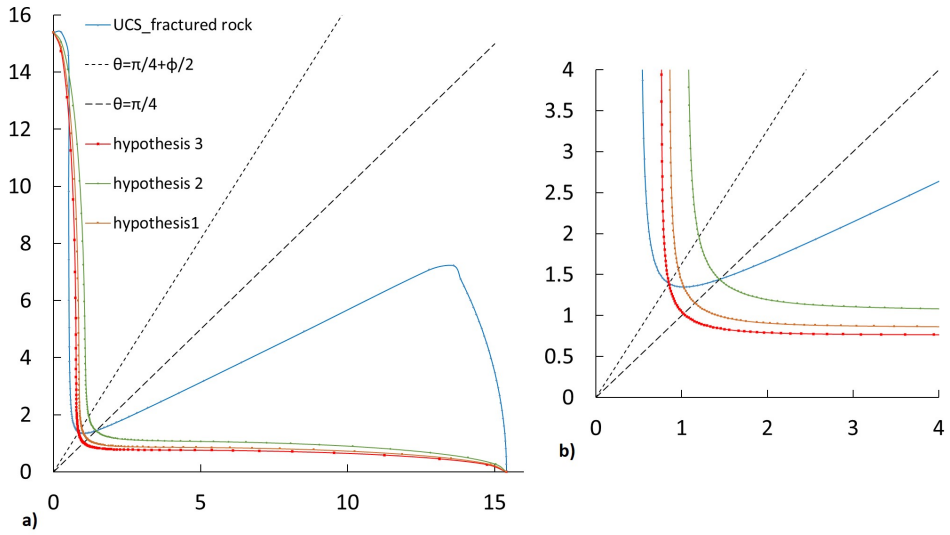

Fig. 4.3.: a) Polar representation of the function UCS_{REV} compared to the UCS in the model ANELVIP for three different hypothesis b) Zoom on the minimum of the functions

4.1.3 Viscous equivalent model: Identification of the anisotropic viscous parameters of ANELVIP

General framework

Again the parameters of viscous anisotropy are determined by working on the viscous strain of a REV constituted by N parallel fractures equally spaced by a distance D. The macroscopic creep strain is expressed for a finite size heterogeneous domain Ω containing a family of cracks which constitute discontinuities in the displacement field. In this case the macroscopic strain tensor is given by:

$$\overline{\varepsilon} = \frac{1}{V}[\int_{\Omega} \varepsilon dv + \sum_{k} \int_{\Gamma_k} \frac{1}{2}(\underline{U} \otimes \underline{n} + \underline{n} \otimes \underline{U}) ds] \tag{4.13}$$

The first part of equation 4.13 is related to the viscous behavior of the rock matrix. Its expression is given in the coordinates system attached to the axes (x, y) in equation 4.14.

$$\varepsilon^{\mathbf{m}} = \frac{1}{V} \begin{pmatrix} \int_{\Omega} \varepsilon_{\mathbf{xx}} dv & \int_{\Omega} \varepsilon_{\mathbf{xy}} dv \\ \int_{\Omega} \varepsilon_{\mathbf{xy}} dv & \int_{\Omega} \varepsilon_{\mathbf{yy}} dv \end{pmatrix} \tag{4.14}$$

The vector $\underline{U}$ the discontinuity in the displacement field and $\underline{n}$ the normal to the fracture planes. In our case $\underline{n}$ is constant in the domain as the fractures all have the same orientation in the coordinates system attached to the axes (t,n) we have:

$$\underline{U} = \begin{pmatrix} u_t \\ u_n \end{pmatrix} \tag{4.15}$$

$$\underline{n} = \begin{pmatrix} 0 \\ 1 \end{pmatrix} \tag{4.16}$$

$$\underline{t} = \begin{pmatrix} 1 \\ 0 \end{pmatrix} \tag{4.17}$$

The second part of equation 4.13 is related to the viscous behavior of the fractures, it can be written in the system of axes (t,n):

$$\varepsilon^f = \frac{N}{V} \begin{pmatrix} 0 & \frac{1}{2}\int_\Gamma u_t ds \\ \frac{1}{2}\int_\Gamma u_t ds & \int_\Gamma u_n ds \end{pmatrix} \tag{4.18}$$

We assume that the domain contains N fractures with the length of the fractures noted L. If the viscous strains of the rock matrix are homogeneous in the domain Ω, and if the vector discontinuity of displacement $\underline{U}$ is constant along the fractures, then equation 4.13 becomes equation 4.19. As a matter of fact, the length of the REV is L (the length of the REV is equal to the length of the fracture) and its width is equal to $(N+1)D$ with D the distance between two fractures. The integration of the vector discontinuity of displacement $\underline{U}$ on Γ gives uL. There are N fractures in the REV and the expression is divided by the volume, which is equal to $(N+1)LD$ thus equation 4.18 becomes:

$$\overline{\varepsilon} = \varepsilon^{vm} + \frac{N}{2(N+1)D}(\underline{u}^v \otimes \underline{n} + \underline{n} \otimes \underline{u}^v) \tag{4.19}$$

Where ε^{vm} is the viscous deformation of the rock matrix and $\underline{u}^v$ is the viscous displacement in one fracture. The idea now is to apply simple loading (pure shear stress, uniaxial compressive stress in the direction $\underline{x}$, and uniaxial compressive stress in the direction $\underline{y}$) to the REV in order to identify the macroscopic viscous strain tensor. The principle of homogenization is to go back to the macroscopic behavior i.e. when the size of the REV is infinitely large compared to the size of the heterogeneity D thus we make N tend to infinity in equation 4.19. Hence the macroscopic viscous strain as the addition of the viscous strain of the sound rock matrix and the viscous slip of the fractures is given by equation 4.20.

$$\overline{\varepsilon} = \varepsilon^{\mathbf{vm}} + \frac{1}{2D}(\underline{u}^v \otimes \underline{n} + \underline{n} \otimes \underline{u}^v) \tag{4.20}$$

Parameters of viscous anisotropy

The expression of the parameters of anisotropy are determined by applying simple loading to the REV. Under certain hypothesis the parameters of anisotropy can be expressed as a function of the viscous slip of the fractures.

Considering a state of pure shear stress parallel to the fractures in the rock matrix, the resulting stress tensor is:

$$\boldsymbol{\sigma} = \tau(\underline{n} \otimes \underline{t} + \underline{t} \otimes \underline{n}) \tag{4.21}$$

The deviatoric stress corresponding to such a state of stress is equal to the stress tensor, $\mathbf{S} = \boldsymbol{\sigma}$. And the equivalent Von Mises stress is given by equation 4.22:

$$\sigma_e = \sqrt{3}|\tau| \tag{4.22}$$

Under constant stress the viscous deformation of the sound rock is given by equation 4.23, which corresponds to the Lemaitre's creep model, or also the strain hardening creep model widely used for geomaterials including for COx claystone. This constitutive law is the creep law in the ANELVIP model:

$$\boldsymbol{\varepsilon}^{vm} = \frac{3}{2} a \sigma_e^{n-1} t^{\alpha} \mathbf{S} \tag{4.23}$$

This leads to the following expression for the shear creep strain under pure shear stress:

$$\varepsilon_{tn}^{vm} = \frac{3}{2} a (\sqrt{3}|\tau|)^{n-1} t^{\alpha} \tau \tag{4.24}$$

It is assumed that the fractures are only creeping in the shear direction hence: $u_n^v = 0$. Besides, if we assume the same power of the stress n, and the same power of time α, for rock joints (fractures) creep as for the rock matrix, the shear viscous displacement of the rock joint is given by the following expression:

$$u_t^v = b|\tau|^{n-1} t^{\alpha} \tau \tag{4.25}$$

All the same by using equation 4.22, one can write equation 4.25, as follows:

$$u_t^v = b \frac{\sigma_e}{\sqrt{3}}^{n-1} t^{\alpha} S_{tn} \tag{4.26}$$

The contribution given by the fractures to the macroscopic viscous deformation is obtained by introducing the expression of u_t^v in equation 4.20

$$\varepsilon_{tn}^{vf} = \frac{b}{2D} \frac{\sigma_e}{\sqrt{3}}^{n-1} t^{\alpha} S_{tn} \tag{4.27}$$

In ANELVIP the viscous deformation are given by:

$$\varepsilon^{vA} = \frac{3}{2} a \beta^v \sigma_e^n \frac{\tilde{\mathbf{S}}}{\tilde{\sigma}_e} t^\alpha \tag{4.28}$$

With β^v the coefficient of anisotropy and $\tilde{\sigma}$ the transformed stress tensor for anisotropy. By definition, β^v is, for uniaxial stress, given by equation 4.29:

$$\beta^v = \frac{\tilde{\sigma}_e}{\sigma_e} \tag{4.29}$$

As already explained in the previous chapter, the viscous anisotropy in ANELVIP is built by replacing the stress tensor σ by a modified tensor $\tilde{\sigma}$. The linear transformation is defined, in the specific coordinates system attached to the fractures and specific anisotropy parameters f_N^v and f_T^v, by the following relation:

$$\tilde{\sigma} = \begin{pmatrix} \sigma_{tt} & f_T^v \sigma_{tn} & 0 \\ f_T^v \sigma_{tn} & f_N^v \sigma_{nn} & 0 \\ 0 & 0 & 1 \end{pmatrix} \tag{4.30}$$

Under pure shear stress equation 4.28 becomes:

$$\varepsilon_{tn}^{vA} = \frac{3}{2} a f_T^v \sigma_e^{n-1} S_{tn} t^\alpha \tag{4.31}$$

With $\tilde{\sigma}_e = \sqrt{3} f_T^v |\tau|$, hence $\beta^v = f_T^v$. The tangential component of the anisotropic deviatoric stress tensor is $\tilde{S_{tn}} = f_T^v S_{tn}$.

The macroscopic viscous deformation of the REV is given by equation 4.20. Considering that the viscous deformation of the rock matrix ε^{vm} is given by the ANELVIP model and that the viscous deformation under shear stress is given by equation 4.27, the macroscopic viscous deformation of the REV under pure shear stress becomes:

$$\varepsilon_{tn}^{vH} = \frac{3}{2} a \left(1 + \frac{b}{3aD} \left(\frac{1}{\sqrt{3}}\right)^{n-1}\right) \sigma_e^{n-1} t^\alpha S_{tn} \tag{4.32}$$

Under a unidirectional compressive test normal or perpendicular to the fractures the macroscopic viscous deformation is equal to the creep deformation of the rock matrix.

$$\varepsilon_{nn}^{vH} = \frac{3}{2} a \sigma_e^{n-1} t^\alpha S_{nn}, \qquad \varepsilon_{tt}^{vH} = \frac{3}{2} a \sigma_e^{n-1} t^\alpha S_{tt} \tag{4.33}$$

This equation remains true for every uniaxial stress, which imposes that $f_N = 1$. And by identifying equation 4.32 to the shear deformation in equation 4.31 we obtain an expression of the parameter f_T:

$$f_T = 1 + \frac{b}{3aD}\left(\frac{1}{\sqrt{3}}\right)^{n-1} \tag{4.34}$$

As expected, we find that in equation 4.34, if $b = 0$, i.e., if the fractures are not creeping, or if D tend towards infinity (which means that the fractures are very far away one from another and so the density of fracture tends to zero), then $f_T = 1$ and the macroscopic viscous deformation is equal to the viscous deformation of the sound rock. In the following numerical simulations, the continuous equivalent creep behavior of the rock composed by the sound rock and the fractures is described by the ANELVIP continuous transverse isotropic model, with a the viscous parameter of the sound rock, $f_N = 1$ and f_T given by equation 4.34. The parameters of viscous anisotropy are expressed in order to take the viscous slip of the fractures into account in the description of the viscous deformations of a REV represented in Figures 4.1 and 4.2 under simple stress state. The continuous equivalent model is validated by comparing its viscous strain under compressive stress (the direction x or y is not specified on the graph as the results are the same in both direction) and under shear stress, to the viscous strain of a fractured REV. The fractured REV contains parallel equally spaced fractured by $D = 0.14$m, either horizontal, or 55 degrees inclined. The correspondence between the predicted viscous strain in the fractured model and in the continuous equivalent model is respected as shown in figures 4.4 and 4.5. The small

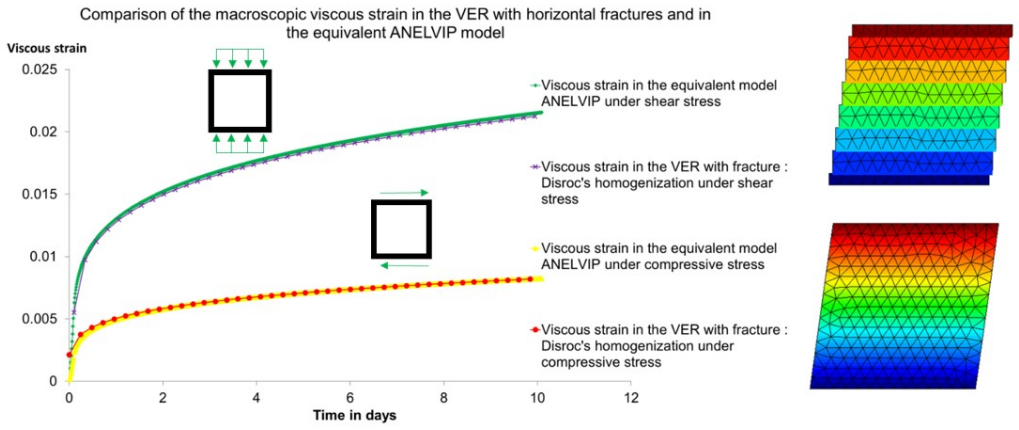

Fig. 4.4.: Comparison between the fractured model containing explicit horizontal fractures and the continuous equivalent model regarding the viscous deformations for two cases of shear and compression tests.

difference between the viscous strain in the REV and in the equivalent ANELVIP model under compressive stress in Figure 4.5 (curves yellow and red) is due to the fact that in the

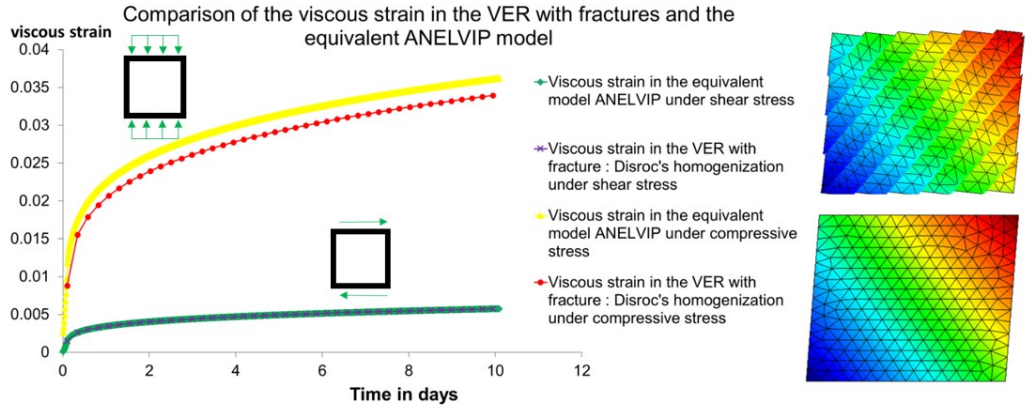

Fig. 4.5.: Comparison between the fractured model containing explicit inclined fractured by 55° and the continuous equivalent model regarding the viscous deformations

numerical simulations a finite number of fractures is used, whereas in the equivalent model the number of fractures is supposed to tend toward infinity.

4.2 Description of the fractured zone

In situ observations, as described in [4], have shown that depending on the direction in which a drift is excavated, the fractured zone may develop mostly in the vertical direction (e.g. GED drift, excavated along the minor principal horizontal stress) or mostly in the horizontal direction (e.g. GCS drift, excavated along the major principal horizontal stress). Recall that the *in situ* stress state in MHM URL is anisotropic with $\sigma_v \approx \sigma_h \approx -12$ MPa and $\sigma_H \approx -16$ MPa [91]. Deep underground excavations in argillaceous rocks result in the creation of a fractured zone in the immediate vicinity of the tunnel wall. Fracture initiation and propagation is a complex hydro mechanical problem, as evidenced by [47], nevertheless, since the near-field deformations is controlled by fractures, it is a major topic of interest among research teams. In order to use the continuous equivalent model presented in the previous sections, the fractured zones of both types of galleries excavated in the URL, are described in terms of fracture density and orientation. For this purpose, the coring data around several excavated galleries, respectively in the major principal horizontal direction and in the minor principal horizontal direction are used. Nearly 400 boreholes have been drilled in the URL drifts, since 2005, with more than 4 000 excavation-induced fractures counted [4]. Note that the shape of the fractured zone depends on the direction in which the gallery is excavated, but does not depend on the size of the excavation. Figure 4.6 shows the fractured zone around different excavation scales in the direction of the major principal horizontal stress. The boreholes were drilled in the vertical, horizontal and oblique direction.

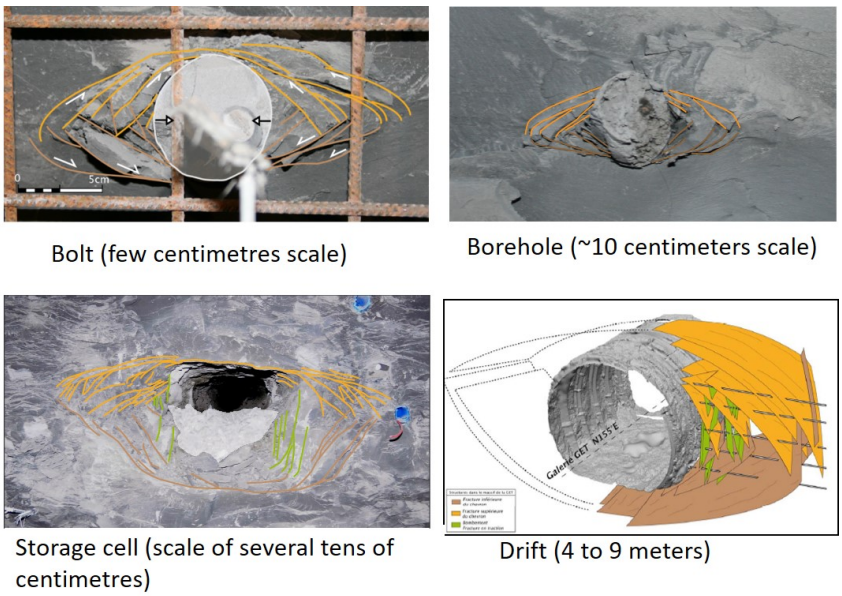

Fig. 4.6.: Four different excavation in the direction of the major principal horizontal stress present the same fractured zone.

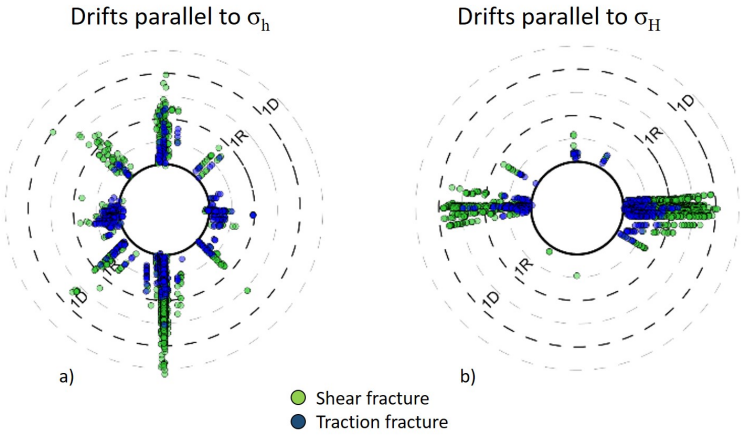

Fig. 4.7.: a) Distribution of shear and tensile fractures around the drifts excavated in the direction of the minor principal horizontal stress. b) Distribution of shear and tensile fractures around the drifts excavated in the direction of the major principal horizontal stress.

All fractures are classified and counted according to two types: shear fracture or tensile fracture, as shown in Figure 4.7. Figure 4.8 shows the average number of fractures counted by interval of 20 cm moving radially from GCS drift's wall. Tensile fractures are mostly present at the drift wall while shear fractures extend more deeply in the rock mass.

In order to have a better estimation of the number of fractures around the drifts, the data are collected from a core drilling campaign carried out on the drifts excavated according to the

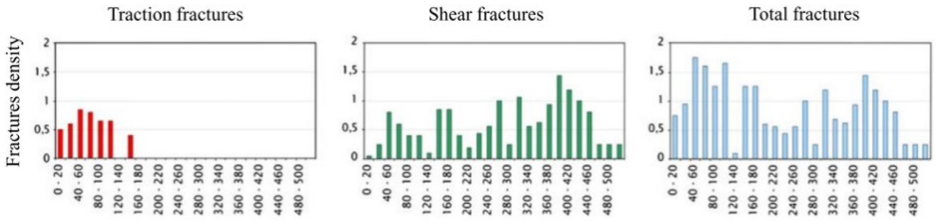

Fig. 4.8.: Estimation of the fractures density moving radially from GCS drift's wall [4].

minor and major principal horizontal stress. From these data two models are constructed, one for each types of drifts. Fractures are counted on boreholes drilled in vertical, oblique and horizontal directions over a maximum distance of one diameter (corresponding to the maximum extension of the fractured zone). The database is a list of every fracture found in a core, with the following information: the type of fracture (shear or tensile), its position in the core and its orientation. Note that regarding the identification of fracture type, depending

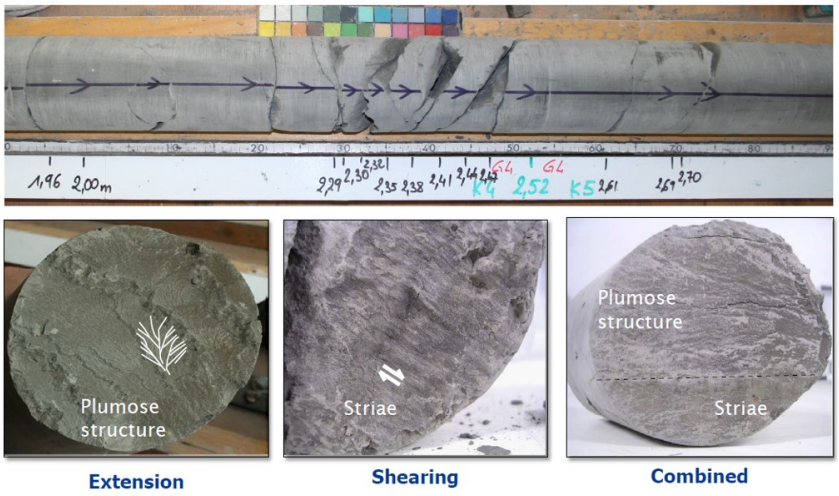

Fig. 4.9.: Picture of a core drilled around the drift of the URL. Fractures are located and identified as tensile or shear fractures.

on the geologist's experience, identification errors may be done. An example of core with different fractures is presented in Figure 4.9. The fracture density is deduced from the number of fractures counted at different distances from the drift wall. Note that with this method, some fractures are possibly counted multiple times, because the same fracture may cross several cores. For the sake of simplicity the models are constructed with only three different zones constituting the fractured zone.

4.2.1 Fractured zone of drifts in the direction of the major principal horizontal stress

The model of fractured zone is based on the average number of fractures around the galleries excavated in the direction of the major principal horizontal stress. The number of fracture is an average value based on the number of fractures found in cores that are drilled around different drifts excavated in the same direction. For example, in the horizontal direction, 55 cores around 6 different drifts are listed in the database. For each core in the horizontal direction, the total number of fractures is divided into those located between the tunnel wall and up to a radius distance, and those located farther at a distance between a radius and a diameter of the drift wall. In the vertical direction, the fractures are all located between the drift wall and half a radius. At 45° of the horizontal direction, the fractured zone extend up to one radius from the drift wall. The average number of fractures counted in all three directions is given in Table 4.2. The coring campaign allows us to estimate the fracture

Tab. 4.2.: Average number of fractures counted in the vertical direction, horizontal direction and at 45° of the horizontal direction in drifts that are excavated in the direction of the major principal horizontal stress. The average value is given alongside the maximal and minimal number of fractures counted among all the core.

Direction	Distance	Average number of fractures
Vertical	0 - 0.5R	4 (max: 6; min: 1)
Horizontal	0 - 1R	8.4 (max: 23; min: 2)
Horizontal	1R - 1D	10.4 (max: 30; min: 0)
45°	0 - 1R	5.5 (max: 8; min: 3)

density along three distinct directions of the fractured zone. Given the quantity of available data, as well as the standard deviation from the mean value, we felt that we could only reasonably describe the fractured zone with 3 zones of different densities and orientations. For each area, the average fracture spacing D and orientation are given in Figure 4.10. The average fracture spacing D is the extension of the fractured zone in the considered direction L, divided by the number of fractures n minus one: $D = \frac{L}{(n-1)}$.

4.2.2 Fractured zone of drifts in the direction of the minor principal horizontal stress

In the same way as for drifts excavated in the direction of the major principal horizontal stress, a description of the fractured zone around drifts excavated in the direction of the minor principal horizontal stress is proposed based on the average number of fracture counted during a coring campaign. Again, the number of fracture is an average value based

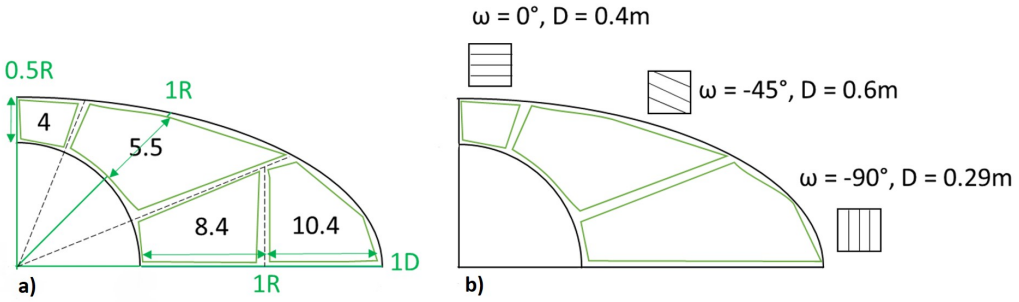

Fig. 4.10.: a) Average number of fractures counted in the different cores. With R corresponding to the drift radius and D to the drift diameter. b) Description of the fractured zone of drifts excavated in the direction of the major principal horizontal stress in terms of fracture's density and orientation.

Tab. 4.3.: Average number of fractures counted in the vertical direction, horizontal direction and at 45° of the horizontal direction in drifts that are excavated in the direction of the minor principal horizontal stress. The average value is given alongside the maximal and minimal number of fractures counted among all the core.

Direction	Distance	Average number of fractures
Horizontal	0 - 1R	2.4 (max: 8; min: 0)
Vertical	0 - 1R	6.5 (max: 12; min: 0)
Vertical	1R - 1D	3.2 (max: 6; min: 0)
45°	0 - 1R	7.4 (max: 12; min: 3)
45°	1R - 1D	1.8 (max: 4; min: 0)

on the number of fractures found in cores that are drilled around different drifts excavated in the same direction. The database is summarized in Table 4.3. For each area, the average fracture spacing D and orientation are given in Figure 4.11b).

4.3 Numerical Simulations

The theoretical expression of the anisotropy parameters has been established in the sections 4.1.2 and 4.1.3. The Figures 4.12and 4.14 represent the possible numerical values of the said anisotropy parameters as a function of the values of the parameters describing the behavior of the fracture. Although the numerical models presented in this chapter were designed to be fed by the results of an experimental campaign to characterize the behavior of a fracture, the calculations were performed before the results of the experimental measurements were available; therefore, assumptions had to be made to select the values of the parameters of the model. In Figure 4.12 three graphs are plotted in order to give the order of magnitude of the parameter of plastic anisotropy b_T^p, which depends on the fracture's cohesion and friction

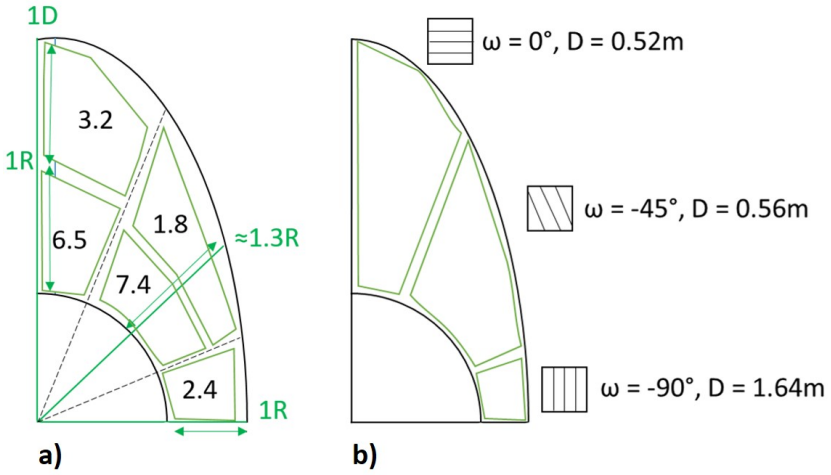

Fig. 4.11.: a) Average number of fractures counted in the different cores. With R corresponding to the drift radius and D to the drift diameter. b) Description of the fractured zone of drifts excavated in the direction of the major principal horizontal stress in terms of fracture's density and orientation.

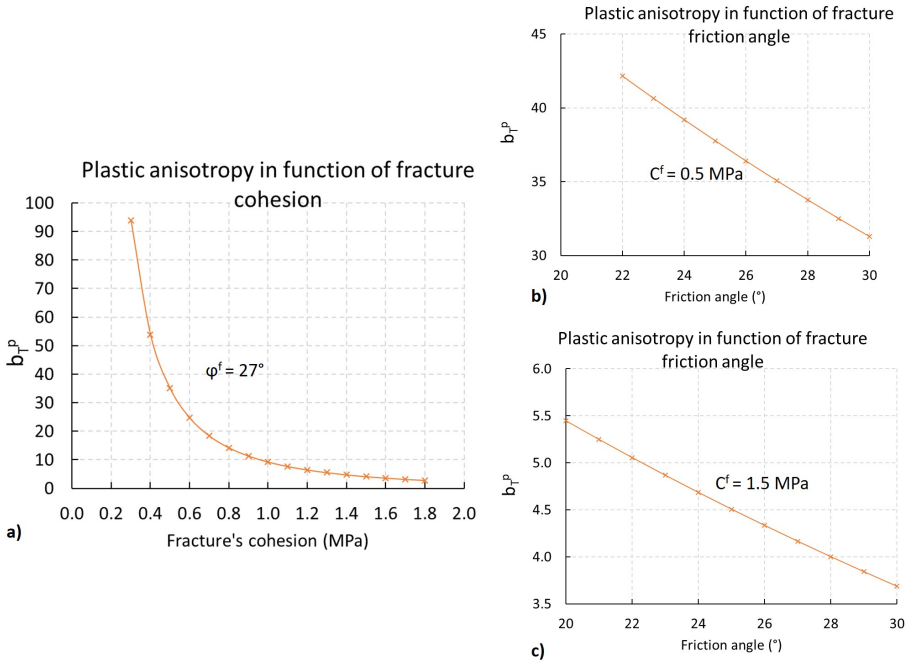

Fig. 4.12.: a) Values of parameter b_T^p as a function of the fracture cohesion for $\phi = 27°$ b) Values of parameter b_T^p as a function of the fracture friction angle for $C^f = 0.5$MPa c) Values of parameter b_T^p as a function of the fracture friction angle for $C^f = 1.5$MPa.

angle. When the fracture's cohesion tends toward zero the plastic anisotropy tends to infinity. For a fracture's cohesion of about 0.5 MPa depending on the friction angle, the order of magnitude of b_T^p is about 25, while it becomes around 2.5 for a fracture's cohesion equal

to 1.5 MPa. The strength parameters of a rock joint are measured during direct shear tests, however the measured value, may be subject to discussion as shown by Rulliere et al., (2020) [71]. In particular, for large values of normal stress on *in situ* joints, the apparent cohesion may be higher than that measured in the laboratory. Nevertheless, caution should be taken, as increasing the joint cohesion is not a conservative assumption and most recommendations for engineers even suggest considering zero cohesion. Figure 4.13 illustrates the possible difference between the measured cohesion and the apparent cohesion for higher normal stresses. Note that the plastic anisotropy only depends on the strength parameters of both

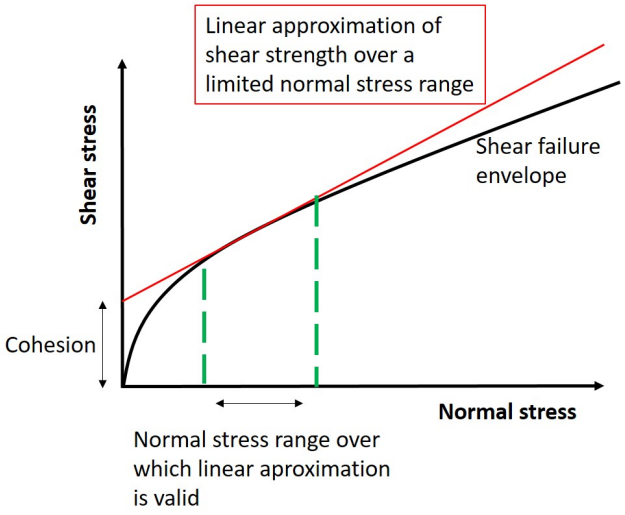

Fig. 4.13.: Representation of the shear failure envelope. Discussion of the value of apparent cohesion and apparent friction angle as a function of the range of normal stresses considered.

the rock matrix and the fracture. For instance, it does not depend on the fracture's density. The order of magnitude of the viscous anisotropy b_T^v is given in Figure 4.14, assuming three different hypothesis regarding the relative viscous flow in the fracture in comparison with the viscous flow in the rock matrix. Figure 4.14 shows that if the viscous flow in the fracture is 10 times bigger than in the rock matrix, the parameter of viscous anisotropy is pretty sensitive to the average distance between the fractures. As a matter of fact, $b_T^v = 538$ for $D = 0.2$ m and $b_T^v = 53$ for $D = 0.7$ m. However, if the viscous flow in the fracture is 10 times smaller than in the rock matrix, b_T^v only varies between 0.49 and 0.13 for D between 0.2 and 0.7 m.

In the numerical simulations presented in the next sections, four material zones are differentiated: near the tunnel walls, three fractured rock zones with different parameters depending on fracture orientation and density, and beyond the fractured zone, sound COx claystone is considered. Two different types of models have been built to represent on the one hand the tunnels excavated in the direction of the major principal horizontal stress and on the other

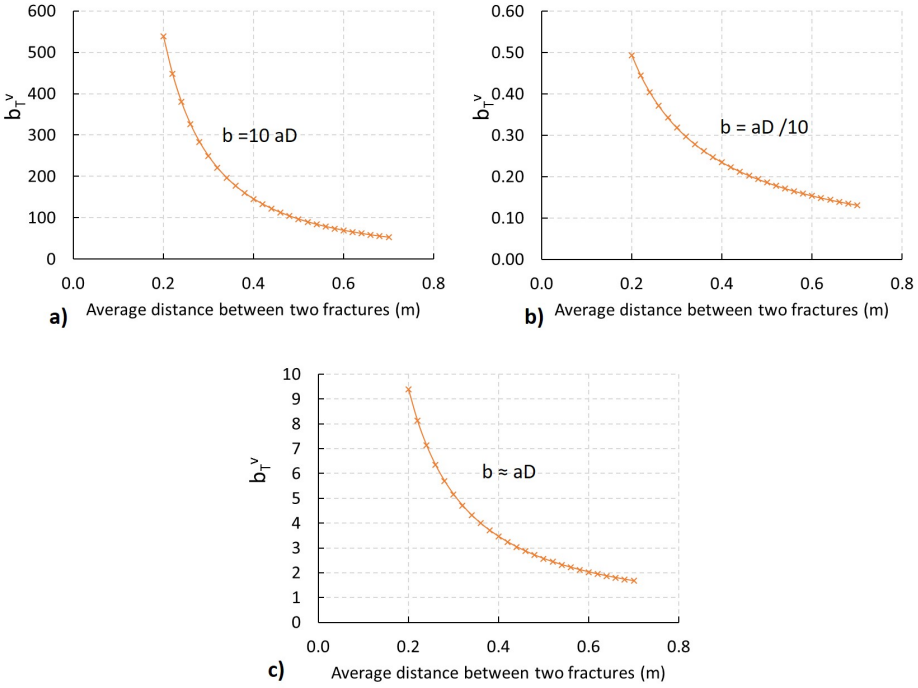

Fig. 4.14.: Parameter b_T^v as a function of the average distance between two fractures D. a) viscous flow in the fracture bigger than the viscous flow in the rock matrix. b) viscous flow in the fracture smaller than the viscous flow in the rock matrix. c) viscous flow in the fracture is of the same order of magnitude as the viscous flow in the rock matrix.

hand those excavated in the direction of the minor principal horizontal stress. All the four materials in the model are modeled with the ANELVIP model present in FEM code Disroc, which was presented in section 3.2. For sake of simplicity, sound COx claystone is assumed to be an isotropic elasto-viscoplastic material. The value of the parameters considered for sound COx claystone are recalled in Table 4.4. ANELVIP is also used for the fractured zones. The parameters are determined with the expression given in section 4.1.

It should be remembered that these models were calculated before the first experimental results were obtained, so some assumptions had to be made regarding the behavior of

Tab. 4.4.: Numerical values of the parameters used for the simulation of GCS drift

Elasticity	Plasticity	Viscosity
$E_{\parallel} = 5000$ MPa	$C = 5$ MPa	$a = 1.5 \times 10^{-4}$MPa^{-1}day$^{-0.2}$
$E_{\perp} = 5000$ MPa	$\phi = 24°$	$n = 1$
$\nu_{xy} = 0.3$	$\psi = 24°$	$\alpha = 0.215$
$\nu_{xz} = 0.3$		$\sigma_c = 3.6$ MPa
G= 1923 MPa		

fractures in the COx claystone. Without forgetting that the choice we made regarding the way of modeling the fractured zone itself implies some assumptions or simplifications of the reality. The first relates to the behavior of the fracture: As a matter of fact, by using ANELVIP model it is assumed that the elasto-viscoplastic behavior of a fracture in COx claystone can be represented by Mohr-Coulomb perfect plasticity and Lemaitre's creep law. Moreover, in order to establish the continuous equivalent model further assumptions were made. Indeed, the continuous equivalent plastic model is not exactly identical to the behavior of the fractured REV as shown in Figure 4.3. Similarly, regarding the viscous model, in order to establish the expression of b_T^v we had to make the assumption that in Lemaitre's model the power describing the dependence of viscous deformations with stress and with time are parameters that will be identical for the behavior of the rock matrix and for the fractures. In a second step, hypotheses are made concerning the fracture geometry in the fractured zones. In the model, only shear fractures are considered, as it is generally assumed in this work that viscous slip on fractures dominates long-term drift convergence. In other words, tensile fractures are not counted, even though they necessarily have an effect, at least on the short-term behavior and therefore on the elastoplastic part of the response. The model is based on an idealized distribution of evenly spaced fractures in the same area, all oriented in the same direction. It is worth noting that, the data used to calculate the average fracture spacing are very scattered (Tables 4.2 and 4.3). In the following section, the model is tested by using it to simulate the convergences of the two types of drifts of the URL. A sensitivity study of the mesh is presented in the appendix A.4. As the geometries of the two models are similar at a 90° rotation, we have performed the verification only on the mesh of GCS gallery model.

4.3.1 Drifts in the direction of the major principal horizontal stress

Unlike the model presented in Chapter 2, here the anisotropy of the model is explicitly related to the fracture behavior. Also to have a more reliable representation of the fractured zone the description has to be based on a maximum of data, thus all the data collected on the drifts excavated in the same direction have been considered. However, the results of the numerical simulations are compared to the measurements made on GCS drift, and it is the excavation procedure established in section 3.4.2 that has been used. The elastic anisotropy is calculated with equations 4.1 and 4.3 assuming that the tangential stiffness of the fracture is $K_t = 21200$ MPa/m, and the normal stiffness of the fracture is $K_n = 42400$ MPa/m. The tangential stiffness is obtained by a first experimental test conducted with the experimental set up presented in the next chapter. The normal stiffness was deduced from usual values of $\frac{K_t}{K_n}$ from Chalhoub's work [22]. Thus, in the model, the intact rock zone whose material parameters were given in Table 4.4 is separated from the three fractured

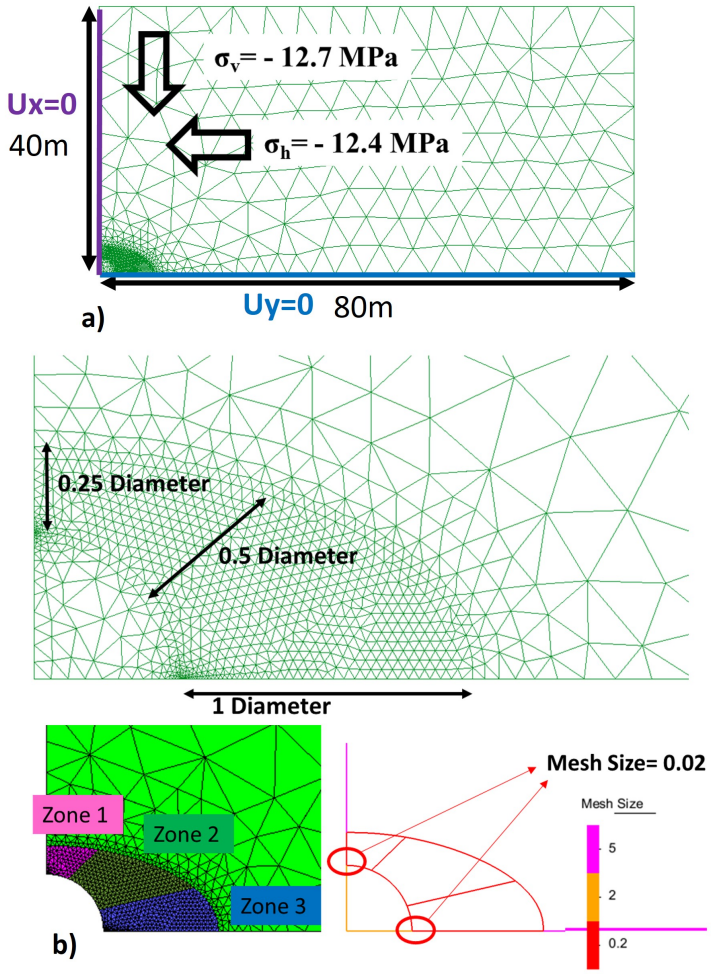

Fig. 4.15.: a) global description of the mesh used for the simulations of drifts excavated along the major horizontal stress, along with the boundary conditions. b) zoom on the three different zones.

rock zones (see Figure 4.15). The elastic parameters in the fractured zones are fixed once

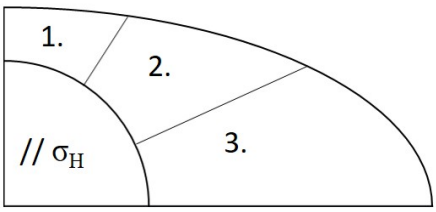

zones	D (m)	E⊥ (MPa)	G (MPa)
1.	0.4	3862	1568
2.	0.6	4179	1671
3.	0.29	3555	1465

Fig. 4.16.: Elastic parameters in the three different zones constituted by fractured rock around drifts excavated in the direction of major principal horizontal stress.

and for all and they are given in Figure 4.16. As in Chapter 2, the results of the numerical simulations are evaluated by comparing the simulated wall displacements with the measured convergence data from the URL tunnels. For the simulation of galleries excavated in the

Tab. 4.5.: Numerical values of the plastic parameters used in the different fractured zones.

$\phi(^\circ)$	C (MPa)	$\phi^f(^\circ)$	C^f (MPa)	b_T^p
24	6	27	0.5	32
24	6	27	1.3	5

direction of the major horizontal stress, data from the GCS drift are used to validate the model. Furthermore, even if we had a perfect description of the fracture behavior, it may still be necessary to adjust the anisotropy parameters in the macroscopic model since we made simplifying assumptions about the fracture distribution in the fractured zone. Since there is no experimental campaign describing the visco-plastic behavior of a fracture in the Callovo-Oxfordian claystone, we have given ourselves a calibration margin for the plastic and viscous model parameters in the fractured zones of the numerical simulations.

As explained in the section 4.1.2 in which the plastic equivalent model was explained, the parameter of plastic anisotropy only depends on the fracture's behavior and not on the fracture's density, thus the parameters describing the plastic behavior must be the same in the three zones of fractured rock. The plastic anisotropy parameter b_T^p is calculated within the framework of assumption 2, i.e. $UCS_{\text{ANELVIP}}(\frac{\pi}{4}) = UCS_{\text{REV}}(\frac{\pi}{4})$. Two hypotheses have been tested regarding the plastic behavior. First numerical simulation is run assuming that the fractures' cohesion is equal to 0.5 MPa which corresponds to values measured in direct shear tests presented in chapter 5. The second simulations are run assuming that the apparent cohesion of the fracture is bigger *in situ* than under laboratory conditions, as the normal stress *in situ* is bigger than in the experimental campaign, which comes to assume that $b_T^p = 5$. Figure 4.17a) shows the results of the two simulations, in the case where $b_T^p = 32$ or $b_T^p = 5$. The effect of plasticity plays an important role on the short-term convergence but the long-term convergence rates are not affected much. For the rest of the models, $b_T^p = 5$ is kept. Besides, we have greatly simplified the fracture orientations in the model, so it is natural to wonder how sensitive the numerical simulation is to a small variation in the fracture plane orientation. In the simulation presented in Figure 4.17b), the fracture planes are tilted in all three zones by +3°. It is mainly the horizontal convergence that is sensitive to this variation because it is in zone 3 that the anisotropy parameters are the most important and therefore the effect of the fractures on the rock behavior is the most important.

The work on viscosity is a bit more complicated because the viscous behavior of fractured COx claystone is not described in the literature. It was assumed that the viscous behavior could be modeled with Lemaitre's creep law. Indeed, we know that Lemaitre's model allows to represent the viscous behavior of the intact COx claystone (see Figure 3.4). Concerning the behavior of fractures, we can quote the pioneer work of Stavropoulou [81], which concerned the study of the behavior of COx/concrete interfaces. In this work Lemaitre's

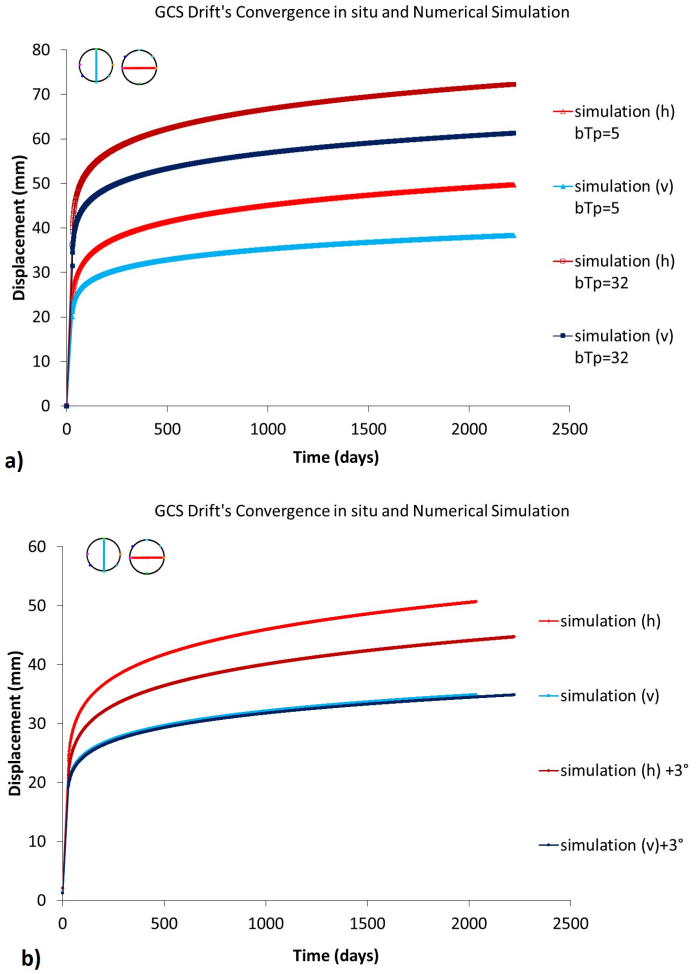

Fig. 4.17.: Plot of the convergences in vertical and horizontal direction obtained in numerical simulation of drifts excavated in the direction of the major principal horizontal stress. a) Comparison of the convergences obtained for two different simulations: one considering $b_T^p = 5$ in all three fractured zones (in light blue and red) and the other considering $b_T^p = 32$ in all three fractured zones (in dark blue and red). b) Comparison between the convergences obtain for fractures' orientation given by Figure 4.10 (in light blue and red) and the convergences obtain for fractures' orientation tilted in all three zones by $+3^\circ$ (in dark blue and red).

model was proposed to model the behavior of the COx/concrete interfaces. In order to assess qualitatively the effect of parameter b_T^v, three numerical simulations were carried out by assigning each time a value of $b_T^v \neq 0$ in one of the zone and $b_T^v = 0$ in the two other zones. The results of those three simulations are presented in Figure 4.18. The effect of the viscous slip on the fractures in zones 1 and 3, on the vertical and horizontal displacements at the drift wall is shown by Figure 4.18a) and Figure 4.18c). As a matter of fact, in Figure 4.18a) the fractures' viscous slip is only taken into account in zone 1; which result in a bigger vertical convergence than horizontal. On the contrary, if fractures' viscous

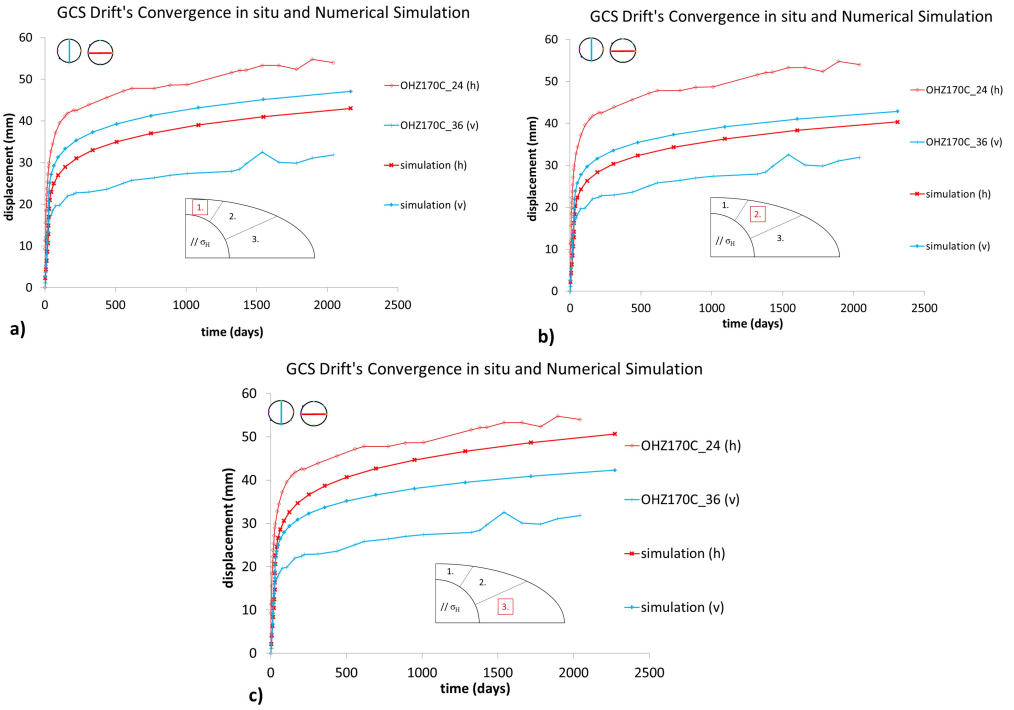

Fig. 4.18.: Comparison between the displacement at the drift wall in the numerical simulation and the convergence measurements obtain *in situ* in the section C of GCS drift. a) $b_T^v = 7.8$ in zone 1 and $b_T^v = 0$ in zones 2 and 3. b) $b_T^v = 7.8$ in zone 2 and $b_T^v = 0$ in zones 1 and 3. c) $b_T^v = 7.8$ in zone 3 and $b_T^v = 0$ in zones 1 and 2.

Tab. 4.6.: Numerical values of the viscous parameters used in the different fractured zones for drifts excavated in the direction of the major horizontal stress.

a MPa^{-1}day$^{-0.2}$	α	n	b_T^v zone 1	b_T^v zone 2	b_T^v zone 3
0.4×10^{-4}	0.215	1	0	0	350

slip is only taken into account in zone 3, the horizontal convergence become bigger than the vertical convergence. Recall that, as shown in Figure 4.14, the order of magnitude of parameter b_T^v strongly depends on the relationship between the viscous behavior of intact rock and the viscous behavior of a fracture $\frac{b}{aD}$. Finally, the viscosity parameters taken for the fractured rock are given by Table 4.6. The resulting convergence are given in Figure 4.19. The horizontal convergence is perfectly reproduced, but the vertical convergence is slightly overestimated. This can certainly be solved by working on the short-term part of the response via the plastic model. On the other hand, it is rather the long-term behavior that interests us and the convergence rate is well reproduced. The convergences rate measured in section C of GCS drift are compared to the convergences rate predicted by the numerical simulation in Figure 4.20. Finally, we present the strain fields in Figure 4.21. With the viscous strain field in Figure 4.21 a) and the visco-plastic strain field in Figure 4.21 b).The

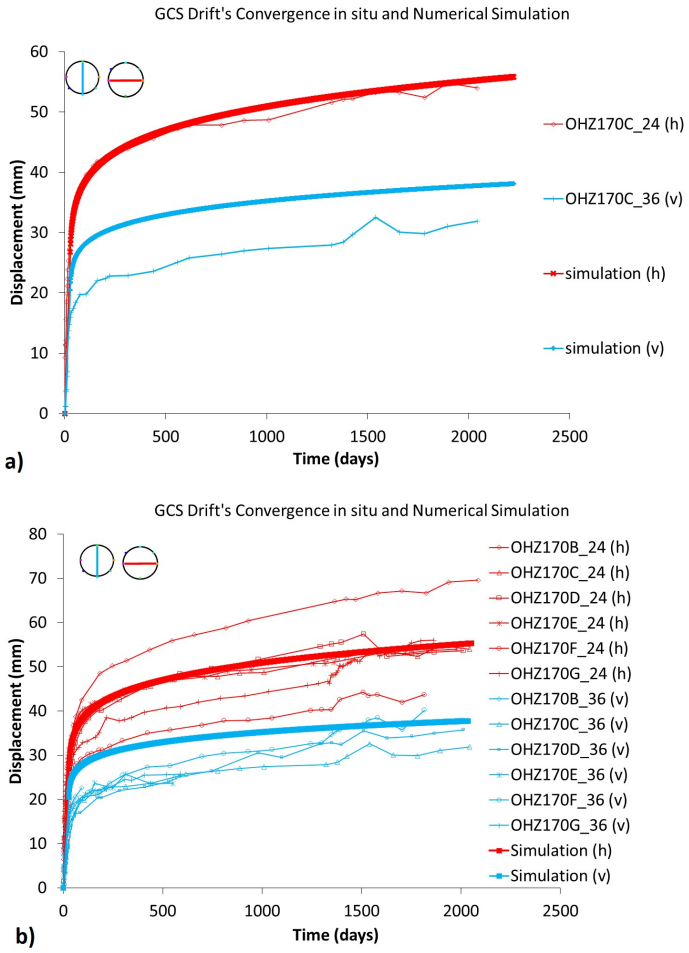

Fig. 4.19.: Comparison between the simulated horizontal and vertical convergences and the measurements in GCS drift. a) The results of the numerical simulation are compared to the measurement of section C of GCS drift which is the section which is the section used to define the excavation protocol. b) The results of the numerical simulation are compared to the measurement in different sections of GCS drift.

deformation fields are not meant to reproduce the fractured zone, as the objective of our study is not to explain and reproduce the fractured zone but just to propose a method that can accurately reproduce the convergences of the URL tunnels. Especially since in the model we imposed the geometry of the fractured zone as well as the effects of the fractures by adjusting the anisotropy parameters in the three sub-parts of the fractured zone. We aim to provide a method to extrapolate the long-term convergences and use these predictions to size the supports. Finally, we represent the vertical and horizontal displacement fields around the drifts in Figure 4.22. It is from these displacements at the drift wall that the vertical and horizontal convergences are calculated.

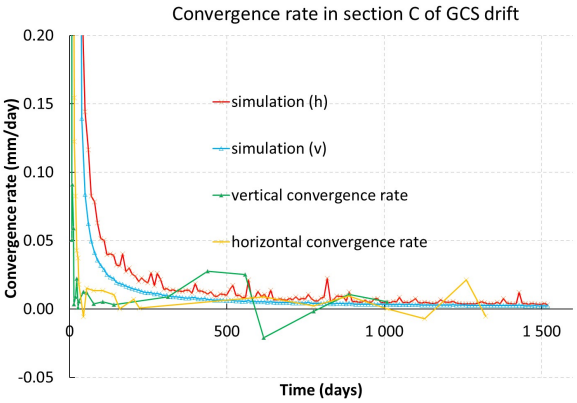

Fig. 4.20.: Comparison between the convergences rate measured in section C of GCS drift and the convergences rate predicted by the numerical simulation.

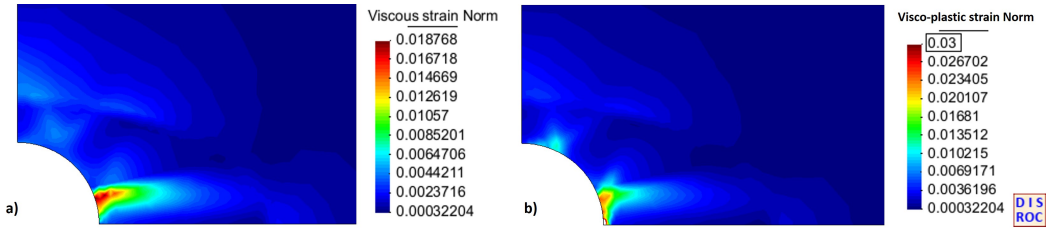

Fig. 4.21.: Strain field around the drift excavated in the direction of the major principal horizontal stress at 2700 days after the beginning of the excavation. a) Viscous strain, b) Visco-plastic strain.

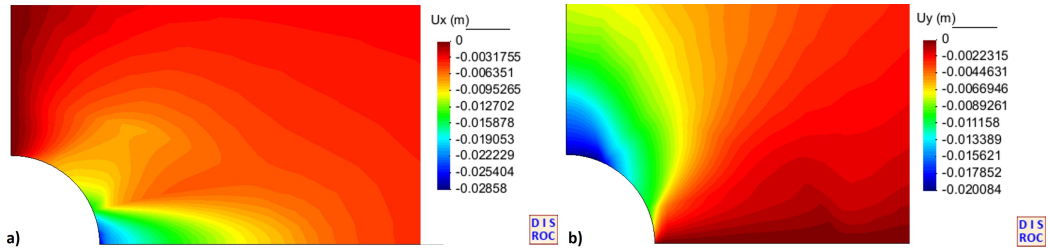

Fig. 4.22.: Displacement field around drift excavated in the direction of the major principal horizontal stress at 2700 days after the beginning of the excavation. a) Horizontal displacement field, b) vertical displacement field.

4.3.2 Drifts in the direction of the minor principal horizontal stress

In this section the convergence models for the drifts excavated in the direction of the minor principal horizontal stress are presented. As a reminder, the state of stress in the cross section of these drifts is anisotropic with $\sigma_v = -12.7$ MPa and $\sigma_H = -16.2$ MPa. As for the convergence models of the drifts excavated in the direction of the minor horizontal stress, in the models presented here four zones are differentiated: three zones of fractured

rock with different densities and orientations of fractures and a zone of intact rock assumed isotropic. A description of the mesh used for modeling the drift excavated along the minor

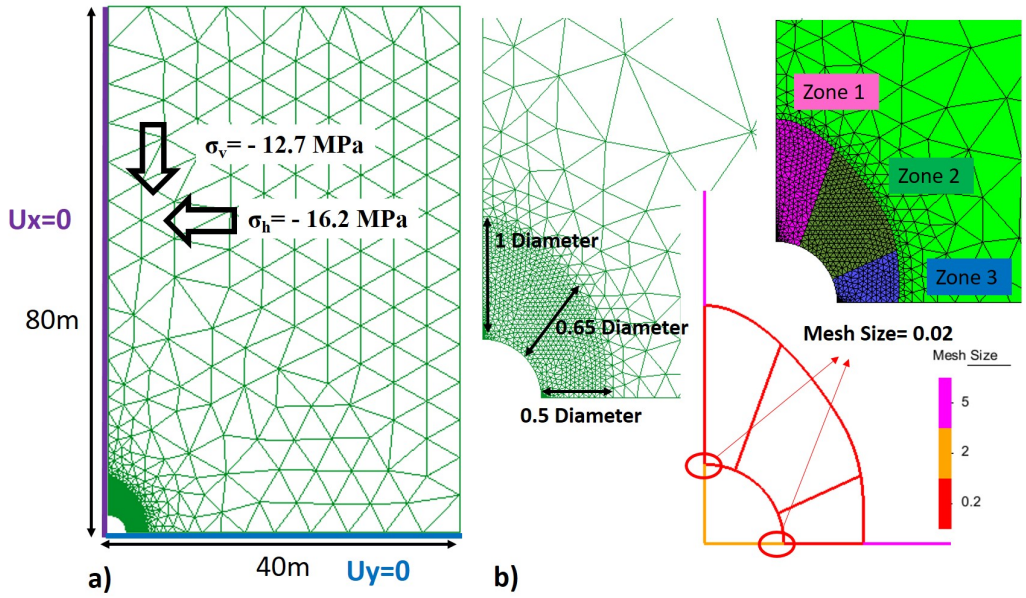

Fig. 4.23.: a) global description of the mesh used for the simulations of drifts excavated along the minor horizontal stress, along with the boundary conditions. b) zoom on the three different zones.

horizontal stress is given in Figure 4.23. The elastic anisotropic parameters only depends on the fracture's density, the tangential stiffness and normal stiffness of the fractures. The tangential and normal stiffness are the same as in section 4.3.1. The parameters of elastic

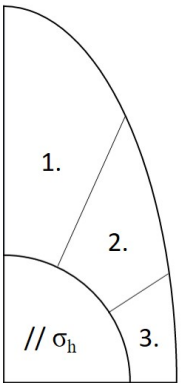

zones	D (m)	E⊥ (MPa)	G (MPa)
1.	0.52	4076	1637
2.	0.56	4130	1654
3.	1.64	4665	1822

Fig. 4.24.: Elastic parameters in the three different zones constituted by fractured rock around drifts excavated in the direction of minor principal horizontal stress.

parameters in the fractured zone are given in Figure 4.24. As the parameters of plasticity do not depend on the fractures' density, the parameters are the same as those used in the models in section 4.3.1 given in the second line of Table 4.5. As for the viscosity, since it depends on the average distance between two fractures (parameter D in equation 4.34), the viscous

Tab. 4.7.: Numerical values of the viscous parameters used in the different fractured zones for drifts excavated in the direction of the major horizontal stress.

a (MPa^{-1}day$^{-0.2}$)	α	n	b_T^v zone 1	b_T^v zone 2	b_T^v zone 3
3.0×10^{-4}	0.215	1	0	0	400

parameters in the fractured zone are readjusted to reproduce the convergences measured *in situ*. The viscosity parameters adopted for the simulation of the drifts excavated in the direction of the principal minor horizontal stress are given in Table 4.7. The comparison of

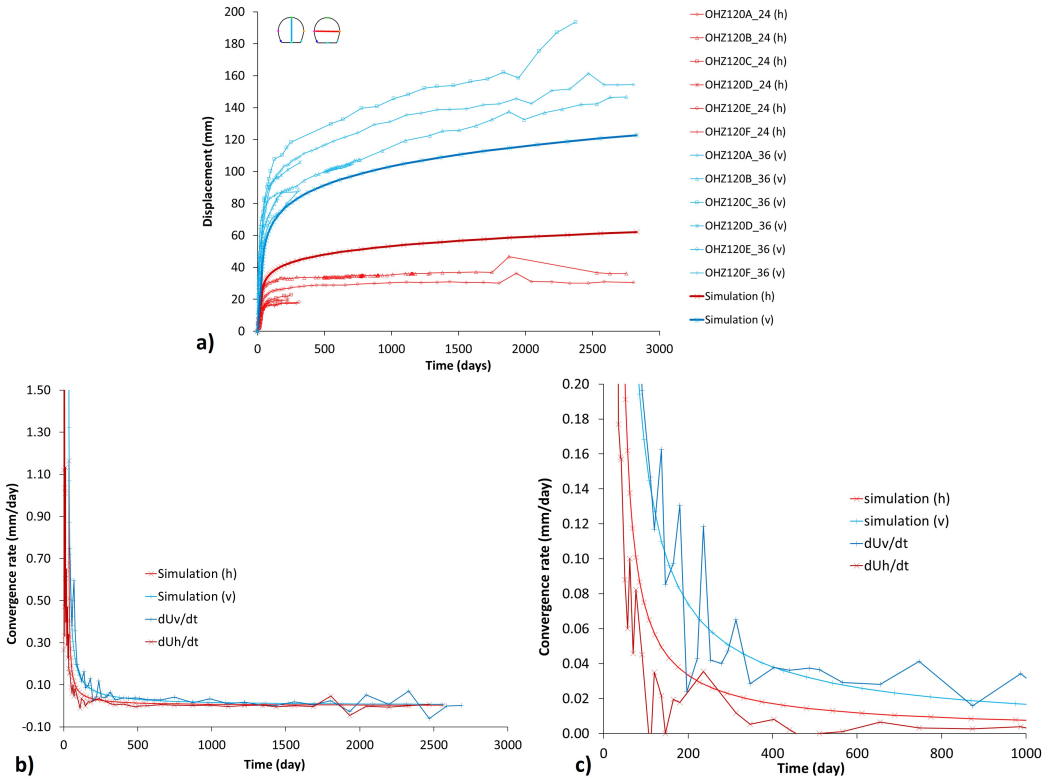

Fig. 4.25.: a) Comparison between the simulated convergences and the convergences measured *in situ* on GED drift. b) Comparison between measured and simulated convergences' rates. c) zoom on the convergence rates.

the simulated and measured *in situ* convergences and convergence rates is given in Figure 4.25. If there is a discrepancy between the measured and simulated convergences (see Figure 4.25 a)), they are underestimated for vertical convergence and overestimated for horizontal convergence, the convergence rates are well reproduced (see Figure 4.25b) and c)). Indeed, the difference between the simulated and measured convergences is not surprising. This discrepancy can be explained by an insufficiently accurate modeling of the excavation phase, i.e. the short-term response. It should be remembered that the excavation procedure was calibrated on the field data of the excavation of the section A of GED drift. Moreover, it

should be noted that our model does not take into account the presence of tensile fractures, which probably play an important role on the short-term response.

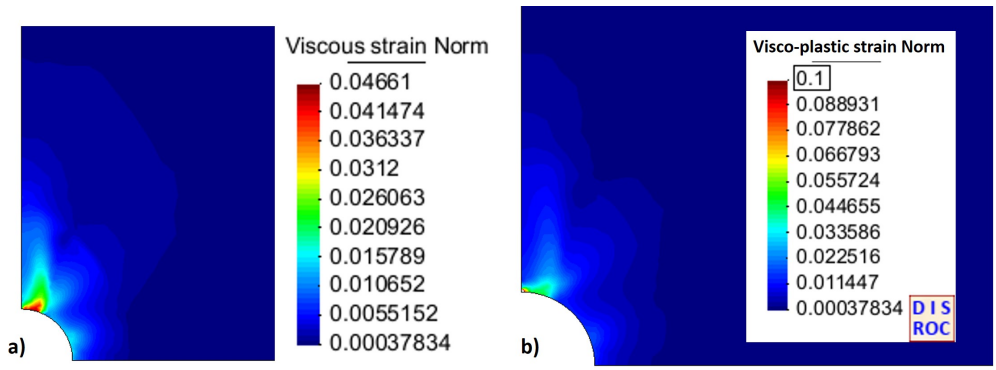

Fig. 4.26.: Strain field around the drift excavated in the direction of the minor principal horizontal stress at 2800 days after the beginning of the excavation. a) Viscous strain field, b) Visco-plastic strain field.

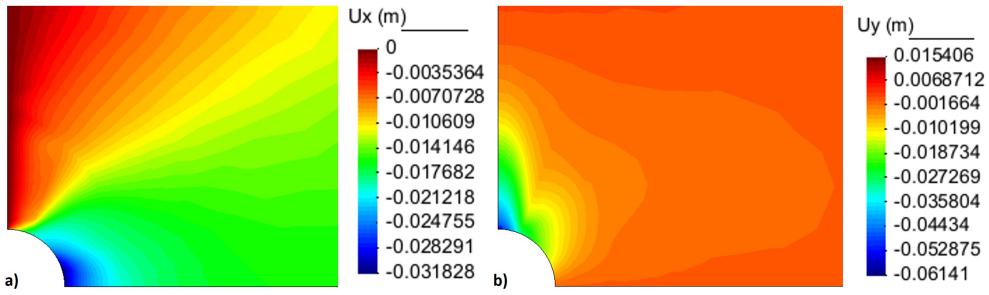

Fig. 4.27.: Displacement field around drift excavated in the direction of the major principal horizontal stress at 2800 days after the beginning of the excavation. a) Horizontal displacement, b) vertical displacement.

The viscous and visco-plastic strain field are presented in Figure 4.26. The vertical and horizontal displacement fields around the drifts are given in Figure 4.27. It is from these displacements at the drift wall that the vertical and horizontal convergences are calculated. Viscosity plays a much more important role for drifts excavated in the direction of minor principal horizontal stress (e.g. GED drift) than for drifts excavated in the direction of major principal horizontal stress (e.g. GCS drift). Indeed, we find that the anisotropy of the convergence rate for tunnels parallel to GED drift is much larger than for tunnels parallel to GCS drift. This may seem surprising because in our model the spacing between fractures in zone 1 of tunnels parallel to GED drift is greater than the spacing between fractures in zone 3 of tunnels parallel to GCS drift: $D_{\mathrm{GED}} = 0.52$ m $> D_{\mathrm{GCS}} = 0.29$ m. The conditions are not exactly symmetrical between the behavior of the fractures in zone 3 of GCS drift and the fractures in zone 1 of GED drift. First, the stress state is different between the two galleries. Also, in one case the fractures are vertically oriented and in the other case horizontally

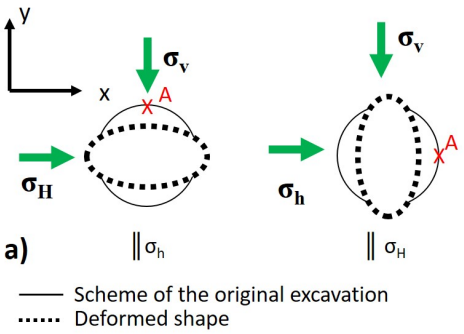

	ε^v	ε^{vp}	U_x (m)	U_y (m)
$//\sigma_H$ (in point A)	0.019	0.03	-0.03	-0.02
$//\sigma_h$ (in point A)	0.047	0.05	-0.03	-0.06

b) Maximum values after 2500 days

Fig. 4.28.: a) Diagram of the tunnels and their deformed shape. b) Result of viscous deformations, viscoplastic deformations and horizontal and vertical displacements. The measurements are made in the direction of maximum convergence in each drift (named point A).

oriented, while it is possible that the actual orientation of the fractures in the fractured zones is more complex than in our models. This simplification of the fractures' orientation could have a great influence on the effect of the fracture slip, hence on the overall strain field around the drifts.

4.4 Conclusion

To recall the objective of the models presented in this chapter: it is to reproduce the convergence of the drifts of the URL with an anisotropic continuous equivalent model. The objective here is basically the same as in chapter 3: with relevant reproduction of the convergences, we aim to provide a reliable tool for the design of the linings. The improvement of the model presented in this chapter compared to the previous model is the explicit link established between the anisotropy parameters and the fracture behavior. The material around the drifts excavation is divided into different zones, three zones of fractured rock in the vicinity of the drift wall and sound rock further away. The threefold elasto-visco-plastic anisotropy account for the effect of the fracture in the fractured zone. Here, we made many assumptions about fracture behavior, but the idea was that these assumptions would be superseded by the results of an experimental campaign conducted to determine the viscous behavior of a fracture in a COx claystone.

The difference between the two types of numerical simulations presented in this work (chapter 3 and 4) is not in the results or the accuracy of the results, but in their approach. Indeed, the models presented in Chapter 3 reproduced very well the convergences measured in the two types of drifts of the URL. The advantage of these first models is their simplicity, since they use one unique continuous material to model a very complex fractured massif. However, if we wanted to use this model for another tunnel, we would have to do all

the numerical calibration work of the anisotropy parameters again, which is not simple and time-consuming, as it requires running several simulations. This is where the models presented in this chapter become very interesting, as they provide a method for modeling fractured rock. Thus, this method can be applied to other tunnels than GCS and GED drifts. Of course, this method is not applicable to any type of tunnel, it is still necessary to ensure that the models really describe the behavior of the intact rock and fractures. Nevertheless, it is reasonable to think of extending it to rocks similar to COx claystone, such as Boom clay and Opalinus clay, used in radioactive waste storage projects in Belgium and Switzerland. The calibration of the parameters is also long because it relies on both an experimental campaign to characterize the behavior of the sound rock and the behavior of fractures in this same rock. In addition, it is necessary to have a description of the fracturing of the rock. Nevertheless, all radioactive waste disposal projects are accompanied by a characterization of the behavior of the host rock and a study of the fractured zones around the tunnels, so it is not unreasonable to offer a modeling method that requires this type of prior study. The only novelty is the characterization of the viscous slip on the fractures. The elasto-plastic parameters of fractures can be measured by conventional direct shear and compression tests, but characterizing the viscous slip of a fracture is a new challenge. Thus, the following two chapters are devoted to the development of an experimental device to characterize the viscous slip on fractures in the Callovo-Oxfordian claystone.

5 An original experimental setup for the analysis of the creep of an interface in COx claystone

This chapter provides a detailed description of the design of the experimental setup used to study viscous slip along a planar interface in the Callovo-Oxfordian claystone. Indeed, in the previous chapter we have highlighted the need to characterize the viscous behavior of a fracture to feed our numerical models. In fact, the whole approach of this work is based on the role played by fractures in the rock mass and more precisely on their viscous slip. This chapter marks a change of scale in the overall approach of this work. We abandon the macroscopic scale of structures to focus on the study of the local behavior of an individual fracture in rock. As the experimental work was carried out in parallel with the numerical simulations, we have built a numerical model relying on an *a priori* assumption on the behavior of the fractures. As a matter of fact, in our numerical simulations, the fractures' viscous behavior is assumed to be represented by Lemaitre's creep law. As a reminder, the choice of this model is based on the behavior of the intact rock (see in Figure 3.4) and on the work done by Stavropoulou [81], who has been working on the long-term behavior of COx/concrete interfaces. However, to our best knowledge, no data exists on the viscous behavior of a COx/COx interface, thus we are not sure that this interface behaves according to Lemaitre's model. In this work, we have chosen to approach the problem from this point of view, as a first attempt. In a second stage it needs to be evaluated if it is really reasonable to model the viscous behavior of chevron fracture in COx claystone like that. The experimental campaign is conducted to answer a specific problematic, namely to characterize the creep behavior of shear fractures in the Callovo-Oxfordian claystone with the objective of modeling the long-term convergences of drifts excavated in this rock. It is not intended to provide a general characterization of creep slip of any rock fractures. Working in this context allowed us, in a first approach to the problem, to set many of the parameters of the experiments (rock used, normal stress, surface roughness...). However, one must be aware that in order to propose a real characterization of the viscous slip of these fractures it would be necessary to further explore these parameters and their influence on the fracture behavior. The experimental setup is coupled with Digital Image Correlation to

get a local measurement of the slip along the fracture. The experimental device is described as it is not a classical well known setup. The experimental method is explained from the sample preparation to the experimental protocol itself. The setting up of Digital Image Correlation, its basic principles and the software CMV [18] used to treat the images are presented. More importantly, the general methodology leading to the particular choices adopted for the optical setup (choice of camera and optics, image definition and resolution, numerical aperture, image acquisition protocol) and the image processing options (DIC parameters, post-processing methodology) are discussed.

For clarity, in the next two chapters, fractures artificially created for the study are referred to as *interfaces* and the word *fracture* is left for discontinuities already present in the rock sample or discontinuities that were unintentionally created during sample loading.

5.1 Objective of the experimental setup

The objective of this work in general is to reproduce and estimate the long-term convergences of the drifts of the URL. As already explained in the first chapter, the convergences of the drifts seem to be connected to the behavior of the fractured rock as a fractured zone develops at the vicinity of the drifts' wall, during the excavation. Two types of fractures are identified in the fractured zone, first tensile fractures, located very closed to the drifts' wall. Those fractures are assumed to be mostly involved in the short-term response of the rock, thus their behavior would be taken into account in the elasto-plasticity of the model. The other fractures are shear fractures or chevron fractures, which develop deeper in the rock mass than the tensile fractures (up to one diameter away from the drifts' wall). They are assumed to provoke additional deformation as they constitute surfaces of weakness in the rock mass, and, we assume, are subject to viscous slip. The experimental setup is designed to study the viscous slip of such a shear fracture. In this work, the time-dependent behavior of an interface is understood as the displacement $\underline{U}$ defined in equation 2.9 that occurs when the interface is subjected to an average constant normal and shear stress $\underline{\sigma}$ along its length. We focus on the tangential component $\underline{u_t}$ of the displacement $\underline{U}$ vector which develops under constant stress $\underline{\sigma}$ along the interface. The time-dependent normal displacement is assumed to be zero. Thus the experimental device presented in this chapter is design to measure u_t understood as a 1D quantity. These assumptions are summarized in Figure 5.1.

However, as it is the deformation of the fractured rock mass that are relevant at the scale of the drifts, it has been decided to design a setup able to measure the coupled deformation of both the bulk rock and the fractures. If the viscous behavior observed to follow a power law such as Lemaitre's creep law, then the measurements need to enable to measure and

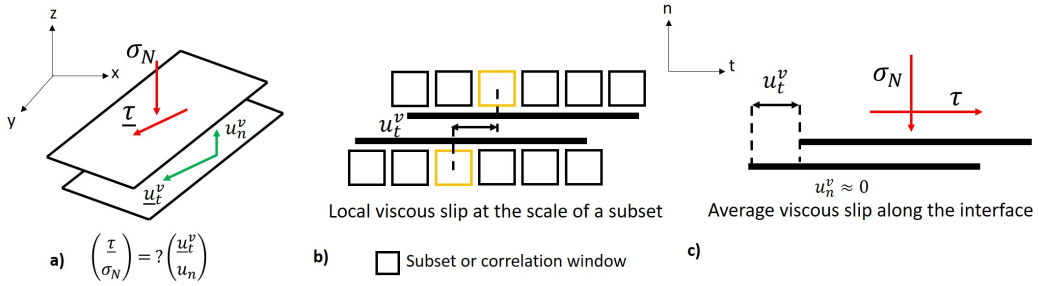

Fig. 5.1.: Scheme of the time-dependent behavior of an interface, a) representation of a planar interface in the (x, y, z) coordinate system, the viscous displacement is assumed to be the response to constant stress $\underline{\sigma}$. b) and c) Simplification of the problem: schematic view of the measurement made during the experiment. The time-dependent displacement in the normal direction is assumed to be zero. The tangential displacement is measured between two subsets: b) Local value measured at the scale of the subset (further explained in Chapter 6), c) average value along the interface.

calibrate the parameters of such a model. In other words, the experimental protocol must allow to study the time dependence of the viscous slip, but also the stress dependence and the possible existence of a stress threshold below which nothing happens. In the numerical simulations the elasto-plastic parameters of the fractures are taken into account with a Mohr-Coulomb yield criterion. Thus, the setup must first allow to verify that such a law is relevant to describe the instantaneous response of a real interface, then to determine its parameters (the normal and tangential stiffness and the cohesion and friction angle).

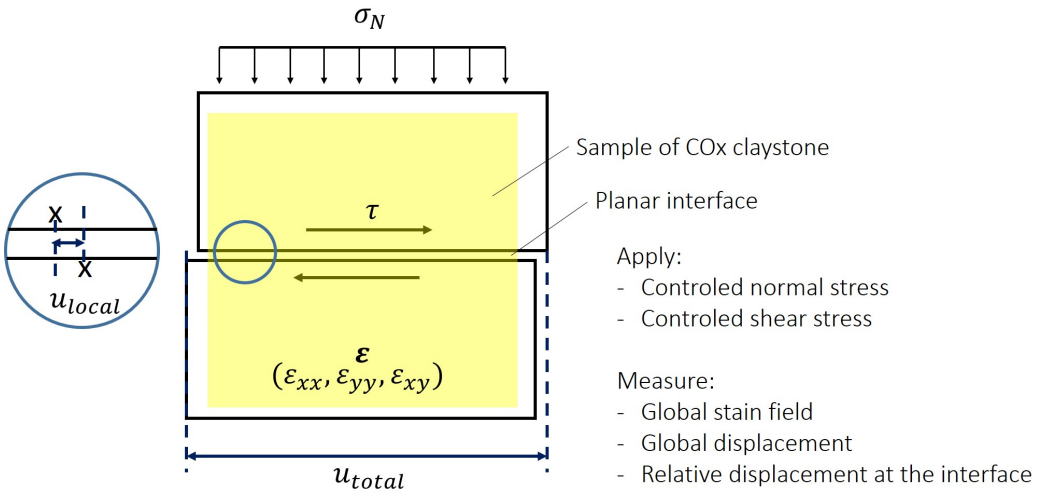

Fig. 5.2.: Scheme of the specifications of the experimental setup.

The specifications of the experimental setup, shown in Figure 5.2 can be summarized as follows. We want a sample with a planar interface. We must be able to impose a controlled normal stress and a controlled tangential stress on this interface. We want to measure the

relative displacement between the two sides of the interface, the strain fields over the entire sample, and the global displacements.

5.2 Description of the experimental device

As there is no standard experimental setup dedicated to the study of the viscous behavior of a fracture, an experimental setup has been designed specifically for the needs of this work. Some experimental devices, intended to study the behavior of fractures or faults, are described in the literature [29, 86]. Most of the existing works are realized in the context of the study of earthquake behavior. The design of our experimental device, as well as the experimental protocol itself, were largely oriented towards the specificity of the context of the storage of nuclear waste in the COx claystone, by the choice of the studied rock and the conditions in which the study was carried out (load, surface condition, ...). Besides, to our knowledge, no other experimental setup integrates in the measurements Digital Image Correlation (DIC). In fact, this way of making measurements had design implications, which are presented in the following sections of this chapter.

5.2.1 Experimental setup and instrumentation

Figure 5.3 shows an overview of the experimental setup. In this chapter both the mechanical part and the instrumentation part are described. The mechanical part of the experimental setup is composed of a dead load loading frame used to hold the interfaces under constant normal stress and an electromechanical linear screw actuator controlled by a Labview software that will prescribe the shear force. The mounting frame of the sample onto the loading system was designed to allow a clear view of the sample and to be able to image it with a digital camera during the experiments. A camera is installed in front of the sample on two motorized micrometric linear stages, which are controlled by another Labview program. The control of the camera motions will be described with more details later. The whole set (camera + linear stages) is mounted on a metallic tripod to ensure the stability of the camera, and to reduce vibrations during the recording of images. The whole experimental device is installed in a room with controlled temperature and humidity, all the instruments being remotely controlled so that the room can be kept closed during the test in order to limit temperature and humidity variations. In addition to the camera, three sensors are used. A force transducer is placed in the actuator rod and the movement of the actuator is controlled so that a constant force is applied. To measure the displacement, two Linear Variable Displacement Transducers (LVDTs) are placed on either side of the sheared block as shown in Figure 5.4. From the camera's point of view, one LVDT is on the right side

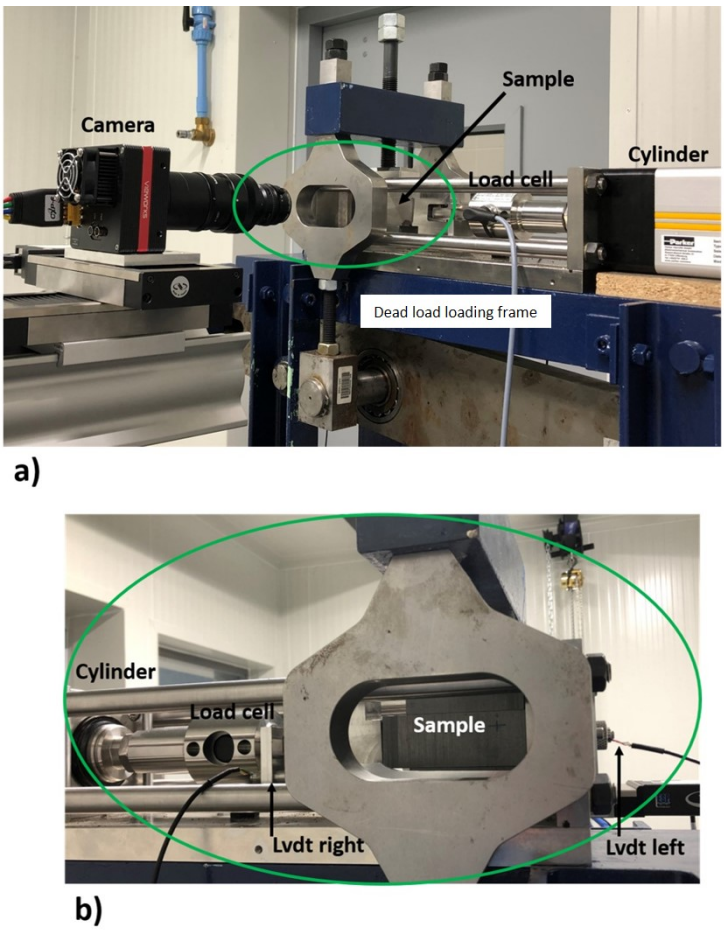

Fig. 5.3.: Image of the experimental setup. a) Overview of the experimental setup with camera for DIC, the dead load loading frame and the actuator. b) zoom on the sample with the LVDTs on both sides of the middle block.

of the middle block, i.e. on the side where the displacement is prescribed and it will be referred to as the *right LVDT* and the other one, which is on the side where the middle block is free is called *left LVDT*. The *right LVDT* is placed between the piston and the frame measuring the displacement of the right face of the sheared block with respect to the frame, as shown in Figure 5.4. Together the measurements of both LVDTs provide the average displacement of the middle block with respect to the frame. In addition, although with these measurements it is not possible to separate the rock bulk deformation from the interface slip, the measurements on each side of the sheared block provides information on the relative importance of the viscous deformations of the rock bulk versus the viscous slip of the interface. This will be further discussed in the next chapter. Temperature and humidity sensors are installed in the room to control their stability during the test.

Studying the viscous behavior of a fracture comes to investigate the slip of the interface, between two blocks, under constant shear stress. In order to avoid the contact between the rock and the frame of the device, the choice was made to use three blocks of rock. In the following, the three blocks, cut in a core of COx claystone, and used in an experiment are referred to as *a sample*. The middle block is sheared with respect to the two others

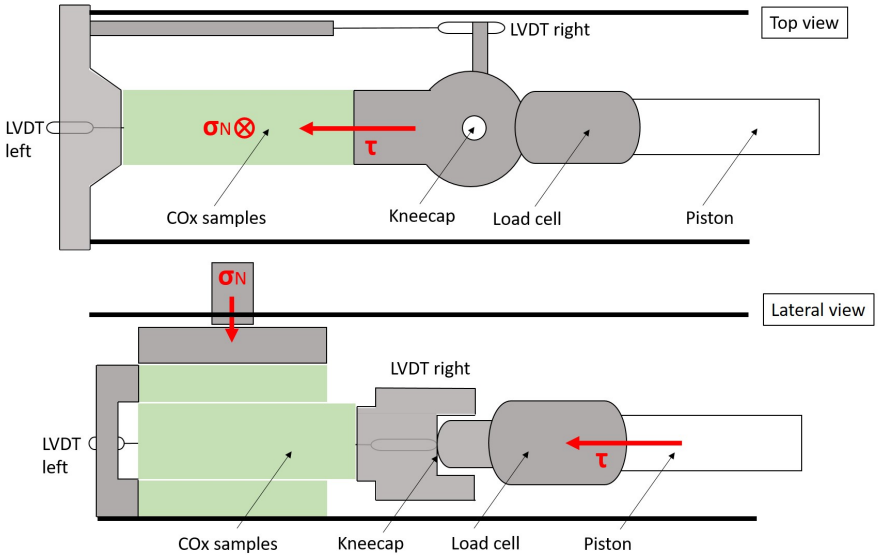

Fig. 5.4.: schematic views of the experimental setup. One view from the top, and underneath a view from the side.

by being pushed by the piston on its right face, while the two upper and below blocks, are blocked against the frame at their left ends. For global comprehension, a scheme of the experimental device is provided in Figure 5.4, where the essential elements of the experiment are indicated: Two linear variable displacement transducers (LVDT), the sample, the load cell and the actuator.

In order to study the viscous slip of the interfaces, the idea is to impose a constant shear stress on the interfaces in order to work under creep conditions. Obviously, it is not possible to directly measure the shear stress along the interface. Nevertheless, in the following, average shear stress is imposed along the interfaces and it is kept constant by holding constant the force by which the middle block is set in motion. Therefore, the movement of the actuator is controlled, with a Labview program, so that the force measured by the sensor located in the actuator rod remains constant. In fact, the actuator is ordered to move forward as long as the force to be prescribed is not reached. When the prescribed force is reached, the actuator stops, which causes the sample to relax. Once the stress has fallen below a tolerance level, the actuator is restarted to move forward, and the stress is kept constant in that way throughout the test. Obviously, the tolerance level is chosen to be small enough

so that the sample experiences an almost constant force and does not undergo load/unload cycles. In practice a tolerance of plus or minus 0.1 kN is set.

The stress normal to the interfaces σ_N is generated by a system of lever arms and dead weights, which presents the advantage of being totally stable in time. The lever arm system allows to increase the force applied in relation to the number of weights used. Here the lever arm allows to multiply the weight by 50, which comes to impose a normal stress of 7.6 MPa on a surface of 2625 mm^2 with 40 kg. Given the size of the sample we imposed an average normal stress of 7.6 MPa during the tests presented in the next chapter. It is worth discussing the relevance of this value to the problem we propose to reproduce. The normal stress which needed to be applied on the interfaces, in order to work under conditions similar to those experienced by the fractures *in situ* can be estimated with a simple elastic calculation under certain assumptions. The calculus is detailed in appendix A.5 and gives an estimated normal stress on the chevron fracture of 10 MPa. Nevertheless, in reality we are looking for the normal stress acting on a fracture, which is itself surrounded by other fractures, so a relaxation of the stress, not taken into account by the elastic calculations, must take place in reality. Indeed, a redistribution of stresses can take place in the fractured medium compared to the elastic calculation. Since the global loading is always the same, the elastic calculation may overestimate the stress at some locations and underestimate it at others. The dependence of the shear creep of the interface on the intensity of the normal stress on the interface has not been investigated in detail in this work. This is, however an interesting question that will be part of its perspectives. Note that in some models, it is supposed that the normal compressive stress decreases the slip rate, similar to frictional effects. The effect of normal stress can be considered in the model as a stress which is added to the stress threshold which leads to a reduction in viscous slip as the normal stress at the interface increases. Thus, the normal stress on the fractures around the tunnels must be estimated more accurately. This can be done quite easily by numerical simulations, assuming however that one has a fairly good idea of the geometry of the fracture distribution in the fractured zone.

5.2.2 Preparation of the samples and experimental protocol

The samples consist of two interfaces created artificially by the superposition of three blocks of COx claystone. However there are also fractures in the sample that are not intentionally introduced. They are either already present in the rock, or they are caused by the loading of the sample. To clarify our message, we recall that hereafter we will refer only to *fractures* for unwanted discontinuities inside the blocks and refer to *interfaces* to speak of the artificial fractures of which we want to quantify the delayed slip.

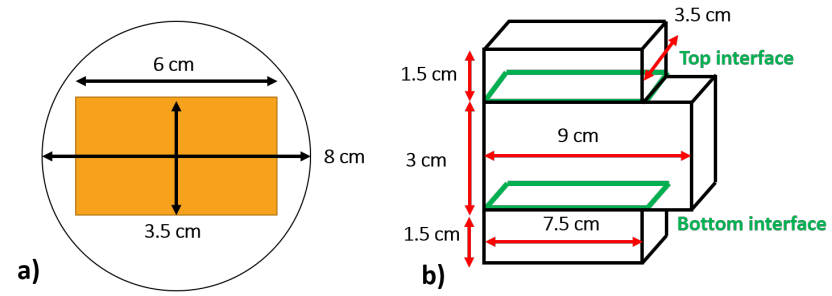

Fig. 5.5.: a) Scheme of the cross section of a core of COx claystone in which the sample are cut. The sample is represented in orange. b) global dimensions of the three blocks constituting one sample.

Geometry and cutting of the sample

The global dimensions of the samples are fixed by the dimensions of the cores provided by ANDRA. Indeed, the cores are cylinders of 8 cm in diameter, so the three blocks can be cut in a rectangular section of 6 cm $\times$ 3.5 cm. Furthermore, Tzortzopoulos et al., [86] have showed that, in order to have the optimal stress distribution along the interfaces, i.e. the most homogeneous stress possible along the interface, the two outer blocks should be half as wide as the central block. They have simulated the shear of an interface between two blocks under constant normal stress, and they have looked at the relative error on normal stress for different block thicknesses. The relative error is calculated from the difference between the measured normal stress and the imposed normal stress of 0.5 MPa: $e = \frac{\sigma_n - 0.5}{0.5}$. Figure 5.6 presents their results: the difference between the applied normal stress and the measured normal stress is minimal for an outer block that is half as thick as the center block.

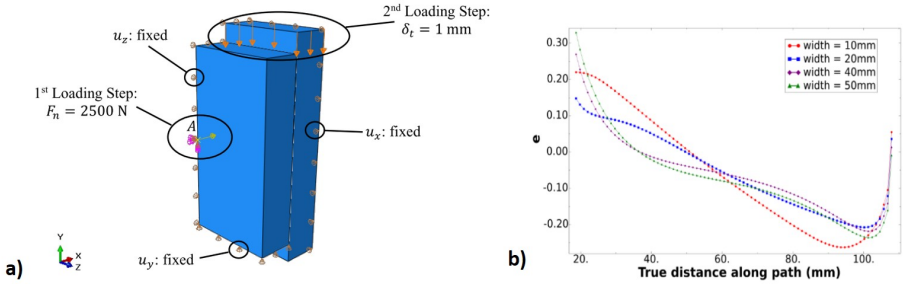

Block thickness (mm)	10	20	40	50
Error	0.368	0.357	0.390	0.416

Fig. 5.6.: a) Scheme of the numerical simulation with the boundary conditions b) relative error on the normal stress along the interface for different block thickness. The error along the interface (given by $\frac{1}{L}\int|e|dy$) is minimum for an outer block half as wide as the central block [86].

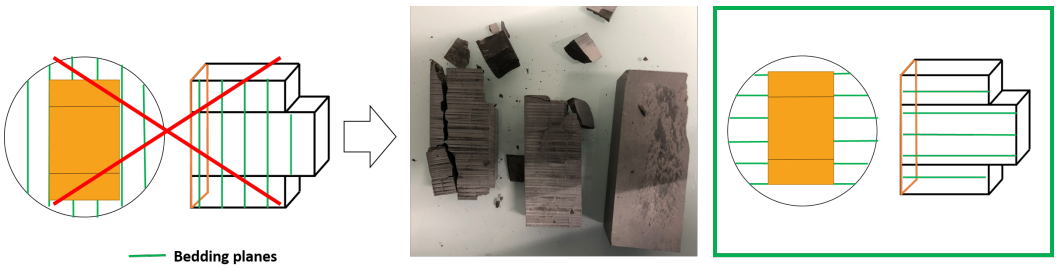

Fig. 5.7.: Green lines represent the bedding planes in the cross section of a core and in the sample. Schematic representation of the proper orientation of the interfaces with respect to the bedding planes naturally present in the rock.

The middle block is 1.5 cm longer than the two other blocks in order to keep the sheared surfaces of constant area during the experiment. The three COx blocks are cut with a wire saw to the dimensions shown in Figure 5.6. Note that COx claystone is a bedded rock. Therefore one could wonder how to cut the sample in the core regarding to the bedding planes. However, in all this work, both for the numerical and the experimental part, the anisotropy induced by the bedding planes is neglected next to the anisotropy due to the fractures: The way the interfaces are oriented in the sample with respect to the bedding planes was initially considered of minor importance. This all the more that the shape of the chevron fracture is such that the orientation of the fractures with respect to the bedding planes is neither trivial nor constant. For the sake of simplicity, the orientation of the bedding planes in the sample was thus disregarded. However, another problem arose during the preparation of the samples. It has been noticed that, in order to assure a better integrity of the samples during the tests, the interfaces have to be cut parallel to the bedding planes. It actually turned out that, for other orientation of the interfaces with regard to the bedding planes, the blocks are weakened and may collapse either during preparation (cutting or polishing) or at the very beginning of the test, during the application of the normal stress, as shown in the image in Figure 5.7.

Preparation of the surfaces and of the sheared interfaces

After cutting the blocks, the preparation of the samples ends with the polishing of some of the surfaces. The four surfaces sheared in the experiment are polished so that the roughness of these faces is as close as possible to the roughness of the shear fractures present around the URL structures. The comparison between the surface roughness of the samples and the roughness of the chevron fractures found *in situ* was performed by the company named Tortoise. This company has developed a quantitative fractography technique allowing to determine local values of mechanical properties of a material from a non-destructive analysis of its fracture surface based on Ponson's work [66]. In the context of this study, we

called upon Tortoise to analyze the surface of our samples and compare it to the roughness of the fractures *in situ*, which allowed us to define a protocol for preparing the surfaces to be sheared. Thus the protocol to prepare the sheared surfaces has been decided by comparing the polished surfaces to the surfaces of the chevron fractures found in the COx claystone with their technique. Two different protocol of polishing have been compared. The protocols were first proposed by trying to reproduce the roughness of the chevron fractures by touch. The surfaces are either polished only with P40 sandpaper or, in the second protocol, they are also post-polished with P60 sandpaper. Several surfaces are analyzed to check the repeatability of the polishing. In addition, in order to verify the uniformity of the polishing on the entire surface, each surface of 9×3.5 cm was analyzed in six different locations. A fractured surface has roughness at different scales, from millimeter

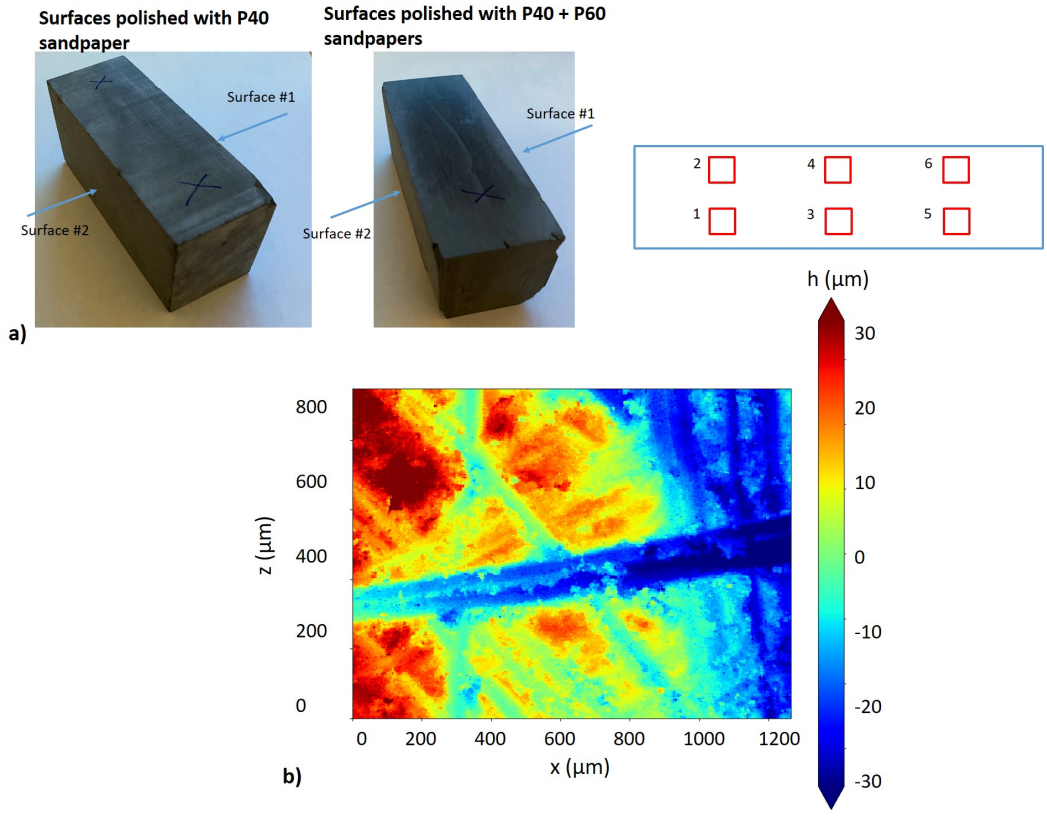

Fig. 5.8.: a) Location of the six different surfaces analyzed, b) example of an analyze of the surface roughness (area 2 polished only with P40 sandpaper).

to micrometer. Qualitative differences exist between the polished surface and the *in situ* chevron fracture. A roughness of the order of hundreds of microns (in other words a 10 micrometer deep crack) is highlighted on the polished surfaces whereas these patterns are not present on the *in situ* fractures. The result of the analyze are presented in appendix A.6, and it concludes that polishing with P40 sandpaper provides a roughness closer to the *in situ*

roughness than the other protocol. Therefore, this polishing protocol was chosen, however, the analysis also shows that the roughness values measured are more scattered than when the surfaces are post-polished with P60 sandpaper.

The last step of sample preparation is the polishing of the photographed faces. As a matter of fact, to use DIC, the faces that are photographed need to be polished to bring out the microstructure of the rock to create a natural speckle. Thus three faces of the samples were mechanically polished (on a turntable of a polishing machine) with four different sandpaper from grade 500 to grade 4000 [93]. The usefulness and concept of *good speckle* will be further discussed at the end of this chapter. Indeed, it is essential to have a good speckle to be able to use DIC. Moreover, as we want to avoid any alteration of the claystone the choice was made to use the natural speckle of the rock by revealing its microstructure, instead of using paint for example.

Figure 5.9 represents the different steps of the sample preparation from the core to the three resulting blocks that will be sheared. To summarize, the preparation of the samples

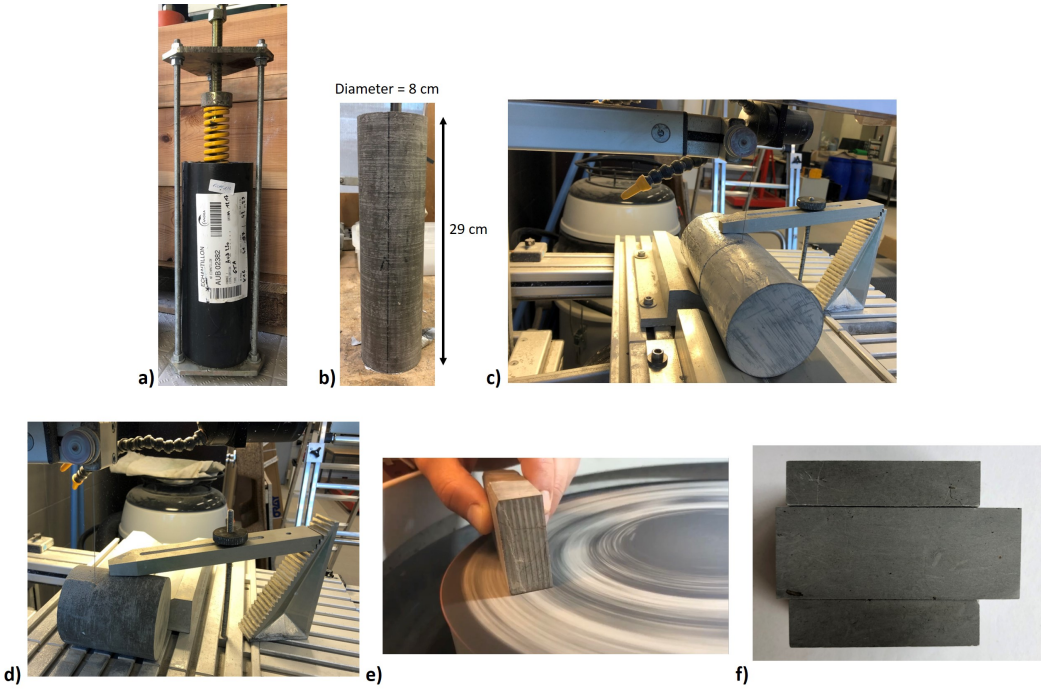

Fig. 5.9.: Preparation of the sample from the core to the resulting three blocks. a) T1 cell provided by ANDRA, b) core of COx claystone with the black line indicating the bedding planes c) and d) cut of the block with the wire saw e) polishing of the faces, f) sample used in the tests.

is as follows. The core sample sent by ANDRA must first be unsealed and the blocks are immediately cut with a wire saw. Using the wire saw, it is quite easy to ensure the parallelism of the faces. Ensuring flatness of the surfaces is essential to facilitate the use of

the DIC. Three samples can be cut from one core. However, it often happens that during the preparation of the sample one of the blocks breaks, hence it is very rare that three complete samples are extracted from the same core. Then, the surfaces that will be photographed are mechanically polished with great care to ensure that when the three blocks are superimposed their three faces remain in the same plane. We say that we proceed *with great care* because we have no mechanical technique to ensure the planarity of the surfaces. Each block is polished, one after the other, by hand on a turntable of a polishing machine. During the process, it is regularly checked that no facets have been created and that the three surfaces remains in the same plane. Occasionally we have had to discard flawed blocks. Four different grains of sandpaper are used to properly bring out the microstructure of the rock. Finally, the samples are stored under vacuum and wrapped in wax paper before being used. Prepared samples are not stored for long periods of time. It is usually only just before testing that the four sheared faces are polished with P40 paper. This last procedure is very fast compared to the other preparation steps. Indeed the cutting of the samples with the wire saw takes between one and a half and two days. One sample at a time is cut and the rest of the core is always repacked (under vacuum and wrapped in wax paper) while waiting to be cut to avoid the drying of the samples.

Monitoring of the relative humidity of the sample

The relative humidity or suction of the sample varies throughout the preparation process, as the different processes tend to dry out the sample. A device, the dew point hygrometer, is used to measure the suction of a rock sample. The measurement is made from some fragments of the rock sample placed in the machine. This measurement is done at the opening of the core, after cutting with the wire saw and finally after polishing which is just before using the sample. Kelvin's law (given in Equation 5.1) is then used to relate the suction measurement to the relative humidity of the rock being tested.

$$s = -\frac{\rho_w RT}{m_w} \ln\left(\frac{HR\%}{100}\right) \tag{5.1}$$

The suction in kPa in given by Equation 5.1, with the universal gas constant: $R = 8.31432$ J/molK, the absolute temperature $T = 273.16 + t$ (with t the temperature in °C), the molecular weight of water vapor $M_w = 18.016$ g/mol, and the volumic mass of water $\rho_w = 1000$ kg/m^3. The different values are given in Table 5.1.

Tab. 5.1.: Evolution of the suction and relative humidity in the COx sample after the different preparation steps of the sample.

Preparation step	Temperature (°C)	suction (MPa)	Relative humidity (%)
Opening of the core	21.3	-18.35	87.3
Cutting of the blocks	21.2	-37.98	75.5
Polishing	21.1	-57.1	65.6

Loading protocol

The experimental device is placed in a relative humidity (70%) and temperature (17°C) controlled room of size (3×3×3 m). The relative humidity is set to 70% because it is the highest relative humidity that can be controlled in our chamber. The temperature was chosen accordingly as it is the most stable temperature with 70% relative humidity. The sample is carefully placed on the loading frame, ensuring that the lateral surfaces of the three blocks are aligned in a single plane. Next, the weights are put in place to apply the normal force to the interfaces. This operation must be done carefully because the three blocks are only constrained by the application of this force. The blocks might be rotated during this operation. The left end of the upper and lower blocks rests on the frame, while the left end of the middle block passes through a hole in the in the loading structure, see on the lateral view of scheme Figure 5.4. Once the normal force at the interfaces is applied, a camera autofocus procedure is initiated to make an initial estimate of the position the camera should have during the test. Then, the image capture procedure is started. The image capture procedure is further explained in the section 5.4.1. The actuator is then moved at a constant speed of 0.01 mm/min until the maximum force is reached. We notice that each time the maximum force is reached, a plateau is reached, and not a peak followed by a softening phenomenon. It is from this maximum force that we define the prescribed force which will be maintained constant during the test. Finally, the actuator is controlled to maintain a constant force throughout the test. As far as image taking is concerned, each image is preceded by an auto-focusing procedure described in section 5.4.1.

5.3 Digital Image Correlation (2D)

5.3.1 Principle of DIC

Digital Image Correlation is a field measurement technique that dates back to the early 1980's [16]. The general principle of DIC, represented in Figure 5.10, is to acquire a couples of digital images, at different stages of loading, of the same area of the tested specimen, then

proceed to the search for homologous points between the reference image and the deformed image based on the similarity of their vicinity, and finally deduce the displacement field, and then, by derivation, the deformation field, or some average strains or other kinematic information over some areas of interest. The technique requests that the studied surface presents a so-called speckle pattern. In fact it is necessary that the grey level differences, or contrast, from some elementary unit, or pixel, to its near neighbors, are strong enough to ensure the sensitivity of the technique to small displacement. DIC works from the gray levels of the reference image, noted f and of the deformed image, noted g. To every point $\underline{X}$ in the reference image, correspond a point $\underline{x}$ in the deformed image related by equation 5.2.

$$\underline{x} = \phi(\underline{X}) \tag{5.2}$$

With ϕ the 2D (apparent) mechanical transformation between the two images. If the gray

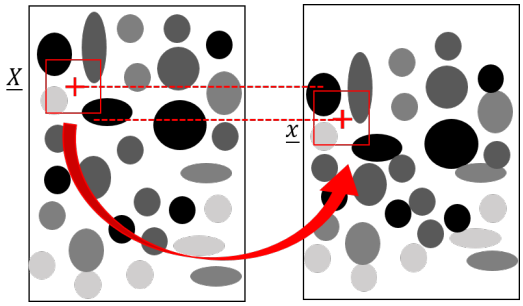

Fig. 5.10.: One point in the reference image is found in the deformed image based on the similarity of their vicinity.

levels are perfectly consistent between the two images (perfect conservation of grey levels) one can write:

$$g(\phi(\underline{X})) = f(\underline{X}) \tag{5.3}$$

In practice, gray levels are never perfectly preserved and an often adopted relaxed version of equation 5.3 is:

$$g(\phi(\underline{X})) = c.f(\underline{X}) + b + g' \tag{5.4}$$

with c the contrast variation, b the brightness variation and g' noise which might have various origins. The problem is to determine the unknown mechanical transformation ϕ by locating the homologous points from the knowledge of the discrete gray levels f and g of the recorded images. In fact, this inverse problem is ill-posed because the objective is to determine a 2D vector field (the displacement field) from a scalar information (the gray level). Thus we look for an approximation ϕ_0 of the transformation ϕ over some domain D around a point $\underline{X}_0$ in the reference image, the so-called correlation window. The similarity between the grey level distribution $f(\underline{X})$ in the domain D in the reference image and grey level distribution in the deformed image, back convected according to the transformation ϕ_0,

namely $g(\phi_0(\underline{X}))$ is measured by the correlation coefficient $C(\phi_0)$. In the CMV software used here, the correlation coefficient is defined by [31].

$$C(\phi_0) = 1 - \frac{\sum_{i\in D}(f(\underline{X_i}) - \bar{f})(g(\underline{x_i}) - \bar{g})}{\sqrt{\sum_{i\in D}(f(\underline{x_i}) - \bar{f})^2}\sqrt{\sum_{i\in D}(g(\underline{x_i}) - \bar{g})^2}} \tag{5.5}$$

where $\bar{f}$ and $\bar{g}$ are the average gray levels over respectively the correlation domain D, and in its transformation by ϕ_0. This correlation coefficient varies between 0 (in the case of a perfect match) and 2 (in the case of a perfect contrast inversion). It is insensitive to global variations in brightness b and contrast c in the correlation domain between both configurations, and thus it is only sensitive to the local contrast between the two configurations, which is assumed to be the signature of the material point $\underline{X}_0$ (i.e. this contrast is assumed to follow the mechanical transformation). The minimization of ϕ_0 gives an estimate of ϕ on a domain D.

$$\phi_D = \text{argmin}_{\phi_0} C(\phi_0) \tag{5.6}$$

More precisely, this minimization with respect to ϕ_0 is performed with respect to a limited set of scalar parameters that fully describe the transformation ϕ_0 over the window D. The definition of the correlation coefficient, the setting of ϕ_0 and the method of solving the optimization problem vary between the different correlation methods. The interpolation methods allowing the passage from discrete gray level information (pixel) to continuous information required to evaluate $g(\phi_0(\underline{X}))$ for any subpixel position $\phi_0(\underline{X})$. Once the transformation ϕ_D established, the displacement field over a set $(X_i, i = 1, N)$ of N points distributed over some region of interest in the reference image (and usually distributed over a regular grid of correlation points) is estimated by:

$$\underline{u_i} = \underline{x_i} - \underline{X_i} = \phi_D(\underline{X_i}) - \underline{X_i} \tag{5.7}$$

The strain field is according to the theory of continuum mechanics obtained by spatial derivation of the displacement field. The gradient of the mechanical transformation is given by:

$$\underline{\underline{\mathbf{F}}} = \frac{\partial \underline{x}}{\partial \underline{X}} \tag{5.8}$$

The Green-Lagrange strain tensor is given by:

$$\underline{\underline{\mathbf{E}}} = \frac{1}{2}({}^t\underline{\underline{\mathbf{F}}}\,\underline{\underline{\mathbf{F}}} - \underline{\underline{\mathbf{I}}}) \tag{5.9}$$

However, in practice, the ϕ transformation is only known in a discrete way at the different correlation points. Thus, the gradient of the transformation cannot be computed by continuously differentiating the displacement field. The deformation tensor is calculated from the average of the gradients of the transformation $\underline{\underline{\mathbf{F}}}$ over an integration domain of finite size Ω

delimited in practice by some neighboring points, see [2] for details. The average of the gradients of the transformation is calculated by an integral on the contour of the domain Ω considered, assuming linearity of displacement between neighboring points. Different integration schemes, defined by [2], implemented in the CMV software and presented in Figure 5.11, corresponding to the choice of the used contour which allows to determine the level of accuracy of the calculation of the deformation but also its spatial resolution. Indeed, the wider the scheme, the more precise the deformation will be, but the less local it will be. The Green-Lagrange strain tensor on the domain Ω is given by equation 5.10, and which is

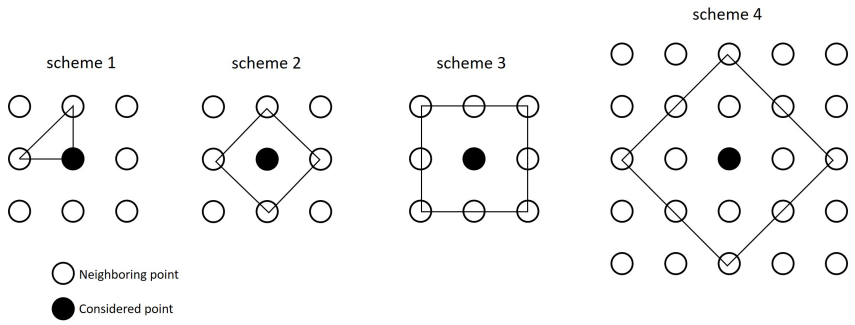

Fig. 5.11.: Different integration schemes for the calculation of the strain tensor with DIC [2]

linearized in case of small deformations to become equation 5.11.

$$\underline{\underline{\mathbf{E}}}_{\Omega} = \frac{1}{2}({}^{t}\langle\underline{\underline{\mathbf{F}}}\rangle_{\Omega}\langle\underline{\underline{\mathbf{F}}}\rangle_{\Omega} - \underline{\underline{\mathbf{I}}}) \tag{5.10}$$

$$\underline{\underline{\mathbf{E}}}_{\Omega} = \frac{1}{2}({}^{t}\langle\underline{\underline{\mathbf{F}}}\rangle_{\Omega} + \langle\underline{\underline{\mathbf{F}}}\rangle_{\Omega}) - \underline{\underline{\mathbf{I}}} \tag{5.11}$$

In the context of this work the software used to do DIC was the 2D version of CMV. This software was developed by Michel Bornert and co-authors, from the laboratoire de Mécanique des Solides (LMS) at Ecole Polytechnique and the laboratoire Navier at l'Ecole des Ponts Paritech [18]. The process of work with this software basically can be divided into three principal steps.

First the images of the sequence are loaded. Each creep sequence contains a lot of images (about 1000) and the images being quite heavy (about 150 Mb per image), we proceed to a sorting of the images to have to process only a part of them. We manage to process about 100 images at a time. It is also more interesting to have more images from the beginning of the test, when the largest displacement increments occurs, and fewer images from the last hour, when the deformation rate is smaller. Therefore, each image taken is mapped to the displacements measured by the *right LVDT*, and only those images for which a constant increase in displacement has occurred are retained. In other words, the images,

instead of being taken at regular intervals of time, are taken at regular intervals of LVDT displacement.

The second step consists in finding in the deformed image the homologous points to the points defined in the reference image. The points defined in the reference image are first placed on the edges of the interfaces in order to calculate the slip along the interfaces. It is important to ensure that the correlation window borders run along the edges of the interfaces without crossing them. Then, once the points are placed on either side of the interfaces, the other correlation windows are placed to grid the entire image. The initialization of the search for homologous points in the deformed image is done either automatically or manually if the displacement is too important. This is particularly the case in the first images close to the fractures that are closing.

The last step consists in the the post treatment. It is during this last step that the strain field maps and other quantities of interest are computed, as a function of either time or space.

5.3.2 Quantification of displacement jumps

We find in the literature several different approaches used with DIC algorithms to quantify a displacement jump on a discontinuity. In our case, since we are working on relatively straight and well-identified interfaces, we have simply placed the correlation windows on either side of the interfaces, then subtracted the coordinates in the x-direction (horizontal direction) from two windows above and below the interface. It is assumed that the camera is well aligned with the sample and that the interfaces are well aligned with the horizontal. Thus, we can assume at the first order of analysis that the slip is along the x-direction and that even the effect of asperities (or effect of dilatancy) does not significantly deviate the slip from the x-direction. This method gives the slip at the correlation window scale, and then by averaging these displacements along the interface we get the average slip of the interface.

Other people have used similar methods, i.e. placing correlation windows on either side of the discontinuity, to quantify the displacement jumps around a discontinuity. We can cite the work of Rupin who worked on two-phase metals and used similar approach to quantify the interphase slip [72]. As a matter of fact, when quantifying the deformation of a continuous medium, the average gradient of the transformation is given by $\langle \underline{\underline{\mathbf{F}}} \rangle$. If the continuous medium consists of several phases, $\langle \underline{\underline{\mathbf{F}}} \rangle$ can be written as follows:

$$\langle \underline{\underline{\mathbf{F}}} \rangle = c^{\alpha} \langle \underline{\underline{\mathbf{F}}} \rangle_{\alpha} + c^{\gamma} \langle \underline{\underline{\mathbf{F}}} \rangle_{\gamma} \tag{5.12}$$

with c^{α} and c^{γ} the volume fraction of the phases. The presence of a discontinuity leads to an additional contribution noted $\Delta\underline{\underline{\mathbf{F}}}$. Thus the average gradient of the transformation becomes:

$$\left\langle \underline{\underline{\mathbf{F}}} \right\rangle = c^{\alpha} \left\langle \underline{\underline{\mathbf{F}}} \right\rangle_{\alpha} + c^{\gamma} \left\langle \underline{\underline{\mathbf{F}}} \right\rangle_{\gamma} + \Delta\underline{\underline{\mathbf{F}}} \tag{5.13}$$

Eventually, $\Delta\underline{\underline{\mathbf{F}}}$ can be estimated by knowing $\left\langle \underline{\underline{\mathbf{F}}} \right\rangle$, $\left\langle \underline{\underline{\mathbf{F}}} \right\rangle_{\alpha}$ and $\left\langle \underline{\underline{\mathbf{F}}} \right\rangle_{\gamma}$. These different terms can be calculated using contour integrals. Figure 5.12a) shows the application of this method in [72].

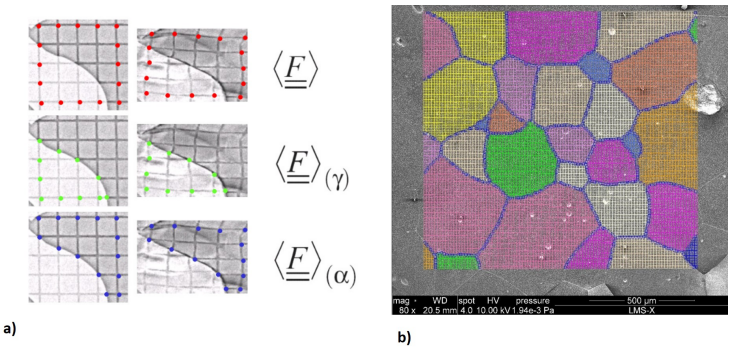

Fig. 5.12.: a) Interphase slip quantification method by Rupin [72], b) grid of point in the grain and on the interfaces [36].

Another method was used by Gaye to quantify the grain boundary sliding in halite rock [36]. As they noticed that the discretisation of the grains interface with a regular DIC grid led to error in the estimation of the slip, they proposed a new formulation. Their method, which also use contour integrals consists in positioning the points on the grain interfaces and then split the correlation in two by attributing two distinct displacements to it.

We can also mention the methods of enrichment of the transformation with discontinuities inside the correlation windows. Réthoré et al., have introduced an extended correlation technique to capture, in images, shear-band like discontinuities [69], which is operated on a correlation algorithm which rely on continuous displacement field basis with a finite element shape functions [12]. Let us recall that the correlation algorithms mentioned so far are based on the local analysis of correlation windows subjected to different kinematics and gray level interpolations [82].

Another DIC technique used to study the deformation of cracked medium is an improvement of Heaviside-based DIC (H-DIC) algorithm [43]. This method enables to quantify the opening, shearing and orientation of a discontinuity in the correlation windows. More recently this H-DIC has been applied to study the mixed-mode behavior of desiccation cracks in a clayey rock. This technique allowed the authors to observe the behavior of

fractures (opening and sliding) under desaturation and saturation paths of the rock mass [44].

5.3.3 Sources of DIC errors and their quantification

Like in all measurement techniques, the measurement given by DIC is subject to some error, which must be evaluated. The errors of displacement field measurements with 2D DIC can be divided into two principal types:

– The *errors extrinsic* to the DIC errors, that is to say the errors that are not directly related to the process of image correlation, but arise from the image acquisition.

– The *errors intrinsic* to the DIC which are directly related to the image processing technique.

Extrinsic errors

DIC 2D only enable the measurements of displacements and strain in a plane, or more precisely the components of the 3D mechanical transformation that is parallel to the plane of the 2D optical projection. The out-of-plane motion of the sample and the eventual bad re-positioning of the camera with respect to the sample (for example if the optical axis of the camera and the analyzed plane are not well perpendicular and when this misalignment evolves during the experiment) induce parasitic apparent deformations. This occurs however only when displacements are large, which is not the case in our experiment.

The geometrical defects of the optical devices can induce a bad positioning of the pixels coordinates which finally introduce an error on the measured deformations.

Finally, there is the intrinsic noise of the images. Indeed, two images acquired under the same conditions do not always have the same gray level. We must try to minimize this noise by choosing a highly contrasted texture, which will improve the signal to noise ratio of the images, and by choosing a correlation window size large enough to reduce the sensitivity to noise. Effect of noise, window size and image characteristics are for instance discussed in [15] as well as later in this chapter for our specific experimental conditions.

Intrinsic errors

Errors intrinsic to the DIC are related to:

The description of the ϕ function. Indeed, the ϕ transformation is approximated by a ϕ_0 function which is defined by a set of shape functions. If these shape functions are not adapted to describe the real transformation undergone by the analyzed sample, then the measurement of the displacement will necessarily be marred by errors. For more details on this type of error the reader can refer to the work of Bornert et al., [15].

Interpolation of the correlation coefficient for non-integer values of displacements. Indeed, the gray level of the non-integer coordinate points (expressed in pixels) is determined by interpolation on the gray levels of the neighboring pixels. The higher the order of the interpolation, the better the continuity of the correlation coefficient, but on the other hand, the longer the calculation time will be. Due to this interpolation, the displacement will be overestimated or underestimated, in some systematic way, which depends however on the properties of the image contrast and image noise, see in [15].

5.4 Experimental setup regarding DIC

An important part of the development of the experimental setup was the setting up of the tools needed to use DIC. For this it was necessary to define the optical system to be used, including the choice of the camera and associated optics and the configuration in which to use it (magnification, aperture size, optical setup...). Note that three assumptions are commonly made when using 2D-DIC to estimate the motion of an object. First the observed surface of the object is assumed to be planar. Second, the plane of study of the sample is assumed to be parallel to the plane of the camera sensor. Third, the out-of-plane component of the displacement and its gradients in the observation plane are small with respect to the gradient of the in-plane components of the displacements.

In this section we will describe the implementation of DIC in our experimental setup. The use of DIC implies the setting up of an optical system. The optical details are beyond the scope of this work and our experimental setup is determined assuming a simple optical system. Nonetheless, the setting up of the optical device deserves to be discussed because the position of the few elements (sensor, lens, diaphragm, and object) has an influence on the quality of the images. The distance between the sensor and the object and the focal distance of the lens are used to define the magnification and thus the effective size of the pixels. The aperture of the lens (or its diaphragm) defines both the size of the Airy dots on the sensor, due to diffraction effect, and the depth of field and thus has a consequence on the

blur of the image. The depth of field is the distance in front of and beyond the object that appears to be in focus, the smaller the aperture, the greater the depth of field and the smaller the out-of-focus blur when the object in not perfectly focused. Conversely, the larger the aperture, the smaller the Airy dots, and the sharper the image.

In this section the implementation of DIC in our experimental setup is described. The implementation of DIC is based on three different choices:

– The camera.

– The conditions of the experiment (magnification, aperture,...).

– The correlation parameters (size of the subset, interpolation function).

These different *choices* are made on the basis of an error analysis. In general, the more we try to make a local measurement, the more the error is important. The idea is to choose the configuration that allows the best compromise between a sufficiently local measurement and the most accurate measurement possible, knowing that we want to measure *a priori* very small displacement of the order of micrometers and even below, with a good accuracy. This requires displacement errors to be significantly small. The errors were evaluated in the configuration chosen for our experiments. A last point is dedicated to the automatic focusing procedure used during the test.

Note that since we are handling Callovo-Oxfordian claystone in our tests, we will have to use the microstructure of the rock as a natural speckle (as the use of any additional product, such as paint, may alter the mechanical properties of the rock). Indeed, the rock is composed of a clay matrix with mineral particles, which is perfectly suitable as speckle [17]. The microstructure is mainly composed of $Si0_2$ and $CaCO_3$ particles. The typical size of these particles is 20 µm, and their distribution is approximately of 1 µm to 100 µm. Assuming that the polishing is done well enough to correctly reveal the microstructure, we have no further control over the quality of the speckle. As a matter of fact, the ideal surface texture should be isotropic, i.e. without a preferred orientation. A good speckle pattern should on the one hand have a high content of information which makes the pattern matching more efficient. Therefore, a good speckle enables to consider a relative small neighborhood around a point, which corresponds to a small subset or correlation window, and thus a high spatial resolution of the DIC measurement. However, on the other hand, the speckle pattern should not get too small with respect to the pixel size, in order that subpixel accuracy can be reached without to large artifact due to the systematic errors induced by grey level interpolation, as already discussed above. As a matter of fact, the choice of magnification and other optical parameters will be the result of a compromise, which need to be optimized by a reliable evaluation of the DIC errors for all possible combinations of options. The method used in this work to perform this optimization is an extension of the one described in [93]. It

requires first a simple way to quantify accurately DIC errors (both random errors induced by image noise and systematic error associated with subpixel grey level interpolations).

The evaluation of errors due to DIC consists in determining the difference between, the measured displacement with DIC, and the actual displacement. The technique employed here to study the errors has already been used by several authors [93, 27]. The principle of this technique is to impose an isotropic deformation to the whole image by slightly varying the magnification of the camera. This modification of the magnification was achieved by using a stage on which the camera is fixed and which allows a translation of the camera along its optical axis. The correlation of the image, after the camera movement with the one before the movement allows to evaluate the measurement errors. The statistical treatment of errors makes it possible to distinguish systematic errors from random errors. The **systematic errors** are mainly related to the gray level interpolation method and **correspond to the average of the differences between the measured and theoretical displacements** for all points with the same interpolation errors. The **random errors** are induced by the image noise and **represent the standard deviations between the real and measured displacements**. Figure 5.13 shows the random error as a function of the normal displacement of the camera for two different apertures of the used lens, and two optical magnifications. It shows that in the configuration with D8 aperture, and a camera translation of less than 70 µm the errors are stable (black symbols in the Figure 5.13), while for a wider opening (open symbols in the Figure 5.13) the error increases drastically for a camera translation higher than 150 *mu*m.

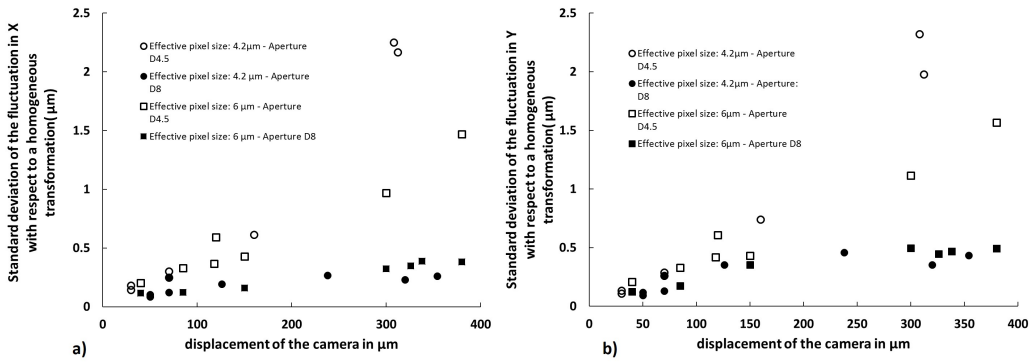

Fig. 5.13.: Standard deviation of the fluctuations a) of the x component of the displacement and b) of the y ones, with respect to a homogeneous transformation (random errors) in function of the normal displacement of the camera in μm and for two apertures of the used lens (4.5 open symbols, and 8, black symbols) and two optical magnifications (effective pixel size of 4.2, triangles, and 6 micrometers, squares).

A preliminary study of systematic and random errors was performed for different effective pixel sizes with a provisional camera, in order to choose the camera (sensor size and number of pixels) to acquire for the actual experiments. The provisional camera and optical lens

are a JAI Spark, SP-12000M-CXP4 monochrome camera, with a 12 million-pixel sensor (4096×3072 pixels) with a sensor size 22.5×16.9 (thus a pixel size of 5.5 μm) and a Macro Varon 85 mm optical lens. The idea is to choose the configuration that allows the best compromise between a sufficiently local measurement and the most accurate measurement possible. The random and systematic error curves obtained for optical configurations giving 4.2 μm, 5.3 μm, 6.4 μm and 7.5 μm of effective pixel size, allow to simulate the use of 4 cameras with different sensor sizes and number of pixels. For each pixel size, the error analysis is performed for two different apertures. The two different aperture sizes correspond to a D4.5 diaphragm and a D8 diaphragm. The D8 aperture corresponds to a smaller aperture and therefore a greater depth of field, in other words, a larger range over which the image remains focused. The curves of systematic errors (Average X and Average Y) are characterized by an S shape. Note that, in all the Figures 5.14, 5.15, 5.16 and

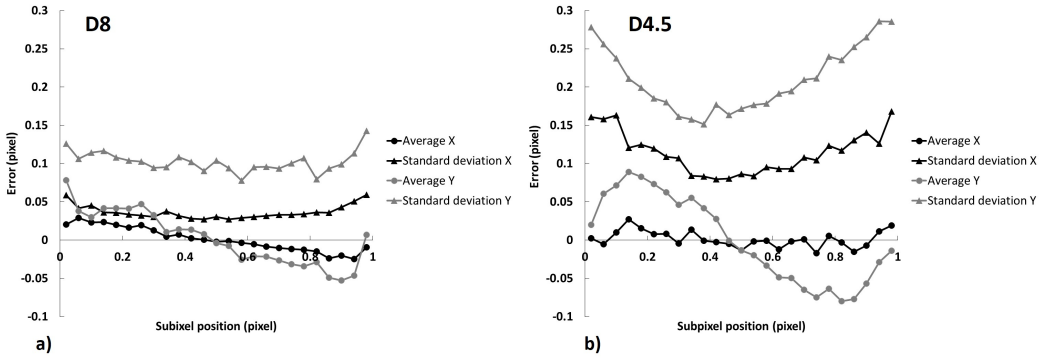

Fig. 5.14.: Systematic (Average) and random (Standard deviation) errors on horizontal X and vertical Y displacement determined with CMV for an effective pixel size of 4.2 μm a) with a D8 diaphragm b) with a D4.5 diaphragm

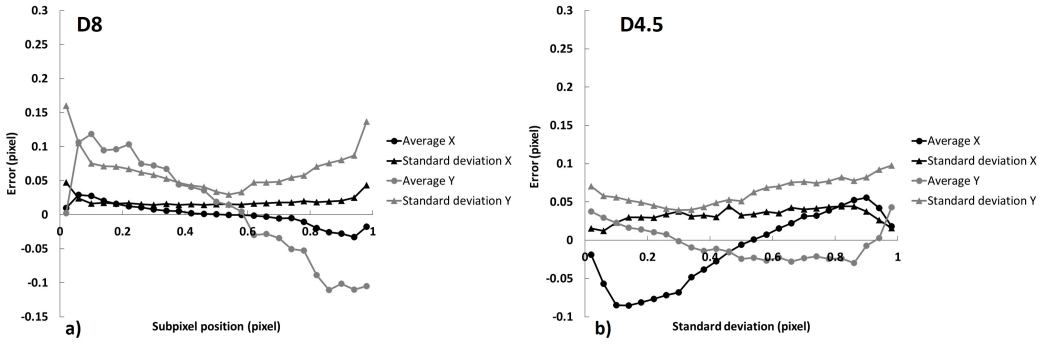

Fig. 5.15.: Systematic (Average) and random (Standard deviation) errors on horizontal X and vertical Y displacement determined with CMV for an effective pixel size of 5.3 μm a) with a D8 diaphragm b) with a D4.5 diaphragm

5.17 the random error is always bigger than the systematic error. Moreover, the error is globally reduced by using a smaller aperture. Finally, since the error for the D8 aperture

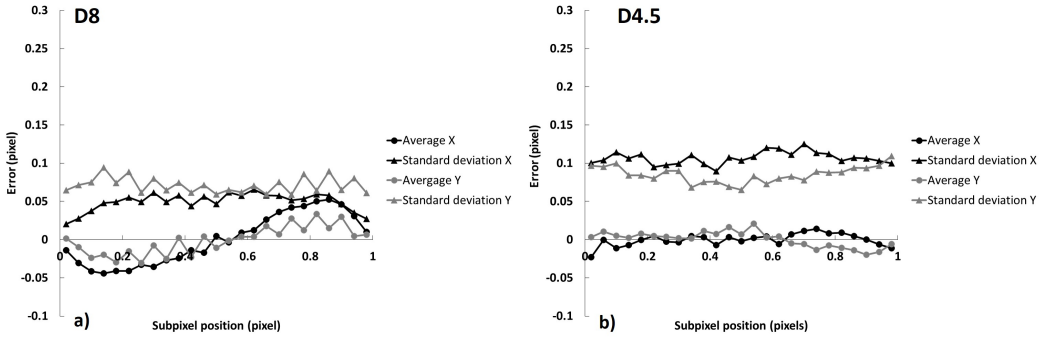

Fig. 5.16.: Systematic (Average) and random (Standard deviation) errors on horizontal X and vertical Y displacement determined with CMV for an effective pixel size of 6.4 μm a) with a D8 diaphragm b) with a D4.5 diaphragm

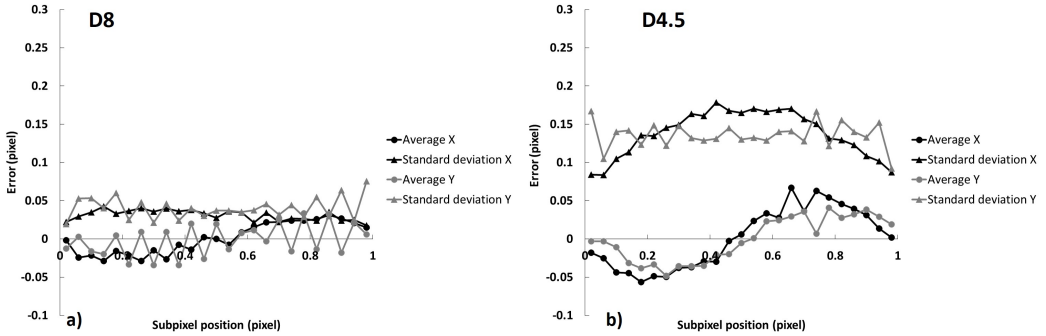

Fig. 5.17.: Systematic (Average) and random (Standard deviation) errors on horizontal X and vertical Y displacement determined with CMV for an effective pixel size of 7.5 μm a) with a D8 diaphragm b) with a D4.5 diaphragm

presented in Figure 5.14a) gives an error comparable to the error for a larger effective pixel, we retain the camera that provides the best resolution and the smallest effective pixel size (4 μm). Note in Figure 5.13 a difference between the random error in the x component of the displacement and of the y one. We have no explanation for this, but we notice that the error is twice as large in the y-direction when expressed in pixels, and is of the same order of magnitude as the other magnifications when expressed in micrometers. Thus, for the same field of view, the random error in the y component of the displacement is overall at least as good as for other magnifications and even better in the x direction. Consequently, we will use a Vieworks monochrome camera with a 151 million-pixel sensor (14192×10640 pixels of $3.76 \times 3.76 \mu m^2$) and a Macro Varon 85 mm optical lens mounted such as to obtain an effective pixel size of about 4 μm to acquire images.

A new error study was conducted with this Vieworks monochrome camera and with a D8 lens aperture, by testing two effective pixel sizes which correspond to taking one image of the whole sample (then the effective pixel size is 6.4 μm) or to divide the sample surface into two images (then the effective pixel size is 4.2 μm). One is not the double of the other

because in the case where we take two images, the two images partially overlap, and also because in that case the camera and therefore also the sensor are turned. The ideal ratio of pixel sizes is $\sqrt{2}$ so that the area ratio is 2 ($\sqrt{2} \times 4.2 = 5.9$ which is almost equal to 6.4). Indeed, working with an effective pixel size of 4.2 μm will give better accuracy, but we have to make sure that the actual measurement error does not get larger than with only one image. Figure 5.18 shows the systematic and random errors in different configuration

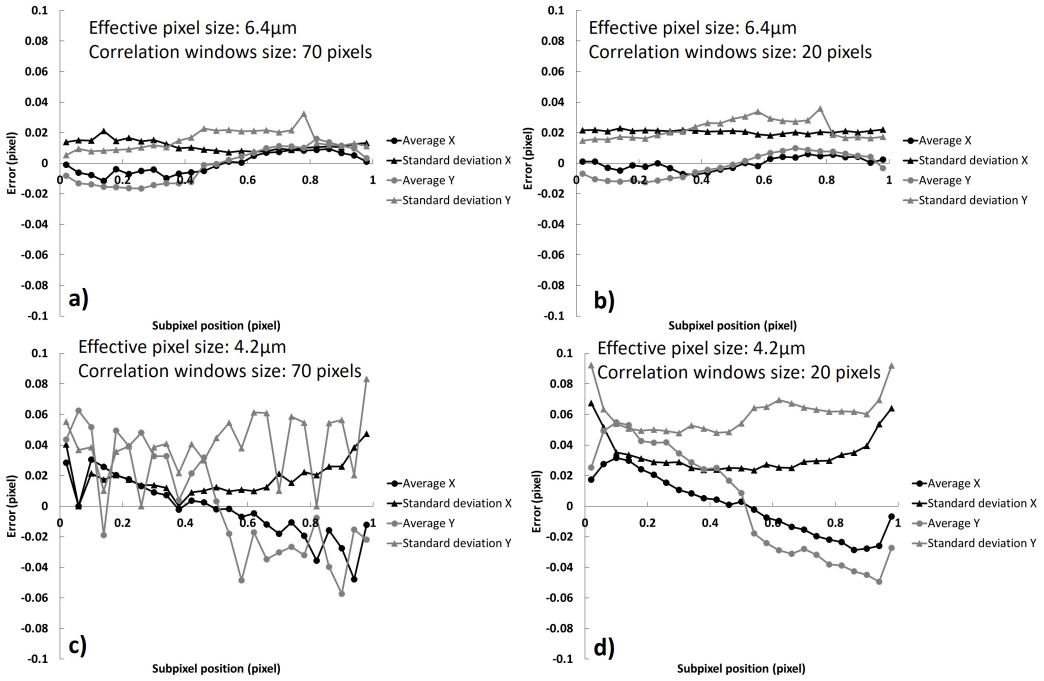

Fig. 5.18.: Systematic and random errors on horizontal X and vertical Y displacement determined with CMV, with bilinear interpolation for a) an effective pixel size of 6.4μm and a correlation windows size of 70 pixels b) an effective pixel size of 6.4μm and a correlation windows size of 20 pixels c) an effective pixel size of 4.2μm and a correlation windows size of 70 pixels d) an effective pixel size of 4.2μm and a correlation windows size of 20 pixels.

of effective pixel size and correlation windows size. It is normal that the error is larger for a smaller correlation window size as a more local measurement is more affected by error than a global measurement. As mentioned in the previous paragraph, the size of the correlation window has an effect on the errors induced by the intrinsic noise of the images on the measured displacement. Increasing the size of the correlation window minimizes the effect of this noise, but at the cost of a lower spatial resolution of the displacement field. It is therefore necessary to find a compromise. It is less obvious for the effect of the effective pixel size, according to the results presented in Figure 5.18, it seems that the error is larger for smaller pixel size, however, the error depends on various parameters: type of marking, optical performance of the lens, surface preparation, focus precision, aperture... Nevertheless, the maximum error in the worst case configuration (see Figure 5.18d)) is

not disproportionately large either. The maximum values of the worst-case systematic and random errors with the smallest correlation window size and smallest pixel size are 0.067 and 0.09 pixels. An analysis of the variation of the random error only as a function of the

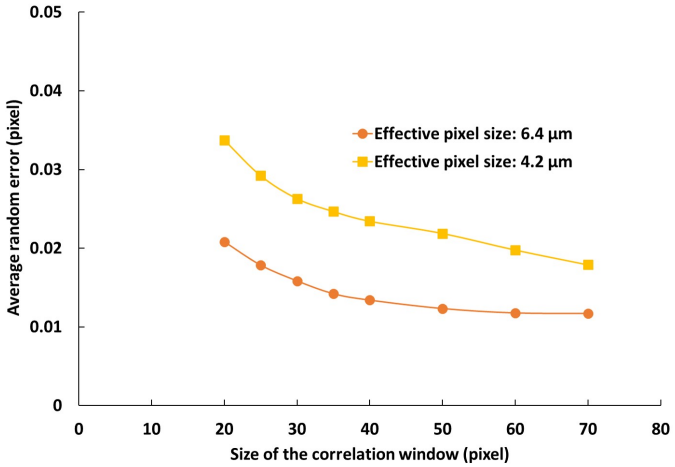

Fig. 5.19.: Average random error in pixel in function of the size of the subset for different effective pixel size.

subset size is given in Figure 5.19 for the two different effective pixel size. As the error is not disproportionately large by using an effective pixel size of 4.2μm this configuration will be used in the experiments. Also, to reduce the error to a minimum, subsets of 58 pixels are retained. Finally, we examined the effect of the interpolation function on the systematic

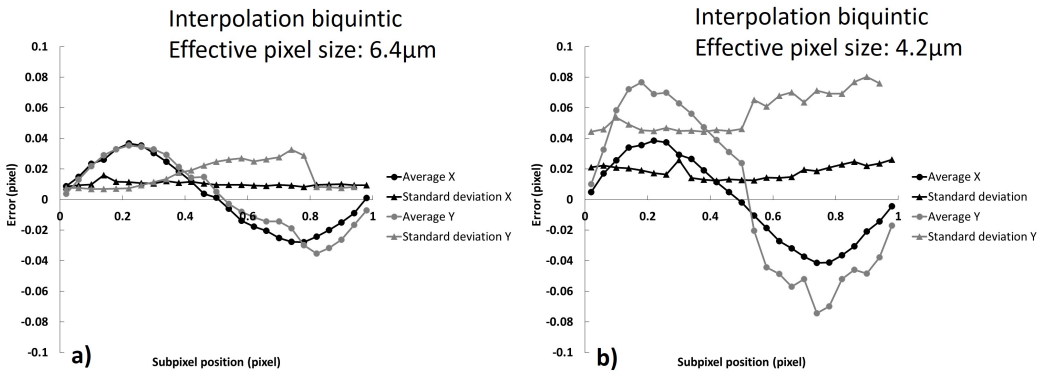

Fig. 5.20.: Systematic and random errors on horizontal X and vertical Y displacement determined with CMV, with biquintic interpolation and a correlation windows size of 20 pixels for a) an effective pixel size of 6.4μm b) an effective pixel size of 4.2μm

error. Figure 5.20 shows that considering biquintic interpolation with an effective pixel size of 4.2μm does not really reduce (it essentially modifies the shape of the error curve, not its amplitude) the systematic error but is more expensive in terms of computation time, that is why in the following we have used a bilinear interpolation.

The error on the displacement propagates to the calculation of the strain tensor. The standard deviation $\sigma(E_{XX})$ of the error on the global deformations in the X direction is given by Dautriat et al., [27].

$$\sigma(E_{XX}) = \sqrt{\frac{2}{N}}\frac{\sigma(u_X)}{L} \tag{5.14}$$

Where $\sigma(E_X)$ is the standard deviation on the global strain in the X direction, N is the number of lines in the measurement grid and L is the distance in pixels between the first and the last column. We apply this calculation of the error on the local component X, calculated on the basis of a 2×2 neighborhood with a step of 58 pixels and $\sigma(u_X) = 0.025$ from Figure 5.19 assuming that the systematic error is smaller.

$$\sigma(E_{XX}) = \sqrt{\frac{2}{2}}\frac{0.025}{2 \times 58} = 2 \times 10^{-4} \tag{5.15}$$

The error on the global component X on a vertical domain of 12000×9000 pixels (the studied area is smaller than the size of the image) which corresponds to about 205×155 correlation windows:

$$\sigma(E_{XX}) = \sqrt{\frac{2}{205}}\frac{0.025}{155 \times 58} = 3 \times 10^{-7} \tag{5.16}$$

This comes to a very small error which will certainly be dominated by other sources of error, notably extrinsic error (for example, the variation of the zoom due to the uncontrolled movement of the camera).

5.4.1 Autofocus procedure

A Vieworks monochrome camera with a 151 million-pixel sensor (14192×10640 pixels of $3.76 \times 3.76 \mu m^2$) and a Macro Varon 85 mm optical lens were used to acquire images. To avoid taking blurry images, the camera movements, whether to focus or to move it along the sample, are driven by two Newport motorized displacement stages with an accuracy of +/-2 μm, as shown on the left image, underneath the camera, in Figure 5.3. These stages are setup on an aluminum tripod structure that supports the weight of the system and reduces vibrations during the displacement of the camera. In order to maximize the resolution, two images are taken, instead of one image of the whole sample. Thus one stage is used to move the camera parallel to the sample to go from the left to the right side of the sample. Another technical difficulty was that during the test the out-of-plane displacement could be such that the sample goes out of the depth of field making the image too blurred and therefore impossible to analyze. In addition, such motions induce magnification variations which superimpose with extrinsic errors on the DIC measurements. Indeed a global relative out-of-plane motion ΔZ of the camera with respect to the sample surface, induces a spurious

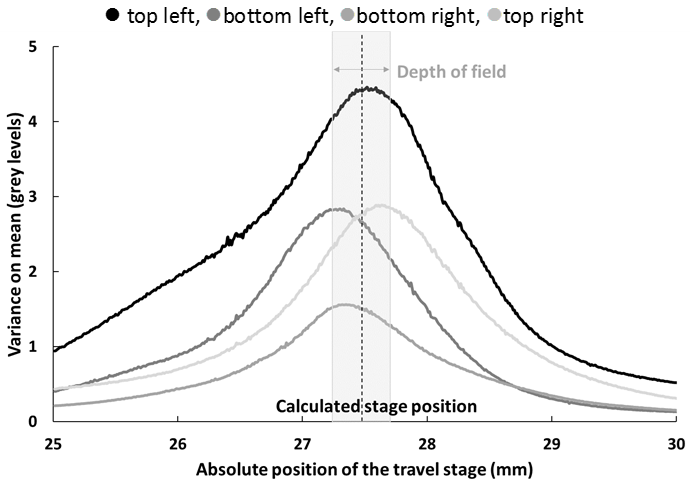

Fig. 5.21.: Variance of gray levels normalized by its mean value as a function of camera movement towards the sample

isotropic strain of $\frac{\Delta Z}{Z_0}$, where Z_0 is the distance between the sample and the optical center of the lens (which is about 170 mm in our setup). An accuracy of better than 10^{-5} ($\frac{\Delta Z}{Z_0} < 10^{-5}$) would thus require to control out of plane motions ΔZ with an accuracy of 1.7 µm. Therefore, the other stage is used to move the camera in the direction perpendicular to the sample and focus accurately the image. The stages are entirely driven by a Labview software which controls both the acquisition of the images of the tested sample, with a magnification and a resolution respectively equal to 1.09 and 4.1μm, and an automated focusing. The focus is optimized by analyzing the variance of the grey level of the pixels in some region of interest normalized by its mean value while the camera is moved forward with an increment of 10 μm (one image per second is recorded). This analysis is made for four regions of interest (size 500×500 pixels) selected on each corner of the middle block. Note that the focus procedure is only performed relative to the middle block, thus, the upper and lower blocks are not taken into account in the process. An example of the curves obtained for the automated focus is shown in Figure 5.21. The curves have a Gaussian form with a maximum corresponding to a sharp image in accordance with the focus of the camera [64]. If the maximum value of each of the four curves are too different, it means that the sample is no longer parallel to the camera. The parallelism between the sample and the camera is considered to be good enough if the biggest difference between the maximums of the four curves is less than the depth of field, because in that case the image of the whole sample is sharp. Before each new image is recorded for the DIC analysis, the camera is moved to the average position of these optimal positions. As shown in Figure 5.21, the focusing accuracy is of the order of 100 µm so that the absolute accuracy on the diagonal strain components is of the order of 10^{-3}. This extrinsic errors is the main limitation of the accuracy of the technique. Local heterogeneities are however not affected by this global,

essentially uniform offset. In addition, deviatoric strains are not sensitive to this error (i.e. ε_{xy} and $\varepsilon_{xx} - \varepsilon_{yy}$ components). As emphasized later, slip discontinuities are not sensitive to such errors either.

5.5 Conclusion

In this chapter, a complete description of the experimental setup is provided. First of all, the objectives of this experimental setup were given. The different components of the setup are described, as well as how to prepare the sample and finally the experimental protocol. The last two sections were devoted to the DIC technique. First a brief presentation of the principle of DIC was made, then the implementation of this measurement technique is described in the context of our experimental setup. The different choices of parameters were presented and argued by evaluating the resulting errors. The analysis presented in this chapter allowed us to retain the following DIC parameters: 4 μm of effective pixel size with a subset of 58 pixels (60 pixels spacing between two subset) and bilinear interpolation, which will then be used in the following chapter which deals, strictly speaking, with the experimental campaign.

Regarding the autofocus, a new procedure is currently under development in the laboratory. Indeed, the problem with the current procedure is that it cannot do anything if the three samples are not well placed, in other words if their three faces are not in the same plane. Moreover, since the procedure is based on the analysis of the middle block only, it does not notice if one of the upper or lower block is out of the plane. The idea would be to perform the focusing from several reference images taken at different distances from the sample. Then the correlation would be optimized on all the images which would allow to chose the optimum correlation coefficient in different planes. This work raised a point to keep in mind in view of the work presented in this chapter: regarding the autofocus it would seem that working with a more open diaphragm and therefore a smaller depth of field would actually improve the results because it is easier to eliminate a clearly blurred image compared to the sharp image. An idea could be to take a larger aperture to facilitate the autofocus procedure, and then switch back to the smaller aperture defined optimal for the DIC in the plane.

6 Analysis and discussion of the experimental results

> *A picture is worth a thousand words. An interface is worth a thousand pictures.*
>
> — **Ben Shneiderman**
> (Professor for Computer Science)

After having presented the experimental setup in chapter 5, we present in this chapter the results of the experimental campaign. Here, local DIC measurements of viscous slip along the fractures are compared to global estimates of the motion of the whole blocks obtained with the LVDTs. A preliminary section is devoted to the numerical modeling of the experiments followed by a discussion to clarify what was measured and how. The preliminary experimental results, which were produced before the complete implementation of the DIC technique, are briefly presented. Then the results of the two creep tests are described along with an analysis and discussion. The two tests are of about the same duration, but one was conducted under constant load and the second under different load levels. The interfaces are subjected to a viscous flow the physical nature of which is potentially different from that of the viscous flow of the rock bulk and this behavior is likely to affect the overall response of the repository structure. The characterization of the underlying flow law is important for a better knowledge of the material, but also to perform numerical simulations at relevant time scales for nuclear waste storage.

6.1 Numerical simulations of the experiment

Considering that the sample is not subjected to homogeneous loading conditions during the test, the measurements correspond to the response of a structure, rather than to the behavior of a material point. Preliminary numerical simulations allow to get a rough idea of the stresses and strains actually experienced by the sample. The 2-D numerical simulations are run with the Finite Element code Disroc, under plane stress conditions. To simplify the calculations, the loading steps are made time-independent, which comes to consider that the loading is fast enough compared to the duration of the test (which also means that

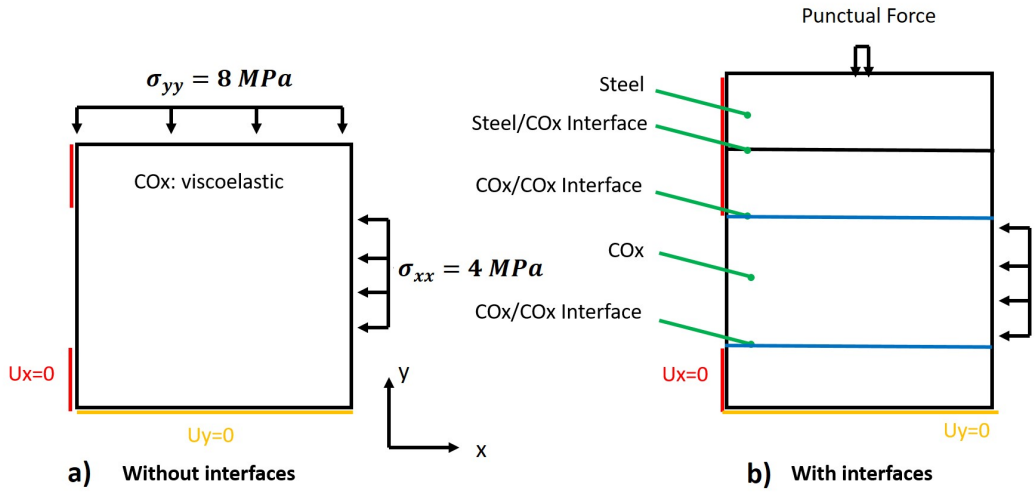

Fig. 6.1.: Schematic representation of the two models used for the numerical simulations. a) The model without interfaces, b) the model that takes into account the interfaces and the steel block through which the normal load is applied.

this calculus is purely elastic). A final step is run in order to simulate the strain field in the sample under constant load after a certain time of creep. The objective of these numerical simulations is to obtain a qualitative idea of the stress and strain fields likely to develop in our sample, given the boundary conditions imposed in our experimental setup. Two simulations, shown in Figure 6.1, are presented in this section. The first one is the most simplified description of the experiment and considers that the three blocks of isotropic COx claystone are perfectly bonded, i.e. ignores the presence of fractures, as illustrated by the scheme in Figure 6.1 a). This model allows us to evaluate the delayed behavior of the sample due to the sole creep behavior of the bulk material. The second more complex model integrates the presence of interfaces, and corresponds to the scheme Figure 6.1 b), This more elaborated model also takes into account the fact that the normal stress is applied through a deformable metal piece which distributes the punctual force over the surface, the steel/COx interface.

6.1.1 Model used in the simulations

In the model, COx claystone is considered as a viscoelasto-plastic isotropic material. The total strain rate is decomposed into the elastic and viscous components:

$$\dot{\varepsilon} = \dot{\varepsilon}^{\mathbf{e}} + \dot{\varepsilon}^{\mathbf{v}} \tag{6.1}$$

The viscous strain rate is modeled by Lemaitre's creep law:

$$\dot{\varepsilon}^{\mathrm{v}} = \frac{3}{2}\alpha\xi^{\alpha-1}\dot{\xi}\frac{\mathbf{S}}{\sigma_e} \tag{6.2}$$

with $\mathbf{S}$ the deviatoric stress tensor, σ_e the Von Mises equivalent stress and $\dot{\xi} = (a\sigma_e^n)^{1/\alpha}$. For uniaxial creep, with a stress σ prescribed from time t=0 on an unstrained sample, the viscous deformation is directly given by $\varepsilon_v(t) = a\sigma^n t^\alpha$. The numerical values of the parameters

Tab. 6.1.: Numerical values of the parameters of COx claystone

Elasticity	Viscosity
$E = 5000$ MPa	$a = 1.5\times10^{-4}\mathrm{MPa}^{-1}\mathrm{day}^{-0.2}$
$\nu = 0.3$	$\alpha = 0.215$
	$n = 1$

considered for the modeling of the rock bulk are given in Table 6.1. The interfaces follow a similar elastic-visco-plastic constitutive relation which relates the normal σ_n and tangential τ stresses to the normal u_n and tangential u_t displacement jumps, already implemented in FEM code Disroc. The total displacement jump rate is given by:

$$\dot{\underline{u}} = \dot{\underline{u}}^v + \dot{\underline{u}}^e \tag{6.3}$$

The displacement vector are related to the stress vector by the joint stiffness rock bulk $\mathbf{K}$.

$$\underline{\sigma} = \mathbf{K}(\underline{u} - \underline{u^v}) \tag{6.4}$$

$$\begin{pmatrix}\tau\\ \sigma_n\end{pmatrix} = \begin{pmatrix}K_t & K_{tn}\\ K_{nt} & K_n\end{pmatrix}\begin{pmatrix}u_t - u_t^v\\ u_n - u_n^v\end{pmatrix} \tag{6.5}$$

with K_n and K_t the normal and tangential stiffness of the joint. Parameters $K_{nt} = K_{tn}$ allow to account for coupled dilatancy effects; in the following they are assumed to be equal to zero. A Lemaitre's creep model is also considered to account for the tangential viscous slip of the joint:

$$\dot{u}_t^v = \alpha\xi_t^{\alpha_j-1}\dot{\xi}_t \tag{6.6}$$

with $\dot{\xi}_t = (b_t\langle|\tau| - \tau_c\rangle^q)^{1/\alpha_j}$. The stress threshold τ_c of the creep law is assumed to be equal to zero here but its existence or not will be further discussed later in the chapter. The values of the parameters of the interfaces are given in Table 6.2. The values used to describe the behavior of the fractures in the numerical simulations have no real physical reality in the sense that they do not result from any calibration on experimental results, but they are a first

Tab. 6.2.: Numerical values of the parameters of COx/COx interface and COx/steel interface

COx/COx interface	COx/steel interface
$b_T = 5.8 \times 10^{-6}$MPa^{-1}day$^{-0.3}$m	$K_t = 0$ MPa/m
q = 1	K_n very large
$\alpha_j = 0.3$	
$K_t = 21200$ MPa/m	
$K_n = 23100$ MPa/m	

order of magnitude used to explore qualitatively the state of stress and strain that can be expected during our tests.

6.1.2 Boundary conditions

The loading steps are simulated independently of time, thus only elastic without development of viscous deformations, then a step of calculation under constant loads by activating the viscosity makes it possible to obtain the strain fields further discussed in the following subsections. The normal stress is applied on the upper face of the top block. In the numerical simulations, a uniform normal stress is applied on the top border, while in the real test the normal stress is generated by a system of lever arms and weight that applies a concentrated force on the upper steel plate which is then transmitted to the sample, and might turn into uniform stresses. This situation is approached in the second loading case. The punctual force is simulated by applying a normal stress equivalent of the 8 MPa normal stress applied over the whole top edge of the sample, only on the sides of two triangular elements located in the middle of the top edge of the steel block. Another normal stress is imposed to the right face of the middle block to provoke the shearing of the interfaces. Again in the real test it is a displacement condition that is actually imposed. The boundary conditions used in the simulations without interfaces are drawn in Figure 6.1a), and the boundary conditions used in the simulations with interfaces are drawn in Figure 6.1b). A vertical compressive stress of $\sigma_{yy} = 8$ MPa, and a horizontal compressive stress of $\sigma_{xx} = 4$ MPa are applied. The vertical displacements are constrained on the bottom edge of the models and the horizontal displacements are constrained on the left edges of the top and bottom blocks.

6.1.3 Simulations without interfaces

Insofar as the behavior of the fractures is *a priori* unknown, we have decided to start the analysis without their presence, by modeling perfectly bonded blocks. Thus, the first simulations regard the most simplified version of the experiment by considering three blocks

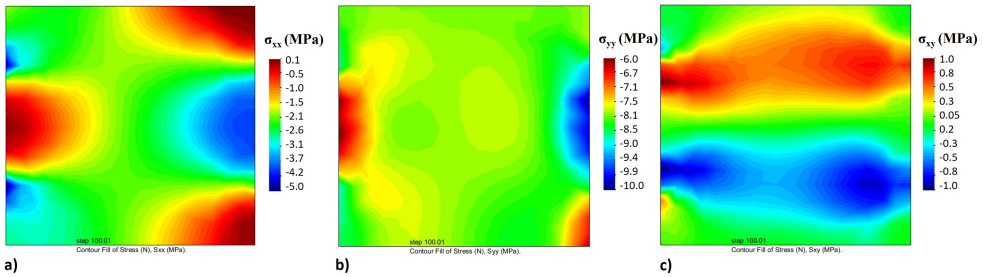

Fig. 6.2.: Simulation of the stress field after 100 days of creep in a sample of COx claystone without interfaces but under the same boundary conditions as the experiment a) σ_{xx} b) σ_{yy} c) σ_{xy}.

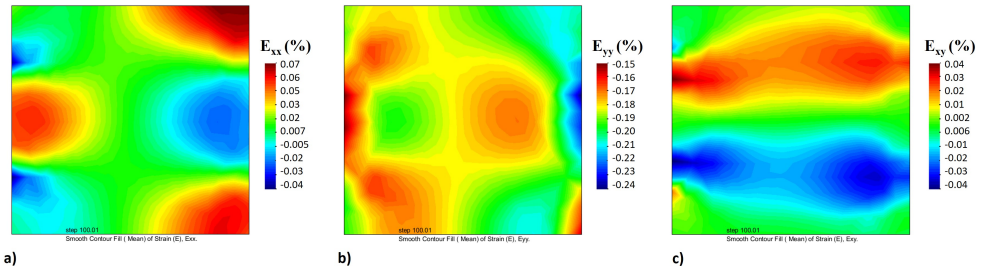

Fig. 6.3.: Simulation of the strain field after 100 days of creep in a sample of COx claystone without interfaces but under the same boundary conditions as the experiment a) ε_{xx} b) ε_{yy} c) ε_{xy}.

of isotropic COx claystone perfectly bonded subject to similar boundary conditions as in our experimental setup. Figures 6.2 and 6.3 gives the three components of the stress and strain tensor in the sample. The stress field is globally heterogeneous, especially on σ_{xx} and σ_{xy} components, mainly due to the complex loading mode which is non-uniform on the lateral face. The spatial distribution of the strain field is very close to that of the stress field, due to the isotropic behavior adopted. We have globally a top/bottom and left/right symmetry, but it is not perfect, because of the mixture between kinematic and static boundary conditions. For example, mixed conditions were applied on the upper and lower blocks: free surface on their right edges and constrained horizontal displacement on their left edges. Similarly, for the top block: Stress is imposed on its top edge while for the bottom block, it is the u_y displacement that is constrained. These small asymmetries induce that the y component also fluctuates around its mean value imposed by the uniform axial loading imposed on the top, and that these fluctuations are not perfectly symmetrical. As a matter of fact, the ε_{yy} strain field shows that even if we put aside the problems of sample placement and contact with the interface, the expected response is not symmetrical. The right side of the sample is slightly more compressed than the left side as shown by the ε_{yy} field measurement in Figure 6.3b). The shear deformation field, however, is rather symmetrical. The ε_{xx} strain field shows a gradient of the deformation, with contraction on the right side of the middle

block and extension on the left side as a consequence of the heterogeneity of the σ_{xx} stress due to the complex loading and the Poisson effect associated with the axial load.

6.1.4 Simulations with interfaces

Secondly, a more complex model that integrates the presence of interfaces is run. In this simulation it has also been taken into account the fact that the normal stress is applied through a metal piece to distribute the force on the surface of the sample. The COx/steel interface is introduced to further investigate whether our experimental boundary conditions achieve the desired stress state in the interfaces or not, the objective being to obtain a stress state as homogeneous as possible in both interfaces. However, a rotation of the rigid metal block may exist. The COx/steel interface is therefore modeled as a perfectly sliding interface (no normal jump and no interfacial shear stress) assuming a perfectly rigid normal stiffness but no tangential stiffness. The bottom contact between the sample and the frame is also in reality a steel/COx contact. However, since the lower block is placed against the frame edge, we consider that this block is sufficiently constrained by the mechanical system, so that it does not rotate. The adopted boundary conditions (u_y= 0 and free u_x) describe then a perfectly sliding steel/COx interface. With this second type of model we have investigated two extreme cases: what happens if the viscous flow of the rock bulk is very important compared to the viscous flow of the interfaces $a = 1000 \times b_t$, or on the contrary if the viscous flow of the interfaces is very important compared to the viscous flow of the rock bulk $b_t = 1000 \times a$. In the first case, the interfaces can slip during elastic loading, but they almost do not slip during creep phase, and the results are very similar to those obtained with the model without interfaces. In this case, the displacements measured at the two ends of the central block are not equal. Numerical simulations in Figure 6.4 show that if the

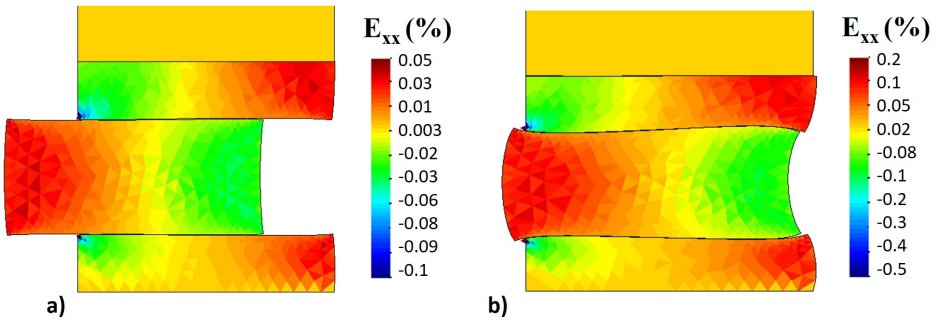

Fig. 6.4.: Numerical simulation, map of the strain field ε_{xx} after 4 days of creep in a sample of COx claystone with interfaces, a) interfaces' viscous flow bigger than rock bulk viscous flow (deformation $\times 100$) b) rock bulk viscous flow bigger than interfaces' viscous flow (deformation $\times 100$).

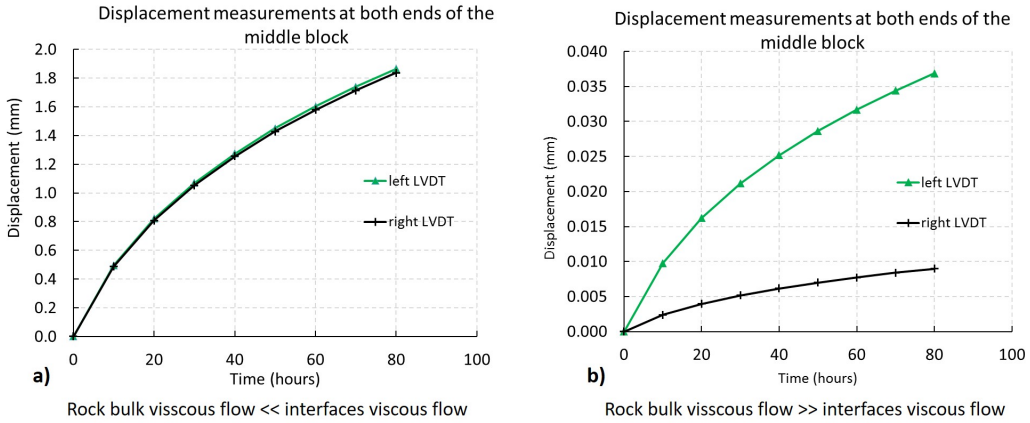

Fig. 6.5.: Displacement measured in both ends of the middle block. Qualitative comparison of the measured displacement depending on whether the interfaces' flow the most or the rock bulk, a) interfaces' viscous flow bigger than rock viscous flow, b) rock viscous flow bigger than interface viscous flow.

interfaces viscous flow is very large compared to the rock bulk viscous flow, then the relative displacement of the lateral faces of the central block due to its distributed deformation in the bulk is negligible with respect to the overall slip of this central block with respect to the upper and lower ones, so that the displacements measured at each of its extremities, shown in Figure 6.5a), are almost the same. However, if the rock bulk has a larger viscous flow than the interfaces, a different displacement is measured on each side of the middle block. Note that these numerical simulations show qualitative trends, as the material parameters are not realistic, the corresponding numerical values have no real physical meaning. The real situation is likely to be in between these two limit cases but the study of the differences between the two LVDTs signals should inform us about the dominance of the interface or the rock bulk creep.

Besides, the stress state and the viscous slip in the interfaces are analyzed considering viscous parameters of the same order of magnitude for the rock bulk and for the interfaces as given in Table 6.1 and in Table 6.2. The shear stress and the viscous slip in the interfaces are presented in the Figures 6.6 and 6.7. Figure 6.6 shows that the shear stress in both top and bottom interfaces is almost identical. The top interface is on one side a little more sheared than the lower one, which may be due to different boundary conditions on the upper and lower edges of the sample. However, it is not quite constant along the interface. The normal stress is qualitatively similar to the shear stress. A part of the left side is slightly unloaded compared to the rest of the interface, which may be due to a slight rotation when the normal stress is applied. Note that the state of stress in both interfaces is almost identical, which suggest that both interfaces are submitted to a similar loading history. Indeed, the simulated viscous slip is the same in both interfaces of the numerical simulation, thus only the results on the bottom interface is plotted in Figure 6.7. The slip is not uniform along the

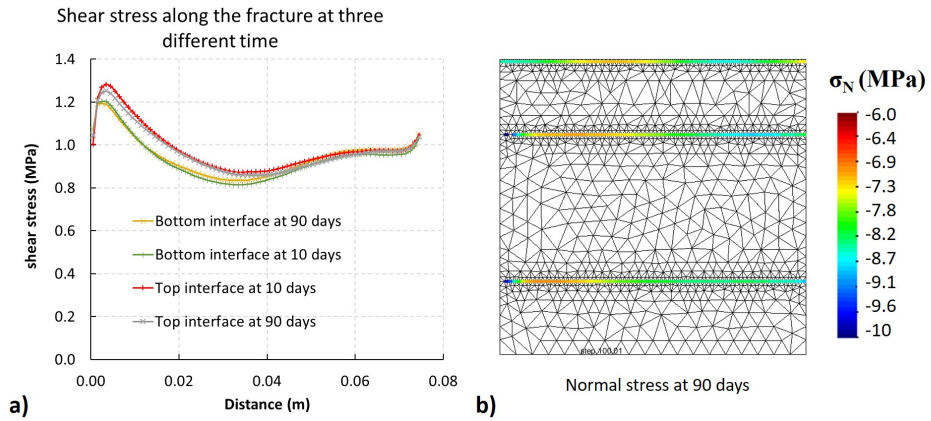

Fig. 6.6.: Simulation of the evolution of the shear stress along the interfaces at 10 and 90 days. a) Shear stress in the top and bottom interfaces, b) Normal stresses in top and bottom interfaces at 90 days.

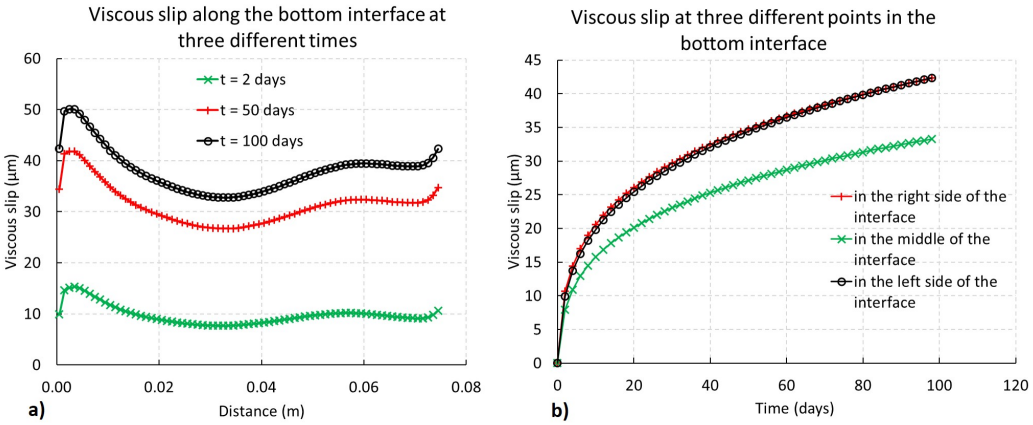

Fig. 6.7.: Viscous slip in the interface resulting from the numerical simulation. a) Graph of the viscous slip along the interface at 2 days, 50 days and 100 days. b) Evolution of the viscous slip during 100 days at both ends of the interface and in the middle.

interface, but it is maximal on the side where the shear stress is maximal, and it is minimal close to the middle of the interface. With DIC, we will be able to measure the viscous slip profile along the interface and see if we observe the same type of kinematics in reality on the interfaces in the COx claystone as in those numerical simulations. The viscous slip does not seem to become more homogeneous over time, quite on the contrary: the viscous slip profile after two days of creep is more homogeneous than after 100 days of creep. However, the viscous slip rate shown in Figure 6.8, becomes uniform along the interface over time, while it was not in the early stage of creep.

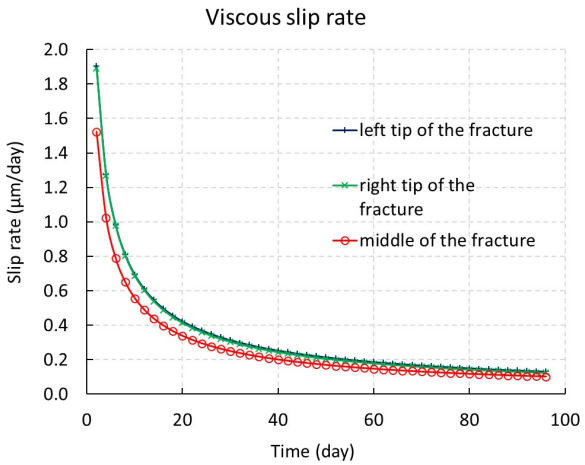

Fig. 6.8.: Plot of the viscous slip rate in the interface in function of the time. The slip rate becomes homogeneous along the interface in time.

6.1.5 Expected strain field

One of the main difficulties in the analysis of the experimental results is related to the understanding of the test sequence in terms of stress and strain in the specimen, as we are dealing with a structure subjected to different loads and asymmetrical boundary conditions. In addition, there are several interfaces that allow or prevent displacements: two steel/COx contacts on the upper and lower faces of the sample, and the two COx/COx interfaces.

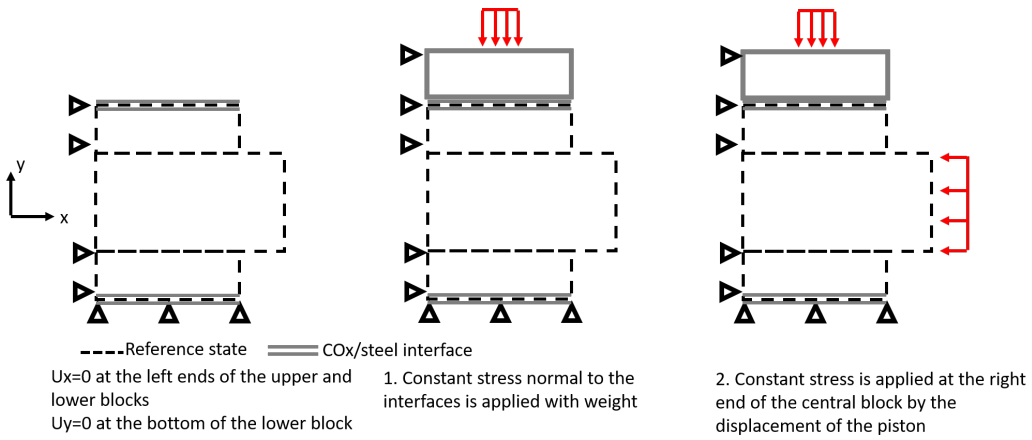

Fig. 6.9.: Schematic representation of the boundary conditions and the loading steps.

Thus, on the basis of the results of the numerical simulations, which provided a qualitative idea of the stress and strain fields experienced by the sample, and doing a thought exercise on what could happen in terms of deformation, a brief summary of the expected strain field in the samples is discussed. In order to help the reading of the experimental results, we have

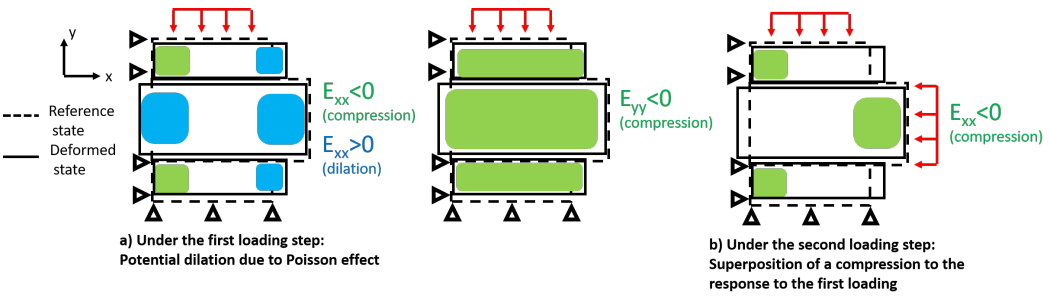

Fig. 6.10.: Simplified scheme of the expected strain field ε_{xx} and ε_{yy} a) after first applying the stress normal to the fractures and b) with the adding effect of shearing the middle block

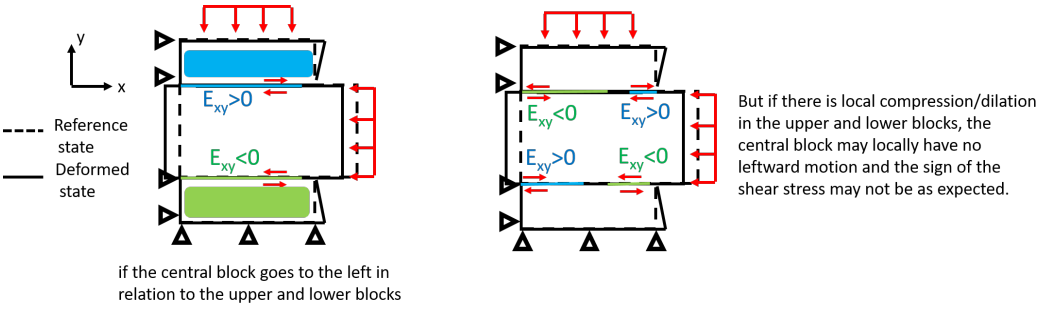

Fig. 6.11.: Simplified scheme of the expected shear stress on the interfaces. The left scheme represents the shear of the interfaces if the central block has a leftward motion as expected while the right scheme represent the shear of the interfaces in the case of more complicated local strain in the different blocks.

represented the deformations likely to develop during the loading (under stress normal to the interface planes and under the shear of the interface). Figure 6.9 recalls the boundary conditions and loading steps experienced by the sample. Obviously, this is only a starting point from which to analyze the real data provided by the experience. Figures 6.10 and 6.11 are only thought to provide a framework to analyze complex experimental results. Regarding the strains that the loading may cause in the specimen, Figure 6.10 illustrates the following possible features:

First under the normal load, due to Poisson's effect, the blocks may expand, along the x-direction. Opening of fractures under the effect of the normal load can also disturb the strain field. In the y-direction the blocks are assumed to be globally in compression.

Second, the horizontal constant stress is applied to shear the interfaces. This loading will probably induce a compression on the right side of the middle block, which will be transmitted to the supports (at the left ends of the upper and lower blocks) through the interfaces. The expected shear strain is represented in Figure 6.11. Globally if the central block is moving to the left with respect to the upper and lower blocks, a positive average shear strain ε_{xy} is expected in the upper block and top interface, and negative in the lower

block and bottom interface. The middle block should undergo an average zero shear strain. As will be shown later in the analysis of the experimental results, the reality may be more complicated than that, especially due to local heterogeneities near the interfaces (existing or apparent cracks, or non-uniform sliding), the distribution of sliding and shear strain on both sides of the interface may be more complex, with even sign inversions with respect to the expected mean value, as shown in Figure 6.11. As represented in Figure 6.11 it is quite conceivable that, if the interfaces are not properly in place, or if a local dilation or compaction happens in the blocks (due to opening or closing of fractures for example), locally the relative movement of the middle block with respect to the upper and lower block will not be leftward.

6.2 Methodology for the analysis of the experimental results

The experimental protocol used for the creep tests and the preparation of the samples have been presented in the previous chapter. Two different sets of experimental results: One creep test under constant normal and shear loads at a same normal load on the one hand, and a test under different levels of shear loads on the other hand, for which the protocol followed allows to draw some conclusions on the viscous behavior of an interface.

The tests will be analyzed by DIC. We recall that at regular time intervals, two images are recorded of the sample surface. Indeed, we explained in the previous chapter that by taking two images, the size of a pixel is 4μm, and the precision of the measured displacement is of the order of a tenth of μm. The principle of DIC was explained in the previous chapter. As a reminder, starting from the definition of reference points, it consists in tracking the homologous points in the successive deformed images based on the recognition of their neighboring pixels (Figure 5.10). The tracking of points from one image to another allows then to deduce the displacement field and then, after post-treatment, the deformation field. Thus, it is possible, in particular, to estimate the slip developed along an interface from the relative displacement between the correlation windows (the size of a correlation window is 58×58 pixels) carefully positioned on the two sides of the interface. In the previous chapter our method to quantify the displacement jump was explained alongside with other method existing in the literature. The perfect positioning of the correlation windows on the two edges of the interface prevents a subset from overlapping two blocks, which would result in a false slip value measurement. Figure 6.12 shows the calculation of the interface slip as well as the sign of the displacement corresponding to a movement of the middle block to the left. In the same way, the compaction of the interfaces will be calculated by measuring the

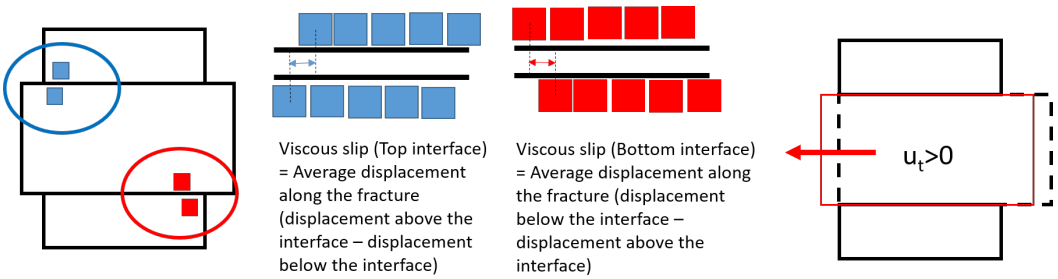

Fig. 6.12.: The slip of the interfaces is calculated from the correlation windows placed above and below the interfaces.

relative displacement in the vertical direction between the two lines of correlation windows located above and below the interface.

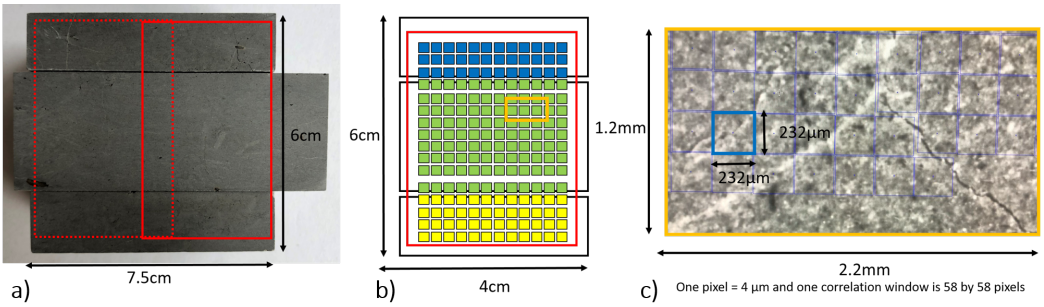

Fig. 6.13.: a) Image of one sample with the two red frames corresponding to the two images taken along the test b) Each image is covered by a grid of correlation windows in support of the DIC technique c) the resolution used for our experiment is such as displacement of the 0.1μm can be tracked.

The use of two images of the sample instead of one provides an improved spatial resolution with a pixel size corresponding to 4 µm on the image and displacements measured at a precision smaller than a tenth of micrometer, however, it must be admitted that it makes the results quite overwhelming. As a matter of fact, for each tested sample the results are divided in four measurements (Figure 6.13): the left and right images, and on each image the top and bottom interfaces. Each image is analyzed with a grid of correlation windows (58×58 pixels, and 60 pixels spacing between two points, which means that two pixels are left between the subset to avoid any overlap), showed in Figure 6.13 b). The top interface is defined by the separation between the blue phase and the green phase, and the bottom interface is defined by the separation between the green phase and the yellow phase. The question of a good contact between the COx blocks also arises, especially at the beginning of the test. In fact, by *good contact* we mean the ideal situation in which the two sides of the interface overlap perfectly and the forces are transmitted as uniformly as possible over the entire interface. A bad contact between the interfaces can possibly oppose the sliding

of the interfaces and induce local compression. By *bad contact*, we mean a contact that is not homogeneous along the interface and thus would induce non-homogeneous normal and shear stress along the studied interface. This bad contact can come from a bad positioning of the blocks, a bad flatness of the sheared interfaces (we remind that the treatment of the roughness of these interfaces is done by hand), or possibly because of the cracks which cross the blocks and which can loosen a part of the interface by leverage effect. In the Figure 6.14

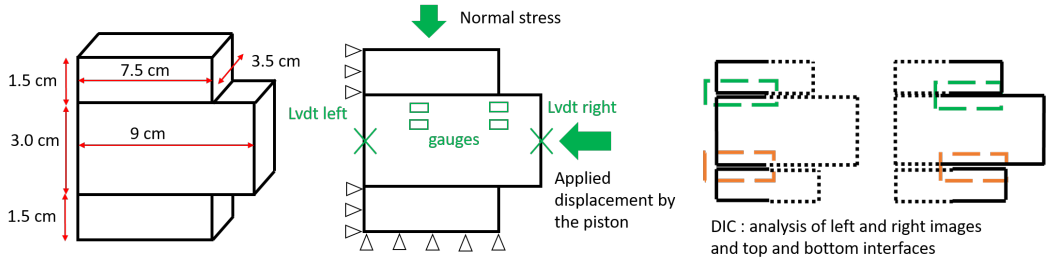

Fig. 6.14.: From left to right: reminder of the dimensions of the samples, boundary conditions and different measurement points on the samples.

three schemes are drawn, from left to right, first the dimensions of the samples are recalled, then the boundary conditions and the different measurement points are represented with the two LVDTs on each side of the middle block, the gauges and the four different slip provided by DIC measurement. With the DIC, we are able to measure very small displacements. Indeed, the LVDT measured in the preliminary tests displacements of the order of ten μm, but we are interested here in displacements which will be even smaller than that (because we want to measure the slip of the interface without the contribution of the deformation of the rock bulk). In our experimental setup, LVDTs measure the coupling between the strain of the rock bulk and the slip of the interfaces, but with DIC we can separate the two quantities. Since DIC allows the measurement of very small displacements, we hope to be able to accurately determine the viscous slip threshold. The results are presented in the following way, first we focus on the global behavior of the sample by looking at the average strain fields of the three blocks of the left and right images, to finally focus the analysis more specifically on the interfaces.

6.3 Results and discussion of the preliminary tests performed with LVDTs only

A first series of tests was carried out with LVDTs only, i.e. without digital image correlation. Direct shear tests have been carried out in order to determine the normal K_n and tangential K_t stiffness of the interfaces, but also the cohesion C and friction angle φ. The displacements

measured by the LVDTs placed on the edges of the blocks also encompass the influence of the deformation of the rock bulk. However, these first values give us a first order of magnitude of the fracture parameters and a point of comparison with the values provided by DIC. Those preliminary tests were performed on sample and sheared surfaces prepared according to the protocol described in the previous chapter. The cohesion and friction

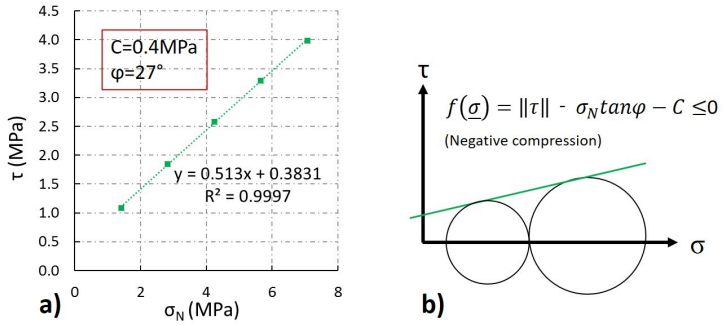

Fig. 6.15.: a) Results of multiple direct shear test conducted under different load to estimate the interface cohesion and friction angle. b) Reminder of Mohr-Coulomb strength criteria

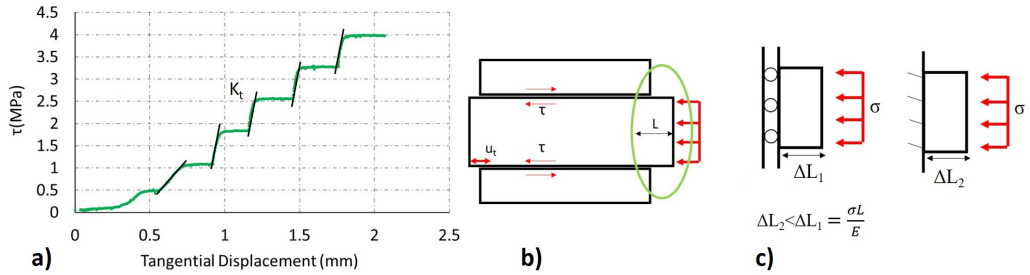

Fig. 6.16.: Estimation of the tangential stiffness of an interface in COx claystone with the horizontal displacement measured with a LVDT placed on the right face of the central block. The displacements measured by the LVDT are 1.5 cm before the beginning of the interface, so the displacement measurement is therefore flawed by the measurement of some deformation of the rock that can be estimated by a quick calculation represented by c). This calculation allows to calculate the deformation of a block in simple compression. Nevertheless, the boundary conditions assumed by the theoretical calculation are not the same as the real boundary conditions (embedding) so our calculation overestimates the error.

angle are measured equal to $C = 0.4$ MPa and $\phi = 27°$ as shown in Figure 6.15. A direct shear test was performed after a 7-day creep test (under $\sigma_N = 4.3$ MPa and $\tau = 1.2$ MPa) to determine the evolution of these parameters. A first series of direct shear test was done directly after creep test, resulting in $C = 0.06$ MPa and $\phi = 27.4°$. Another series was conducted after having removed the gouge layer formed during the shearing of the interface and gave: $C = 0.15$ MPa and $\phi = 27°$.

The normal stiffness was measured by applying increasing weight to the sample while measuring the displacement with a LVDT on top of the sample. The deformation of the rock bulk is however included in the measurements. As such, the data need to be corrected by subtracting for every increment in normal stress $\frac{\Delta\sigma_N L}{E}$ with $\Delta\sigma_N$ the load increment, L the height of the sample and E the Young's modulus of the COx claystone. Bandis et al., (1981) have proposed a hyperbolic law to relate joint closure to applied normal stress (equation 6.7).

$$\sigma_n = \frac{k_0 u_n}{1 + u_n/e} \tag{6.7}$$

When u_n tends to zero the slope of the fit between the normal stress and normal displacement measurements gives the normal stiffness k_0. The slope of the fit between the measurements of normal stress and normal displacement (when u_n tends to infinity), crosses the x-axis, which gives the maximum closure of the interface e. As there are two interfaces in the sample, we find $K_n = 7600$ MPa/m. The tangential stiffness was calculated as the average stiffness under different shear load as shown in Figure 6.16. The fits are made on each slope as the shear stress increases with the tangent displacement (see Figure 6.16a)). Indeed, this measurement also contains the displacement in the x-direction of the rock bulk. The displacement increment due to the 1.5 cm protruding from the middle block is calculated assuming that its behavior can be assimilated to that of a 1.5 cm high block in simple compression. In reality, this calculation overestimates the error because the condition of support at the base of the block in a simple compression test is a simple support (the displacement in the direction of the applied load is inhibited), but here the base of the block is embedded in the continuation of the middle block (Figure 6.16). For a normal stress maximum equal to 20 MPa the induced error in displacement $\Delta L = \frac{\sigma L}{E} = \frac{20\times0.015}{5000}$ is of 6×10^{-5} m for a measured displacement of 10^{-2} m. Thus, the error is assumed to be negligible. The tangential stiffness is estimated at 21 200 MPa/m.

6.4 Multilevel creep test

The choice was made to perform a multi-level stress test in order to obtain information on the dependence of the creep behavior on the shear stress level. By going through different stress levels, the test can also assess the existence of a creep threshold.

6.4.1 Description of the different creep stages

The multilevel test was performed under a 40 kg load on the interfaces, which is equivalent to a normal stress of 7.6 MPa through the lever arm system. The sample is subjected to

constant shear stress in several steps over time, each step, corresponding to a certain level of shear stress, was held for at least three days, after which the piston was set to the next step. The creep test is preceded by a direct shear test in order to determine the value of the peak shear stress of the sheared surfaces (which is equal to 21 kN of force applied by the piston which corresponds to 4.6 MPa shear stress), subsequently, the following shear steps were applied to the sample: 20% of peak stress, 40% of peak stress, 60% of peak stress and 80% of peak stress, then again 60% of peak stress and 40% of peak stress. During the phases of decreasing shear stress, the creep of the interface is preceded by a stress relief. The measurements of the LVDTs located on both sides of the sheared block, and the stress path followed during the experiment are presented in Figure 6.17. Each stress level will be analyzed separately from the other. This approach is chosen only to facilitate the DIC analysis, without forgetting that the steps preceding the analyzed step have a certain influence on the displacement and the deformations then measured. Figure 6.17 shows the

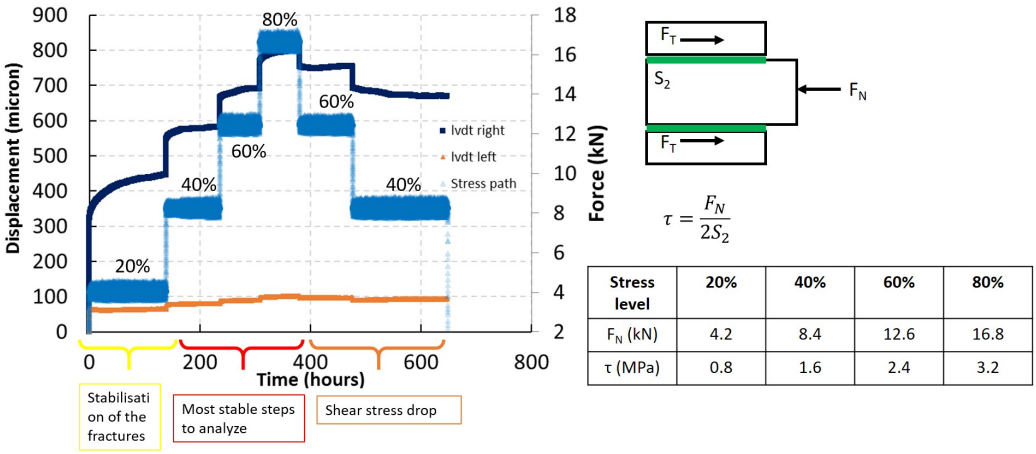

Stress level	20%	40%	60%	80%
F_N (kN)	4.2	8.4	12.6	16.8
τ (MPa)	0.8	1.6	2.4	3.2

Fig. 6.17.: Graphs of the displacements measured by the LVDTs on each sides of the sheared block and stress path. The analyze of the test is principally focused on the steps during which the interfaces have the most stable behavior (40%, 60% and 80%).

macroscopic displacement measurements obtain with the left and right LVDTs. Note that the left LVDT measures very small displacements compared to the right LVDT, suggesting that the interfaces have slipped only slightly but the rock bulk has deformed significantly. DIC only measures the differences in displacement between two images, so the choice of the reference image conditions the measured physical phenomena. For the analysis of the results, the slip and strains measured by DIC are plotted under two different assumptions. (1) In one case, the beginning of the loading phase is taken as reference, i.e. the shearing of the blocks until the prescribed force is reached is included in the measurement. In the other case, the measurement start once the prescribed force is reached. (2) The second hypothesis comes to analyze the fracture behavior under creep hypothesis (under constant loading). It is under the second assumption that we have calibrated the parameters of the viscous

law. Practically the images are taken every 10 minutes so to measure the total slip, which means including the loading phase, the image that was taken the closest to the change of loading (before or after) was set as reference. The idea is to measure all the loading phase, which only lasts about 20 minutes for the first stress level and only about 10 minutes for the following stress level, by moving the actuator at 0.01mm per minute. In the other case, where the focus is chosen on the viscous displacement, the image set as reference is the first image taken after reaching the prescribed stress level for. The important thing in this case is to take an image recorded after the prescribed force has been reached, as a reference image. The two hypotheses are illustrated in the Figure 6.18 as well as the times corresponding

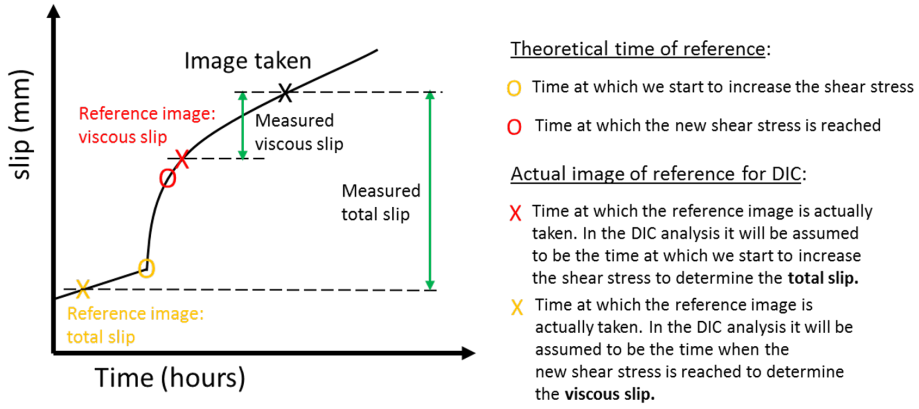

Stress level	20% τ^{pic}	40% τ^{pic}	60% τ^{pic}	80% τ^{pic}
Beginning of the shearing	25/01/22 14:06:42	31/01/22 08:45:58	04/02/22 10:09:51	07/02/22 10:32:21
Picture of reference (Right)	14:04:48	08:37:59	10:02:48	10:25:06
Picture of reference (Left)	13:59:48	08:42:59	10:07:49	10:30:06

Stress level	20%τ^{pic}	40% τ^{pic}	60% τ^{pic}	80% τ^{pic}
Reach of the stress level	25/01/22 14:27:25	31/01/22 08:56:30	04/02/22 10:19:31	07/02/22 10:42:11
Picture of reference (Right)	14:34:47	08:58:02	10:22:50	10:45:06
Picture of reference (Left)	14:29:48	09:03:02	10:27:50	10:50:05

Fig. 6.18.: Definition of the two different hypothesis considered to analyze the slip of the fractures.

to the recording of the images. The time schedules show that the first loading step last 20 minutes while the three other stress step were reached in 10 minutes. Bear in mind that there is a 5-minute delay between the data collected on the left side of the sample and the data collected on the right side of the sample.

The sample is analyzed at different scales. LVDTs give macroscopic measurements at the whole sample scale, while DIC gives microscopic information at the interface scale. As a matter of fact, while the LVDTs on each side of the sheared block gives an idea of the average strain of the block coupled with the slip of the interfaces, DIC provides both global strain field on the whole sample, and more local information such as the slip of the interfaces. In other words, LVDTs give a mixed measurement of bulk strains and fracture

slip, while DIC enables to separate the two physical quantities. Image are taken every 10 minutes in each side of the sample. This comes to make about 1000 images from each stress level, and each image is worth 150 Mb. Each image is analyzed by 33600 correlation windows and we remind that each analysis must be done twice, once with the left images and once with the right images. Analyzing so many images would take too much time, especially since the analysis is partly done manually. When the displacements are too large, the software is not always able to place the correlation windows and it is necessary to place the correlation window manually. The high resolution camera allows access to an incredible amount of information, but the computer management of such images quickly becomes a real challenge. Nevertheless, the Navier laboratory teams are used to working with heavy data, as they work with a tomograph. In order to enable the treatment of the images, the number of actually treated image needs to be reduced. Hence, for each stress step, the images are picked so that each image corresponds to an equal increase in the displacement measured by the *right LVDT*. We use the right LVDT because it is the one that measures the largest displacement. With such a procedure, we end up with about 100 images that describe best both the loading stage and the creep phase. The results of the multistage test are presented in the following section. Different curves and strain maps are highlighted in this section to support our arguments, but to avoid making the section too heavy all the data are not systematically shown for each stress level. The DIC produces local displacement measurements. Indeed, we have seen in the previous chapter that sub-pixel measurements can measure displacements smaller than the tenth of a micrometer. However, what we are interested in here is the behavior of the whole interface, so we can return to a more global information by aggregating the correlation windows and thus analyze the average slip along the interface. The Figures 6.19, 6.20, 6.21 and 6.22 show the macroscopic displacements

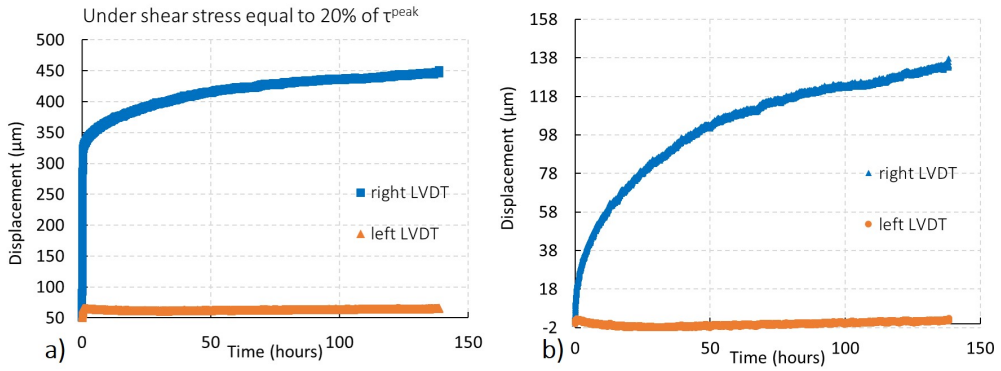

Fig. 6.19.: Left and right displacement measured with the LVDTs at each end of the sheared block under 20% of peak stress a) with the shearing phase before reaching a constant shear stress b) displacement from the point where constant shear stress is reached.

measured on both sides of the middle block by the two LVDTs for all loading levels. The difference in the measurements of the two LVDTs suggests a significant amount of rock

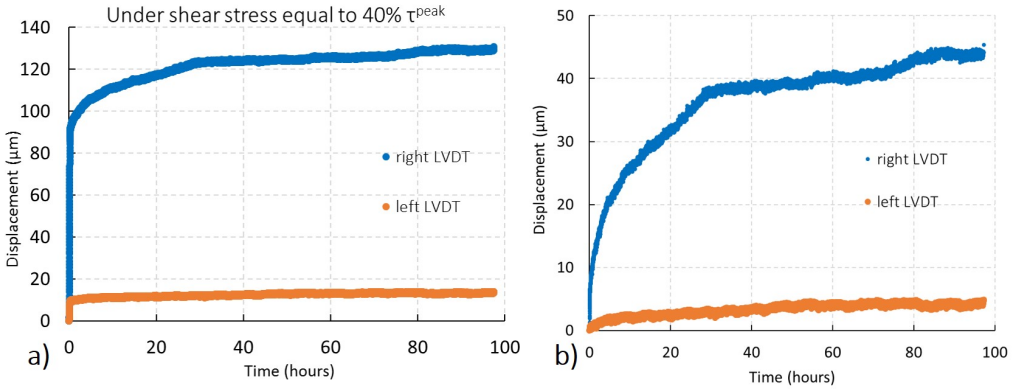

Fig. 6.20.: Left and right displacement measured with the LVDTs at each end of the sheared block under 40% of peak stress a) with the shearing phase before reaching a constant shear stress b) displacement from the point where constant shear stress is reached.

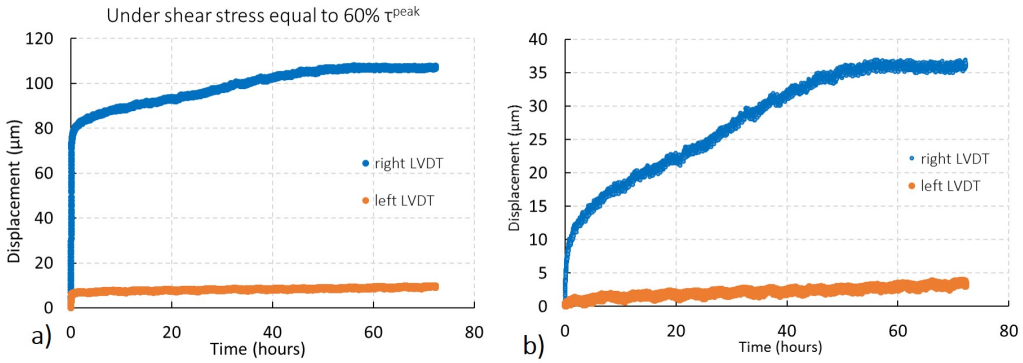

Fig. 6.21.: Left and right displacement measured with the LVDTs at each end of the sheared block under 60% of peak stress a) with the shearing phase before reaching a constant shear stress b) displacement from the point where constant shear stress is reached.

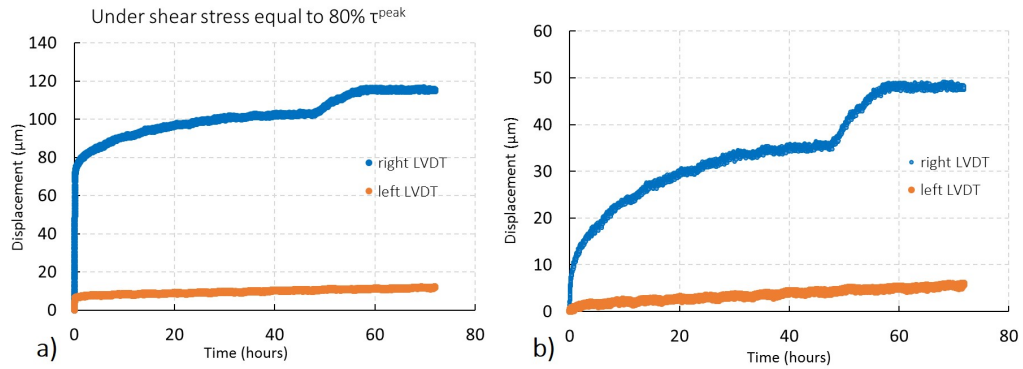

Fig. 6.22.: Left and right displacement measured with the LVDTs at each end of the sheared block under 80% of peak stress a) with the shearing phase before reaching a constant shear stress b) displacement from the point where constant shear stress is reached.

bulk creep in the experiment, and little or no slip along the interface during loading. It is again the rock bulk that undergoes the deformation, but we see that this is less true at higher stress level: the displacement measured by the left LVDT increases with the increase in shear stress. Strain gauges were placed on one side of the central block to measure the

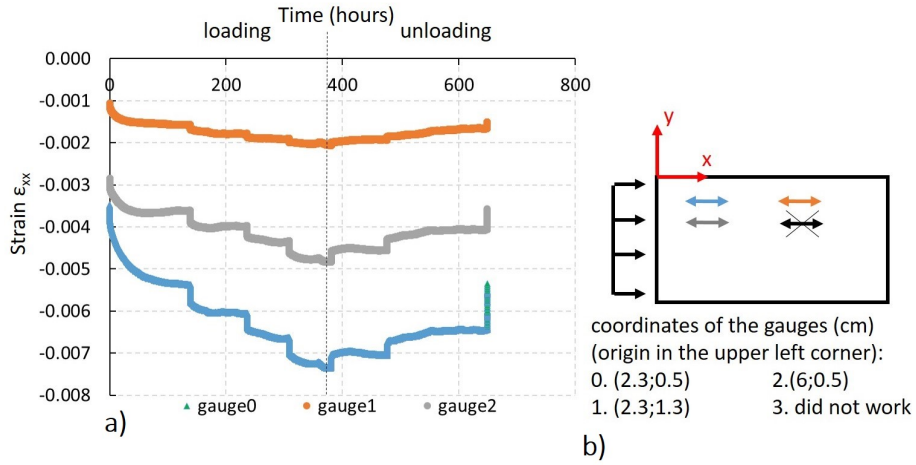

Fig. 6.23.: a) Plot of the total axial strain ε_{xx} measured by three gauges, for the duration of the experience. Negative values show a compression. b) Location of the gauges on the central block.

horizontal deformation. The exact position of the gauges is shown in Figure 6.23. Overall, the gauges show that the central block is in compression during the test, as shown in Figure 6.23. This compression is not uniform, the gauges measure a gradient of the deformation ε_{xx}, with a more important compression at the top of the block and on the side where the force is applied. The measurements of the gauges can be compared to the average strain measured by the LVDTs by the end of each loading steps. The average strain of the block is given by:

$$\varepsilon_{xx} = \frac{\Delta u}{L} = \frac{\mathrm{LVDT}^{\mathrm{right}} - \mathrm{LVDT}^{\mathrm{left}}}{L} \tag{6.8}$$

The average strain at the end of each stage is calculated from the displacements measured by the LVDTs (Equation 6.8). It is found that $\varepsilon_{xx}^{20\%} = 0.0043$, $\varepsilon_{xx}^{40\%} = 0.0013$, $\varepsilon_{xx}^{60\%} = 0.0011$ and $\varepsilon_{xx}^{80\%} = 0.0012$ which is consistent with the measurements provided by the gauges.

20% of peak stress stage

The first loading stage is the most difficult to analyze, since we suspect that the interfaces were not perfectly in contact yet. It is this stage that is most susceptible to manual placement errors. Moreover, the overall response of the rock bulk and the interfaces is disturbed by the opening of fractures under the vertical loading of the sample followed by the closing of

those same fractures by the displacement of the actuator. Thus, probably many mechanisms are at work which may mask the viscosity that is assumed to be very low at these load levels, making it difficult to draw any conclusions regarding the general behavior of the interface.

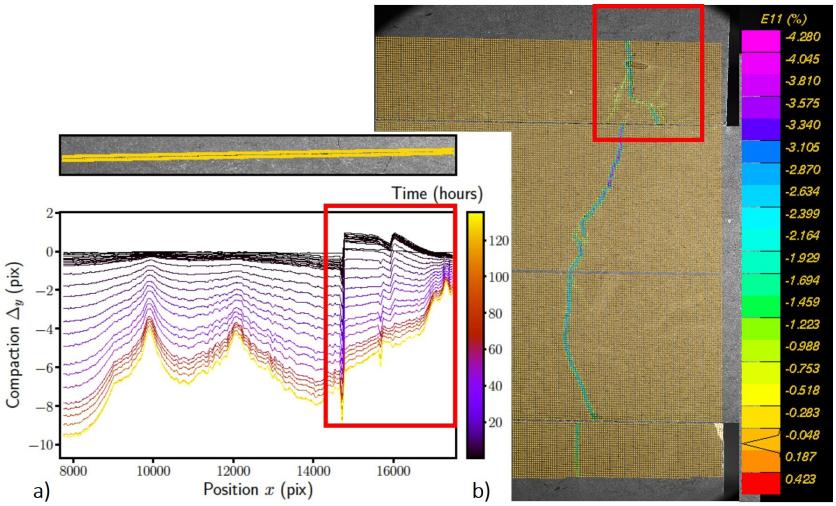

Fig. 6.24.: a) Plot of the compaction along the top interface on the right side of the sample b) Total deformation ε_{xx} plotted at the end of the first stress level of 20% of peak stress, showing the closure of a fracture in the sample

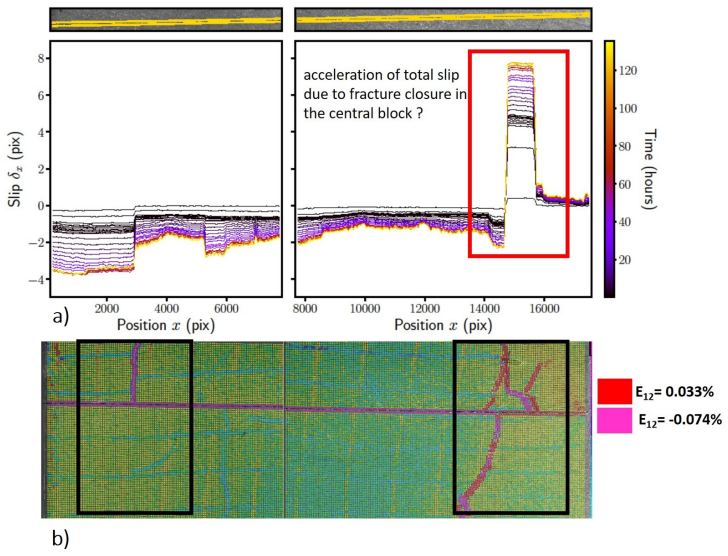

Fig. 6.25.: Profile of the total slip in the top interface during the first stress level of 20% of peak stress.

In Figure 6.24, the image of the right side of the sample shows that the global behavior of the sample is disturbed by the closure of a fracture (in green) that crosses the whole surface

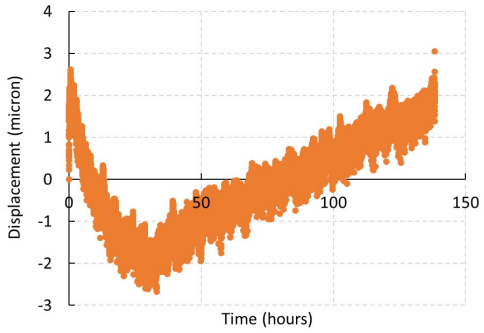

Fig. 6.26.: Displacement during the 20% of peak stress stage measured by *left LVDT*.

of the sample, note that this fracture is only on the surface and does not completely cross the blocks. Besides the compaction of the top interface also plotted in the Figure 6.24 shows a local decompression framed in red (the black lines in the profile of compression). This is evidence that the normal load is not correctly transmitted to part of the upper interface located on the right of the top interface. Moreover, the total slip profile along the top interface in Figure 6.25 shows a negative slip along the part of the interface that is located at the left of the vertical fracture. This can be due to the fact that the horizontal force would not be completely transmitted to the part of the middle block located after the vertical fracture, certainly absorbed by the closing of this fracture. The acceleration of the interface slip at the fracture is explained by a relative leftward displacement of the middle block with respect to the upper block due to the closure of the fracture in the middle block. The fact that the top interface appears to slip in the wrong direction (negative slip indicates that the relative motion of the middle block compared to the top block is to the right) is confirmed by the total shear strain at the end of the loading step being negative in Figure 6.25. This can be explained by a slight unloading of the interface causing the interface to relax or by a more complex mechanism in the sample resulting in a relative displacement of the middle block compared to the top block toward the right. Note that Figure 6.26 shows that *left LVDT* also measures a displacement of the central block that goes to the right and not to the left, which indicates that it is not only a problem of bad contact of the interface, but it is in fact at the scale of the whole middle block that a movement towards the right is observed, while we recall that the actuator prescribes a movement towards the left. The Poisson effect (related to the creep) could explain the relative movement of the middle block compared to the top block towards the right. However, the block is globally in compression and not in expansion.

Figure 6.27 shows that the strain field, especially around the top interface, is much more complex than expected. The viscous strain field ε_{yy} is rather homogeneous in the center of the middle block, but discontinuous at the vicinity of the interfaces. As an explanation for

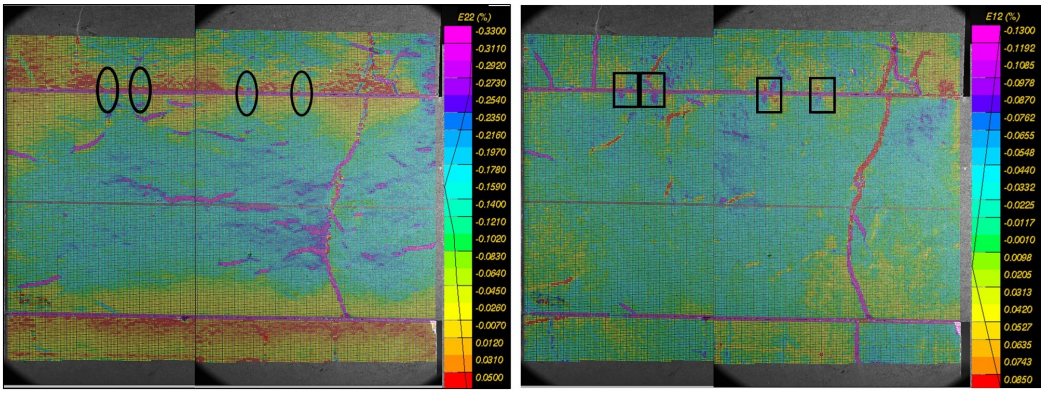

a) b)

Fig. 6.27.: a) Map of the viscous ε_{yy} strain field at the end of the 20% of peak stress stage. b) Map of the viscous ε_{xy} strain field at the end of the 20% of peak stress stage. It is the viscous strain field as the reference image is the image taken as the force has been reached. Points of continuity of viscous deformation ε_{yy} are circled in black which seem to be related to cross patterns of viscous deformation ε_{xy} framed in black.

these discontinuities on the bottom interface, one can mention a phenomenon of dilation caused by the sliding on this interface. It is possible that the contact between the lower COx block and the frame prevents the deformation of this lower block, however, deformation that becomes possible again at the passage of the bottom interface: Hence the discontinuity. What happens around the top interface is again more difficult to interpret. Points of continuity of viscous deformation ε_{yy} are circled in black in the Figure 6.27 a) which seem to be related to cross patterns of viscous deformation ε_{xy} framed in black in the Figure 6.27 b). The deformation continuity can be seen as slip-free contact points with shear stress concentration (proportional to ε_{xy}). In view of these uncertainties, it has been decided, for the rest of the analysis, to leave aside the data brought by this loading stage considering that we are not able to separate in the measurements the different mechanisms that took place.

6.4.2 Analysis of stress level 40%, 60% and 80% of the peak stress

Before going further into the details of each of the three loading levels, Figure 6.28 shows that globally the viscous behavior of the interfaces tends to become more homogeneous, during the test. Which means that the left and right part of the top and bottom interfaces almost equal viscous slip. Finally, the four part of the interfaces have an almost uniform response of the interfaces for the 80% stress level. It is rather the proof of the good progress of the test. Note also that the order of magnitude of viscous slip remains the same under the different loads. The viscous slip is much smaller than the displacement measured by the LVDTs, about 1 μm measured by DIC by the end of the stress step, while the displacement measured by the *right LVDT* is about 50 μm. The difference between the LVDTs and DIC

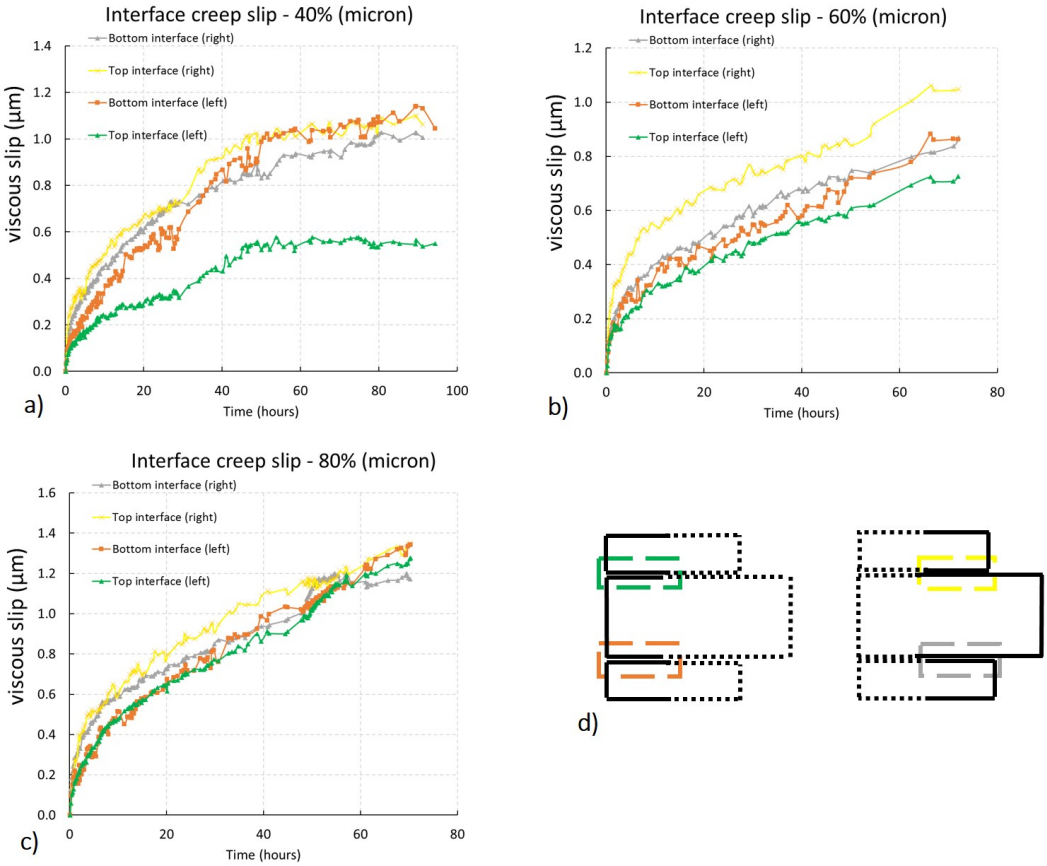

Fig. 6.28.: Average viscous slip measured in the top and bottom interfaces from left and right images in the three stress level a) 40% of the peak stress b) 60% of the peak stress c) 80% of the peak stress.

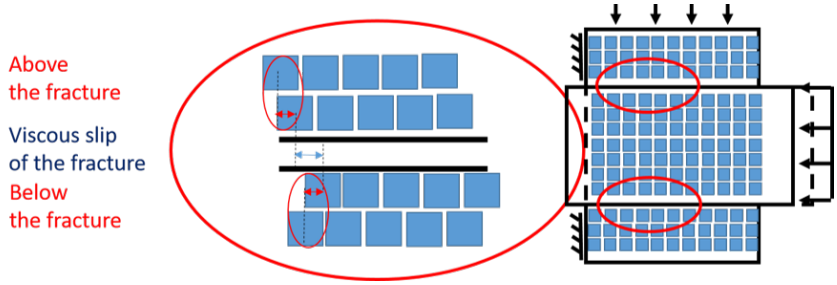

Fig. 6.29.: Calculation of the *bulk slip* at the vicinity of both interfaces. The slip of the interface is compared to the slip that would be measured between any two lines of correlations windows in the rock bulk. Indeed, the relative displacement of the blocks between two correlation window lines corresponds to a slip which is related to the elastic deformation of the blocks. The larger the correlation windows, the more important this *apparent strain-induced slip* is. Thus, the slip measured at the interfaces corresponds to the sum of this *apparent strain-induced slip* and the real slip along the interface. The calculus is done with the two lines of correlation windows, above and below the interfaces.

measurements is not at all surprising. Indeed, one expects to measure a larger displacement with LVDTs than with DIC because LVDTs actually measure the addition of the slip on interfaces and the deformation of the rock bulk, whereas with DIC one isolates the former. Furthermore, based on the numerical models presented at the beginning of the chapter, we infer from the difference in measurements between the right and left LVDTs that the creep of the rock bulk is not negligible compared to the viscous slip along the interfaces.

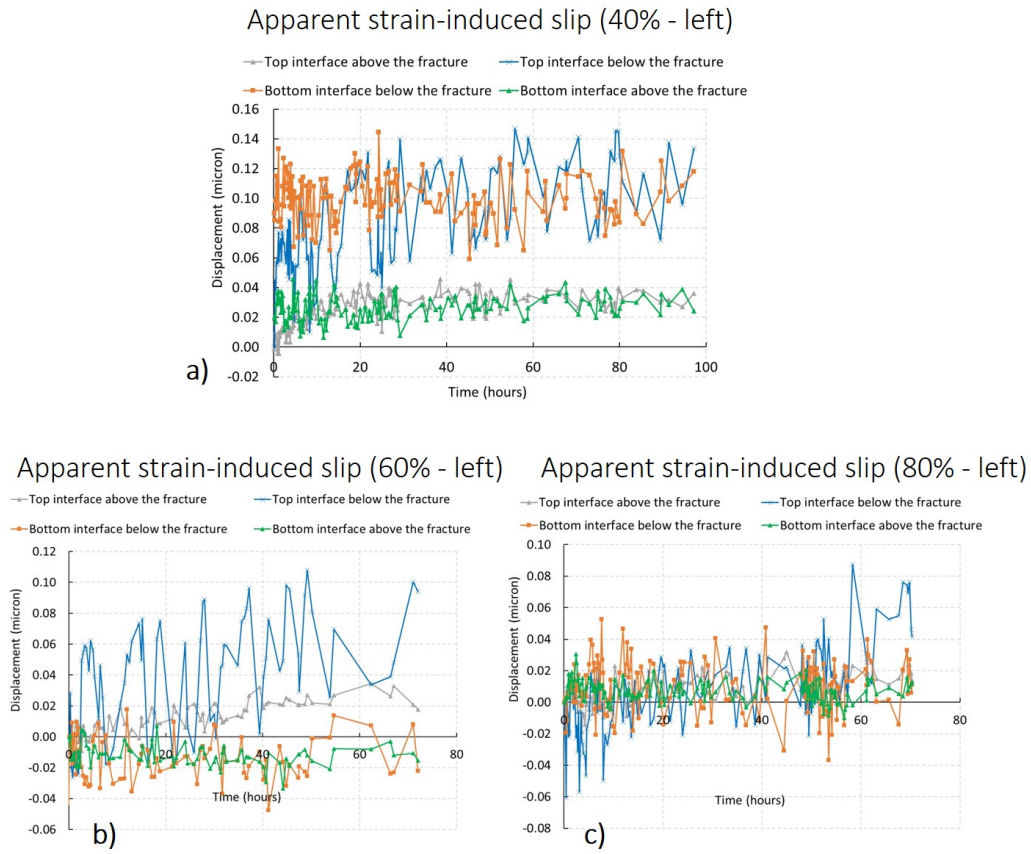

Fig. 6.30.: Apparent strain-induced slip calculated on the rows of correlation windows located above and below the two interfaces in the left image. a) For the 40% stress level, b) for the 60% stress level, c) for the 80% stress level

However, we measure very small viscous slip. Thus, one could start by wondering if the measured slip is not an apparent strain-induced slip coming from the deformation of the rock bulk. Indeed, the relative displacement of the blocks between two correlation window lines corresponds to a slip which is related to the elastic deformation of the blocks. The larger the correlation windows, the more important this *apparent strain-induced slip* is. Thus, the slip measured at the interfaces corresponds to the sum of this *apparent strain-induced slip* and the real slip along the interface. However, it is possible to estimate this apparent strain-induced slip. This displacement has therefore been calculated according to the scheme

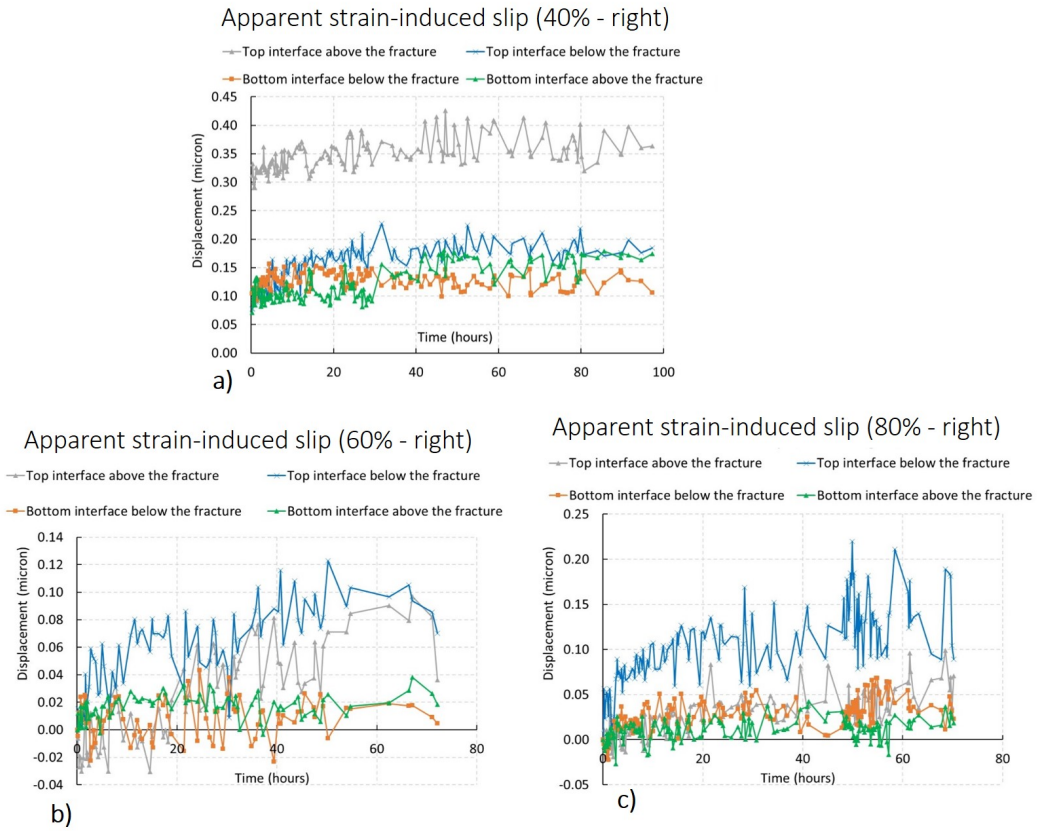

Fig. 6.31.: Apparent strain-induced slip calculated on the rows of correlation windows located above and below the two interfaces in the right image. a) For the 40% stress level, b) for the 60% stress level, c) for the 80% stress level

presented in Figure 6.29. The results are plotted in Figure 6.30 for the left images and in Figure 6.31 for the right images. This apparent strain-induced slip has the shape of noise, and is indeed smaller than the viscous slip.

40% of peak stress stage

Figure 6.28a) shows that the left side of the top interface behaves differently than the right side of the top interface, which itself behaves similarly to the left and right sides of the bottom interface. We try to see if the overall behavior of the specimen can provide an explanation for this difference in viscous slip on the upper interface. Figure 6.32 shows that the average total strain, is rather constant over time. At least, this shows that the viscous behavior of the rock bulk has stabilized. Moreover, the total strain ε_{xy} plotted in Figure 6.32c) is rather symmetrical between the upper and lower blocks of the two images. There is just an oddly large shear strain on the right side of the middle block. However, the viscous strain ε_{xy} presented in Figure 6.33 shows that the top interface and more particularly its

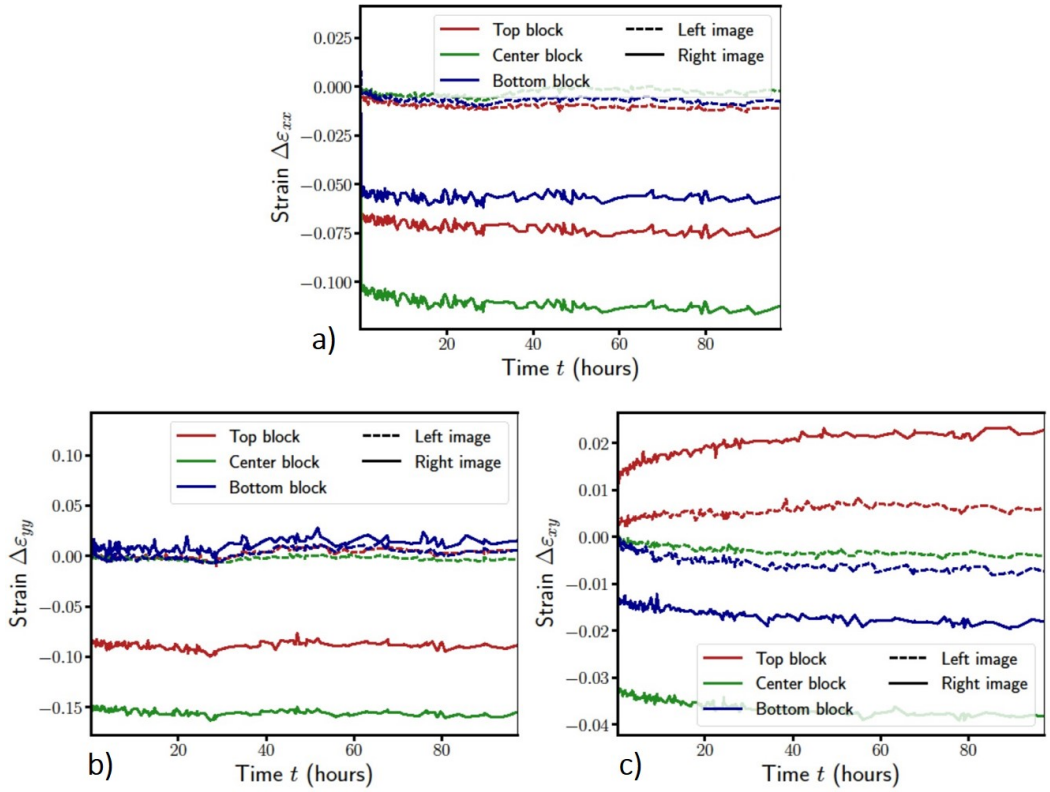

Fig. 6.32.: Average total strain field in the three blocks of left and right images for the 40% stress level a) ε_{xx} b)ε_{yy} and c) ε_{xy}

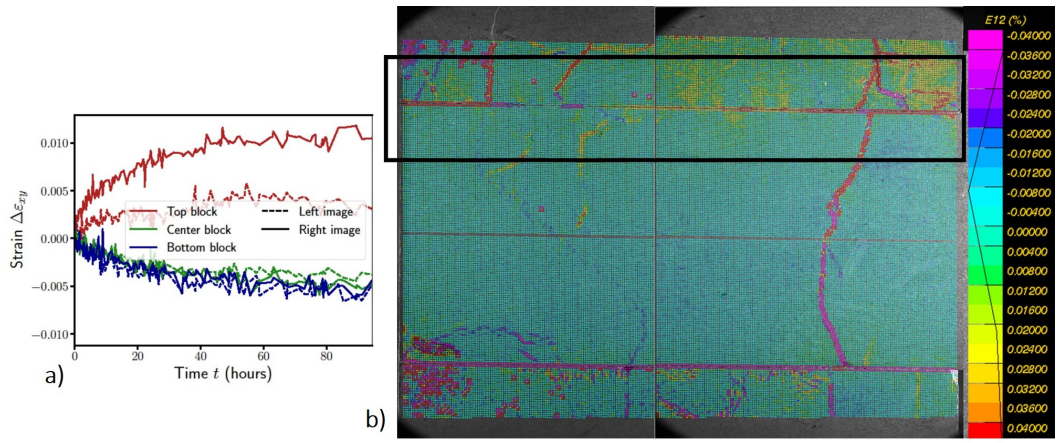

Fig. 6.33.: a) Average value of the creep strain ε_{xy} in each block at the end of the 40% of peak stress step, b) map of the creep strain ε_{xy} obtained with DIC.

left part does not have a homogeneous strain at all, indicating perhaps that it is not yet completely set in place. As a matter of fact, if the shear strain would have been homogeneous along the interface, the top interface framed in black in Figure 6.33 would have been a red line.

60% of peak stress stage

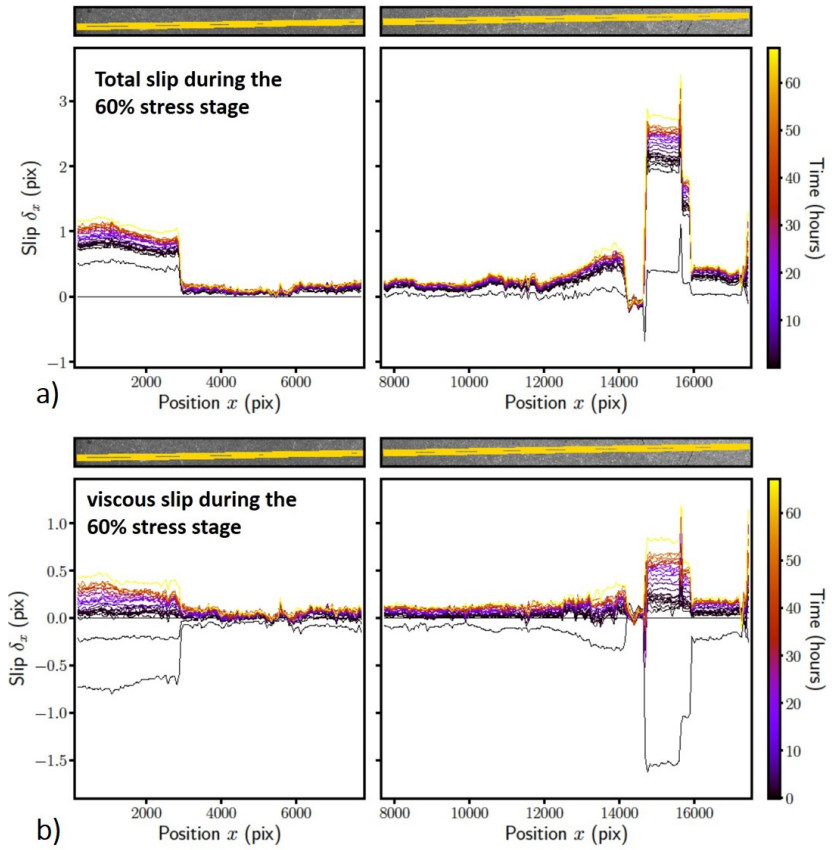

Fig. 6.34.: Plot of the slip profil along the top interface under 60% of peak stress. a) Total slip, b) Viscous slip

Regarding the next stage, loaded at 60 percent of the τ^{peak}, the top interface of the sample seems to have a more stabilized behavior than in the previous stress level. By *more stabilized* we mean that it is less affected by the closure of other fractures and thus the interface has a more homogeneous behavior. As a matter of fact, by comparing the profile of the total slip and the viscous slip in the top interface (which are respectively presented in Figure 6.34a) and Figure 6.34b)), it can be noticed that the two fractures framed in black in Figure 6.25 that were disturbing the slip of the top interface, seem to have a weaker and weaker effect during the different stages of loading. Comparison of the two slip profiles in Figure **??** shows that it is mainly the loading phase, which corresponds to the total slip, that is disturbed by the closure of the fractures mentioned above. Note that the black lines in the profile of the viscous slip, with negative values, have to be ignored as they correspond to the slip during the loading phase, hence before the reference image. We recall that when we are interested in the viscous behavior, we choose as reference image the first image for which the prescribed force has been reached. This means that some images were actually taken

before the reference image, therefore have been taken before the arbitrarily defined zero time used in the analysis of the results.

80% of peak stress stage

In this last phase of stress increment, the interfaces have reached a satisfying homogeneous behavior along their length as shown by Figure 6.28, which emphasizes the importance of starting the tests with a phase of setting the interfaces and closing the fractures. One may wonder if the uniformity of the response under 80 percent peak stress shows that far from the static friction threshold, the shear behavior is more dominated by heterogeneities than by the kinematics imposed by the loading, because indeed the behavior under 20 percent peak stress was much less uniform. The question would then be, if the stress were reduced to 20 percent, would the response of the interfaces become less uniform again? Also it can be noticed that the amount of slip does not vary much with the applied stress. In fact, for the three loading levels a viscous slip of about 1 μm is measured. Note that between each stage a constant increment of 20% of the peak stress has been applied. Finally, a sudden increase in the creep rate is noticed in Figures 6.22. This led us to look at the evolution of the relative humidity and temperature in the room during the test.

Influences of relative humidity on the viscous slip

Figure 6.35 shows an acceleration in viscous slip at the end of the step of 80% of peak stress, which seems to be directly correlated to a decrease in the relative humidity in the experimental room. We recall that the tests are performed in a closed room, maintained at a constant temperature (17°C) and relative humidity (70%). This acceleration is caught not only at the scale of the sample with displacement measured by the LVDTs in Figure 6.35c) but also in the viscous slip measured by DIC, as shown in Figure 6.35d). A closer look at the LVDTs measurements of the three loading stages shows that changes in viscous slip velocity can be directly related to changes in relative humidity. It seems that a decrease in relative humidity induces an acceleration of the displacement, whereas an increase in relative humidity decrease the displacement rate. Figure 6.35 shows that the effect of relative humidity can actually be noticed on all the stress level, always consistent with what has been deduced on the 80% peak stress level: a decrease in relative humidity induces an acceleration of the displacement, whereas an increase in relative humidity decreases the displacement rate. Several explanations can be proposed to link the variation in relative humidity content ant the variation in viscous slip velocity. Indeed, an increase in relative humidity content may cause a dilation of the material and thus an increase in internal stresses. Increasing the normal stress on the interface would decrease the viscous slip rate. Alternatively, the

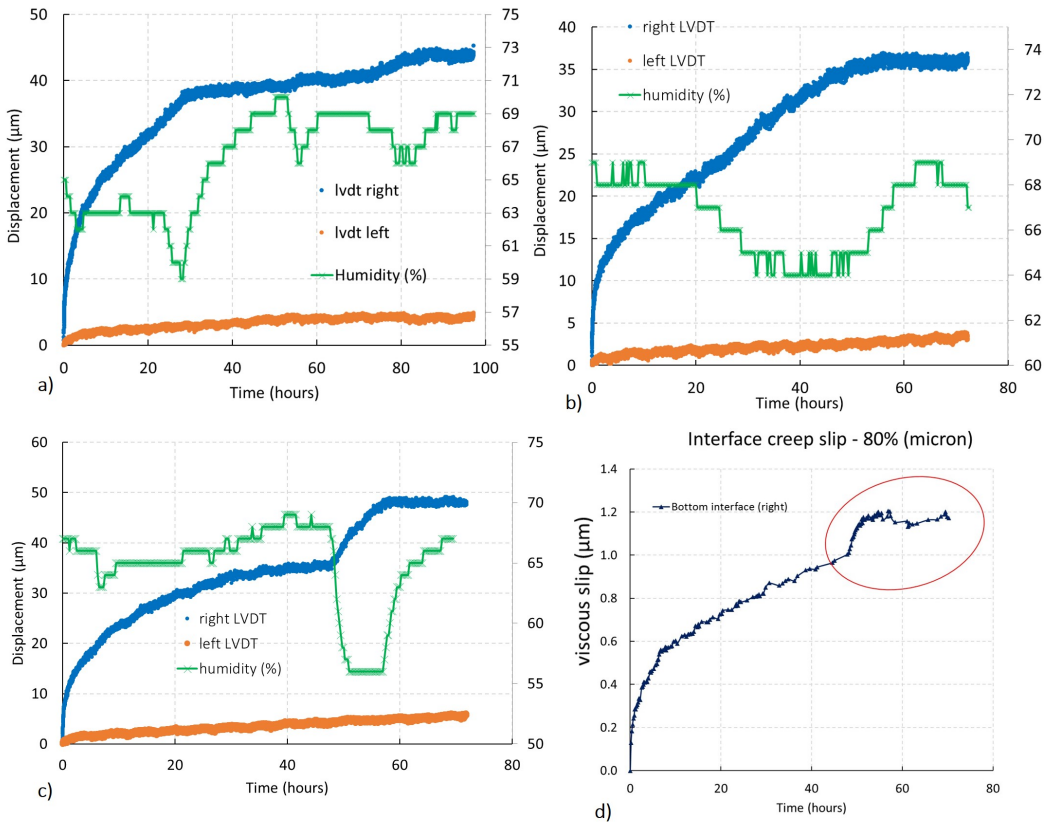

Fig. 6.35.: Plot of the displacement measured by the LVDTs along with the percent of relative humidity in the experimental room. The decrease and increase in relative humidity have a direct influence on the measured displacement. a) stress level 40% b) stress level 60% c) stress level 80% d) viscous slip during the stress level 80% measured with DIC.

increase in relative humidity content may induce an increase in the apparent cohesion of the interface and thus prevent slip. Otherwise, one could argue that the temperature could be the cause of the increase in viscous slip rate, as well as on the relative humidity level. Indeed, one could imagine that changes in temperature would induce rapid responses, while relative humidity would need more time to induce an effect on the rock. Therefore, the temperature evolution presented in Figure 6.36 during the test has been checked. However, the variation in temperature seems not to be relevant, which would confirm that the relative humidity level has a great influence on our experimental results. From this, it can be concluded that it is very important to ensure that the humidity level does not vary during the experiment in order to characterize the creep of an interface in the COx claystone.

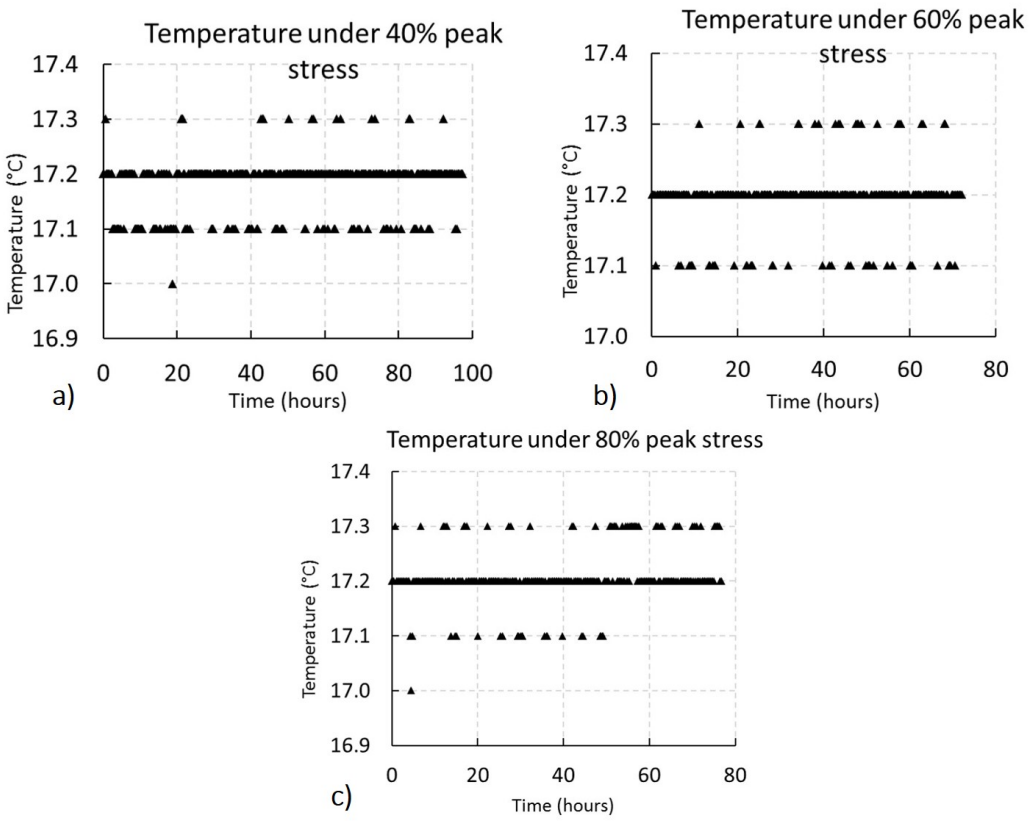

Fig. 6.36.: Evolution of the temperature in the experimental room under a) 40%, b) 60% and c) 80% peak stress

6.5 Analysis and discussion of the results

It has been shown previously that the results of the first loading step of the multilevel test are more complex than the subsequent steps, and therefore it is quite difficult to draw conclusions from it about the viscous slip of an interface. For this reason, it has been decided to focus the study of interface creep on the 40, 60 and 80 percent loading stages.

6.5.1 Identification of the elastic parameters: normal and tangential stiffness of the fracture

Tangential stiffness

The elastic parameters of the interfaces can be determined from the loading phases measured under the hypotheses consisting in taking the beginning of the shearing phase as reference. However, it should be remembered that this loading phase, regarding the tangential behavior,

only contains a small number of measurement points, as it only lasts about ten minutes between steps. The displacement related to the increase in shear stress provides the

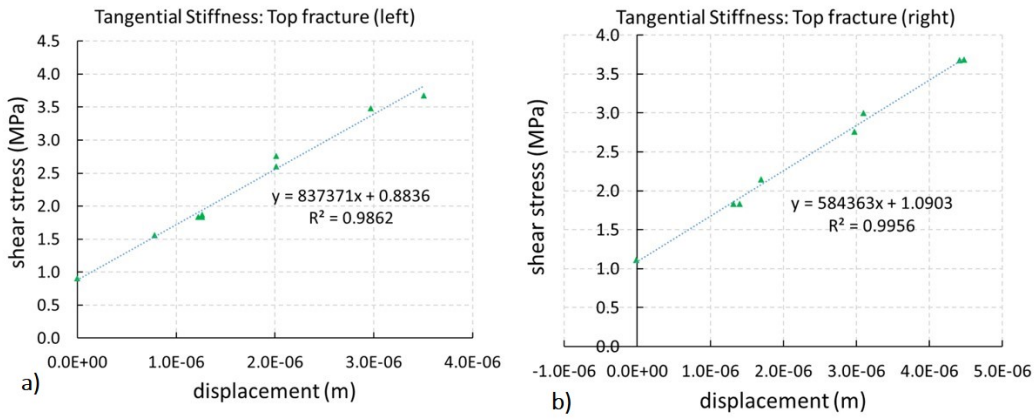

Fig. 6.37.: Calibration of the tangential stiffness of the top interface K_t. Data from the images of a) the left and b) right side of the sample.

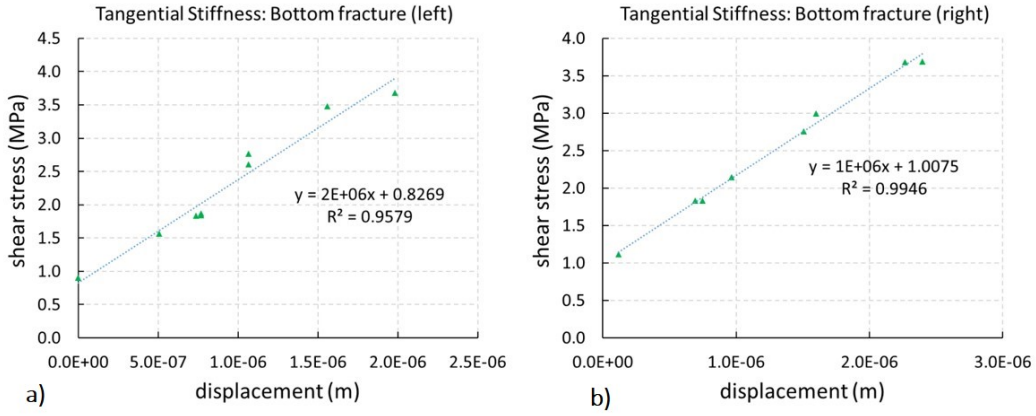

Fig. 6.38.: Calibration of the tangential stiffness of the bottom interface K_t. Data from the images of a) the left and b) right side of the sample.

tangential stiffness of the interface. The fact that the values are slightly different between the top and bottom interfaces is not surprising as the surfaces of both interfaces might be a little bit different, as the polishing of the sheared faces is not perfectly repeatable. The actual stress state in the interface may also differ from one interface to another. Also, the closure of the fractures at the vicinity of the interfaces (fractures that are not symmetrically distributed between the two interfaces) necessarily have an influence on the average slip used to determine the parameter K_t. The top interface has a K_t between 0.8×10^6 MPa/m and 0.6×10^6 MPa/m. The fact that $K_t^{\text{right}} < K_t^{\text{left}}$ is consistent with the fact that an important fracture perturbed the slip of the right side of the top interface. The bottom interface has a higher K_t between 1×10^6 MPa/m and 2×10^6 MPa/m. The parameters measured with DIC

are significantly larger than those measured with the LVDTs. This is consistent with the fact that DIC measure more accurate displacements, hence smaller displacement, as the LVDTs which measure a coupled slip of the fracture and strain of the rock bulk.

Normal stiffness

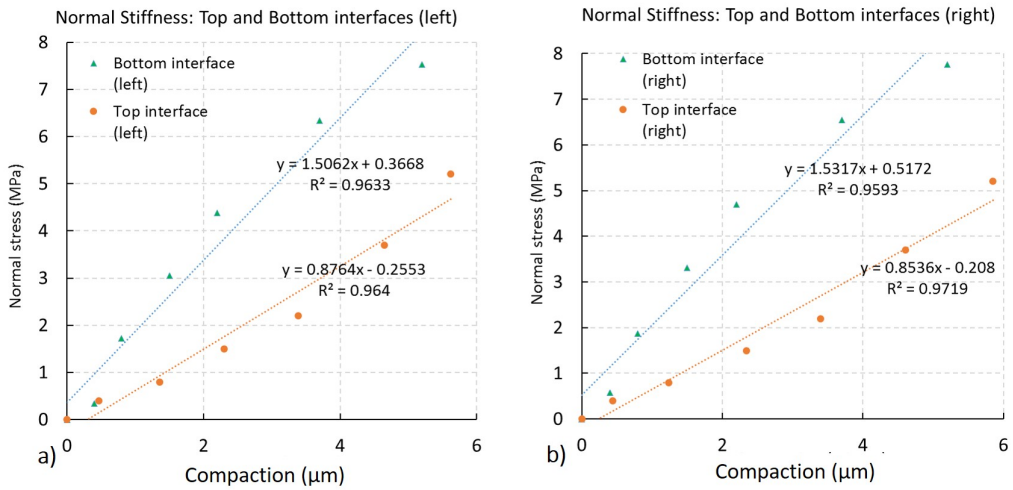

Fig. 6.39.: Calibration of the normal stiffness K_n of both interfaces. Data from the images of a) the left and b) right side of the sample.

Figure 6.39 shows the calibration of the normal stiffness of the interfaces. The images used to determine the normal stiffness of the interfaces were made after the multilevel test while the weights applying the normal load are gradually removed. The advantage of doing this measurement at the end of the test is that the interfaces have the most stable behavior (with the least amount of artifacts related to the surface preparation). The disadvantage is that in studying the normal loading phase that way, it does not account for the response of the sample to the first loading and the possible loading defects. The results are consistent between the left and right images, and the top interface has a smaller normal stiffness than the bottom interface: $K_n^{\text{left}} = 0.88 \times 10^6$ MPa/m and $K_n^{\text{right}} = 0.85 \times 10^6$ MPa/m for the top interface and $K_n^{\text{left}} = 1.53 \times 10^6$ MPa/m and $K_n^{\text{right}} = 1.51 \times 10^6$ MPa/m for the bottom interface. Again, the results provided by the DIC are larger than those estimated based on the measurements provided by the LVDTs.

6.5.2 Calibration of the viscous model

For the sake of simplicity, we have chosen to study and calibrate the viscous slip of interfaces using Lemaitre's power law. The proper method to calibrate the parameters of the model used in the numerical simulations chapters 3 and 4, with a multilevel creep test, is described in appendix A.7. However, the actual application of this method raises other practical problems and requires making certain assumptions, which is why we have used a simplified method here. The following equation has been assumed to describe the viscous slip of the interface and thus the parameter A and α have been calibrated on the data of the 40%, 60% and 80% levels considering the top and bottom interfaces (with no separation of the right and left data).

$$\dot{u}_v(t) = A(t-t_f)^{\alpha-1};\ A = a\tau^n \tag{6.9}$$

Assuming that the shear stress is constant, one can write $A = a\tau^n$. The idea is to calibrate the parameters of the viscous law, assuming that some viscous and elastic deformations have already happened during the previous steps. Let us assume that t_f is the time when the appointed force is reach. Thus, for $t > t_f$ the stress is constant, and the total measured displacement can be expressed by:

$$u_{tot}(t) = A(t-t_f)^{\alpha} + u_{tot}(t_f) \tag{6.10}$$

with $u_{tot}(t_f)$ the viscous and elastic displacement from the previous step. Which then gives the following expression of the displacement measured by DIC which is the equation that we used to calibrate the parameters A and α.

$$\Delta u_{DIC} = u_{tot}(t) - u_{tot}(t_0) = A(t-t_f)^{\alpha} - A(t_0-t_f)^{\alpha} \tag{6.11}$$

t_0 corresponds to the time when the reference image is taken. In this context t_0 is considered as the time for which the viscous slip, in the considered stress level, is starting. At t_0, the stress is constant: $t_0 > t_f$. Different calibrations have been tested. On the concatenated data from left and right images or on the data of the left images on the one hand, and on the data from the right images on the other hand. It has also been tested to fit directly equation 6.11 or after application of the log to the equation. As a matter of fact, this allows to choose whether to give more importance to the short-term values (with log) or to the long-term values (without log). It is reminded that the data obtained by DIC are not all used in the analysis, since about 1000 images of 150 Mb each were too long to deal with. Thus, a selection of the image was made to only keep the images corresponding to an equal increase in displacement. This has for a consequence that more data are treated at the beginning of the step than in the long-term, because the displacement increase faster at the beginning of the step than at the end. An example of the different calibration tested done

on the data of 80% τ^{peak} stage is provided in Figure 6.40. The parameters obtain for the

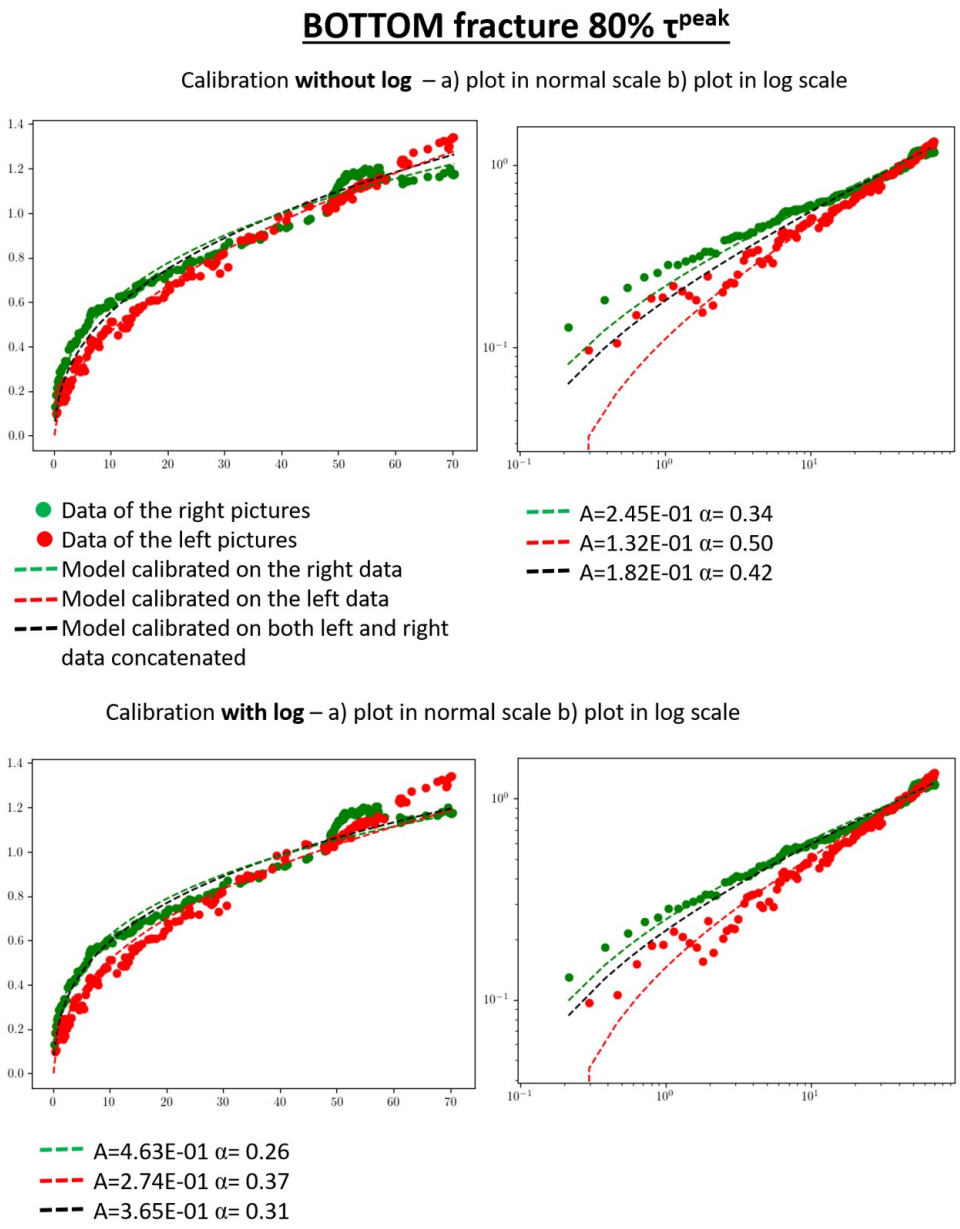

Fig. 6.40.: Calibration of the parameters of the viscous slip of the interface.

calibration with log on the concatenated values of the left and right images of the bottom image were used to calibrate the power of the dependency in shear stress of the viscous slip. The data obtained for the three different level of shear stress are plotted ($ln(A)$ in function of $ln(\tau)$) in Figure 6.41 and a value of almost one is found. The final values of

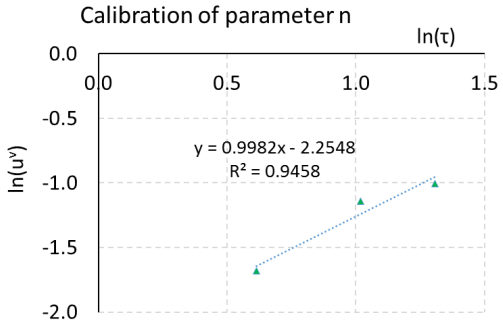

Fig. 6.41.: Calibration of the parameter n, describing the stress dependency, of the viscous slip of the interface.

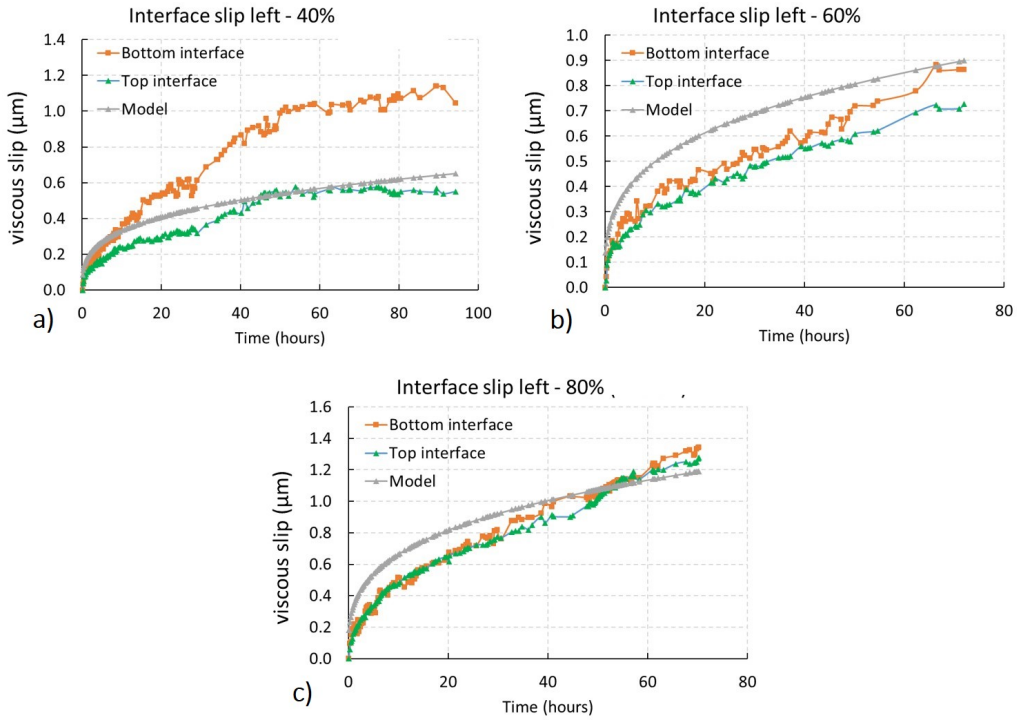

Fig. 6.42.: Calibration of the parameters of the viscous slip of the left side of both interfaces under a) 40% of peak stress b) 60% of peak stress c) 80% of peak stress.

the parameters are $a = 0.09 \times 10^{-6}$ m MPa^{-1}h$^{-0.3}$, $\alpha = 0.3$ and $n = 1$. In Figures 6.42 and 6.43 the comparison between the experimental data and the model is presented. The model reproduces quite well the viscous slip under 60% and 80% of the peak stress. As for the behavior at 40% the model largely underestimates the viscous slip. Further tests are needed to explore the relationship between the load and the viscous response of the interface.

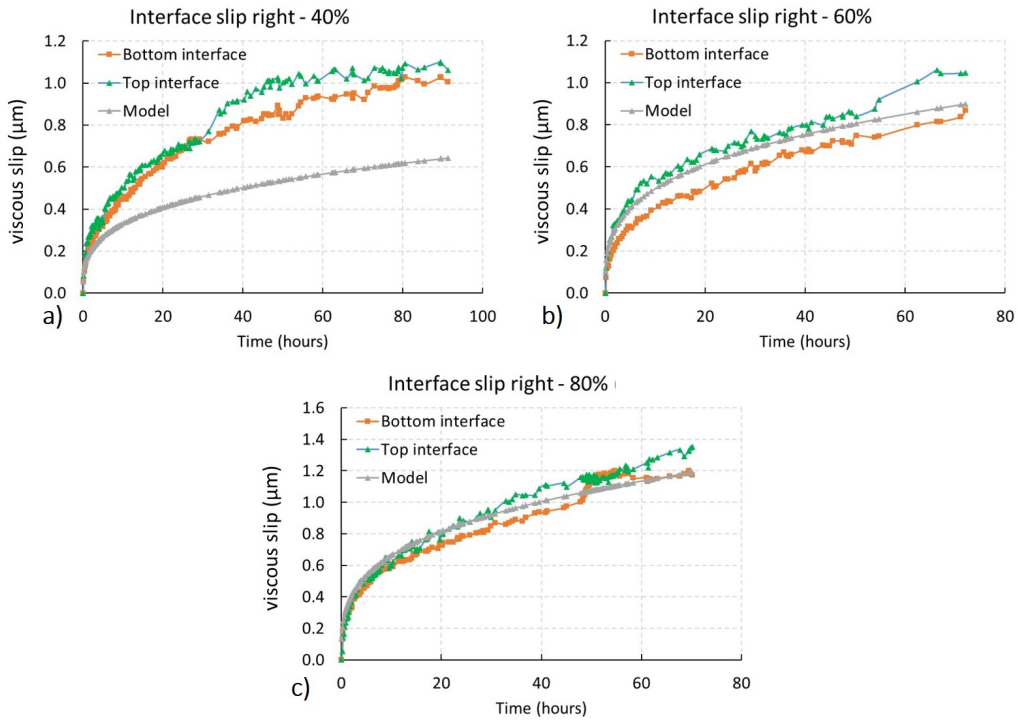

Fig. 6.43.: Calibration of the parameters of the viscous slip of the right side of both interfaces under a) 40% of peak stress b) 60% of peak stress c) 80% of peak stress.

6.6 Single level creep test

A two-week test was conducted under a single loading level. This test was actually performed before the multistage test, so the experimental protocol is similar to the protocol used for the multistage test. However, as this test was then analyzed with the same protocol of analysis as the previous test, in particular with regard to the hypotheses on the reference images, it has been chosen to present it in a second time. The conditions under which this test was conducted were as follows: the normal stress applied to the interface planes was of 8 MPa. The central block is pushed with a prescribed force equal to 22 kN corresponding to an interface shear of 4.8 MPa, for 14 days. The loading phase of the interfaces lasted about 2 hours, which allowed fourteen images to be recorded of each side of the sample. The measurements of the LVDTs are presented in Figure 6.44. Again, different displacements on both sides of the middle block is evidence that the rock bulk viscous flow is relatively important compared to the viscous flow in the interfaces. The ε_{xx} horizontal strain measured with gauges in four different points of the middle block are presented in Figure 6.45. The order of magnitude of the measurements of the LVDTs and gauges are consistent with the same measurements during the first loading of the multilevel test.

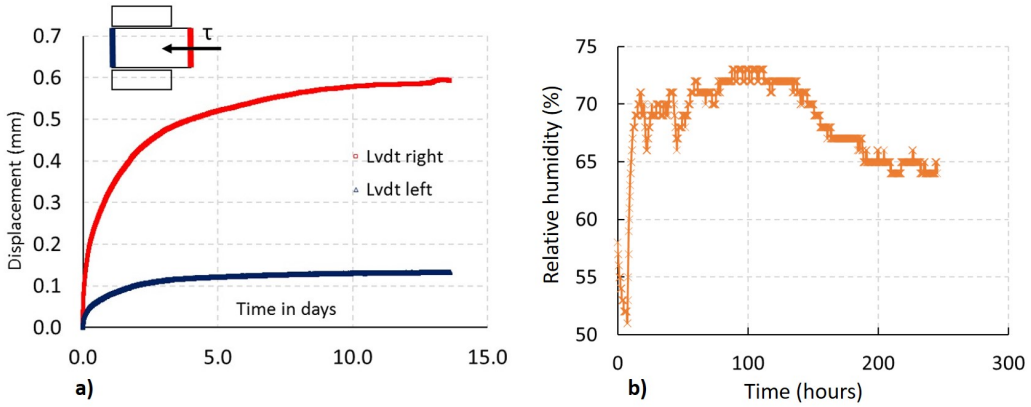

Fig. 6.44.: a) Measurement of the displacement at the right and left ends of the middle block with the LVDT, b) relative humidity variation during the single-level test.

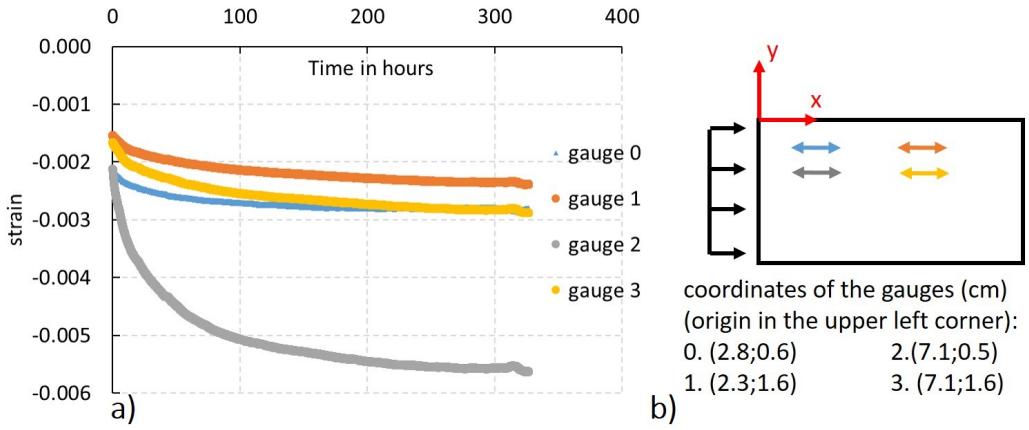

Fig. 6.45.: a) Plot of the total εxx strain measured by three gauges, for the duration of the experience. b) Location of the gauges on the central block.

6.6.1 Loading phase

First the loading phase is analyzed to get a better overall understanding of the experiments. During this phase 14 images were taken. The actuator was moving at 0.01 mm/min to reach a force of 22 kN (which corresponds to an average shear stress in the interfaces of 4.8 MPa). The reference image is the first image taken while the normal stress has already been applied but no shear is applied to the sample yet. In Figures 6.46, 6.47 and 6.48 the three components of the strain field are plotted at the end of the loading phase. The local discontinuities are highlighted on the images presented in the above-mentioned Figures. Under each image, the average total strains in the three blocks (for the left and respectively the right image) are plotted during the shearing of the interfaces. The average strains correspond to the strain induced in the sample, after the application of the normal

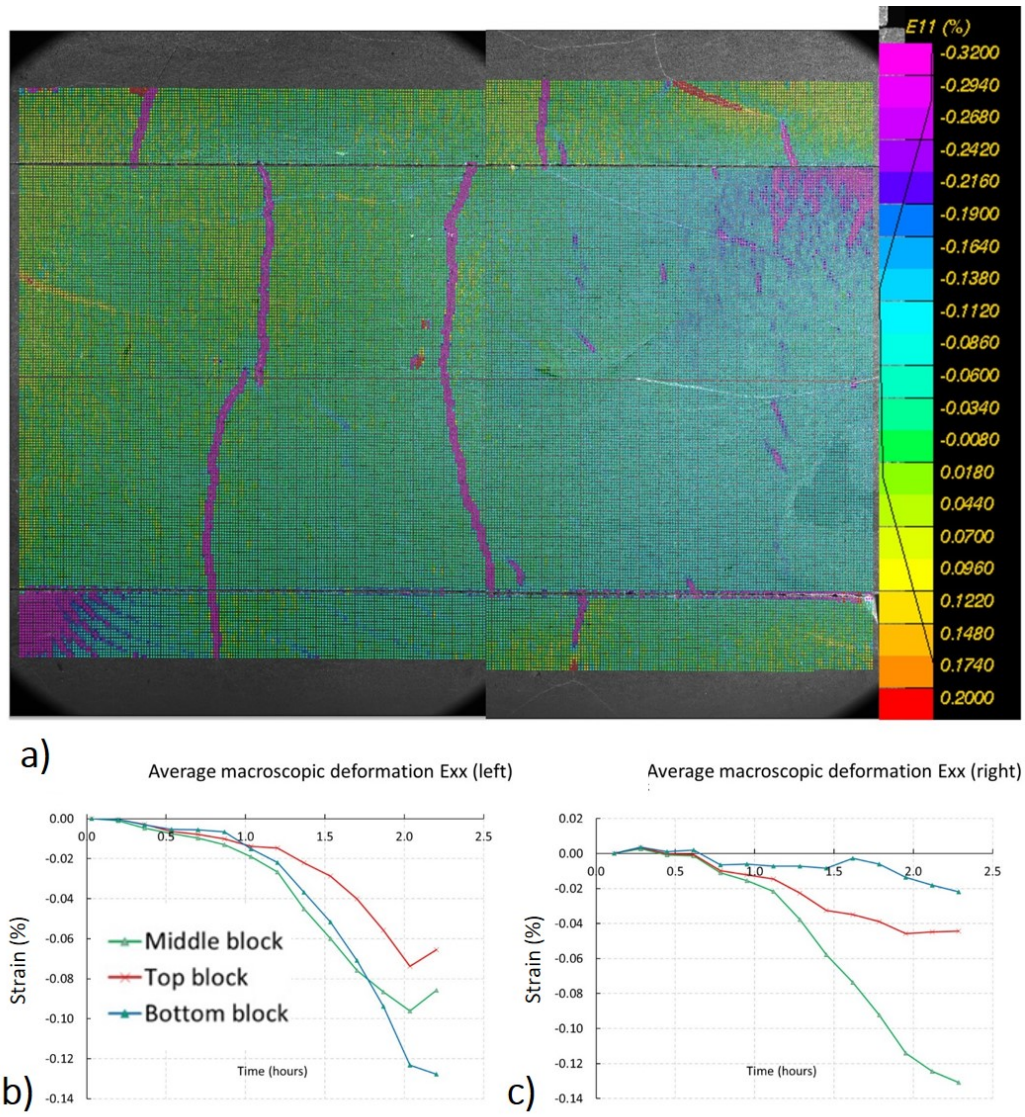

Fig. 6.46.: a) Map of the of the ε_{xx} strain tensor at the end of the shear loading phase. Plot of the average ε_{xx} strain of the top block, the middle block and the bottom block. Results for b) the left images and c) the right images.

load. Figure 6.46 represents the ε_{xx} total strain. The right extremity of the middle block is in compression while the left extremity is slightly dilating, certainly under the Poisson's effect due to the creep induced by the normal load. On average, the blocks are in compression, a compression that concentrated on the closure of the fractures which cross the blocks in pink in the image Figure 6.46. Figure 6.47 shows that the sample is globally in vertical compression state. Note that, the left end of the sample has locally unloaded at the end of the loading phase. This unloading is shown in the white frame in the Figure 6.47: left extremities of both interfaces are red (when all the rest of the interfaces are in pink, which corresponds to compression) and the rock bulk is slightly yellow, corresponding to positive

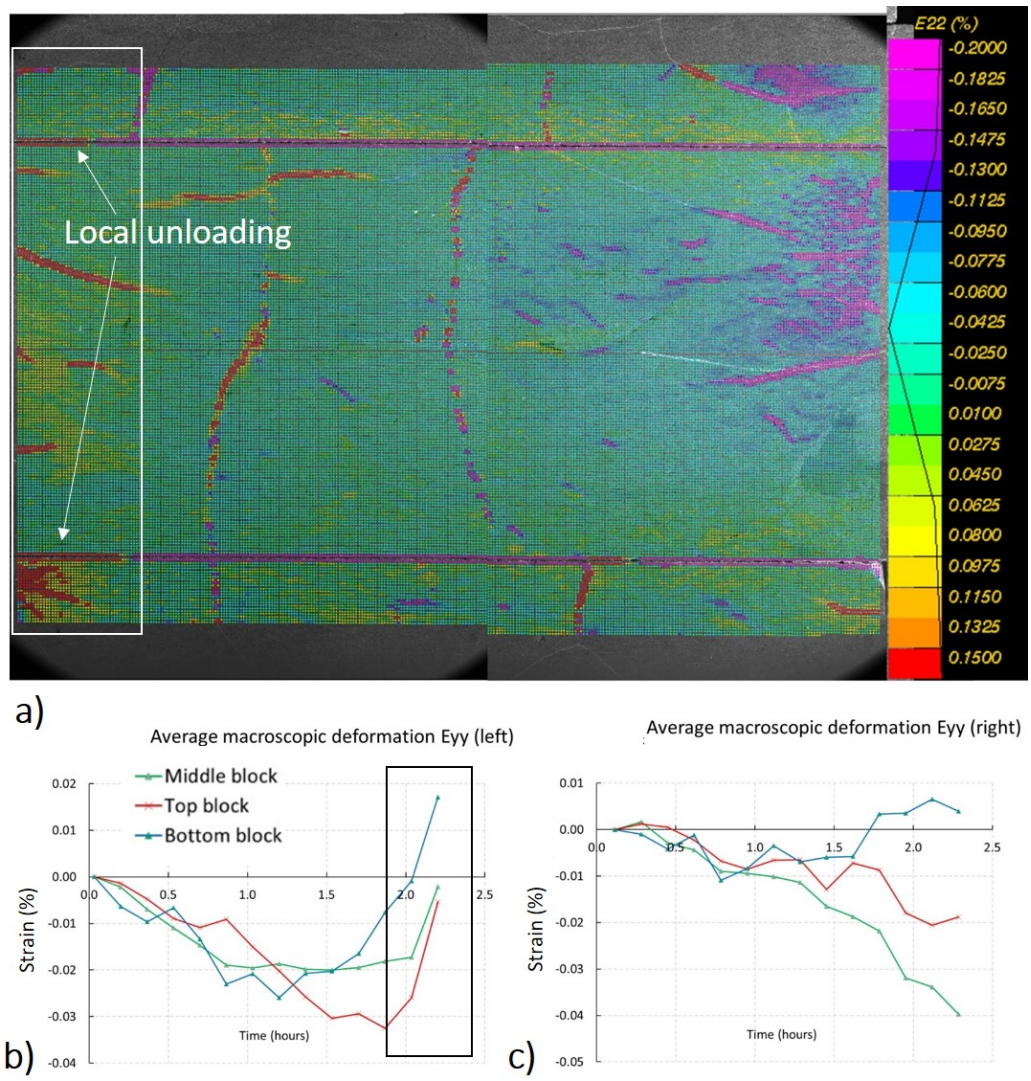

Fig. 6.47.: a) Map of the of the ε_{yy} strain tensor at the end of the shear loading phase. Plot of the average ε_{yy} strain of the top block, the middle block and the bottom block. Results for b) the left images and c) the right images.

values of ε_{yy} (dilation). The unloading is also evidence in the ε_{yy} component of the average strain measured in the left image (framed in black in Figure 6.47). As a matter of fact, the numerical simulations at the beginning of the chapter showed in Figure 6.3 that a gradient in vertical strain would exist due to unsymmetrical boundary conditions. The vertical load is applied in a point, then transmitted to the sample through a metal block that is not restrained other than by the point of application of the force and its own weight, thus it is possible that rotations appear on the top of the sample to balance the applied forces. Figure 6.48 shows a rather good symmetrical distribution of total shear strains, positive for the upper block and upper interface, and negative for the lower block and lower interface. In Figure 6.49 the compaction profile along the two interfaces is plotted over the duration of the experiment,

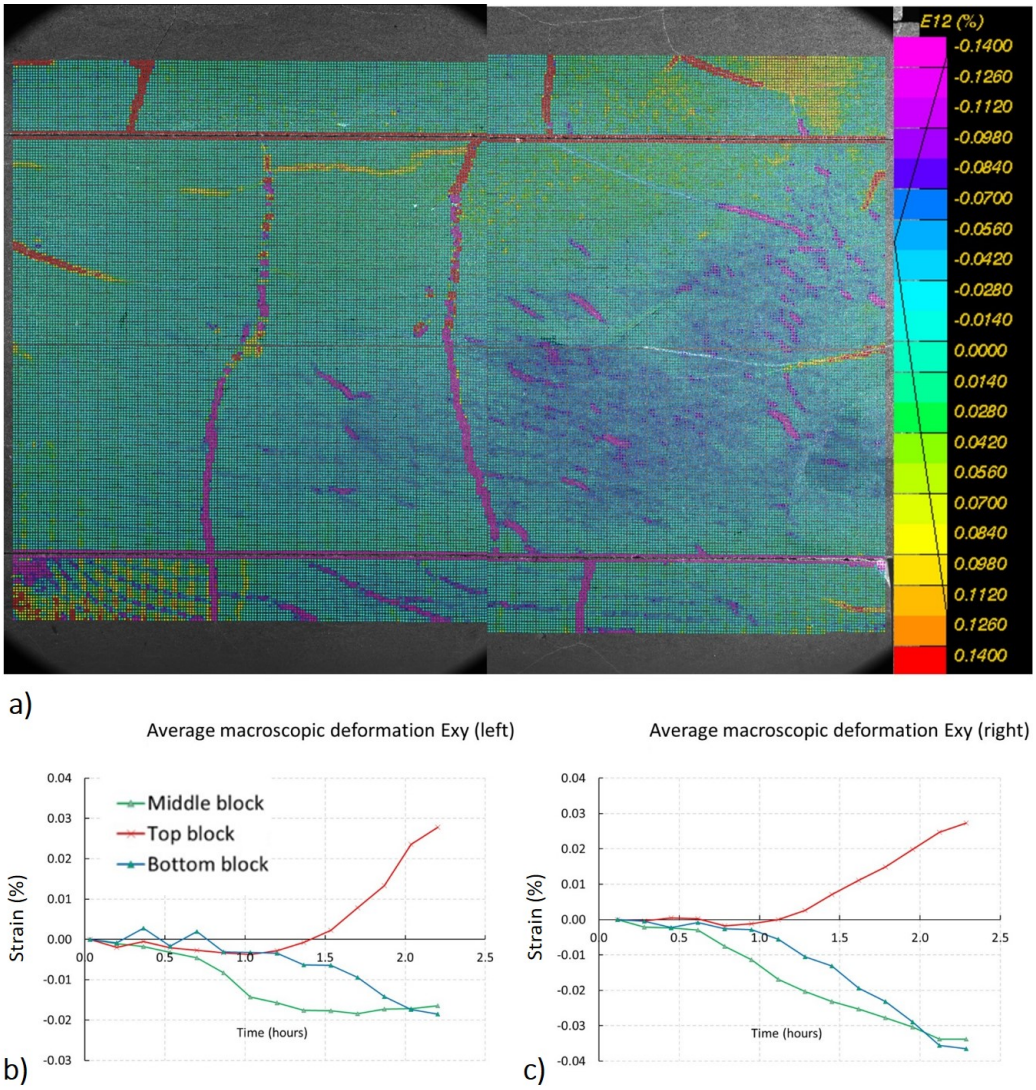

Fig. 6.48.: a) Map of the ε_{xy} strain tensor at the end of the shear loading phase. Plot of the average ε_{xy} strain of the top block, the middle block and the bottom block. Results for b) the left images and c) the right images.

beyond the loading phase. The discontinuities are due to the presence of fractures in the sample. Most of them have a very small influence on the global behavior of the interfaces, except the fracture on the left part of the upper interface, which induces a less good contact of the upper interface compared to the bottom interface. There is a slight asymmetry between the right and left sides of the sample, the right side is more compressed than the left side, which is consistent with the numerical simulations and the other observations. In the same way as for the compaction, the slip profile of the interfaces is presented in Figure 6.50. A larger slip is measured by DIC on the right of the interface, which is shown in Figure 6.50. This can be related to a larger stress at the same location in the numerical simulation

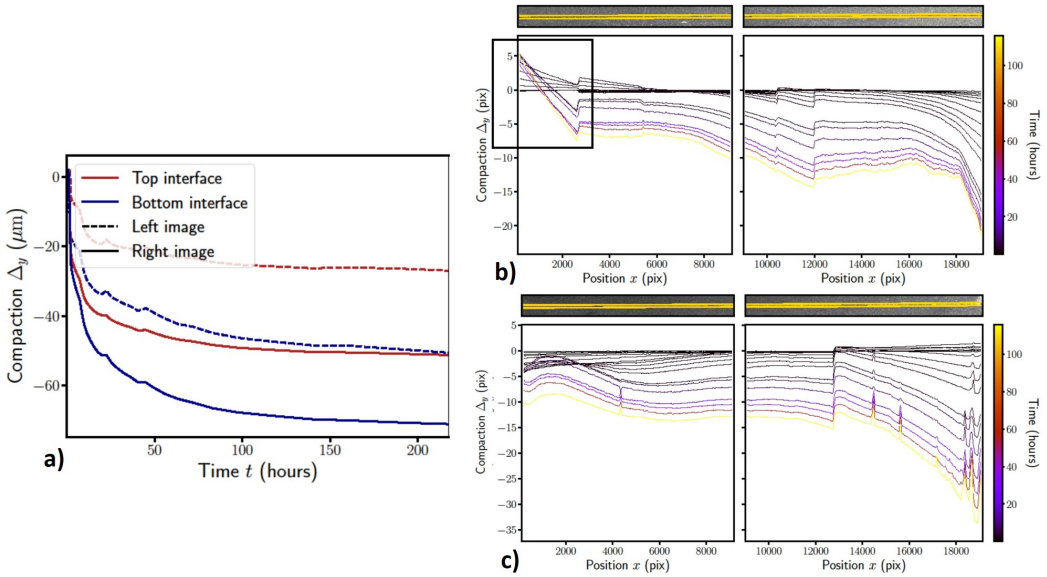

Fig. 6.49.: a) Evolution of the average total compaction of the interfaces in time. Compaction profile along the b) top and c) bottom interfaces.

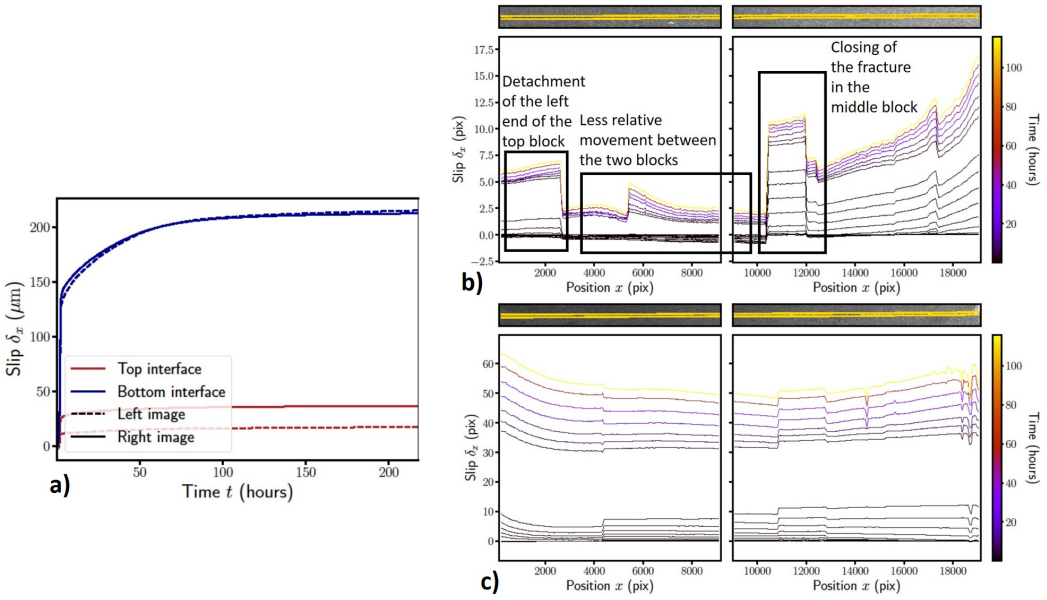

Fig. 6.50.: a) Evolution of the average total slip of the interfaces in time. Slip profile along the b) top and c) bottom interfaces.

shown in Figure 6.6. The slip profiles show also clearly discontinuities that can be related to fractures in the sample. The top interface seems to be much more disturbed than the lower one. However, this is mainly a scale effect due to the fact that the slip on the top interface is much smaller than on the bottom interface. The disturbances are of the order of 5 pixels on both slip profiles.

Remember that the slip profiles are measured as discontinuity jump on either side of the interface. Thus, for the top interface, a positive slip means that the displacement of the middle block near the interface is more to the left than the movement of the top block. So if we take a closer look at the behavior of the top interface, a first acceleration of the slip is probably due to the closing of a fracture in the middle block framed in black in Figure 6.46. The closing of the fracture locally accelerate the leftward movement of the middle block compared to the movement of the top block. The deceleration of the slip is therefore certainly due to a better contact of the interface faces and thus to a decrease of the relative motion between the two blocks. Finally, the last acceleration of the slip might be due to the fracture at the left end of the upper block which detaches the left end of the block from the rest of the sample, which result in this part of the top block being less subject to the stresses imposed on the sample, hence the middle block again moves more to the left than the top block.

6.6.2 Creep phase

In this subsection, the reference image is the last image taken after the completion of the loading phase, i.e. when the prescribed force was reached. Figure 6.51 shows an almost

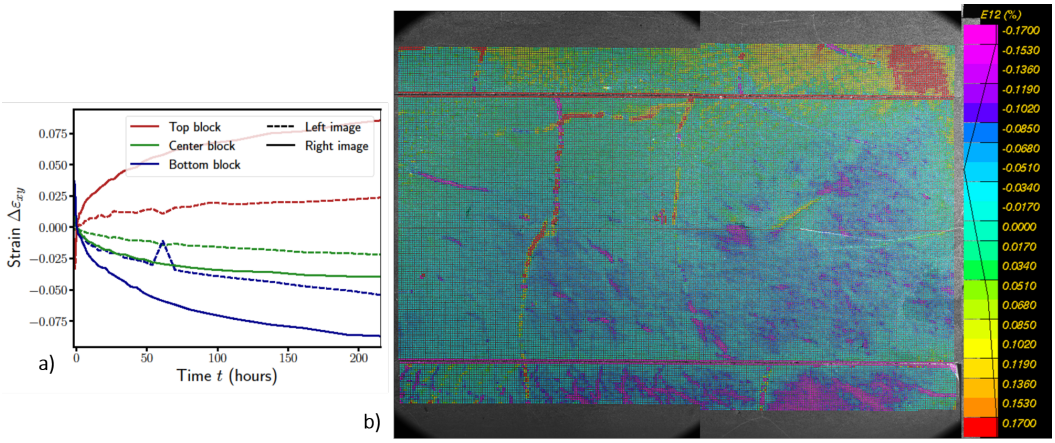

Fig. 6.51.: a) Average value of the shear creep strain ε_{xy} in each block taken at the end of the experiment, b) map of the shear viscous strain field obtained with DIC.

uniform shear strain field in the sample, consistent with what was observed in the numerical simulations. The top and bottom blocks have a symmetrical behavior, positive on the top and negative on the bottom. The middle block should have an average zero shear strain, which is not completely true probably because of some local heterogeneities. We place ourselves under creep conditions to analyze in more detail the viscous slip of the interfaces. The observations made in the previous section invite us to pay particular attention to the

bottom interface which seems to have a more homogeneous behavior than the top interface. Figure 6.52 shows the viscous slip measured during the test. The bottom interface has a

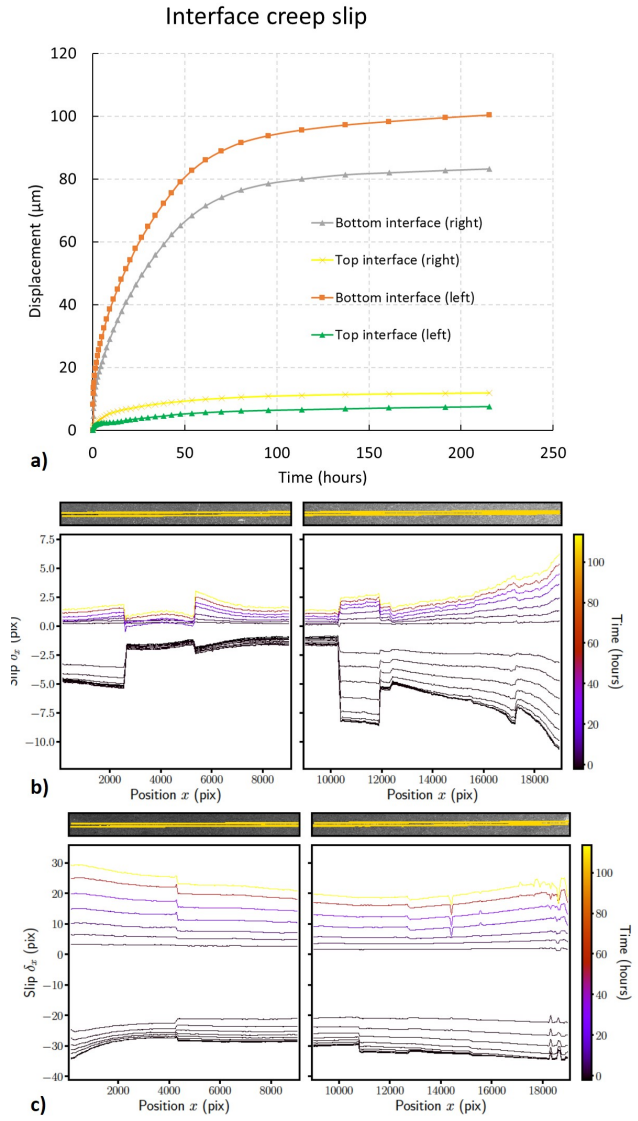

Fig. 6.52.: a) Average creep slip of both left and right sides of top and bottom interfaces. Slip profiles b) of top interface and c) bottom interface.

larger slip than the top interface, which is probably due to the fact that the bottom interface seems to have a more homogeneous stress state than the top interface. In addition, it is possible that the boundary condition on the top edge of the sample allows more movement than might be desired. Thus this could enable some joined movement of the top block and the middle block, resulting in less slip on the top interface than on the bottom interface. The slip profiles show that the viscous slip (in Figure 6.52) of the interfaces are less disturbed by the fractures in the sample than the total slip which includes the loading phase (in Figure

6.50). Note that the black lines in the profile, with negative values, have to be ignored as they correspond to the slip during the loading phase, hence before the reference image. Again, the apparent strain-induced slip between the correlation windows above and below

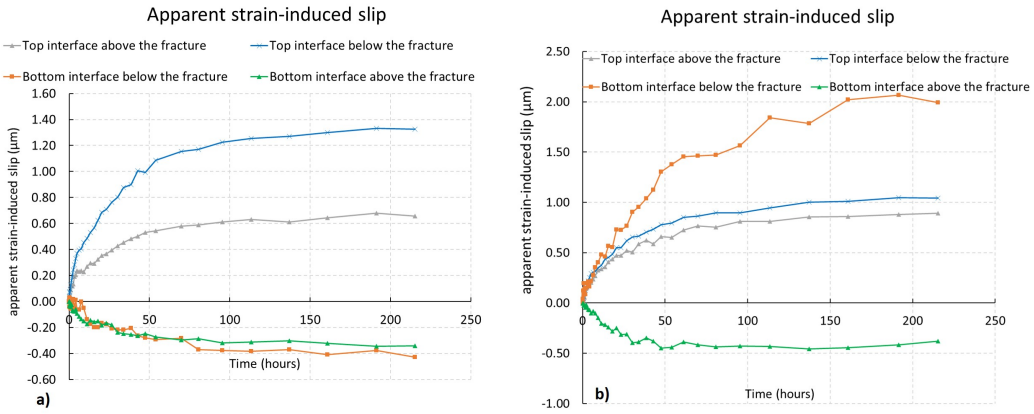

Fig. 6.53.: Apparent strain-induced slip between the correlation windows above and below the interfaces. a) in the left image, b) in the right image.

the interfaces is measured to verify that it remains small compared to the calculated viscous slip.

It is not quite clear why in this experiment the measured viscous slip was so much bigger than in the multilevel test. Though, one can mention some hypotheses that could help explaining the difference between the two slips measured in the two different tests. Indeed, the difference in the behavior of the interfaces can come from the preparation of the sheared surfaces, as our interface preparation protocol was not very repeatable (a large standard deviation from the mean roughness is measured). Also, the COx claystone is very sensitive to changes in relative humidity, and the relative humidity evolution was not the same during the two different tests. As a matter of fact, the change of viscous slip rate apparently correlated to relative humidity happened for variation of about 25% of relative humidity (during the multilevel test shown in Figure 6.35), while the relative humidity during the single-level test was stable between 72% and 65% (see Figure 6.44).

However, the difference between the two measured viscous slip mentioned here is two orders of magnitude, so another rational explanation would be the existence of at least two slip mechanisms involved in the viscous slip of an interface in COx claystone. This would imply that during the multilevel test, even if there was indeed sliding, the load remained under the threshold of the sliding mechanism demonstrated in the single-level test. It is clear that the parameters calibrated on the multilevel experiment will not be adapted to the behavior measured during this experiment, so a new calibration must be proposed. The curves in Figure 6.54 show two distinct slopes, one at times smaller than 54 hours and another beyond

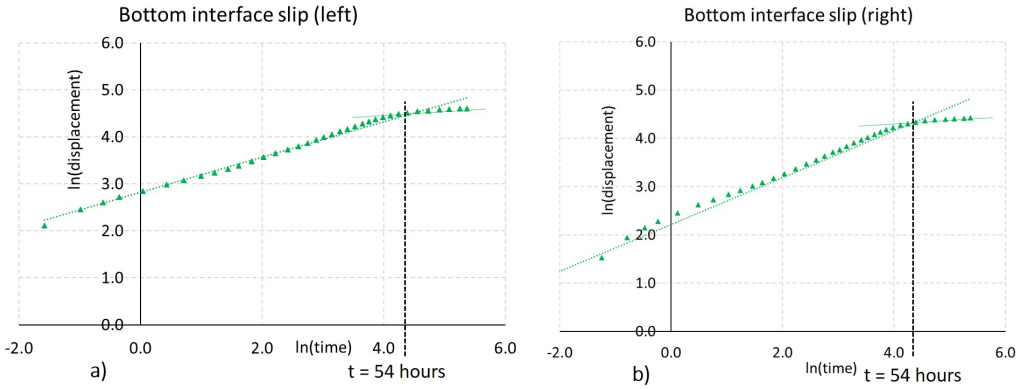

Fig. 6.54.: Plot of the log-log viscous slip of the bottom fracture a) left side of the bottom interface b) right side of the bottom interface.

that time. This suggests that the mechanism involved in this viscous slip may not be modeled by a power law. Figure 6.55 shows the difference between the classical measure provided

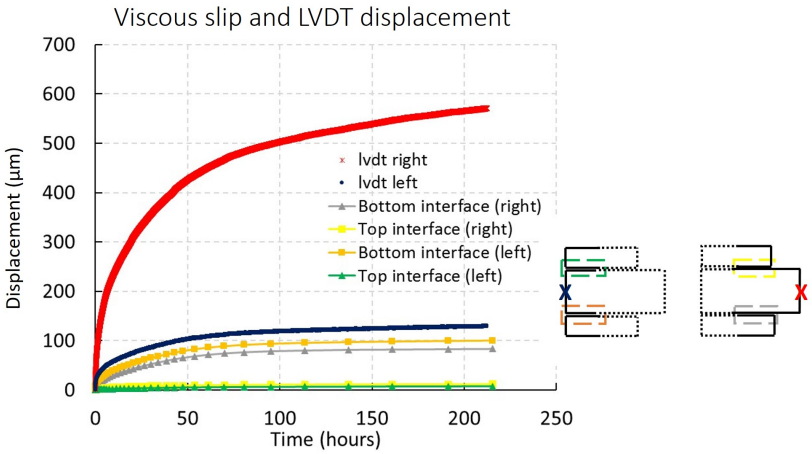

Fig. 6.55.: Comparison between the displacement measured by DIC and the macroscopic displacement measured by the LVDTs.

by LVDTs and the viscous slip measured with DIC. Again the displacements measured with the LVDTs are bigger than the viscous slip along the interfaces measured with DIC. Moreover, the viscous slip on the bottom interface is significantly bigger than the viscous slip on the top interface. It is believed that this is due to the boundary conditions on the upper edge of the sample which allowed a more or less grouped displacement of the upper block and the central block on the bottom interface.

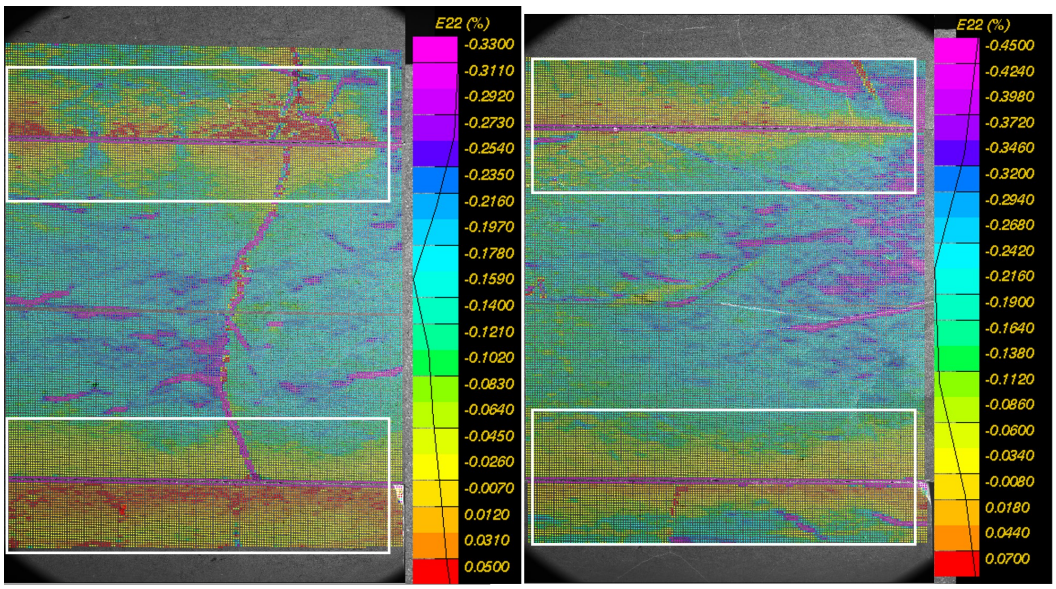

Fig. 6.56.: a) Viscous deformation ε_{yy} in the first stage of the multilevel test and b) viscous deformation ε_{yy} in the single level creep test.

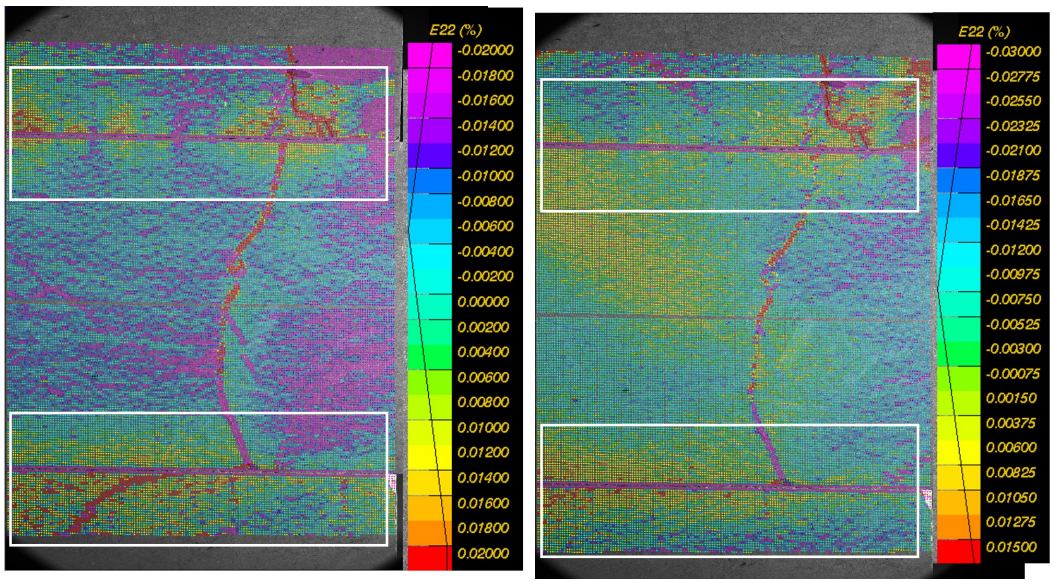

Fig. 6.57.: a) Viscous deformation ε_{yy} in the 40% of peak stress stage of the multilevel test and b) viscous deformation ε_{yy} in the 80% of peak stress stage of the multilevel test.

6.7 Comparison of the experimental results

In both tests the displacements measured with LVDTs on the right side of the sample is much larger than the displacement measured on the left side. According to numerical simulations, this proves that rock bulk creep has a major contribution in the coupled viscous deformation of the fractured COx claystone.

Also, in both tests the behavior of the bottom interface is much homogeneous than the top interface. In the multilevel test, however, the behavior of the two interfaces seems to become more and more homogeneous during the different stress stages, as the average viscous slips measured in the top - bottom - left and right become almost equal. In the single stress level test, it seems that because the contact above the top interface is freer than the contact between the bottom of the specimen and the frame (the top block is only hold by the point of application of the normal load and the weight of the steel block), the boundary conditions are highly asymmetrical between the top and bottom interfaces. It appears that the bottom interface slips over about 100 μm, while the top interface slips less (over only about 10 μm), which let us believe that the two upper blocks had a joint movement and that they have more or less slipped, together as one block, on the bottom interface.

Overall, the horizontal strains measured by the gauges in the two tests are coherent (Figures 6.23 and 6.45). The middle block is globally in compression, the orders of magnitude of the horizontal strain ε_{xx} are also consistent, with a certain gradient, we measure more compression on the side where the horizontal effort is applied than in the center of the block.

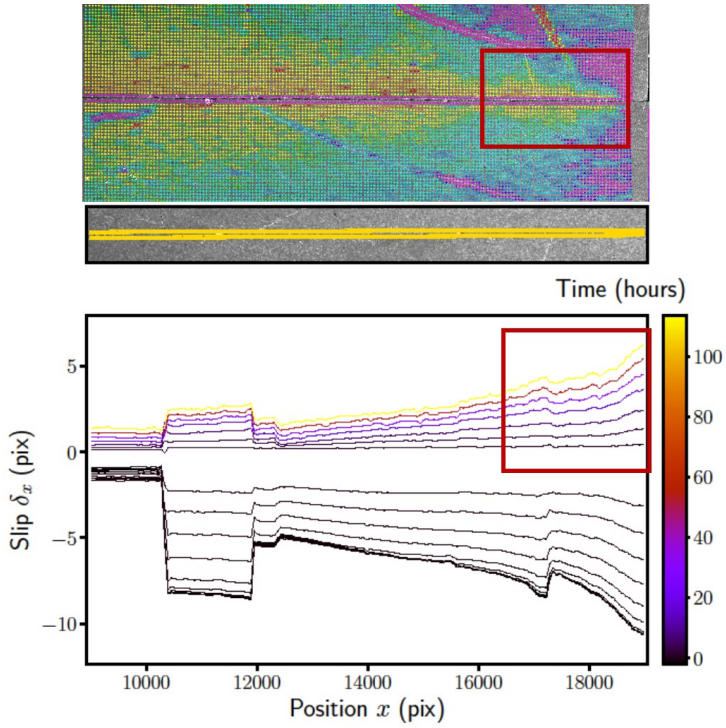

Fig. 6.58.: Plot of profiles of the viscous slip in the top interface in the single level creep test. The extension of the dilation zone is not constant along the interface. Moreover, the minimum extension framed in red is correlated to the maximum viscous slip also framed in red in the profiles. The black lines correspond to images taken before the reference image.

A phenomenon of dilation at the interfaces is also observed in a very repeatable way. Indeed, framed in white on the Figures 6.56 and 6.57, we observe an increase in the y component of the strain. In fact, the samples are globally in compression, rather uniform if we ignore the heterogeneities, but at the interfaces, the sample is less compressed, as if it was expanding. This phenomenon is shown in Figure 6.56 for the single stress level test (on the left) and for the first stage of the multilevel test, and in Figure 6.57 for the 40% and 80% peak stress of the multilevel test. What is strange, however, is that this phenomenon does not seem to correlate with discontinuities in other components of the strain tensor. It can be seen from Figures 6.56 and 6.57 that the intensity of the phenomenon is not constant in the 8 examples framed in white. By *intensity*, it is the extension of the dilatancy into the sample beyond the interface that is understood. The Figure 6.58 also shows that it is not directly related to the amount of slip as the intensity of the phenomena is the smallest for the biggest slip (framed in red in Figure 6.58). It is difficult to relate the points of non-expansion found on the top interface with any other physical quantity. Yet, this expansion effect reminds us of the phenomena observed in rock salt creep tests. Because of fretting, the base of the sample cannot deform and just above it, it expands. It would be interesting to measure and follow over time the evolution of this dilatation zone.

6.8 Discussion and proposal of a new experimental protocol

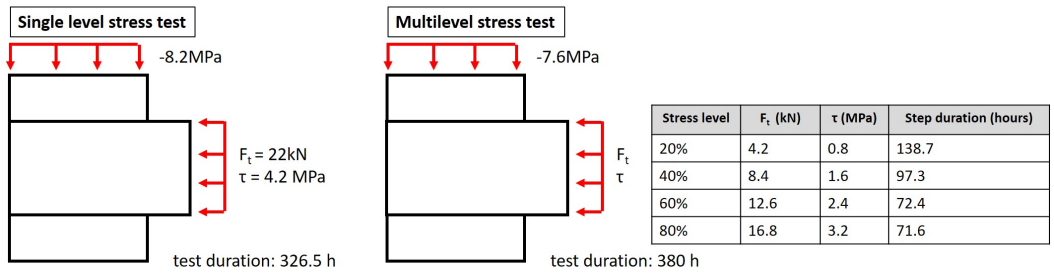

Stress level	F_t (kN)	τ (MPa)	Step duration (hours)
20%	4.2	0.8	138.7
40%	8.4	1.6	97.3
60%	12.6	2.4	72.4
80%	16.8	3.2	71.6

Fig. 6.59.: a) Stress level and duration of the single-level test. b) Stress level and duration of the multilevel test.

In this chapter, we have presented the experimental results of two tests. Figure 6.59 recalls the different conditions under which the two tests were conducted. The presented experimental data provide a first understanding to model the viscous slip of fractures in Callovo-Oxfordian claystone. However, the quantity of results obtained during this experimental campaign is not statistically representative, and therefore further data are required for a comprehensive characterization of the behavior of the fractures. Nevertheless, the scrupulous analysis of the experimental results allowed us to identify the main practical

challenges of this experiment and to some improvement to the experimental protocol. Eventually, this new protocol will allow to carry out an efficient experimental campaign with the objective to characterize the creep of a fracture in Callovo-Oxfordian claystone.

We were interested in the global response of the interfaces, i.e. the slip as a function of time. But we also looked at the stress dependence with the multilevel test, which also allowed us to explore the question of the existence of a possible creep threshold. In terms of strain fields, the two tests are rather consistent. Better yet, they correspond quite well to the expectations provided by the numerical simulations. There is a gradient in the horizontal component of the deformation with more compression on the right side of the central block (where the force is applied) than on the left side, while the compression is transmitted to the left ends of the upper and lower block (corresponding to the supports), through the interfaces. The shear strain field is mostly as expected: positive shear deformation field on the upper block and interface and a negative one on the lower interface and block. However, there is a dilation phenomenon observed on the vertical component of the strain field that is not yet very clear.

In terms of interface slip, bigger slip is measured on the right of the interface than on the left, which is consistent with the prediction of the numerical simulation. Nonetheless, the slip tends to become more homogeneous along the interface by the end of the tests. Nevertheless, a question remains, why two orders of magnitude difference between the bottom interface slip in the multilevel test and in the single level test were measured.

The level of shear stress applied in the single-level test was determined based on the C and ϕ coefficients calculated in the preliminary tests (Figure 6.15). The interfaces in this single-level test were sheared to 90% of peak stress, while the maximum stress level for the multilevel test was 80% of peak stress. Actually, the 80% of peak stress in the multilevel test was measured experimentally before the creep test. Indeed, a direct shear test was conducted before the multilevel test. The middle block was sheared at 0.01 mm/min up to the saturation of the measured force, established to be the 100% peak stress. In order to compare the stress level in the multilevel test with the stress applied in the single-level test, the peak stress defined by the C and ϕ coefficients (Figure 6.15) is calculated and 74% of τ^{peak} is found. Hence, the difference in applied shear stress is 90% of τ^{peak} for the single-level test and 74% of τ^{peak} for the maximum shear stress in the multilevel stress. Thus, the difference in viscous slip measured in the two tests might be explained by a creep threshold located between 74 and 90% of τ^{peak}. However, even if the viscous slip during the multilevel test was low, there was indeed a viscous slip measured, hence our conclusion lean more in favor of at least two different slip mechanisms. In the case of the multilevel test, we would have stayed below the threshold of the slip mechanism observed in the single level test. Note that this definition of the maximum shear stress (100% of the maximum

stress) assumes a Mohr-Coulomb failure criterion for the interfaces. Regarding viscosity, it is possible that the response depends on the slip velocity that is imposed by the velocity of the actuator displacement during the experiment. It may be interesting in future tests that aim to explore this threshold issue to work with higher shear stresses by working at a higher actuator displacement speed.

Also when it comes to calibrating the parameters of the viscous model, we can ask ourselves at what time scale and under what stresses we need to calibrate our model. Indeed, this is all the more important as it seems that we have raised the possibility of several viscous slip mechanisms. Our numerical simulations of the drifts are especially thought to reproduce the long-term behavior of the drifts. Nevertheless, even if we wish to calibrate our model in the long-term, it is totally unthinkable to perform a creep test over a time comparable to the characteristic time of radioactive waste, which is about 100 000 years. The time of the experiment can therefore reasonably be set as the time after which the slip increment is no longer measured by DIC. A simple elastic calculation allowed us to estimate the shear stress on the chevron fractures to be 2 MPa (see section 5.2.1), which corresponds approximately to the 60% peak shear stress of the multilevel test ($\tau_{60\%}$ = 2.8 MPa). We therefore rely on the model of viscous slip obtain after calibration in section 6.5.2 (see Figure 6.42b)) to do the following estimation. We can assume that DIC enables to measure a displacement of about 0.05 μm. Thus we obtain that after four days we measure in one day a displacement lower than 0.05 μm. This means that after four days of test, we have to wait for more than one day to measure any displacement. If we consider that we have a little more time and that we can look at the displacement measured in one week, the calculation gives us that the displacement measured in 1 week becomes lower than 0.1μm after 5 weeks and lower than 0.05μm after 15 weeks. Thus it is reasonable to make loading stages of about 4 days. For a longer experiment less data can be processed because a significant displacement only happens in a week.

The fact that we observe almost equal values of viscous slip for the three loading levels (40%, 60% and 80% of the peak stress) raises questions about the fact that the interface would have seen the load increments and not the total load. Finally, considering that only two proper experimental results were obtained, more tests have to be conducted in order to be able to draw proper conclusions.

New experimental protocol

The improved protocol regards minor aspects of the experiment, mostly to make the measurements more accurate or to have access to additional measurements. However, the philosophy of the device is not modified. As a matter of fact, when the experimental was

thought, the viscous slip on the interface was imagined to be dominant in comparison with the viscous flow of the rock matrix. The results presented in this chapter shows that on the contrary, the behavior of the rock bulk take a great part in the global viscous behavior of the fractured COx claystone.

First, regarding the experimental protocol itself, the previous tests have shown the importance of properly setting up the interface before starting the test. By *setting the interface*, it is understood that the contact between the interfaces is as homogeneous as possible and that the fractures which would have appeared during the loading phase have been closed in such a way as to disturb the sliding of the interfaces as little as possible. This is done by initially submitting each sample for a few days only to compressive stress (normal to the interface). The application of the shear load is thus applied afterwards when the rate of delayed axial strain has decreased. As a matter of fact, it has been shown that if the mechanical response of the sample subjected to 20% of the peak stress was complicated to analyze as various competing phenomena were masking the viscous effect, the behavior of both interfaces for the 80% peak stress of the multilevel test is quite homogeneous. However, this might also be due to the fact that for low shear load the slip mechanism could be driven by the heterogeneities in the sample. Concerning the conduct of the test itself, it would be interesting to further investigate the question of viscous threshold. In particular, to find out for which stress ranges a slip of the order of 1μm is measured and in which case it can increase to 100 μm. In view of the results presented in this chapter, it would be interesting to explore higher stresses than those presented in this chapter.

Specifically, the new experimental protocol is as follows: We start by applying the normal stress on the sample which is then left to creep for a day. Next, an initial creep stage is performed at 30-40% of the peak shear stress for two to three days. This step is only done to set up the interfaces and create the gouge. Then we reduce the shear stress to 10% of the peak shear stress, to set up the sample before applying increasing shear steps. The different level of stress are applied during five days. The steps are 20%, 40%, 60%, 80%, 85%, 90%, 95%, 100% of peak shear stress up to the point of failure. A buffer step of 10% of peak shear stress is done before repeating multilevel test. By repeating the loading procedure twice, and by comparing the results of the two 20% stress step, we are willing to analyze the importance of the interfaces set up on the mechanical response. In particular, we can ask ourselves if at low load it is not the heterogeneities that dominate the kinematics of viscous slip on the interfaces.

The second improvement regards the shape of the sample. In order to be able to do numerical simulations that better reflects the experiment and for instance with the same boundary conditions than in the experience, the whole sample, including the borders need to be photographed and then analyzed with DIC. Thus, in order to take an image of the

whole sample without changing the magnification and the whole experimental set up, the dimensions of the sample need to be reduced. As a consequence, the sample can be photographed at once, which make the process of image recording way easier because the movement of the camera won't need to be managed anymore. One image of the whole sample will also enable to choose any interval of time between two images, as the camera doesn't need the time to move from one side of the sample to another. For instance, we want to increase the acquisition rate during the loading phase and decrease it at the end of the test when the viscous strain rate becomes very small. The new dimensions of the sample were calculated and are given in appendix A.8. One downside of using a smaller sample though would be that the effect of unwanted fractures may disturb more the slip of the interfaces and the strain field in the rock than for samples of current dimensions. However, the multilevel experiment has shown that even though some fractures are created by the stress conditions, little by little the fracture are being closed and the global behavior of the sample stabilizes. The question of the boundary condition of the upper limit of the sample also deserves more attention. Maybe it would be better to clamp the steel block and or the COx upper block to allow the top interface to have a more stable behavior like the bottom interface.

7 Conclusion

The objective of this thesis, sponsored by ANDRA, was to model the time-dependent behavior of the underground disposal structures excavated in the COx claystone. If many research teams have been working on modeling the convergence of those drifts over the past few years, in this work our goal was to propose a new modeling approach that can be used as a design tool for engineering companies that will design the structures of the Cigéo project. *In situ* measurements led us to postulate that viscous slip on chevron fractures controls the anisotropic convergences and convergence rates of the URL structures. Two studies were carried out in parallel: numerical simulations of two characteristic drifts of the URL on the one hand, and on the other hand an experimental campaign aiming at studying the viscous slip along an interface in the COx claystone.

7.1 Numerical modeling

Two different types of model are presented in this work. A transverse isotropic continuous model in chapter 3 and a continuous equivalent model of the fractured zone in chapter 4. 2D plane strain simulations are performed with the objective to faithfully reproduce the convergences measured on the URL drifts. Two tunnels, designated as the GED drift and the GCS drift, were used as case studies and allowed us to evaluate the quality of the numerical simulations by comparing the numerical results to the *in situ* convergences. In the following we will refer to those two drifts as *the characteristic drifts*. The GED drift represents the behavior of tunnels excavated in the direction of the minor principal horizontal stress, and the GCS drift represents the behavior of tunnels excavated in the direction of the major principal horizontal stress.

Numerical models presented in Chapter 3 have shown that with a transverse isotropic viscous model, one can reproduce the long-term behavior of *the characteristic drifts*. Successfully reproducing both behaviors with a single model is a real challenge. Here, these results were obtained by matching the direction of the main chevron fractures with the direction of transverse isotropy. The parameters of the elasto-viscoplastic model remain identical for the numerical simulations of the two galleries and only a simple rotation of 90° of the transverse isotropy plane is operated between the simulations of GCS and GED drifts. The anisotropy parameters are first pre-determined from laboratory tests on the intrinsic anisotropy of COx

claystone. They are then numerically calibrated on the *in situ* convergence data. Finally, the calibration of these four parameters of anisotropy allowed us to faithfully reproduce the horizontal and vertical convergences of the two *the characteristic drifts*.

The aim of models presented in Chapter 4 was to transform our hypothesis into a systematic method that can be used by engineers to model the long-term behavior of drifts excavated in rock that present a similar behavior as COx claystone. Therefore, a continuous equivalent model of the fractured zone is presented in Chapter 4. Assuming a simplified representation of the fracture distribution in the fractured zone, we identify the anisotropy parameters with the fracture behavior, so that the equivalent continuous model has the same macroscopic behavior as a rock specimen fractured by equidistant parallel fracture planes. These new models establish a systematic method for building tunnel simulation models taking into account the existence of a fractured zone, assuming a certain behavior of the rock and a certain geometry of the fractures.

7.2 Experimental study

In parallel with the work on the numerical models at the tunnel scale, an original experimental setup was designed in order to characterize the viscous slip of fracture in the COx claystone. A whole new device was set up in the laboratory to study the viscous behavior of the chevron fractures developing in COx claystone. The coupling of the DIC technique with the shear box allowed to measure local viscous slip along the interfaces and the global strain field. In order to measure viscous displacements in the micrometer range along the interfaces, we first had to make sure that the resolution of the images was high enough to actually measure such small slips. Two tests were analyzed in detail and allowed to observe viscous slip along two interfaces in COx claystone. The DIC provides a lot of information that had to be sorted out beforehand in order to make the process of analyzing the experimental results easier. and Then the data were systematically processed in order to provide a description of the measured viscous slip along the interfaces. The viscous slips measured in the different stress step of the multilevel test show a very good correlation with a power law model. However, the viscous slip measured in the sign level test was of greater magnitude and did not appear to be able to be modeled by a power law. Thus, it is possible that several mechanisms are involved to explain the viscous slip of an interface in the COx claystone. The results allowed us to improve our experimental protocol in order to better characterize the interface creep behavior in COx claystone.

7.3 Perspectives and future work

It is worth mentioning the new questions that emerged during the development of the studies presented in this manuscript, as they could not be addressed immediately but could lead to new insights.

Numerical modeling

Concerning the numerical models, further work could be done to improve the short-term response. Indeed, in our models we have put aside two important elements that influence the short-term behavior of the convergence of the drifts: the hydraulic phenomena and the existence of tensile fractures. Many models manage to explain the shape of the fractured zones by taking into account the hydro-mechanical couplings. Also, the tensile fractures that develops directly at the tunnel wall are responsible for a great deal of the short-term displacement happening at the drift wall. Our modeling of short-term behavior was not too penalizing in that the plastic anisotropy parameters finally adjusted on the *in situ* measurements intrinsically allowed to represent both hydro-mechanical couplings and tensile fracture behavior. Nevertheless, a better description of the short-term behavior would make it easier to adjust the anisotropy parameters.

Another improvement could be done with a better description of the fractured zones. As a matter of fact, the data used were very scattered and the counting method can only give a first order of magnitude of the fracture density. One can indeed imagine proposing a more complex model of fracture orientation and finally sorting the data by retaining only the fractures that have an orientation such that they will contribute the most to the global deformation of the fractured rock. This sorting can be done on the basis of experimental results. Indeed, if fracture creep is characterized under several stress states, it may be that in some cases creep is negligible next to the viscous slip of a differently loaded fracture.

Finally, strong hypothesis have been made regarding the definition of the continuous equivalent model of viscosity. Further experimental investigations may disprove the assumption that the viscous behavior of fracture and rock have the same time and stress dependency. It may even be that the viscous slip mechanism of the fracture is not so well modeled by a Lemaitre-type creep law. In this case, we could consider establishing the equivalent continuous models by zones by performing a numerical homogenization.

Experimental campaign

First, there are immediate prospects, which are underway in the laboratory. In particular, we are thinking of carrying out a test campaign according to the new protocol presented at the end of Chapter 6. This new test requires us to resize the samples so that we can take an image of the entire sample, including the edges. The use of smaller samples will allow us to measure with DIC the real boundary conditions undergone by the sample and thus enable us to make numerical simulations closer to the test conditions than what we have been able to do so far. Moreover, with numerical simulations closer to reality, we will be able to explore the behavior of fractures over the very long-term (this will allow us, for example, to numerically simulate a test lasting several years). Resizing the samples requires resizing the test box, something that we are currently doing. Indeed, for the moment we have designed wedges in order to resize the box and to be able to work with new smaller samples under the same DIC conditions (effective pixel size) as those presented in chapter 5.

We have also pointed out the effect of relative humidity on the behavior of the interfaces. Thus it would be interesting to change the relative humidity in the test room according to different cycles in order to analyze in detail the link between relative humidity and slip rate. Indeed, it had previously been shown that an increase in relative humidity tends to increase the deformation rates of COx claystone under a uniaxial compression test [94].

In the longer term, with an initial idea of the fracture behavior, one can consider running numerical simulations in which chevron fractures are explicitly introduced, which would allow a more accurate estimate of the *in situ* stress state experienced by the fractures. This would therefore allow the experimental conditions to be more precisely defined so as to better reproduce the *in situ* conditions. Also a more repeatable protocol of preparation of the sheared surfaces should be established, which would make the data from different tests easier to compare.

Bibliography

[1]L. R. Alejano and E. Alonso. “Considerations of the dilatancy angle in rocks and rock masses”. In: *International Journal of Rock Mechanics and Mining Sciences* 42.4 (2005), pp. 481–507 (cit. on p. 41).

[2]L. Allais, M. Bornert, T. Bretheau, and D. Caldemaison. “Experimental characterization of the local strain field in a heterogeneous elastoplastic material”. In: *Acta Metallurgica Et Materialia* 42.11 (1994), pp. 3865–3880 (cit. on p. 108).

[3]Andra. *Le socle de connaissances scientifiques et techniques de Cigéo - Les referentiels de connaissances - Tome IV: Le comportement hydro-mecanique des formations géologiques*. Tech. rep. 2022 (cit. on p. 13).

[4]G. Armand, F. Leveau, C. Nussbaum, et al. “Geometry and properties of the excavation-induced fractures at the meuse/haute-marne URL drifts”. In: *Rock Mechanics and Rock Engineering* 47.1 (2014), pp. 21–41 (cit. on pp. 2, 6–10, 73, 75).

[5]G. Armand, A. Noiret, J. Zghondi, and D. M. Seyedi. “Short- and long-term behaviors of drifts in the Callovo-Oxfordian claystone at the Meuse/Haute-Marne Underground Research Laboratory”. In: *Journal of Rock Mechanics and Geotechnical Engineering* 5.3 (2013), pp. 221–230 (cit. on pp. 1, 6, 8, 13, 46).

[6]G. Armand, N. Conil, J. Talandier, and D. M. Seyedi. “Fundamental aspects of the hydromechanical behaviour of Callovo-Oxfordian claystone: From experimental studies to model calibration and validation”. In: *Computers and Geotechnics* (2017) (cit. on pp. 14, 15).

[7]S. Bandis, A Lumsden, and N Barton. “Experimental studies of scale effects on the shear behaviour of rock joints”. In: *International journal of rock mechanics and mining sciences geomechanics abstracts* 18 (1981), pp. 1–21 (cit. on pp. 21, 25).

[8]G. Barla, D. Debernardi, and D. Sterpi. “Time-Dependent Modeling of Tunnels in Squeezing Conditions”. In: *International Journal of Geomechanics* 12.6 (2012), pp. 697–710 (cit. on p. 34).

[9]N. Barton. “Review of a new shear-strength criterion for rock joints”. In: *Engineering Geology* 7.4 (1973), pp. 287–332 (cit. on p. 20).

[10]M. Belmokhtar, P. Delage, S. Ghabezloo, and N. Conil. “Drained Triaxial Tests in Low-Permeability Shales: Application to the Callovo-Oxfordian Claystone”. In: *Rock Mechanics and Rock Engineering* 51.7 (2018), pp. 1979–1993 (cit. on p. 13).

[11]F Bernier, X.-L. Li, and W Bastiaens. “Twenty-five years ’ geotechnical observation and testing in the Tertiary Boom Clay formation”. In: 2 (2007), pp. 229–237 (cit. on p. 12).

[12]G. Besnard, F. Hild, and S. Roux. “"Finite-element" displacement fields analysis from digital images: Application to Portevin-Le Châtelier bands”. In: *Experimental Mechanics* 46.6 (2006), pp. 789–803 (cit. on p. 110).

[13]A Bobet. “Elastic Solution for Deep Tunnels . Application to Excavation Damage Zone and Rockbolt Support”. In: *Rock Mechanics and Rock Engineering* (2009), pp. 147–174 (cit. on p. 42).

[14]E Boidy, A Bouvard, and F Pellet. “Back analysis of time-dependent behaviour of a test gallery in claystone”. In: *Tunnelling and Underground Space Technology* 17 (2002), pp. 415–424 (cit. on pp. 19, 53).

[15]M. Bornert, F. Brémand, P. Doumalin, et al. “Assessment of digital image correlation measurement errors: Methodology and results”. In: *Experimental Mechanics* 49.3 (2009), pp. 353–370 (cit. on pp. 111, 112).

[16]M Bornert, F Hild, J. Orteu, and S Roux. “Digital image correlation”. In: *Solid Mechanics*. Vol. 242. Dic. 2016, pp. 157–190 (cit. on p. 105).

[17]M. Bornert, F. Valès, H. Gharbi, and D. Nguyen Minh. “Multiscale full-field strain measurements for micromechanical investigations of the hydromechanical behaviour of clayey rocks”. In: *Strain* 46.1 (2010), pp. 33–46 (cit. on p. 113).

[18]M. Bornert and A. Gaye. *CMV 1.63 mode d’emploi*. 2012 (cit. on pp. 94, 108).

[19]P. Braun, S. Ghabezloo, and P. Delage. “Transversely isotropic poroelastic behaviour of the Callovo-Oxfordian claystone : A set of stress-dependent parameters”. In: *Rock Mechanics and Rock Engineering* (2020), pp. 6–8. arXiv: `arXiv:2004.09277v2` (cit. on pp. 13, 40).

[20]B. E. T. Brown, J. W. Bray, B. Ladanyi, and E. Hoek. “Ground response curves for rock tunnels”. In: *Journal of Geotechnical Engineering* 109.1 (1983), pp. 15–39 (cit. on p. 42).

[21]L. Cantieni and G. Anagnostou. “The effect of the stress path on squeezing behavior in tunneling”. In: *Rock Mechanics and Rock Engineering* 42.2 (2009), pp. 289–318 (cit. on p. 43).

[22]M. Chalhoub. “Apports des méthodes d’homogénéisation numériques à la classification des massifs rocheux fracturés”. PhD thesis. 2009 (cit. on p. 81).

[23]R. Chambon. “General presentation of constitutive moelling of geomaterials”. In: *Revue Française de Génie Civil* (2000) (cit. on p. 16).

[24]A. S. Chiarelli. “Etude expérimentale et modélisation du comportement mécanique de l’argilite de l’est”. PhD thesis. Université Lille I, 2000 (cit. on p. 13).

[25]I. Cormeau. “Numerical stability in quasi-static elasto/visco-plasticity”. In: *International Journal for Numerical Methods in Engineering* 9.1 (1975), pp. 109–127 (cit. on p. 53).

[26]S. Cuvilliez, I. Djouadi, S. Raude, and R. Fernandes. “An elastoviscoplastic constitutive model for geomaterials: Application to hydromechanical modelling of claystone response to drift excavation”. In: *Computers and Geotechnics* 85 (2017), pp. 321–340 (cit. on p. 11).

[27]J. Dautriat, M. Bornert, N. Gland, A. Dimanov, and J. Raphanel. “Tectonophysics Localized deformation induced by heterogeneities in porous carbonate analysed by multi-scale digital image correlation”. In: *Tectonophysics* 503.1-2 (2011), pp. 100–116 (cit. on pp. 114, 119).

[28]J Delay, P Lebon, and H Rebours. “Meuse/Haute-Marne centre: next steps towards a deep disposal facility”. In: *Journal of Rock Mechanics and Geotechnical Engineering* 2.1 (2010), pp. 52–70 (cit. on pp. 1, 6).

[29]J. H. Dieterich. “Time-dependent friction in rocks”. In: *Journal of Geophysical Research* 77.20 (1972), pp. 3690–3697 (cit. on pp. 20, 96).

[30]D. P. Do, M. N. Vu, N. T. Tran, and G. Armand. “Closed-Form Solution and Reliability Analysis of Deep Tunnel Supported by a Concrete Liner and a Covered Compressible Layer Within the Viscoelastic Burger Rock”. In: *Rock Mechanics and Rock Engineering* 54.5 (2021), pp. 2311–2334 (cit. on p. 3).

[31]P. Doumalin. “Microextensométrie locale par corrélation d ’ images numériques . Application aux études micromécaniques par microscopie électronique à balayage”. PhD thesis. 2011 (cit. on p. 107).

[32]P Duffaut, J Bernaix, J Bernede, et al. “Essais et calculs de mécanique des roches appliqués à l’étude de la sécurité des appuis d’un barrage-voute - exemple de Vouglans”. In: *9e Congrès International des Grands Barrages*. Istanbul, 1967, pp. 793–818 (cit. on p. 27).

[33]G. Duveau, J. F. Shao, and J. P. Henry. “Assessment of some failure criteria for strongly anisotropic geomaterials”. In: *Mechanics of Cohesive-Frictional Materials* 3.1 (1998), pp. 1–26 (cit. on p. 36).

[34]E Fjaer and O. M. Nes. “Strength anisotropy of Mancos shale”. In: *47th us rock mechanics/geomechanics symposium*. 2013 (cit. on p. 36).

[35]Fracsima. *Materials ’ Catalogue*. 2016 (cit. on pp. iii, iv, 33, 67).

[36]A. Gaye, M. Bourcier, E. Heripre, et al. “Quantitative investigation of grain boundary sliding in halite rock by SEM in situ testing and full field strains measurements To cite this version : HAL Id : hal-01587092”. In: (2013) (cit. on p. 110).

[37]A. Gens. “On the hydromechanical behavior of argillaceous hard soil-weak rocks”. In: *15th European Conference on Soil Mechanics and Geotechnical Engineering- Geotechnics of Hard Soil- Weak Rocks (Part. 4)*. 2013 (cit. on p. 13).

[38]M. Ghoreychi. “Comportement rhéologique et couplages thermo-hydro-mécaniques dans les argilites de l’est: Experiences macroscopiques et analyses microscopiques”. In: *Journées scientifiques CNRS/ANDRA Etude de l’Est du bassin parisien*. 1997, pp. 109–128 (cit. on p. 14).

[39]Z Guan. “Ground reaction analyses in conventional tunnelling excavation”. In: *Tunnelling and Underground Space Technology* 22 (2007), pp. 230–237 (cit. on p. 42).

[40]L.-M. Guayacán-Carrillo. “Analysis of long-term closure in drifts excavated in Callovo-Oxfordian claystone: roles of anisotropy and hydromechanical couplings”. PhD thesis. 2016, p. 169 (cit. on p. 13).

[41]L. M. Guayacán-Carrillo, S. Ghabezloo, J. Sulem, D. M. Seyedi, and G. Armand. “Effect of anisotropy and hydro-mechanical couplings on pore pressure evolution during tunnel excavation in low-permeability ground”. In: *International Journal of Rock Mechanics and Mining Sciences* 97 (2017), pp. 1–14 (cit. on pp. 40, 41).

[42]L. M. Guayacán-Carrillo, J. Sulem, D. M. Seyedi, et al. “Analysis of Long-Term Anisotropic Convergence in Drifts Excavated in Callovo-Oxfordian Claystone”. In: *Rock Mechanics and Rock Engineering* 49.1 (2016), pp. 97–114 (cit. on pp. 12, 46).

[43]S. Hedan, V. Valle, and P. Cosenza. “Subpixel precision of crack lip movements by Heaviside-based digital image correlation for a mixed-mode fracture”. In: *Strain* 56.6 (2020), pp. 1–11 (cit. on p. 110).

[44]S. Hedan, V. Valle, R. Giot, and P. Cosenza. “Behavior in mixed-mode of desiccation cracks on a clayey rock front gallery”. In: *International Journal of Rock Mechanics and Mining Sciences* 154.April (2022) (cit. on p. 111).

[45]R. Hill. “A Theory of the Yielding and Plastic Flow of Anisotropic Metals.” In: *Series A, Mathematical and Physical Sciences* 193 (1948), pp. 281–297 (cit. on pp. 34, 36).

[46]J. C. Jaeger. “Shear Failure of Anistropic Rocks”. In: *Geological Magazine* 97.1 (1960), pp. 65–72 (cit. on p. 36).

[47]V. Labiouse and T. Vietor. “Laboratory and in situ simulation tests of the excavation damaged zone around galleries in opalinus clay”. In: *Rock Mechanics and Rock Engineering* 47.1 (2014), pp. 57–70 (cit. on pp. 2, 12, 73).

[48]B. Ladanyi, P. Montréal, and G. Archambault. *Rock Mechanics - Theory and Practice Proceedings of the 11th Symposium on Rock Mechanics Berkeley, CA, June 16-19, 1969 - Simulation of Shear Behavior of a Jointed Rock Mass*. Tech. rep. 1969 (cit. on p. 20).

[49]S Lambert and F Nicot. *Géomécanique des instabilités rocheuses, du déclenchement à l’ouvrage*. Lavoisier, 2010, pp. 97–123 (cit. on pp. 25–27).

[50]J Lemaitre, J.-L. Chaboche, A Benallal, and R Desmorat. “Mécanique des matériaux solides”. In: Dunod, 2009. Chap. Elasto-vis, pp. 267–269 (cit. on p. 19).

[51]J. Lemaitre. “Sur la détermination des lois de comportement des matériaux élastovisco-plastiques”. PhD thesis. 1971 (cit. on p. 37).

[52]Z. B. Liu, S. Y. Xie, J. F. Shao, and N. Conil. “Effects of deviatoric stress and structural anisotropy on compressive creep behavior of a clayey rock”. In: *Applied Clay Science* 114 (2015), pp. 491–496 (cit. on pp. 14, 210).

[53]G Lombardi. “Un modele pour le tunnel”. In: *Journees de l’aftes*. 1977 (cit. on p. 18).

[54]T. Manh, V. Jean, S. Didier, and N. Monin. “Semi-Analytical Solution for Stresses and Displacements in a Tunnel Excavated in Transversely Isotropic Formation with Non-Linear Behavior”. In: *Rock Mechanics and Rock Engineering* (2013), pp. 213–229 (cit. on p. 42).

[55]M. Mánica, A. Gens, J. Vaunat, and D. F. Ruiz. “A time-dependent anisotropic model for argillaceous rocks. Application to an underground excavation in Callovo-Oxfordian claystone”. In: *Computers and Geotechnics* 85 (2017), pp. 341–350 (cit. on pp. 11, 34).

[56]M. A. Mánica, A. Gens, J. Vaunat, G. Armand, and M.-n. Vu. “Numerical simulation of underground excavations in an indurated clay using non-local regularisation . Part 1 : formulation and base case”. In: *Geotechnique* (2021) (cit. on p. 11).

[57]M. A. Mánica, A. Gens, J. Vaunat, G. Armand, and M.-n. Vu. “Numerical simulation of underground excavations in an indurated clay using non-local regularisation . Part 2 : sensitivity analysis”. In: *Geotechnique* (2021) (cit. on p. 11).

[58]M. A. Mánica, A. Gens, J. Vaunat, and D. F. Ruiz. “Nonlocal plasticity modelling of strain localisation in stiff clays”. In: *Computers and Geotechnics* 103 (2018), pp. 138–150 (cit. on pp. 11, 12).

[59]P. M. Mestat. “Maillages d’éléments finis pour les ouvrages de géotechnique Conseils et recommandations”. In: (1997), pp. 39–64 (cit. on p. 45).

[60]R. d. B. P. A. Vermeer. “Non-associated plasticity for soils, concrete and rock”. In: (1984), pp. 1–64 (cit. on p. 41).

[61]B. Pardoen and F. Collin. “Modelling the influence of strain localisation and viscosity on the behaviour of underground drifts drilled in claystone”. In: *Computers and Geotechnics* 85 (2017), pp. 351–367 (cit. on pp. 11, 31).

[62]B. Pardoen, S. Levasseur, and F. Collin. “Using Local Second Gradient Model and Shear Strain Localisation to Model the Excavation Damaged Zone in Unsaturated Claystone”. In: *Rock Mechanics and Rock Engineering* 48.2 (2015), pp. 691–714 (cit. on p. 11).

[63]F. D. Patton. “Multiple modes of shear failure in rock”. In: *OnePetro* 1st ISRM C (1966) (cit. on pp. 20, 25).

[64]J. L. Pech-Pacheco, G. Cristöbal, J. Chamorro-Martínez, and J. Fernândez-Valdivia. “Diatom autofocusing in brightfield microscopy: A comparative study”. In: *Proceedings - International Conference on Pattern Recognition* 15.3 (2000), pp. 314–317 (cit. on p. 120).

[65]P Perzyna. “Fundamental problems in viscoplasticity”. In: *Advances in applied mechanics* 9 (1966), pp. 243–377 (cit. on p. 18).

[66]L Ponson, Z Shabir, M Abdulmajid, E. V. D. Giessen, and A Simone. “Unified scenario for the morphology of crack paths in two-dimensional disordered solids”. In: *Physical review* 055003 (2021), pp. 1–13 (cit. on p. 101).

[67]A. Pouya, Z. Bendjeddou, and A. Poutrel. “Determination of equivalent continuum mechanical model for fractured EDZ around underground galleries by homogenization”. In: *ISRM Regional Symposium - 7th Asian Rock Mechanics Symposium, ARMS 2012* April 2013 (2012), pp. 854–861 (cit. on p. 65).

[68]A. Pouya. *Fracsima : Disroc, a Finite Element Code for modelling Thermo-Hydro-Mechanical processes in fractured porous media*. 2016 (cit. on pp. 31, 32, 64).

[69]J. Réthoré, F. Hild, and S. Roux. “Shear-band capturing using a multiscale extended digital image correlation technique”. In: *Computer Methods in Applied Mechanics and Engineering* 196.49-52 (2007), pp. 5016–5030 (cit. on p. 110).

[70]J. C. Robinet. “Minéralogie, porosité et diffusion dans l’argilite du Callovo-Oxfordien de Bure (Meuse/Haute-Marne, France) de l’échelle centimetrique à micrométrique”. PhD thesis. Université de Poitiers, 2008 (cit. on p. 13).

[71]A. Rullière, P. Rivard, L. Peyras, and P. Breul. “Influence of Roughness on the Apparent Cohesion of Rock Joints at Low Normal Stresses”. In: *Journal of Geotechnical and Geoenvironmental Engineering* 146.3 (2020), p. 04020003 (cit. on p. 79).

[72]N. Rupin. “Ecoulement viscoplastique à chaud de métaux biphasés : modèles varationnels , influence de la répartition des phases et confrontations expérimentales”. PhD thesis. 2008 (cit. on pp. 109, 110).

[73]S. Sammartino, A. Bouchet, D. Prêt, J. C. Parneix, and E. Tevissen. “Spatial distribution of porosity and minerals in clay rocks from the Callovo-Oxfordian formation (Meuse/Haute-Marne, Eastern France) - Implications on ionic species diffusion and rock sorption capability”. In: *Applied Clay Science* 23.1-4 (2003), pp. 157–166 (cit. on p. 13).

[74]D. M. Seyedi and G. Armand. *Compte-rendu: Réunion plénière du Groupement de Laboratoires (GL) Comportement Mécanique des Ouvrages et des composants de stockages (MOUV)*. Tech. rep. Andra technical report, 2016 (cit. on pp. 13, 209).

[75]D. M. Seyedi, G. Armand, and A. Noiret. ““Transverse Action” – A model benchmark exercise for numerical analysis of the Callovo-Oxfordian claystone hydromechanical response to excavation operations”. In: *Computers and Geotechnics* 85 (2017), pp. 287–305 (cit. on pp. 11, 47).

[76]J. A. W. Shabnam J. Semnani and R. I. Borj. “Thermoplasticity and strain localization in transversely isotropic materials based on anisotropic critical state plasticity”. In: *International Journal for Numerical and Analytical Methods in Geomechanics* 30.13 (2016), pp. 1303–1336 (cit. on p. 36).

[77]H. L. Shi, J. Hosdez, T. Rougelot, et al. “Analysis of Local Creep Strain Field and Cracking Process in Claystone by X-Ray Micro-Tomography and Digital Volume Correlation”. In: *Rock Mechanics and Rock Engineering* 54.4 (2021), pp. 1937–1952 (cit. on p. 15).

[78]M. Souley, G. Armand, and J. B. Kazmierczak. “Hydro-elasto-viscoplastic modeling of a drift at the Meuse/Haute-Marne underground research laboratoratory (URL)”. In: *Computers and Geotechnics* 85 (2017), pp. 306–320 (cit. on p. 11).

[79]M Souley, M. N. Vu, and G Armand. “3D anisotropic modelling of deep drifts at the Meuse / Haute-Marne URL”. In: *Applied Numerical Modeling in Geomechanics – 2020*. June. 2020, pp. 2–6 (cit. on p. 11).

[80]M. Souley, M. Ngoc, and V. Gilles. “3D Modelling of Excavation - Induced Anisotropic Responses of Deep Drifts at the Meuse / Haute - Marne URL”. In: *Rock Mechanics and Rock Engineering* 55.7 (2022), pp. 4183–4207 (cit. on p. 11).

[81]E. Stavropoulou. “Comportement différé des interfaces argilite / béton : caractérisation et modélisation Time effect on the mechanical behaviour of the clay-rock / concrete interface : experiments and modelling”. PhD thesis. 2017 (cit. on pp. 20, 28, 83, 93).

[82]M. Sutton, W. Wolters, W. Peters, W. Ranson, and S. McNeill. “Determination of displacements using an improved digital correlation method”. In: *Image and Vision Computing* 1.3 (1983), pp. 133–139 (cit. on p. 110).

[83]E. Trivellato, A. Pouya, M. N. Vu, and D. M. Seyedi. “A softening damage-based model for the failure zone around deep tunnels in quasi-brittle claystone”. In: *Tunnels and Underground Cities: Engineering and Innovation meet Archaeology, Architecture and Art- Proceedings of the WTC 2019 ITA-AITES World Tunnel Congress*. Ed. by V. C. E. Peila. May. CRC Press., 2019, pp. 4242–4251 (cit. on p. 11).

[84]E. Trivellato. “Softening damage contributions to the failure zone around deep tunnels in quasi-brittle rocks”. PhD thesis. 2019 (cit. on pp. 1, 13).

[85]E. Trivellato, A. Pouya, and M.-n. Vu. “Damage-Based Cohesive Modelling for Fractures Initiation and Propagation Around a Deep Tunnel in Quasi-brittle Rocks”. In: *Proceedings of GeoShanghai 2018 International Conference: Rock Mechanics and Rock Engineering*. June. 2018 (cit. on p. 31).

[86]G. Tzortzopoulos and I. Stefanou. “Designing experiments for Controllinkg earthQuakes (Co-Quake) by fluid injection”. In: *12th HSTAM International Congress on Mechanics Thessaloniki th HSTAM International Congress on Mechanics* September (2019) (cit. on pp. 96, 100).

[87]J. A. Wang, Y. X. Wang, Q. J. Cao, Y. Ju, and L. T. Mao. “Behavior of microcontacts in rock joints under direct shear creep loading”. In: *International Journal of Rock Mechanics and Mining Sciences* 78 (2015), pp. 217–229 (cit. on pp. 27, 28).

[88]M. Wang and M. Cai. “A Simplified Model for Time-Dependent Deformation of Rock Joints”. In: *Rock Mechanics and Rock Engineering* 0123456789 (2021) (cit. on p. 27).

[89]Z. Wang, L. Gu, Q. Zhang, and B. A. Jang. “Influence of Initial Stress and Deformation States on the Shear Creep Behavior of Rock Discontinuities with Different Joint Roughness Coefficients”. In: *Rock Mechanics and Rock Engineering* 54.11 (2021), pp. 5923–5936 (cit. on p. 27).

[90]Y. Wileveau and F. Bernier. “Similarities in the hydromechanical response of Callovo-Oxfordian clay and Boom Clay during gallery excavation”. In: *Physics and Chemistry of the Earth* 33.SUPPL. 1 (2008), pp. 343–349 (cit. on p. 13).

[91]Y. Wileveau, F. H. Cornet, J. Desroches, and P. Blumling. “Complete in situ stress determination in an argillite sedimentary formation”. In: *Physics and Chemistry of the Earth* 32.8-14 (2007), pp. 866–878 (cit. on pp. 6, 13, 73).

[92]T. Xu, Q. Xu, C. an Tang, and P. G. Ranjith. “The evolution of rock failure with discontinuities due to shear creep”. In: *Acta Geotechnica* 8.6 (2013), pp. 567–581 (cit. on p. 27).

[93]D. S. Yang, M Bornert, H Gharbi, P Valli, and L. L. Wang. “Optimized optical setup for DIC in rock mechanics”. In: *EPJ Web of Conferences*. Vol. 22019. 2010 (cit. on pp. 103, 113, 114).

[94]D. Yang, M. Bornert, S. Chanchole, et al. “Experimental investigation of the delayed behavior of unsaturated argillaceous rocks by means of Digital Image Correlation techniques”. In: *Applied Clay Science* 54.1 (2011), pp. 53–62 (cit. on pp. 14, 180).

[95]C. Yao, J. F. Shao, Q. H. Jiang, and C. B. Zhou. “Numerical study of excavation induced fractures using an extended rigid block spring method”. In: *Computers and Geotechnics* 85 (2017), pp. 368–383 (cit. on p. 11).

[96]Z. Yu, J.-f. Shao, M.-n. Vu, and G. Armand. “Numerical study of thermo-hydro-mechanical responses of in situ heating test with phase-field model”. In: *International Journal of Rock Mechanics and Mining Sciences* 138.November 2020 (2021), p. 104542 (cit. on p. 12).

[97]Z. Yu, J. Shao, G. Duveau, M.-n. Vu, and G. Armand. “Numerical modeling of deformation and damage around underground excavation by phase-field method with hydromechanical coupling”. In: *Computers and Geotechnics* 138.June (2021), p. 104369 (cit. on p. 12).

[98]C. L. Zhang, G. Armand, N. Conil, and B. Laurich. “Investigation on anisotropy of mechanical properties of Callovo-Oxfordian claystone”. In: *Engineering Geology* 251 (2019), pp. 128–145 (cit. on pp. 13, 14, 40).

List of Figures

List of Tables

Appendix

A

A.1 Appendix: 2D stress solution around drift in case of elasticity and in case of elastoplasticity

The description of the state of stress around an excavation, in elasticity and elasto- perfect plasticity, is well known in geomechanics, and is therefore briefly recalled below.

Assuming a circular excavation in an isotropic linear elastic medium, while neglecting the body forces, the analytical solution for the calculation of the stress field around a circular borehole exists. For the sake of simplicity cylindrical coordinates are used, the cross-section of the tunnel is in the (r, θ) plane and the tunnel is assumed to be excavated along the z-direction. Figure A.1 gives the plane of reference for the analysis of stress-strain field in a cross section of the tunnel. The stress field around a circular borehole is deduced from

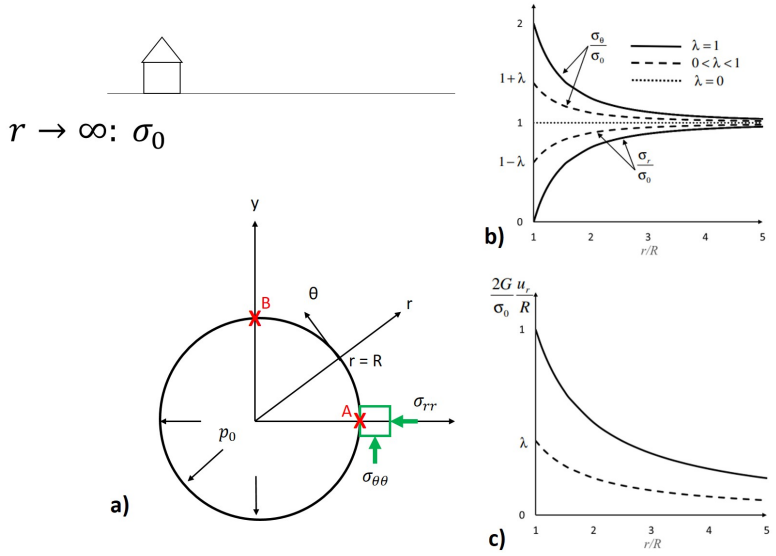

Fig. A.1.: a) Representation of a circular borehole cross section in the (r, θ) coordinate system. b) Evolution of the radial and hoop stresses moving radially away from the drift wall, c) radial displacement moving radially away from the drift wall (with G the shear modulus of the rock mass). Dot curves in b) and c) show the stress state and radial displacement if the excavation is not completed i.e. for $0 < \lambda < 1$.

the equilibrium equation, material behavior and boundary conditions. Its expression in cylindrical coordinates is given in equation A.1 for its general expression, and in the r and θ directions in equation A.2, assuming the absence of body forces and plane strain conditions (i.e. $\varepsilon_{zz} = 0$, and $\sigma = \sigma(r, \theta)$).

$$\nabla \sigma = 0 \tag{A.1}$$

$$\frac{\partial \sigma_{rr}}{\partial r} + \frac{\sigma_{rr} - \sigma_{\theta\theta}}{r} = 0 \; ; \; \frac{1}{r}\frac{\sigma_{\theta\theta}}{\partial \theta} + \frac{\partial \sigma_{r\theta}}{\partial r} + 2\frac{\sigma_{r\theta}}{r} = 0 \tag{A.2}$$

We assume that the tunnel radius is $r = R$. We place ourselves in the case of a tunnel excavated in an isotropic elastic medium and supported by a lining applying a pressure p_0 on its wall. The fictive pressure of the lining can be expressed as a function of the excavation rate is $p_0 = (1 - \lambda)\sigma_0$, with $p_0 = \sigma_0$ before the beginning of the excavation and $p_0 = 0$ without support ($\lambda = 1$). The tensor describing an isotropic *in situ* stress state for every point of the undisturbed (before the excavation) medium is given by equation A.3.

$$\sigma = \sigma_0 \mathbf{I}_{(3\times3)} \tag{A.3}$$

with $\mathbf{I}_{(3\times3)}$ the identity matrix. The solution of the stress components is given by applying the boundary conditions corresponding to the far field conditions ($r \to \infty$) and to the gallery perimeter ($r \to R$) to equations A.2. Thus the radial and orthoradial stress components is given by equations A.4 and A.17.

$$\sigma_{rr} = \sigma_0 - (\sigma_0 - p_0)\frac{R^2}{r^2} \tag{A.4}$$

$$\sigma_{\theta\theta} = \sigma_0 + (\sigma_0 - p_0)\frac{R^2}{r^2} \tag{A.5}$$

if we assume that the excavation is complete and that the tunnel is not supported, we obtain the following stress state at the tunnel wall (i.e. for $r = R$):

$$\sigma_{rr} = 0 \text{ and } \sigma_{\theta\theta} = 2\sigma_0 \tag{A.6}$$

As we move radially away from the tunnel walls, the stresses σ_{rr} and $\sigma_{\theta\theta}$ tend in $\frac{1}{r^2}$ towards the infinite stress σ_0 (see in Figure A.1 b)). Whatever increment of one stress component corresponds to an equal decreasing of the other:

$$\forall r \; ; \; \Delta\sigma_{rr} = -\Delta\sigma_{\theta\theta} \tag{A.7}$$

Under all those hypothesis, the excavation of a circular tunnel induces an increase in the deviatoric part of the stress. The increment of the volumetric part of the stress tensor is null because the sum of the components of the stress tensor is equal to zero (see equation

A.7). Thus, the material is subjected only to distortional deformations, without volumic deformations. The out-of-plane component of the stress tensor σ_{zz} is given by the plane strain condition.

$$\varepsilon_{zz} = \frac{\sigma_{zz}}{E} - \frac{\nu}{E}(\sigma_{rr} + \sigma_{\theta\theta}) = 0 \;\rightarrow\; \sigma_{zz} = \nu(\sigma_{rr} + \sigma_{\theta\theta}) \tag{A.8}$$

E is the Young's modulus and ν the Poisson ratio. Thus one as: $\Delta\sigma_{zz} = 0$. As in the different numerical simulations presented in the manuscript, Mohr-Coulomb's yield criteria is considered, the out-of-plane stress is calculated, under the assumption of equation A.8 to verify that it is indeed an intermediate stress.

In the manuscript, in all the numerical simulations related to the drifts excavated along the minor principal horizontal stress, the stress state in the tunnel cross-section is anisotropic thus it is convenient to have an idea of the hoop stress in two points A and B (because it corresponds to the points of interest when looking at the vertical and horizontal convergences of the drift) shown in Figure A.1. Thus assuming that the initial stress state is anisotropic:

$$\boldsymbol{\sigma_0} = \begin{pmatrix} \sigma_{xx0} & 0 \\ 0 & \sigma_{yy0} \end{pmatrix} \tag{A.9}$$

Assuming that $\sigma_{xx0} < \sigma_{yy0}$, and that the drift is not supported $p_0 = 0$, then the hoop stress in point A and in point B are given by:

$$\sigma_{\theta\theta}(A) = 3\sigma_{yy0} - \sigma_{xx0} \tag{A.10}$$

$$\sigma_{\theta\theta}(B) = -\sigma_{yy0} + 3\sigma_{xx0} \tag{A.11}$$

Thus $\sigma_{\theta\theta}(A) > \sigma_{\theta\theta}(B)$. Recall that these equations are true for an elastic isotropic medium.

Assuming a linear elastic with perfect yielding medium, it is possible to determine the extension of the plastic radius R_p as well as the stress tensor in every point of the medium. The quality of the mesh of the numerical simulations is checked by comparing the analytical value of the plastic radius with the numerically obtained plastic radius. The same coordinate system is assumed as in the elastic calculation. We assume perfect plasticity, and an isotropic stress state σ_0 under plane strain conditions. The yield criterion $F(\sigma_1, \sigma_3) = 0$ is Mohr-Coulomb's criterion. The principal stresses are written σ_1 and σ_3, while σ_{zz} is assumed to be an intermediate stress. Mohr-Coulomb criteria is given by:

$$\sigma_{\theta\theta} - K_p\sigma_{rr} - \sigma_c = 0 \text{ with } K_p = \frac{1 + sin\phi}{1 - sin\phi} \;;\; \sigma_c = \frac{2Ccos\phi}{1 - sin\phi} \tag{A.12}$$

The equilibrium equations A.1 and A.2 still holds. At the drift wall the stress state is given by:

$$\sigma_{rr} = (1-\lambda)\sigma_0 \text{ and } \sigma_{\theta\theta} = (1+\lambda)\sigma_0 \tag{A.13}$$

The yield criterion is reached at the wall for a deconfinement rate λ_e which is such that $F((1+\lambda_e)\sigma_0,(1-\lambda_e)\sigma_0) = 0$. The deconfinement rate for which plasticity occurs is given by:

$$(1-\lambda_e)\sigma_0 = K_p(1+\lambda_e)\sigma_0 + \sigma_c \;\rightarrow\; \lambda_e = \frac{1}{K_p+1}(1+K_p+\frac{\sigma_c}{\sigma_0}) \tag{A.14}$$

The boundary conditions at the drift wall and at the plastic radius are the following:

$$\sigma_{rr}(r=R) = (1-\lambda)\sigma_0 \tag{A.15}$$

$$\sigma_{rr}(r=R_p) = (1-\lambda_e)\sigma_0 \tag{A.16}$$

At failure the hoop stress must respect the equation:

$$\sigma_{\theta\theta} = K_p\sigma_{rr} + \sigma_c \tag{A.17}$$

Thus the radial equilibrium (equation A.2) becomes:

$$\frac{\partial\sigma_{rr}}{\partial r} + \frac{\sigma_{rr}}{r}(1-K_p) = \frac{\sigma_c}{r} \tag{A.18}$$

The solution is:

$$\sigma_{rr} = \frac{1}{1-K_p}\sigma_c + Ar^{K_p-1} \tag{A.19}$$

Constant A is determined by applying the boundary condition equation A.15 to equation A.19. Thus:

$$A = \frac{1}{R^{K_p-1}}((1-\lambda)\sigma_0 - \frac{1}{1+K_p}\sigma_c) \tag{A.20}$$

Thus the radial and hoop stresses in the plastic zones, for $R \leq r \leq R_p$ are:

$$\sigma_{rr} = \frac{\sigma_c}{K_p-1}[(\frac{r}{R})^{K_p-1} - 1] + (1-\lambda)\sigma_0(\frac{r}{R})^{K_p-1} \tag{A.21}$$

$$\sigma_{\theta\theta} = \frac{\sigma_c}{K_p-1}[K_p(\frac{r}{R})^{K_p-1} - 1] + K_p(1-\lambda)\sigma_0(\frac{r}{R})^{K_p-1} \tag{A.22}$$

The plastic radius is given by evaluating the radial stress (given by equation A.21) in $r = R_p$ knowing that the radial stress is also given by equation A.16.

$$R_p = [\frac{2}{K_p+1}\frac{(K_p-1)\sigma_0+\sigma_c}{(1-\lambda)(K_p-1)\sigma_0+\sigma_c}]^{\frac{1}{K_p-1}} \tag{A.23}$$

Tab. A.1.: Data for σ_0 with confining pressure $p_c = 12MPa$ with different inclinations and approximately the same initial water content

$\omega[^\circ]$	q[MPa] ($p_c = 12MPa$)
0	40.9
12	38.4
45	26.0
50	41.0
75	39.6
77	35.3

A.2 Appendix: Estimation of parameters b_T^p and a_N^v

A.2.1 Parameter b_T^p

A first order of magnitude of parameter b_T^p is calculated based on the results of an experimental campaign supervised by ANDRA [74]. The available data for failure of COx specimens, sampled with different orientations and derived from triaxial tests confined at 12 MPa showed that the minimum resistance is found for $\omega = 45^\circ$. Table A.1 reports the over mentioned data in terms of deviator q at failure. Assuming the strength criterion of Mohr Coulomb with $\phi = 24^\circ$ and $C = 4MPa$.

$$\sigma_1 = R_c + K_p \sigma_3 \tag{A.24}$$

With $K_p = \frac{1+sin\phi}{1-sin\phi}$. R_c is determined with the results obtain for $\omega = 0^\circ$. Parameter b_T^p is determined with the results obtain for $\omega = 45^\circ$. In that case $\sigma_1 = 38MPa$ and $\sigma_3 = 12MPa$.

$$\underline{\underline{\sigma}} = \begin{pmatrix} 12 & 0 & 0 \\ 0 & 12 & 0 \\ 0 & 0 & 12 \end{pmatrix} + 26\, \underline{n} \otimes \underline{n} = \begin{pmatrix} 25 & 13 & 0 \\ 13 & 25 & 0 \\ 0 & 0 & 12 \end{pmatrix} \tag{A.25}$$

The strength criterion is applied to the modified stress tensor:

$$\underline{\underline{\sigma}} = \begin{pmatrix} 25 & f_T 13 & 0 \\ f_T 13 & f_N 25 & 0 \\ 0 & 0 & 12 \end{pmatrix} \tag{A.26}$$

This matrix must be diagonalized, knowing that $\lambda = 12$ is eigenvalue. The characteristic polynomial is given by equation A.27. For sake of simplicity we assume that $f_N = 1$.

$$625 - 50\lambda + \lambda 2 - 169 f_T^2 = 0 \tag{A.27}$$

$\Delta = 676 f_T^2$ and the two other eigenvalues are $\lambda_1 = \frac{50+\sqrt{\Delta}}{2}$ and $\lambda_2 = \frac{50-\sqrt{\Delta}}{2}$. Assuming that $\lambda_1 > \lambda_2$, an expression of f_T is deduced from the Mohr-Coulomb criterion.

$$\lambda_1 = R_c + K_p \lambda_2 \tag{A.28}$$

$$\sqrt{\Delta} = \frac{2R_c + 50K_p - 50}{1 + K_p} = 26 f_T \tag{A.29}$$

This gives that $f_T = 1.34$. The eigenvalues corresponding to the principal stress are $\lambda_1 = 42.4$MPa and $\lambda_2 = 7.6$MPa, giving that $\lambda = 12$MPa is the intermediate principal stress. Parameters $b_T^p = f_T^2 - 1 = 0.8$.

A.2.2 Parameter a_N^v

[52] have studied the structural anisotropy on compressive creep behavior of COx claystone.

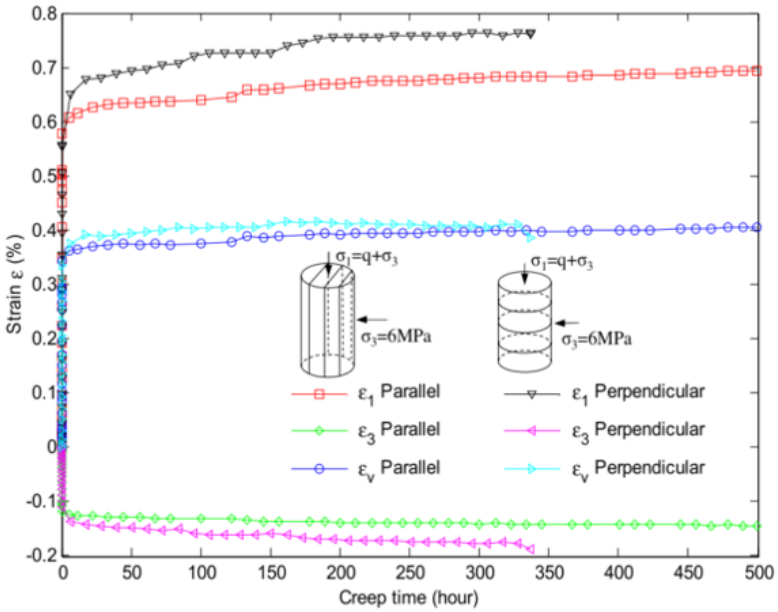

Fig. 8. Comparison of strains between perpendicular and parallel samples with deviatoric creep stress level of $q/q_{peak} = 82\,\%$.

Fig. A.2.: Plot of the viscous strain under stress applied perpendicular and parallel to the bedding planes [52].

$$\frac{\varepsilon_{\parallel}}{\varepsilon_{\perp}} = 1 + a_N^v = \frac{1.95}{2.79} \tag{A.30}$$

Finally, it results in an initial estimate of $a_N^v = 0.43$.

A.3 Appendix: Mesh sensitivity analysis with viscosity

Mesh analysis performed in elasto-plasticity showed that mesh 2 is sufficiently refined, so numerical simulations were conducted with this mesh. Nevertheless, a final examination was performed by introducing the viscous behavior in the last phase of excavation of the drift. This check was only carried out retrospectively because the computation time is considerably increased by the addition of the viscosity in the models with mesh 3. The computation time becomes about three times longer than with mesh 2, knowing that with this mesh the computation time is already about 2 days. Moreover, it was expected that the viscosity has a favorable effect on the convergence of the mesh. However, the comparison of the 3 meshes for an elasto-viscoplastic excavation presented in Figure A.4 shows that mesh 2 is not sufficiently refined. Thus in the further work, the refinement of the mesh should be reconsidered. It can be judicious to think of solutions of refinement of the mesh during the calculations in order to reduce at most the time of calculations. However this raises a lot of questions, if only about the choice between triangular or quadrangular elements, because in this case the handling of triangular elements would be easier. Maybe further development on the discretization of the time step Δt would be helpful. Increasing the viscosity in the model seems to make it necessary to refined more the mesh than for what predicted with the plastic calculation.

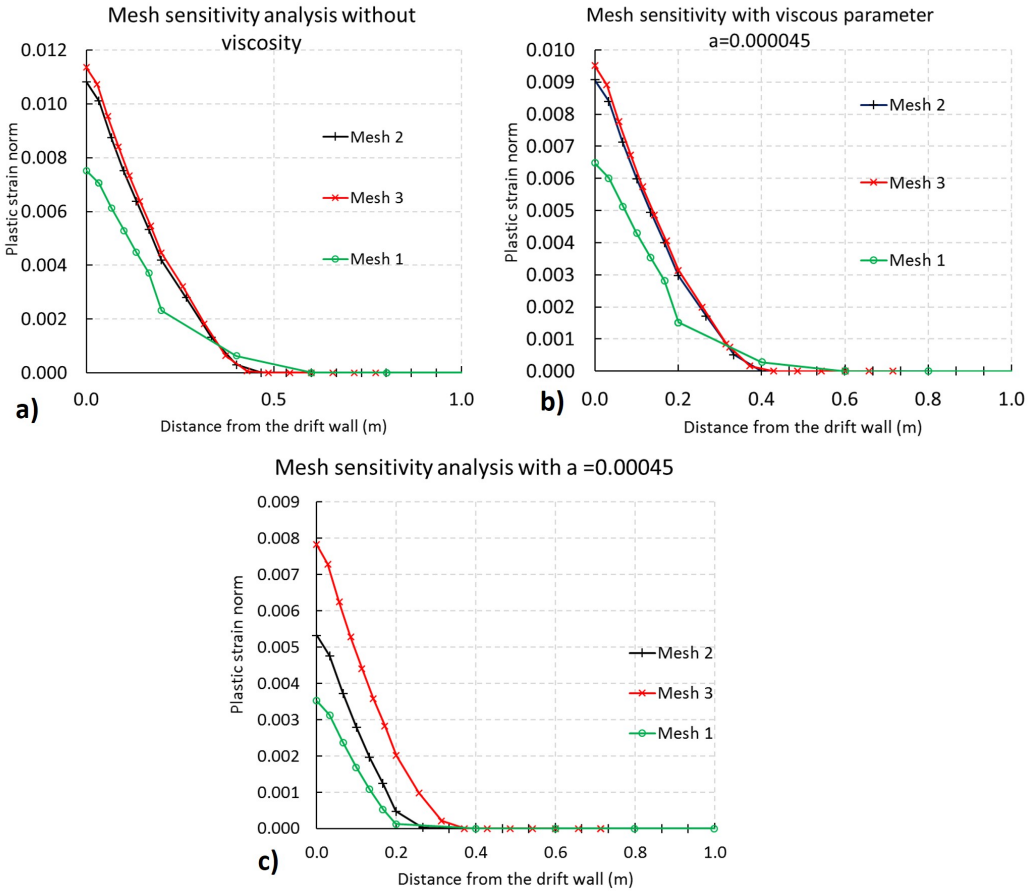

Fig. A.3.: Plot of the plastic strain norm in function of the distance from the wall of the drift for three different mesh. Mesh 1 is the less refined, Mesh 2 is the mesh used in the numerical simulations, and Mesh 3 is the more refined mesh. a) Mesh sensitivity without viscosity b) mesh sensitivity with little viscosity c) mesh sensitivity with viscosity parameter a ten times bigger than in plot b).

A.4 Appendix: Mesh sensitivity analysis

A mesh verification was done by comparing the used mesh *Mesh 2* to a coarser mesh *Mesh 1* and a more refined mesh *Mesh 3*. The element sizes for the three different meshes are given in Figure A.5b). The plastic radii obtained for the three meshes are then compared. Figure A.5 gives the norm of the plastic strain as one moves radially away from the tunnel wall. The theoretical plastic radius is the same as calculated in chapter 3, namely $R_p = 3.03$ m. The error is estimated by comparing the theoretical plastic radius with those obtained in the different numerical simulations. It is found that an error of 63% is made with *Mesh 1*, 6% with *Mesh 2* and 4% with *Mesh 3*.

$$\frac{|r_p(mesh) - r_p(theoretical)|}{r_p(theoretical)}\% \tag{A.31}$$

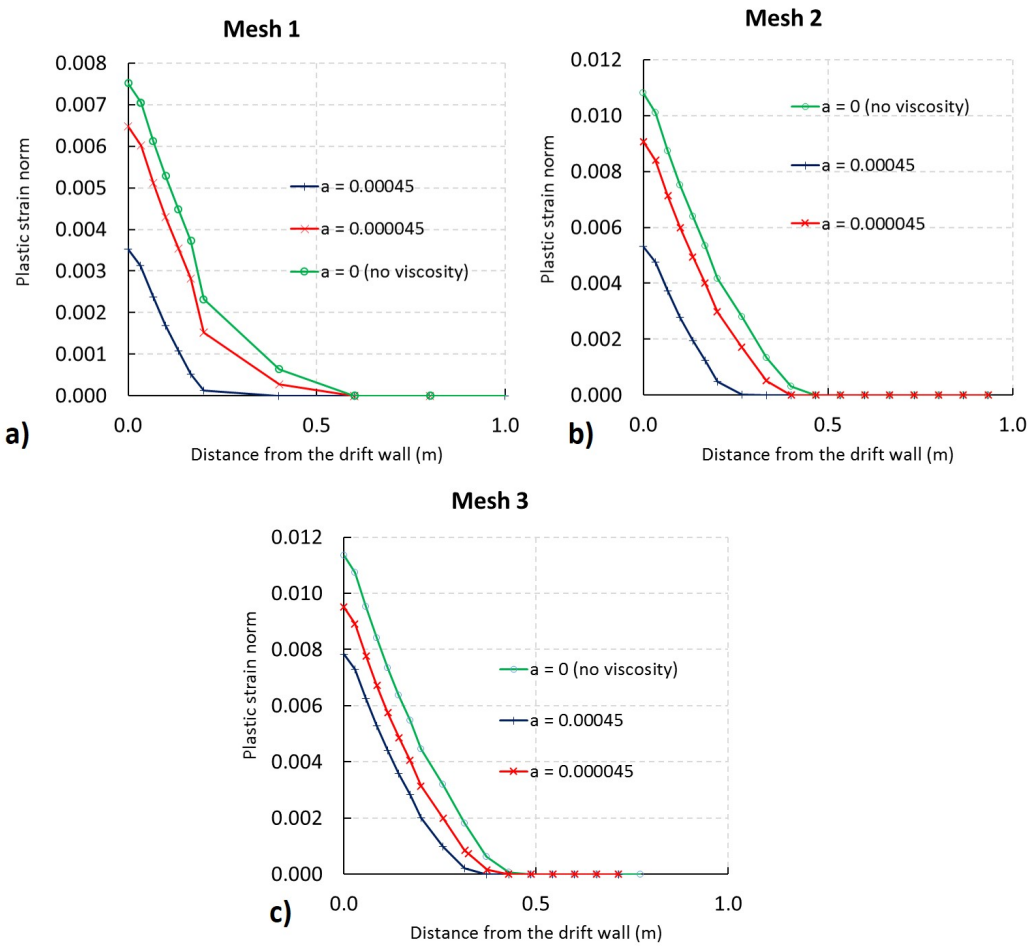

Fig. A.4.: Evaluation of the error due to the finite elements approximation. Plot of the plastic strain norm in function of the distance from the wall of the drift for three different mesh.

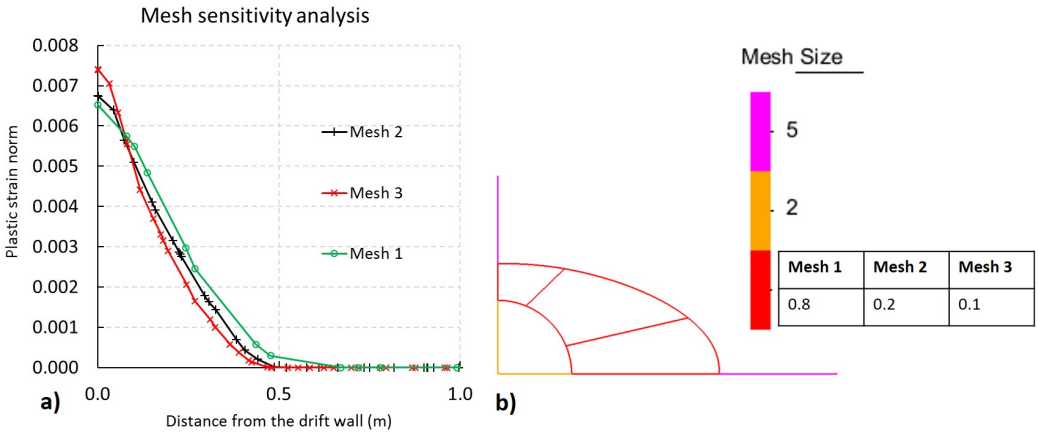

Fig. A.5.: Plot of the norm of the plastic strain as one moves radially away from the tunnel wall for the three different meshes.

Figure A.6 gives the norm of the plastic strain obtained for the three meshes. *Mesh 2* is

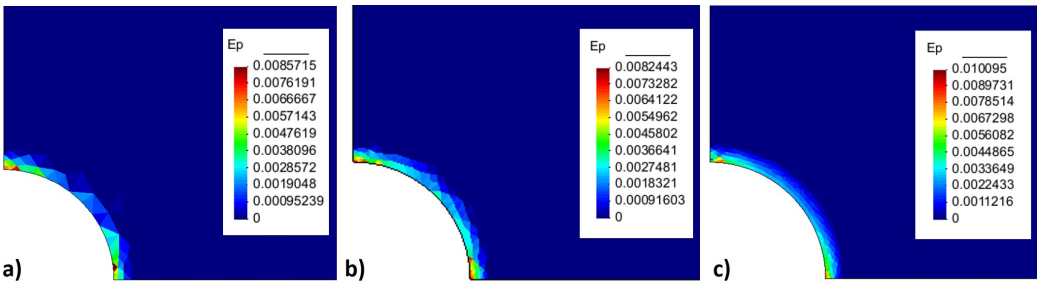

Fig. A.6.: Map of the norm of the plastic strain for a) *Mesh 1*, b) *Mesh 2*, c) *Mesh 3*.

retained for the numerical simulations presented in chapter 4, because the error is almost the same as for *Mesh 3* and the calculation time is much lower.

A.5 Appendix: Estimation of the normal stress on chevron fracture

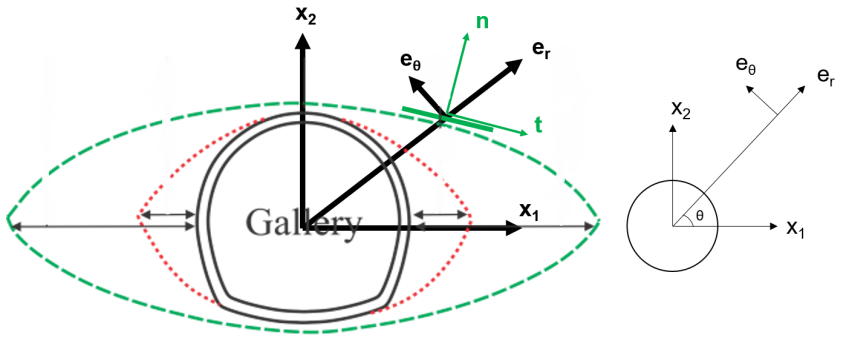

Fig. A.7.: Estimation of the normal stress applied on the chevron fractures assuming an elastic behavior of the rock mass.

We estimate the normal stress on a chevron fracture, its orientation is as shown in Figure A.7. Let us assume that the drift is a circular hole in an infinite elastic isotropic medium subjected to a state of stress (σ_1, σ_2) very far away from the tunnel. The components of the stress tensor are then given by :

$$\sigma_{rr} = \sigma_1 \cos^2(\theta) + \sigma_2 \sin^2(\theta) - \frac{(\sigma_1+\sigma_2)R^2}{2r^2} + \frac{\sigma_1-\sigma_2}{2}(4 - \frac{3R^2}{r^2})\frac{R^2}{r^2}\cos(2\theta) - p\frac{R^2}{r^2} \tag{A.32}$$

$$\sigma_{\theta\theta} = \sigma_1 \cos^2(\theta) + \sigma_2 \sin^2(\theta) + \frac{(\sigma_1+\sigma_2)R^2}{2r^2} + \frac{3(\sigma_1-\sigma_2)}{2}\frac{R^4}{r^4}\cos(2\theta) + p\frac{R^2}{r^2} \tag{A.33}$$

$$\sigma_{r\theta} = \frac{\sigma_1-\sigma_2}{2}(1 + (2 - \frac{3R^2}{r^2})\frac{R^2}{r^2}), \sin(2\theta) \tag{A.34}$$

with $R = 2.6$ m the radius of the drift. The drift is assumed not to be supported: $p = 0$ MPa. The horizontal stress $\sigma_1 = -16$ MPa and the vertical stress $\sigma_2 = -13$ MPa. Assuming that the fracture is at about one radius of the drift wall, $r = 5.2$ m and $\theta = 45°$, we then get:

$$\begin{pmatrix} \sigma_{rr} & \sigma_{r\theta} \\ \sigma_{r\theta} & \sigma_{\theta\theta} \end{pmatrix} = \begin{pmatrix} -10.9 & 2 \\ 2 & -17.9 \end{pmatrix} \text{(MPa)} \tag{A.35}$$

Equation A.35 gives the stress state at the point located at $R = 5.2$m from the center of the drift and $\theta = 45°$. Assuming that the fracture is turned by 15° from the axis e_θ the normal stress applied on the fracture is about -10 MPa.

A.6 Appendix: Analyze of surfaces' roughness

Two different protocol of polishing have been compared by the company called Tortoise. The surfaces are polished by hand either only with P40 sandpaper or, in the second protocol, they are also post-polished with P60 sandpaper. Several surfaces are analyzed to check the repeatability of the polishing. In addition, in order to verify the uniformity of the polishing on the entire surface, each surface was studied in six different locations. The results of

No. Echantillon	No. Surface	ξ (µm)		ξ_{moy} (µm)
P40	1	13.68	16.4 ± 2.8	17.7 ± 4.4
		20.43		
		15.67		
		17.32		
		18.21		
		12.92		
	2	20.02	19.1 ± 5.4	
		16.73		
		16.47		
		14.81		
		17.12		
		29.78		
P40 + P60	1	12.98	13 ± 1	13.7 ± 2
		11.78		
		14.69		
		12.24		
		13.14		
		13.75		
	2	19.01	14.2 ± 2.5	
		14.97		
		14.13		
		12.79		
		11.62		
		13.19		

Fig. A.8.: Results of the roughness measured in different locations of the sample.

the analyze are presented in Figure A.8. The analysis shows that the roughness of the sample only polished with P40 sandpaper is closer to the *in situ* roughness than for the other protocol. However, the measurements are very scattered.

A.7 Appendix: Calibration of the viscous law with multilevel stress path

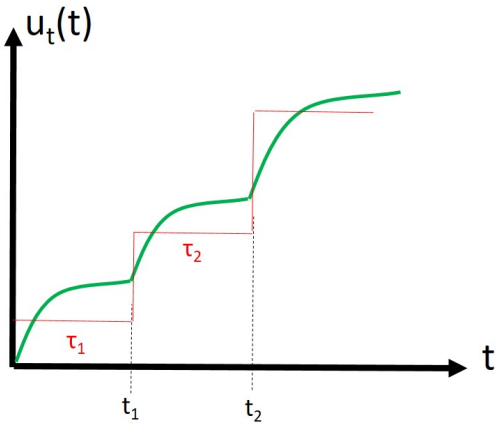

Fig. A.9.: Representation of the total slip (green curve) under multilevel stress

$$u_t^v(t) = a\tau^n t^\alpha \tag{A.36}$$

Assuming that the viscous behavior of our interface can be described by equation A.36, and that we want to fit the parameters a, n and α of the law, the procedure to operate would be the following: Supposing that at $t = 0$, $u_t^v(t) = 0$, the difficulty consists in estimating u_v for $t > t_1$ (for $t < t_1$ the viscous deformation is directly given by equation A.36). As a matter of fact, the measured slip contain the slip due to the first stress level $u_t^v(t_1)$ plus the elastic slip due to the stress increment $(\tau_2 - \tau_1)$ plus of course the viscous slip developing under the current stress τ_2 during $(t - t_1)$.

Therefore we put, $\xi(t) = (u_t^v)^{1/\alpha}$, which varies linearly with time, and to simplify the writing of the following equations $A = a^{1/\alpha}$ and $\frac{n}{\alpha} = m$.

Now for $t > t_1$:

$$\dot{\xi} = A\tau_2^m \tag{A.37}$$

$$\xi(t) = \xi(t_1) + \dot{\xi}(t - t_1) \tag{A.38}$$

The total slip that can be measured during this second stress level τ_2 for $(t_1 < t < t_2)$ is given by:

$$u_t(t) = u_t(t_1^+) + \xi(t)^\alpha = u_t(t_1^+) + [\xi(t_1) + \dot{\xi}(t - t_1)]^\alpha \tag{A.39}$$

$$u_t(t) = u_t(t_1^+) + [\xi(t_1) + A\tau_2(t-t_1)]^\alpha \tag{A.40}$$

With $u_t(t_1^+)$ the contribution from the previous stress level. $\xi(t_1)$ is a constant equal to $A\tau_1^m t_1$. In our experiment we come to measure what we call the viscous slip $u_t(t) - u_t(t_1^+)$. We therefore seek to minimize the function:

$$f(t) = B_1[(1 + B_2(t-t_1))^\alpha - 1] \tag{A.41}$$

With the following constant : $B_1 = (A\tau_1^m t_1)^\alpha$ and $B_2 = \frac{A\tau_2^m}{(A\tau_1^m t_1)^\alpha}$

$$\mathscr{D} = \sum_{t_i} [f(t_i) - u^v(t_i))]^2 . \rho_i \tag{A.42}$$

Using the viscous slip measurements $u^v(t_i)$ under several loading levels and using the method of least squares we can determine the constants B_1 and B_2, by solving:

$$\frac{\partial \mathscr{D}}{\partial B_1} = 0 \tag{A.43}$$

$$\frac{\partial \mathscr{D}}{\partial B_2} = 0 \tag{A.44}$$

By possibly granting different weights ρ_i to part of the data. B_2 being very non-linear it is easier to start from the equation obtained by deriving $\mathscr{D}$ with respect to B_1 to express it as a function of B_2 and α. The calculation of the derivative of $\mathscr{D}$ with respect to B_1 allows us to express the constant B_1 as a function of B_2 and α, given by the equation A.45.

$$B_1 = \frac{\sum_{t_i} [(1 + B_2(t-t_1))^\alpha - 1] u^v(t_i) \rho_i}{\sum_{t_i} [(1 + B_2(t_i-t_1))^\alpha - 1]^2 \rho_i} \tag{A.45}$$

From some reasonable values of alpha, knowing that $0 < \alpha < 1$ (e.g. estimated on a first loading level), $\mathscr{D}$ can be plotted as a function of B_2. B_2 can be varied from 0 to reasonably large values. The value of B_2 is chosen to minimize $\mathscr{D}(\alpha, B_2)$. This minimum is denoted $\mathscr{D}(\alpha)$ as it depends on the value of α, and α is chosen such as to minimize $\mathscr{D}(\alpha)$. If the function $\mathscr{D}$ has several local minima for the same α value, in this case the choice of the value of B_2 deserves further discussion. For instance by returning to the definition of B_2, values that do not make physical sense can be eliminated.

A.8 Appendix: New dimension of the samples

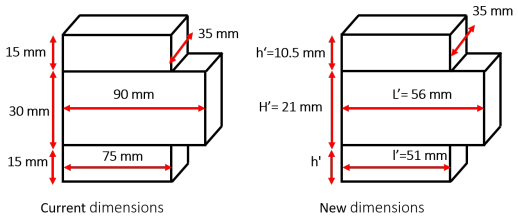

Fig. A.10.: Current dimensions of the samples and new dimensions.

First L' is chosen in order to keep image with 4μm size of effective pixel (as we have already established that for this spatial resolution we are able to measure viscous slip). Thus:

$$L' = 4 \times 14192 = 56.8\text{mm} \tag{A.46}$$

Then two conditions are made on H'. It has to fit the frame of the structure so that the whole sample is capture by one image:

$$2 \times H'_1 = 46 - 2 = 22\text{mm} \tag{A.47}$$

And to keep the same proportion that with the current dimension:

$$H'_2 = \frac{56.8 \times 30}{80} = 21\text{mm} \tag{A.48}$$

The minimum value between H'_1 and H'_2 is 21mm, thus finally H'= 21 mm; $L' = \frac{21 \times 80}{30}$ = 56 mm; $h' = 10.5$ mm an $l' = 51$ mm.